Advanced Synthesis Methods for Lithium Conducting Garnets

by

Jon Mark Weller

A Dissertation Presented in Partial Fulfillment
of the requirements for the Degree
Doctor of Philosophy

Approved March 2021 by the
Graduate Supervisory Committee:

Candace K. Chan, Chair
Peter Crozier
Karl Sieradzki

ARIZONA STATE UNIVERSITY

May 2021

ABSTRACT

Lithium conducting garnets in the family of $Li_7La_3Zr_2O_{12}$ (LLZO) are promising lithium conductors for solid-state batteries, due to their high ionic conductivity, thermal stability, and electrochemical stability with metallic lithium. Despite these advantages, LLZO requires a large energy input to synthesize and process. Generally, LLZO is synthesized using solid-state reaction (SSR) from oxide precursors, requiring high reaction temperatures (900-1000 °C) and producing powder with large particle sizes, necessitating high energy milling to improve sinterability. In this dissertation, two classes of advanced synthesis methods – sol-gel polymer-combustion and molten salt synthesis (MSS) – are employed to obtain LLZO submicron powders at lower temperatures. In the first case, nanopowders of LLZO are obtained in a few hours at 700 °C via a novel polymer combustion process, which can be sintered to dense electrolytes possessing ionic conductivity up to 0.67 mS cm^{-1} at room temperature. However, the limited throughput of this combustion process motivated the use of molten salt synthesis, wherein a salt mixture is used as a high temperature solvent, allowing faster interdiffusion of atomic species than solid-state reactions. A eutectic mixture of LiCl-KCl allows formation of submicrometer undoped, Al-doped, Ga-doped, and Ta-doped LLZO at 900 °C in 4 h, with total ionic conductivities between 0.23-0.46 mS cm^{-1}. By using a highly basic molten salt medium, Ta-doped LLZO (LLZTO) can be obtained at temperatures as low as 550 °C, with an ionic conductivity of 0.61 mS cm^{-1}. The formation temperature can be further reduced by using Ta-doped, La-excess pyrochlore-type lanthanum zirconate ($La_2Zr_2O_7$, LZO) as a quasi-single-source precursor, which convert to LLZTO as low as 400 °C upon addition of a Li-source. Further, doped pyrochlores can be blended with a Li-source and directly sintered

to a relative density up to 94.7% with high conductivity (0.53 mS cm^{-1}). Finally, a propensity for compositional variation in LLZTO powders and sintered ceramics was observed and for the first time explored in detail. By comparing LLZTO obtained from combustion, MSS, and SSR, a correlation between increased elemental inhomogeneity and reduced ionic conductivity is observed. Implications for garnet-based solid-state batteries and strategies to mitigate elemental inhomogeneity are discussed.

DEDICATION

This work is dedicated to my wife Natalie, for her love, constant support, and encouragement, for always being on my team, and who has enabled me to focus on pursuing my PhD studies while caring for our precious children. It is also dedicated to my children, Sadie and Blaise, who bring my heart such joy and who inspire me to continue to learn, to grow, and to be a man worthy of their emulation. It is also dedicated to my parents, who have always supported me and instilled in me a love of learning and curiosity from a young age. Finally, it is dedicated to the One in whom I live and move and have my being, who upholds the universe by the word of His power and has given us this beautiful universe to study and understand, Jesus who loved me and gave Himself for me. *Soli Deo Gloria*.

ACKNOWLEDGEMENTS

There are numerous people to thank and acknowledge, who have encouraged me, supported me, mentored me, and given me opportunities that have led me to this point:

First, I thank my advisor, Prof. Candace Chan, for accepting me into her group, allowing me a high degree of freedom to pursue my research interests, and mentoring me for these last several years. Thank you for pushing me to excel and grow as a scientist and for all your support during challenges and times of stress. I am incredibly thankful to have had you as an advisor and for the my time in your group!

Thank you to Prof. Peter Crozier for your advice, perspective, hospitality, good humor, and for allowing me to be an honorary group member of sorts for collaboration, learning, and recreation. I have learned much from you these last few years and I am grateful for your willingness to be on my committee!

Thank you to Prof. Karl Sieradzki for being on my committee, for helpful perspective, and for helping me to refine my research goals and directions.

I also want to thank all of my fellows in the Chan group, past and present – it has been a pleasure to work and learn with you all.

I want to acknowledge funding from the NSF CAREER award DMR 1553519, which supported my research throughout my doctoral studies.

I gratefully acknowledge the use of facilities within the Eyring Materials Center at Arizona State University supported in part by NNCI-ECCS-1542160.

I want to acknowledge the Diamond Light Source (Didcot, UK) for access to beamline I15-1 (proposal no. CY23152) and D. Keeble for assistance with synchrotron

measurements. Thanks also to Andrew Dopilka for acquiring synchrotron pair-distribution function data at Diamond.

I am also extremely grateful for the financial support provided by the ASU Fulton Schools of Engineering Dean's Fellowship throughout my studies, as well as the generous support of the ARCS Foundation and specifically Bill and Terry Wilhoit.

My deep thanks to my undergraduate advisor, Prof. Fumio Ohuchi for encouraging me to pursue research, advising me and encouraging me in my pursuits.

Thank you to Dr. Brian Marquardt – it was a pleasure working in your group at the Applied Physics Lab and at MarqMetrix. Thank you for the high degree of independence I had in your group even as a recent graduate to pursue novel research and innovate. I grew to love research in your group and for that I am extremely grateful.

I also want to thank Dr. Charles Branham, my supervisor in the Marquardt group as a recent college graduate. Charlie, it was great to work with you and learn from you – thanks for teaching me synthetic chemistry and much more.

Thanks also to Dr. Thomas Dearing for mentoring me, helping me develop as a scientist, and encouraging me in my pursuits. It was a pleasure working with you.

I would like to thank Dr. Barnaby Levin for many helpful discussions and advice regarding electron microscopy.

Thank you to Dr. Shery Chang for your mentorship in electron microscopy – I am glad to have learned from you and your support and tutelage greatly helped my endeavors in microscopy.

I thank Dr. Chih-Long Tsai from Forschungszentrum Jülich GmbH and Dr. Lincoln Miara from Samsung for many helpful discussions regarding LLZO.

TABLE OF CONTENTS

Page

CHAPTER Page

CHAPTER Page

APPENDIX Page

APPENDIX Page

LIST OF TABLES

Table Page

Table Page

Table Page

LIST OF FIGURES

Figure Page

Figure Page

Figure Page

Figure Page

Figure Page

Figure Page

Figure Page

Figure Page

Figure Page

PREFACE

This dissertation is composed in large part of my published works, which are reproduced mostly as-is but edited to fit into a cohesive document. The **Chapters** in this dissertation are summarized as follows:

Chapter 1 – Introduction to the field of research with which I have engaged in my Ph. D. research, an extensive though not exhaustive review of the relevant literature.

Chapter 2 – Introduction to the experimental methods and characterization tools used in my work.

Chapter 3 – This chapter presents my work published in the American Chemical Society publication *Applied Materials and Interfaces* titled – "Non-Aqueous Polymer Combustion Synthesis of Cubic $Li_7La_3Zr_2O_{12}$ Nanopowders." It is mostly reproduced as-is from the published work with minor edits to make it more cohesive with the rest of the document. The supporting information published with the article is reproduced mostly as-is as **Appendix A**.

Chapter 4 – This chapter presents my work published in the American Chemical Society publication *Applied Energy Materials* titled – "Synthesis of Fine Cubic $Li_7La_3Zr_2O_{12}$ Powders in Molten LiCl-KCl Eutectic and Facile Densification by Reversal of Li^+/H^+ Exchange." It is mostly reproduced as-is from the published work with minor edits to make it more cohesive with the rest of the document. Additionally, some of my preliminary experiments in molten salt synthesis not included in the published article are included in this chapter to provide context with the body of my Ph. D. research. The supporting information published with the article is reproduced mostly as-is as **Appendix B**.

Chapter 5 – This chapter presents my work published in the American Chemical Society publication *Applied Energy Materials* titled – "Reduction in Formation Temperature of Ta-Doped Lithium Lanthanum Zirconate by Application of Lux-Flood Basic Molten Salt Synthesis." It is mostly reproduced as-is from the published work with minor edits to make it more cohesive with the rest of the document. The supporting information published with the article is reproduced mostly as-is as **Appendix C**.

Chapter 6 – This chapter presents my work published in the Royal Society of Chemistry publication *Journal of Materials Chemistry A* titled – "Pyrochlore Nanocrystals as Versatile Quasi-Single- Source Precursors to Lithium Conducting Garnets." It is mostly reproduced as-is from the published work with minor edits to make it more cohesive with the rest of the document. The supporting information published with the article is reproduced mostly as-is as **Appendix D**.

Chapter 7 – This chapter presents my work published in the Wiley publication *Advanced Energy and Sustainability Research* titled – "Observation of Elemental Inhomogeneity and its Impact on Ionic Conductivity in Li-Conducting Garnets Prepared with Different Synthesis Methods." It is mostly reproduced as-is from the published work with minor edits to make it more cohesive with the rest of the document. The supporting information published with the article is reproduced mostly as-is as **Appendix E**.

Chapter 8 – This chapter presents unpublished work that is either incomplete but promising with continued investigation or was superseded by some of the other tracks of research that eventually were more fully investigated and published in the peer-reviewed literature. This chapter is split into four sections, each engaging with a specific set of experiments, each of which is intended to be comparable to a very short communication.

These works are included for posterity and as (hopefully) useful information for other researchers working on Li-conducting garnets who could make use of these preliminary results to advance understanding, and I encourage the curious researcher to use this information in any way they desire.

Chapter 9 – Summary of the various research works presented in this dissertation

The organization of this dissertation is split in some sense into two main content sections – the Chapters and the Appendices. Since so much of the published scientific literature is provided with supporting information (including each of my publications) that is important for support but not central to the primary research conclusions, I have opted to adopt a similar convention in organizing **Chapters 3-7** with a corresponding appendix rather than full incorporation of all highly specific details in each chapter. The rationale for this is to present the core conclusions and data in each chapter while not distracting from them with copious details, yet also preserving these details for the curious reader as appendices in one cohesive document.

A list of peer-reviewed publications resulting from my research efforts during my Ph. D. studies is contained **Appendix F**. Permission from co-authors to reproduce co-authored material is contained in **Appendix G** and copyright permissions where applicable were obtained and can be found in **Appendix H**.

1. INTRODUCTION AND BACKGROUND

1.1 Introduction to Lithium-Ion Batteries, Solid-State Lithium Batteries, and Solid-Electrolytes

Lithium-ion batteries (LIBs) are ubiquitous in modern life, most commonly in consumer electronics, and increasingly in electric vehicles and even stationary power storage. Li offers unsurpassed potential cell voltage when applied in a battery.[1] Pure metallic Li has extremely high specific capacity (3860 mAh g^{-1}) and the most negative possible electrochemical potential (-3.040 V vs. the standard hydrogen electrode), thus motivating its use as an anode.[2] However, in practical rechargeable LIBs, Li^+ is contained in a host material to prevent the well-known and potentially disastrous formation of Li-dendrites, which form upon electrochemical cycling and can result in short circuit conditions and uncontrolled, highly exothermic (i.e. explosive) reactions.[2,3] Even in current LIBs using e.g. graphite as an intercalation-type anode, concerns regarding the safety of LIBs require substantial engineering and safety mechanisms including thermal management, shutdown separators, gas vents for volatile electrolyte vapors, fuses or circuit breakers, etc. to ensure safe operation.[3] All told, these components added at the pack level to protect the individual battery cells from destruction reduce the functional energy capacity of a given battery. One of the major hazards associated with LIBs is the toxic, flammable electrolyte mixture that is required to shuttle Li-ions from one electrode to the other during charge and discharge.[1,3,4] In order to increase the safety of future Li-batteries, and potentially allow pure Li anodes for increased energy density, solid

electrolytes have been proposed.[1,2,4,5,6] Where current state of the art LIBs have energy densities on the order of 250 Wh L^{-1}, a solid-state battery (SSB) using metallic Li as the anode could easily achieve an energy density of 750 Wh L^{-1}, even with current cathode technology.[7] An illustration of these differences is shown in **Figure 1.1**. Even higher energy densities may be achievable with next generation cathode systems such as in Li-S or Li-Air (oxygen) batteries.[2,8,9] Finally, reductions in required safety features can be expected to provide increases in overall pack level energy density for SSBs.

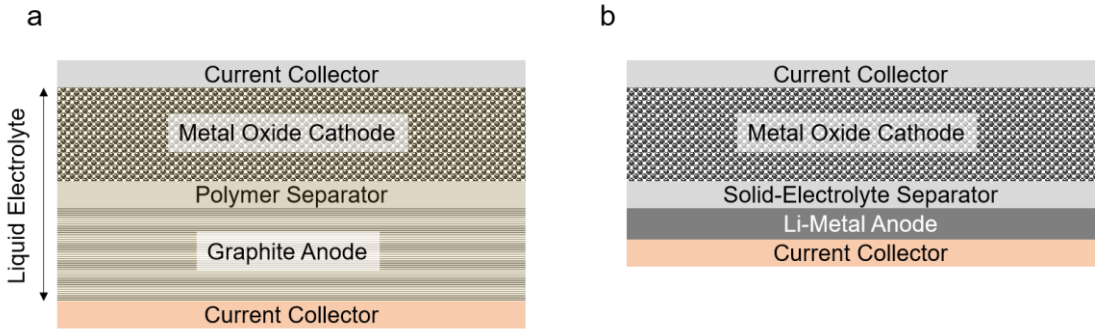

Figure 1.1. Comparison between **a)** conventional Li-ion battery with metal oxide cathode and graphite anode, using a liquid electrolyte to facilitate Li-ion diffusion between each electrodes and a polymer separator to prevent short-circuit and **b)** solid-state Li-metal battery where Li-metal and (for example) a metal oxide are the anode and cathode respectively, with the solid-electrolyte acting as both electrolyte and separator. Even with no other differences between the thickness of the polymer or solid-electrolyte separator and choice of cathode, the use of Li-metal allows equal energy storage in a smaller volume in the case of a solid-state battery.

To-date, a large number of solid electrolytes for Li batteries have been discovered and actively investigated.[5] In general, the following properties are highly desirable if not required for a successful solid electrolyte to be applied to a solid-state battery (SSB)[1,5]:

1. High Li-ion conductivity approaching that of liquid electrolytes (~ 10^{-2} S cm^{-1})
2. Transference number for Li ~ 1
3. Electrochemical stability against metallic lithium in a wide voltage window
4. Electrochemical stability against common cathode materials
5. Resistance to Li-dendrite propagation
6. Negligible toxicity
7. Stability under ambient conditions
8. Ease and low cost of synthesis
9. Environmentally benign components
10. Amenable to thin film deposition or roll-to-roll fabrication

Some examples of such electrolytes are the lithium analogues of NASICON (Na-superionic conductor) type electrolytes such as lithium aluminum titanium phosphate ($Li_{1.3}Al_{0.3}Ti_{1.7}(PO_4)_3$, "LATP"), perovskite types such as lithium lanthanum titanate ($Li_{3x}La_{(2/3-x)}\square_{(1/3-2x)}TiO_3$, "LLTO"), LISICON and thio-LISICON types such as $Li_{14}ZnGe_4O_{16}$ and $Li_{4-2x}Zn_xGeS_4$, glassy oxides and sulfides such as $LiAlSi_2O_6$ and the GeS_2+Li_2S+LiI glass forming systems, lithium phosphorous oxynitride ($Li_{3.0}PO_{2.0}N_{1.2}$, "LIPON"), and finally garnet type electrolytes of the form $Li_xLa_3M_2O_{12}$ (where $3 < x < 7$ and M = Te, Nb, Ta, Sn, Zr, Hf). [5,10] Each type of solid electrolyte has strengths and weaknesses, which must be taken into account when used as an electrolyte.[1,5] In some cases, mainly in sulfide-based electrolytes, severe air reactions may occur resulting in complete degradation of the electrolyte and release of toxic H_2S gas.[11] Many others such as LISICON and perovskite type electrolytes are unstable against Li-metal.[5] Only the garnet family has an advantageous combination of relative stability in ambient conditions

(moisture, oxygen, CO_2 etc.), electrochemical stability against metallic Li[1,5,12] (depending on composition), reasonable chemical stability against most common cathode materials[1], and in the case of lithium lanthanum zirconate ($Li_7La_3Zr_2O_{12}$, "LLZO"), transference number nearly equal to unity[6,13,14], and high conductivity ($\sigma > 0.1$ mS cm^{-1}) approaching that of current liquid electrolytes[4,1,6,15].

1.2. Background on Li-Conducting Garnets

1.2.1. Evolution of Li-Conducting Garnets to $Li_7La_3Zr_2O_{12}$: LLZO

While garnet-structured ($A_3B_2(XO_4)_3$, space group $Ia\bar{3}d$) Li-ion conductors have been under investigation for some time with the first example of garnets of the form $Li_5La_3M_2O_{12}$ being reported in 1988[1], the first synthesis and characterization of LLZO was reported in 2007 by Murugan, Thangdurai, and Weppner.[6] Even before LLZO, many favorable properties were demonstrated such as electrochemical stability against metallic Li, common cathode materials, and relative stability in ambient conditions in garnet systems such as $Li_3Ln_3Te_2O_{12}$ (Ln = Y, Pr, Nd, Sm–Lu), $Li_5La_3Bi_2O_{12}$, $Li_5La_3Ta_2O_{12}$, $Li_5La_3Nb_2O_{12}$, $Li_6BaLa_2Ta_2O_{12}$, and others.[1,6] Depending on the valency of the various 'B' (e.g. Ta) and 'X' (e.g. La) species in the structure, the Li occupancy varies from 3 to 7, with Li-3 being the minimum Li content where Li is located exclusively on tetrahedrally coordinated (24d) lattice sites. Increased Li content increases the amount of Li located on octahedral sites (96h/48g) when total Li-content increases from 5 to 7, with a concomitant increase in ionic conductivity.[1] However, until the advent of the Li-7 type garnets ($Li_7La_3M_2O_{12}$), and specifically LLZO ($Li_7La_3Zr_2O_{12}$), the conductivity of such electrolytes was lacking (i.e. $\sigma << 1 \cdot 10^{-5}$ at RT) and precluded use in a realistic battery.[1,6] Once it was demonstrated that LLZO has significantly higher conductivity than other Li-garnets, many researchers began to actively investigate LLZO over other types of garnets.

1.2.2. Crystal Structure of LLZO and Discussion of Doping Schemes

While most garnets, including Li-conducting garnets adopt a cubic crystal habit (space group $Ia\bar{3}d$),[1,16] LLZO generally adopts a tetragonal structure ("t-LLZO") when extrinsic dopants are absent. Awaka et al. produced phase-pure tetragonal (space group $I4_1/acd$) LLZO, demonstrating that its conductivity was roughly $1x10^{-6}$ S cm^{-1}, with an activation energy for Li-diffusion of 0.54 eV.[17] The crystal structures of cubic and tetragonal LLZO are depicted in **Figure 1.2**. Early on, it was discovered[14,16] that adventitious Al-doping of LLZO from the alumina crucibles used occurred due to the high temperatures and long times required in solid-state reactions (SSR) and sintering, including in the first demonstration of LLZO by Murugan[6] et al. Indeed, Buschmann et al. demonstrated that either addition of alumina to the powder mixture during SSR or use of long sintering times in alumina crucibles was required to form highly conductive cubic LLZO ("c-LLZO") phase over the poorly conducting tetragonal polymorph.[14] For intentionally Al-doped LLZO (ALLZO), the conductivity measured was between 0.3-0.4 mS cm^{-1}, with an activation energy of 0.34 eV.[14] This result was demonstrated similarly by Geiger et al.[16] In both cases, both ^{7}Li NMR and ^{27}Al NMR studies were performed, indicating that Al preferentially dopes Li lattice sites, and results in Li-vacancies, which are believed to result in stabilization of the cubic phase.[14,16] Additionally, Geiger et al. observed that, in their case, Al incorporates into LLZO through a $LaAlO_3$ intermediate phase.[16]

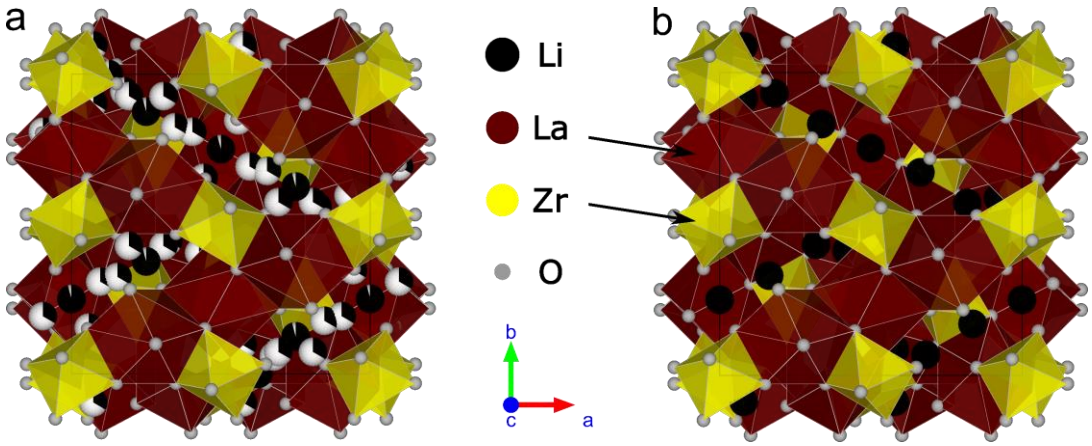

Figure 1.2. Crystal structure of a) cubic (a = 12.975 Å)[16] and b) tetragonal (a = 13.134 Å, c = 12.663 Å)[17] LLZO in (100) orientation. Note that the white / black coloration of the Li atoms in (**a**) relates to partial lattice site occupancy. The primary difference between cubic and tetragonal LLZO is the disordering of the Li-sublattice in the cubic polymorph compared to the highly ordered Li-sublattice in the tetragonal polymorph. Structures generated in VESTA[18] software based on the structures presented in Geiger et al.[16] (**a**) and Awaka et al.[17] (**b**).

A further exploration of the mechanism of cubic structure stabilization of LLZO by Al was performed by Rangasamy et al.[19] In this work, the Al-content on a mole per formula unit (PFU) basis was varied from 0 to 0.24 (i.e. $Al_{0.24}Li_{6.24}La_3Zr_2O_{12}$) in small increments, and it was determined that a minimum of 0.204 moles PFU of Al are required to stabilize the cubic phase over the tetragonal phase.[19] It was also determined that the solubility limit of Al in LLZO is 0.389 moles per formula, and that the critical factor to stabilize the cubic phase over the tetragonal is the Li content.[19] Using inductively coupled plasma mass spectrometry (ICP-MS), it was determined that when the Li content was less than 5.63, some of the pyrochlore phase decomposition product lanthanum zirconate ($La_2Zr_2O_7$, "LZO") formed, with pure c-LLZO forming when the Li content is between 5.63 to 6.24 moles per formula. Finally, as the Li content increases, at some value

between 6.24 and 7.32 (potentially indicating surface Li-species since the maximum content in LLZO is theoretically Li-7), even Al-doped c-LLZO converts to t-LLZO, strongly indicating that Li-vacancies are the main cause of cubic phase stabilization.[19] In a separate work, Matsuda et al. also found that the critical doping level required to stabilize cubic LLZO using Al as the dopant was in the range of 0.2-0.25 moles per formula.[20]

Noting that an aliovalent dopant is required to stabilize the highly conducting cubic phase, other researchers began to incorporate various dopants to understand the effect on crystal chemistry, ionic conductivity, activation energy, and other parameters of LLZO. Gallium is one frequently utilized dopant, with an early example of Ga-doped-LLZO (GLLZO) from Wolfenstine et al. in 2012.[13] In this case, Ga-doping under the same conditions resulted in slightly higher conductivity (0.35 mS cm^{-1}) than ALLZO. Other notable examples of GLLZO in the literature (including some with exceptionally high room temperature ionic conductivity) have been demonstrated, including by El-Shinawi et al. (0.54 mS cm^{-1}),[21] Afyon et al. (0.4 mS cm^{-1}),[22] Wu et al. (1.46 mS cm^{-1}),[15] Yi et al. (1.3 mS cm^{-1}),[23] and Qin et al. (2.06 mS cm^{-1})[24].

While Al and Ga both dope the Li-sublattice, other doping schemes are also possible, including Nb^{5+} [25,26] and Ta^{5+} [26–43] to dope the Zr sublattice, Ca^{2+} [9,35] and other alkaline earths such as Ba^{2+} [44] to dope the La sublattice (often used in conjunction with another site dopant), and even recently F^{-} [45–47] to dope the oxygen sublattice. While La-site and O-site doping, along with co-doping schemes such as Ca/Ta[35] doping, Ba/Ta[44] doping, Ga/F[46,47] doping, and others are of interest, single doping schemes are the most common and, as will be explored in **Chapter 7**, potentially the most practical given the

potential for multiple garnet compositions to form within a single sample even for a single dopant.

Besides Li-site dopants, Zr-site dopants are the next most common doping scheme for LLZO. Ohta et al. synthesized Nb-doped LLZO (LLZNO) of the formula $Li_{7-X}La_3(Zr_{2-X},Nb_X)O_{12}$ (X=0–2), showing very high conductivity of 0.8 mS cm^{-1} and apparent electrochemical stability up to 9V vs. Li^+/Li using cyclic voltammetry.[12] However, subsequent studies by Kim et al., demonstrated that extended DC cycling led to reduction of Nb(V) to Nb(IV), resulting in increased interfacial resistance with Li-metal and eventual short-circuit of the electrolyte.[26] Although such reduction was observed in the studies of Kim et al.,[26] other researchers such as Fu[9] and Hitz[8] have employed Ca and Nb co-doped LLZO seemingly without similar issues. However, Kim et al. demonstrated that Ta-doped LLZO possessed good electrochemical stability even after extended cycling, with comparable ionic conductivity to Nb-doped LLZO.[26] Logéat et al. synthesized Ta-doped LLZO (LLZTO) with varying composition covering the entire $Li_5La_3Ta_2O_{12} – Li_7La_3Zr_2O_{12}$ solid-solution ($Li_{7-x}La_3Ta_xZr_{2-x}O_{12}$ (x=0.125–2)), showing by Rietveld analysis of high-resolution X-ray and neutron diffraction, that when Zr is replace by Ta, the lattice constant shrinks slightly with increasing Ta-content and that Li atoms transition from a highly ordered sublattice correlated with the tetragonal phase to a disordered sublattice, resulting in interconnected tetrahedral and octahedral lattice sites.[48] This disordered, interconnected substructure is identified as the likely cause of higher conductivity in c-LLZO vs. t-LLZO.[48] This result accords with the findings of Rangasamy et al.[19] wherein excess Li-content even in Al-doped LLZO causes similar transition to a tetragonal structure.

Interestingly, Logéat et al. obtained nominally cubic garnets even for low-Ta compositions (x = 0.125 moles PFU). However, further exploration of the critical doping level of Al-free, Ta-doped LLZO by Thompson et al. indicates that the critical doping level is approximately 0.4-0.5 moles Ta PFU, and that tetragonal distortion is present for lower Ta-content (i.e. 0.25 moles PFU).[36] Crucially, Raman spectroscopy and neutron diffraction instead of x-ray diffraction were necessary to clarify that subcritically doped LLZTO is partially tetragonal.[36] Additionally, Thompson explored the effect of Ta-doping level on ionic conductivity in LLZTO, demonstrating that a balance of enough Li-vacancies to stabilize the cubic phase while maintaining a high enough population of mobile Li-ions is crucial to optimize ionic conductivity.[37] This work clarifies that not all Li-ions are available for ion conduction and that slight changes in Li-content can result in substantial variation in ionic conductivity.[37] These results imply that tuning the Li-content by careful incorporation of dopants and processing is crucial to optimize the ionic conductivity of LLZO. The origins of high ionic conductivity in Li-garnets (and other solid-electrolytes) was explored computationally by He et al., who also showed that balancing high Li-content and a critical amount of vacancies is important.[49] In this case, the nature of the Li-sublattice was explored in greater detail, demonstrating that it is the interconnected nature of the disordered Li-sublattice in cubic LLZO along with a large enough population of Li-ions on higher energy lattice sites that acts in conjunction to enable concerted ion hopping.[49]

Clearly, the crystal chemistry, Li-content, and location of Li-ions in the structure all strongly influence the electrochemical behavior of LLZO. For these reasons, Ta-doped LLZO is one of the most popular doping schemes of the many possible compositions of

LLZO, as LLZTO with composition generally within $Li_{7-x}La_3Zr_{2-x}Ta_xO_{12}$ ($0.2 < x < 1$) combines good electrochemical stability with lithium metal[26] and high ionic conductivity (> 1 mS cm^{-1})[38,50,51], and by virtue of doping the Zr sites in the garnet structure, does not block sites on the Li-sublattice[27] unlike other dopants such as Al or Ga. These factors also influenced the transition from Al- and Ga-doped LLZO (**Chapter 4**) to Ta-doped LLZO (**Chapter 3, 5-7**) in the research presented herein.

1.2.3. Challenges with LLZO Solid-Electrolytes – Surface Reactivity

In addition to dopants, surface reactions can also result in Li-vacancies and stabilize the cubic phase. The most well-known example is that of proton exchange, wherein in the presence of water (vapor or liquid), Li from LLZO will spontaneously form LiOH, allowing protons to intercalate into the LLZO lattice, often followed by formation of Li_2CO_3 if atmospheric CO_2 is present (**Equations 1.2.1** and **1.2.2**).[32,52–56] Even in a dry atmosphere, the presence of CO_2 will result in the formation of Li_2CO_3, albeit at a slower rate.[52,53,55] The resultant c-LLZO does not maintain high conductivity: rather Li^+/H^+ exchange[52,53,56], or so-called "CO_2 doping"[57] result in conductivity values often worse than that of t-LLZO.

$$Li_7La_3Zr_2O_{12} + xH_2O \rightarrow Li_{7-x}H_xLa_3Zr_2O_{12} + xLiOH \quad (\mathbf{1.2.1})$$

$$LiOH + \frac{1}{2}CO_2 \rightarrow \frac{1}{2}Li_2CO_3 + \frac{1}{2}H_2O \quad (\mathbf{1.2.2})$$

However, the work of Liu et al. indicates that reasonable Li-ion conductivity can still persist in proton-exchanged LLZO so long as proton-exchange is not too severe, and that protons are essentially immobile in the lattice (i.e. negligible bulk conductivity) at room temperature.[58] This effect implies that LLZO may be suitable[58] for aqueous Li-metal batteries, although this most likely is reliant upon preventing any other proton diffusion mechanisms e.g. grain boundary diffusion or diffusion through pores, and thus can be expected to require highly dense garnet membranes.

1.2.4. Challenges with LLZO Solid-Electrolytes – Interfacial Impedance and Lithium Dendrite Intrusion

Another effect of LLZO surface reactions with atmospheric H_2O or CO_2 is high interfacial impedance between LLZO and Li-metal. The presence of even small amounts of e.g. surface Li_2CO_3 can be quite deleterious and prevents good contact between Li-metal and the LLZO surface. Some researchers such as Sharafi et al. have gone to great lengths to undo the effects of reactions between LLZO and H_2O / CO_2, including polishing dense LLZO pellets to a mirror finish under argon followed by thermally evaporating away the remaining LiOH or Li_2CO_3 at elevated temperature up to 500 °C.[55] While eventually resulting in remarkably low interfacial area specific resistance (ASR) of 2 Ω cm^2, the steps taken to do so are quite involved, and illustrates a remaining challenge in incorporation of LLZO into realistic battery production. On the other hand, a milder thermal treatment of 250 °C under inert atmosphere was still able to reverse protonation and reintroduce Li into the lattice (essentially the reverse of **Equations 1.2.1** and **1.2.2**),

reducing the interfacial impedance from 1.9 MΩ to 750 Ω after heating for 12 h.[59] This initially high interfacial impedance of 1.9 MΩ illustrates the importance of forming a good interface between Li-metal and LLZO. In addition to thermal treatments in inert atmosphere, some other interface modification strategies have been demonstrated. In one case, sintered garnet pellets were soaked with organic solvents containing $LiBF_4$ (a standard salt component of liquid LIB electrolytes), which had the effect of liberating transient HF to react with surface Li_2CO_3 or LiOH and substantially reducing interfacial impedance by a factor of about 8.5.[60] Another solution-based approach utilized phosphoric acid to dissolve Li_2CO_3 and instead form a uniform Li_3PO_4 surface layer with the effect of producing a thin, lithiophilic solid electrolyte interphase and reducing interfacial resistance to as low as 7 Ω cm^2.[61] Other approaches to minimizing interfacial impedance between Li-metal and the garnet electrolyte rely on an atomic layer deposition (ALD) coating such as Al_2O_3 as demonstrated by Han et al., wherein a thin Al_2O_3 conformal coating reduced interfacial ASR from 1710 Ω cm^2 to 34 Ω cm^2.[62] An alternative simple coating method relies on applying a graphite layer to the surface of a sintered garnet membrane, as demonstrated by Shao et al.[63] Finally, Li-metal alloys can also be used to confer better wettability between the Li-metal anode and the garnet surface. In one case, a Li-Mg alloy was employed, which retains an electronic and ionic conducting Mg framework as Li is stripped from the anode during cycling and allows high current densities with ASR as low as 35 Ω cm^2.[64] Another notable example is the use of Li-Sn alloys (20 wt %, 1.5 mol %) in a similar manner, producing ASR as low as 7 Ω cm^2.[65] This last method has been employed extensively in the works presented herein in **Chapters 3, 5, 6, and 7** and is effective and simple to implement.

One of the primary motivations for reducing the ASR of Li-metal / garnet interfaces is the observation that metallic Li can penetrate[56,66–71] through dense solid electrolytes and cause short circuits in SSBs, with the critical current density (CCD) above which Li-metal penetrates the electrolyte observed to be inversely[72] related to the interfacial impedance. It was previously expected that LLZO, with its high shear modulus would be impervious to Li-dendrite propagation.[73] This assumption is based on the Monroe criterion (originally developed with polymeric electrolytes in view), wherein it is expected that a solid electrolyte will be immune to dendrite penetration as long as its shear modulus is > 2x that of Li metal.[56,69,73,74] Where Li metal has a shear modulus of ~ 2.83 GPa[75], that of LLZO is much higher (between 59-61 GPa depending on dopant type)[73], roughly 21 x higher than that of Li metal. However, based on observations that short circuits do occur at high current density in LLZO electrochemical cells, it is clear that the Monroe criterion is insufficient to describe the propensity of Li to penetrate through LLZO and other solid electrolytes. Separate works by Cheng et al.[76] and Porz et al.[69] observed Li filaments extending from fracture surfaces, apparently mainly propagating through the grain boundaries. These observations and others have motivated considerable efforts to understand the mechanism of Li-intrusion and ways to minimize or eliminate it (including the interface modification strategies discussed so far). For example, Cheng et al. demonstrated that there is a grain size effect correlated with air reactivity (i.e. formation of Li_2CO_3), interfacial impedance, and critical current density (CCD) at which Li dendrites form and cause a short circuit.[53,67] In all cases, a finer grained microstructure was correlated with better properties: lower interfacial resistance correlated with reduced formation of Li_2CO_3 upon exposure to air, and a higher CCD

before which Li dendrites caused a short circuit. This was explained by a more distributed Li-ion current through the LLZO when a larger number of grain boundaries are present (i.e. small grain size) compared to more focused current at fewer failure points for larger grain sizes. However, the CCD was still only 0.3 mA cm^{-2} in this case, about 3x lower[68] than the minimum value needed for practical battery applications.

A study by Sharafi et al. demonstrated an opposite trend to that of Cheng et al., wherein very large grain size was correlated with improved CCD.[68] This seemingly contradictory result was explained in terms of separating the grain size effect on interfacial impedance from Li dendrite propagation. In this case, a higher CCD of 0.6 mA cm^{-2} was reported, the highest reported at that time but still lower than necessary for practical applications.[68] More recent work from the same group has shown higher CCD values approaching 1 mA cm^{-2} at room temperature.[77] While it may seem intuitive at this point to propose a single crystalline electrolyte with no grain boundaries as failure points, Porz et al. demonstrated that even a single crystal of LLZTO can be short circuited by a Li dendrite at a CCD as low as 1 mA cm^{-2}.[69] In this case, the effect of surface roughness was investigated as a potential explanation of Li-dendrite initiation, but there was no obvious correlation between roughness and the CCD for polished single crystalline LLZTO, meaning that even very fine surface defects might allow Li-dendrites to nucleate.[69] Crack initiation and propagation by Li metal is hypothesized to result from electrodeposition of Li-metal at the crack tip, which can cause further crack propagation. Expanding on these single crystal studies, Swamy et al. studied the effect of electrical field intensity on current density concentration, showing that rather than defects being the primary source of Li-dendrite intrusion, regions of high or concentrated electric field

(such as the edge of the working electrode) promote initial Li-intrusion.[78] Finally, Porz et al. developed an electromechanical model with which to correlate mechanical stress within defects to the overpotential resultant from interfacial resistant during Li conduction or plating.[69] It has also been shown that increasing the pressure on the Li-LLZO interface can reduce ASR and increase the CCD: this is because at high current densities, voids form between Li-metal and the garnet surface, effectively reducing the contact area and increasing the local current density.[79] Increased pressure has the effect of imposing plastic deformation / creep on the Li-metal to maintain good contact with garnet, and therefore evening out the current distribution. Other researchers have also shown that more uniform Li-ion current improves the CCD through the use of a Au interlayer to uniformly distribute Li-current from Li-metal to the garnet electrolyte.[28]

Other challenges regarding LLZO are related to synthesis and processing, which are discussed in the next section and are the primary subject of my research. While the research presented in this dissertation has not focused directly on the Li-metal / LLZO interface, there are still implications of synthesis and processing on interfacial ASR and CCD, and as will be discussed in greater detail in **Chapter 7**, local deviations in composition and resultant local deviation in ionic conductivity are another potential source of non-uniform Li-ion current, which may also contribute to reduced CCD.

1.3. Synthesis Methods for LLZO

1.3.1. Solid-State Reaction

As alluded to previously, in many cases solid-state reactions (SSR) are used to synthesize LLZO.[1,4,6,12–14,16,17,19,21,26,32,44,48,53,67,68,80–82] In fact, the majority of papers investigating LLZO seem to use SSR, as it is a well-established technique for synthesis of complex oxides. Generally, solid-state reactions rely on intimate mixing to provide physical contact between powdered reagents followed by heating to high temperatures (often at temperatures between 1000-1500 °C) to provide the thermodynamic driving force for diffusion of atomic species and formation of the desired phase.[83] In many cases, SSR is performed by pressing pellets of the reagents to maximize contact area, followed by one or potentially several heat treatments with repeated grinding/milling and pelletizing between each treatment.[83] Clearly, in order to achieve phase purity, a large amount of time and energy are often required, in addition to many repetitive processing steps, and the morphology of resultant materials tends to be irregular.[84] Further, there is a practical lower limit to the size of materials obtainable by SSR when high energy milling techniques are used for particle size reduction.[23] In many cases, deleterious amorphization of oxides also occurs under extensive ball-milling.[85] Ball-milling of LLZO using solvents is quite common, and many common solvents can participate in similar proton exchange reactions as water, introducing further (often overlooked) processing variables.[86] Thus, despite the simplicity of SSR, the high time and energy cost and poor morphology (i.e. large particle size, large size distribution, irregular shaped particles etc.)

of resultant materials has motivated the use of more advanced synthesis methods for LLZO. One outstanding case of using SSR for preparation of LLZO is that of Huang et al.: in this work, LLZTO was synthesized using conventional SSR in large quantities and subsequently attrition milled to result in primary particles of ~300 nm diameter.[87] In this case, 300 nm was apparently the smallest particle size achievable by attrition milling. That said, to mill the as-synthesized powders to such a small size requires substantial amounts of solvent (2:1 to 3:1 solvent to powder). In this case, a 4:1 mixture of water to ethanol was used, resulting in a relatively inexpensive solvent system compared to typical systems used for attrition milling such as acetone or 2-propanol.[87] Still, to obtain the attrition milled powders, spray drying was performed, resulting in particle aggregates on the order of several microns, and requiring handling of a large amount of solvent waste. Despite the larger number of processing steps, the higher surface area of these powders combined with the relative simplicity of SSR make this an attractive approach.

1.3.2. Sol-Gel Synthesis

The sol-gel method is a common synthesis method for production of complex oxides and particularly nanosized oxides.[88,89] Commonly, metalorganic precursors (e.g. metal alkoxides) are employed, although metal salts may also be employed with the correct chelating agents in the solution.[88] A classic example of synthesis of nanomaterials via sol-gel synthesis is that of precipitation of silica spheres from tetraethylorthosilicate in basic aqueous-alcohol solutions.[90] Depending on the conditions used, sol-gel techniques can be used to deposit thin films, precipitate particles, result in aerogels, and

are otherwise versatile in the synthesis of complex oxides.[4,84,88,90] Sol-gel methods have been used in the synthesis of LLZO by several researchers.[91–94]

A notable example of the synthesis of Al-doped LLZO ("ALLZO") is that of Sakamoto et al., wherein Al_2O_3 nanocrystals and soluble Li, La, and Zr precursors were employed to result in a gel network with an Al_2O_3 'backbone,' as demonstrated by supercritical drying of the gelled precursor.[95] In this case, ALLZO formed as low as 600 °C from calcination of the gelled precursors, and induction hot-pressing allowed sintered pellets with densities up to 96% of the theoretical density of ALLZO with conductivities up to 0.4 mS cm^{-1}. [95] Critically, the use of hot-pressing and nanocrystalline starting material allowed a final ceramic with an average grain size of only 260 nm, more than 10x smaller than using conventional SSR-derived powder.[95]

1.3.3. Modified Sol-Gel and Combustion Syntheses

A modification of sol-gel type synthesis is the Pechini method.[89] This method, named after M. P. Pechini from the 1967 patent,[89] utilizes a chelating agent such as citric acid to form complexes with dissolved metal nitrates, followed by addition of a glycol (e.g. ethylene glycol) and subsequent in situ polymerization (i.e. transesterification between citrate and glycol) to form a network of metal chelates entrapped in a citrate-glycol polymer backbone.[89] This precursor is heated to mild temperatures resulting in the decomposition of nitrate anions and partial combustion of the material, yielding a reactive precursor which, upon calcination, generally results in ultrafine crystalline

material. Other similar methods, often termed solution combustion synthesis, rely on similar processes involving metal nitrates and a combustible carbon source.[96]

The literature is rife with variations on this method, and many researchers have used similar methods to synthesize LLZO. An example of this type of sol-gel method is from Afyon et al., in which GLLZO was the target material.[22] Uniquely, fine powders of t-LLZO could be obtained at only 650 °C, which were then combined with Ga_2O_3 after synthesis. Evidently, Ga was incorporated into the LLZO lattice to form c-LLZO at temperatures as low as 150 °C to form GLLZO. Subsequently, these powders were densified at a relatively low temperature of only 950 °C, and exhibited a conductivity of 0.4 mS cm^{-1} at a relative density of only 76%.[22] Shimonishi et al. utilized a similar method to synthesize LLZO starting from Li_2CO_3, La_2O_3, and $Zr(OEt)_4$, all of which were dissolved in HNO_3, mixed with citric acid and ethylene glycol and subsequently treated at elevated temperature.[97] Once the precursor was gelled, it was dried at elevated temperature to form a partially combusted black powder, which could be converted to LLZO via calcination at 800 °C. Similarly, Kokal et al. used a similar so-called "modified-Pechini" method (with different organic components) to synthesize apparently undoped c-LLZO or t-LLZO depending on the processing conditions.[98] It is noteworthy that this method yielded no LLZO, but rather the LZO pyrochlore phase when a calcination temperature of 923 K was used, but phase pure c-LLZO was obtained at 973 K. Heating to higher temperatures yielded t-LLZO, and as such the conductivity was quite low. Janani et al. also used a similar method albeit without ethylene glycol.[99] In this case, both undoped c-LLZO and ALLZO were synthesized at temperature between 700-

800 °C. Conductivity measurements were not performed in this case, but it was noted that dopants were evidently not required to stabilize the cubic phase in some cases.

Sol-gel and combustion methods are well suited to producing LLZO not only at lower temperatures but in nanostructured forms.[84] Yang et al. demonstrated that by utilizing a similar sol preparation method as that used by Janani et al. in conjunction with a solution of poly(vinylpyrrolidone) (PVP), that electrospun PVP-LLZO-sol nanofibers could be formed with nanometric dimensions.[100] Upon calcination at 700 °C, nanofibers derived from both aqueous sols and non-aqueous sols could be converted into LLZO while preserving the nanowire morphology. In this case, no dopants were required to stabilize the cubic phase; the explanation given for this phenomenon is that, similar to many other metal oxide systems (such as TiO_2 or ZrO_2), reduction of crystallite size results in an otherwise non-thermodynamically stable crystalline phase, due most likely to surface energy considerations.[100,101] To confirm this assertion, size reduction of bulk t-LLZO by high energy milling to yield submicron LLZO particles was shown to result in conversion from t-LLZO to c-LLZO, further corroborating the size-stabilization effect.[100] Building on this work, Gordon et al. demonstrated that templating of the same LLZO sol used in Yang's work onto nanocellulose resulted in small undoped c-LLZO particles as well.[102] In this case as well it was supposed that the nanosized pores of the nanocellulose allowed size restriction of the LLZO precursors, which in turn resulted in nanosized undoped c-LLZO. Some potential benefits of employing nanosized LLZO include better sinterability (as nanosized oxides tend to sinter more easily than bulk oxides)[103] and as active materials in composite polymer electrolytes (CPEs)[84], as has been demonstrated using nanosized LLZO prepared via ball-milling[104], hydrogel templating[105], nanocellulose

templating[106], and electrospinning[107,108]. In the case of electrospinning, throughput of material tends to be a challenge, yielding typical production rates of tens of milligrams per hour unless an advanced electrospinning apparatus is used[109,110]. Other templating methods have similar drawbacks.

It is interesting to note at this point that in nearly all cases of combustion synthesis discussed so far, the form of undoped LLZO is that of a coral-like structure of interconnected ligaments. This was observed in the materials synthesized by Kokal et al.,[98] Yang et al.,[100] Gordon et al.,[102] and Afyon et al.[22] Curiously, in the cases of Kokal, Yang, and Gordon, the materials obtained were at least in some cases undoped c-LLZO, whereas in the case of Afyon et al., the material was undoped t-LLZO with very similar size and morphology. This difference likely arises from differences in actual Li content in these various samples. These results taken together may indicate that, rather than conventional size stabilization based on surface energy, small sizes LLZO particles simply have enough vacancies from formation of surface Li_2CO_3 to stabilize the cubic phase.

A different combustion-based synthetic procedure has been demonstrated by Yi et al. based on liquid-feed flame spray pyrolysis (LF-FSP). In this process, metalorganic precursors are dissolved in a combustible solvent, nebulized to result in a high velocity stream, and combusted with the heat generated through combustion used to drive formation of oxides.[23,111] Using this method, the as-synthesized product is not LLZO, but rather nanosized “decomposed LLZO” consisting of the LZO pyrochlore phase, an unknown but most likely non-crystalline La-containing phase, and Li_2CO_3. However, when these powders were tape-cast, thin and phase pure dense (>94%) LLZO membranes

were obtained, with conductivities of 0.2 mS cm^{-1} for ALLZO[111] and up to 1.3 mS cm^{-1} for GLLZO[23]. Advantageously, the sintering process used for these tape-cast films required lower temperature (1080 °C) than many other heating schemes used by other researchers, and took only 1 hour to reach maximum density.[23,111] This approach of synthesizing nanosized precursors followed by tape-casting demonstrates incredible promise for application of LLZO, as membranes / thin films rather than large dense pellets are an ideal geometry for practical battery applications. The primary drawbacks to this synthesis method are the inability to obtain pure LLZO nanoparticles rather than "decomposed LLZO," and the complexity of the reactor.

1.3.4. Thin-Film Deposition

Rather than synthesis of ceramic powders and subsequent 'conventional' ceramics processing, several researchers have investigated thin film deposition methods for formation of LLZO films. Sol-gel spin-coating of Li-garnet has been attempted by Bitzer et al., and while the garnet phase formed the conductivity was quite low (~ 3.4 x 10^{-8} S cm^{-1}).[112] For example, Loho et al. utilized laser-assisted chemical vapor deposition ("CVD") to prepare thin polycrystalline films of t-LLZO with conductivity on the order of 4 x 10^{-6} S cm^{-1}.[113] Using atomic layer deposition ("ALD"), Kazyak et al. were able to form an amorphous stoichiometric ALLZO conformal film on several substrates with conductivity on the order of 1 x 10^{-8} S cm^{-1}.[114] Attempts were made to crystallize the LLZO film, but Li volatility was an extreme challenge, requiring 400% excess Li to allow the LLZO to crystallize, and even in this case impurity phases were present in the

thin films and the conformal nature of the films was destroyed.[114] Garbayo et al. demonstrated that a glass-type polyamorphism is present in some thin film LLZO when formed using pulsed laser deposition ("PLD"). In this case, tuning the local order of the glassy garnet phase can change the ionic conductivity, and presents an opportunity for application of very thin glassy electrolyte films.[115] Unfortunately, depending on heat treatment conditions, Li volatilization was shown to occur with the formation of the LZO pyrochlore phase, and the conductivity of thin films was still quite poor.[115] Generally speaking, the loss of Li_2O[115–117] under heating to crystallize the as-deposited thin films in vacuo is a major challenge, and only recently has it been somewhat mitigated by employing a co-sputtering[118] technique wherein Li_2O is co-deposited with LLZO to form a Li_2O-rich thin film, which after heat treatment has a room temperature conductivity of 1.9×10^{-4} S cm^{-1} for GLLZO, within an order of magnitude of that of bulk LLZO. In short, while thin film deposition techniques are attractive from a processing standpoint, the properties of LLZO films to-date generally fall short of those formed via conventional ceramic processing methods, motivating improved methods of LLZO film deposition.

1.3.5. Molten Salt Synthesis

More recently, molten salt synthesis (MSS) has been applied to formation of LLZO. Briefly, MSS is a frequently used synthetic route for formation of complex oxides, often resulting in high quality nanocrystalline products at temperatures often lower than those required by SSR for the same target material.[119,120] The general process of MSS utilizes a salt or salt mixture of a given composition as a high temperature

solvent for liquid-phase reactions, generally for oxides but also applicable other materials.[119,120] A depiction of this process is shown in **Figure 1.3**:

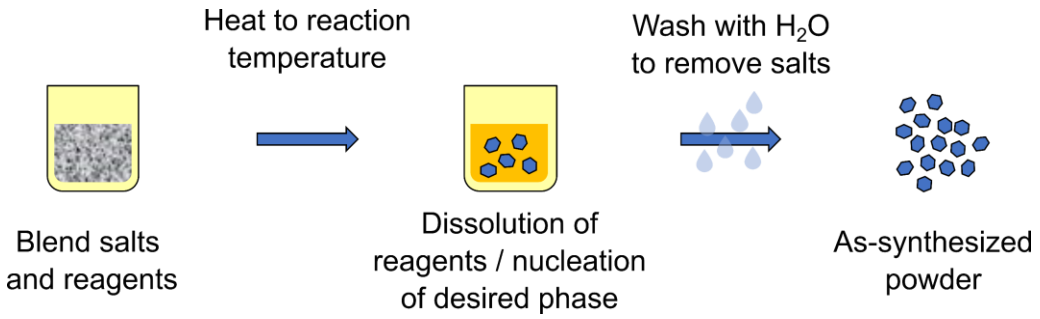

Figure 1.3. Depiction of general flow of MSS process beginning with intimate mixing of salts and reagents, heating of the mixture to the desired reaction temperature, and cooling and washing away salts with water to obtain the as-synthesized product.

One example of a flux-based synthesis of LLZO is that of single crystals of t-LLZO[17] using Li_2CO_3 at 1040 °C or of c-LLZO[121] using a LiNO3 'self-flux' at 1150 °C. However, the first example of conventional MSS of small LLZO powders was by Reddy and Adams, wherein LLZTO of nominal composition $Li_{6.75}La_3Zr_{1.75}Ta_{0.25}O_{12}$ was successfully obtained.[122] In this case, a eutectic mixture of $LiNO_3$ and LiCl (88:12 molar ratio) was utilized as the molten salt or flux, and LLZTO was obtained at temperatures above 700 °C. However, there were several substantial challenges to this route: first, the as-synthesized materials had irregular and agglomerated morphology, more characteristic of SSR than MSS. Second, the material could not be densified and exhibited conductivity ~ 100x lower than expected, on the order of t-LLZO.[122] Most likely, this is due to the fact

that ~ 90% (by mass) of the flux was composed of $LiNO_3$, which decomposes at T > 600 °C.[123] Since LLZTO was only obtained at temperatures above 700 °C in the case of Reddy's work, this implies that possibly a flux-assisted SSR is a more likely scenario under which LLZTO formed, rather than uniform nucleation of LLZTO in the molten salts. In terms of the lack of conductivity and inability to densify the as-synthesized powder, the explanation offered is that substantial Li^+/H^+ exchange resulted in Li-deficient protonated LLZTO, which is well-known[52] to have poor conductivity. Since washing with copious amounts of water is necessary for workup in MSS, protonation presents a severe challenge to application of MSS to LLZO. A more recent paper from Badami et al. utilized the MSS approach based on my research (described in **Chapter 4**) for synthesis of LLZTO.[124] In this case, the use of excess mother powder during sintering allowed proton-exchange to be mitigated, affording LLZTO electrolyte ceramics with high relative density and conductivity up to 0.6 mS cm^{-1}.

1.4. Ceramic Processing of LLZO

Clearly a wide range of synthetic techniques allow LLZO to be obtained, each with various advantages and disadvantages. However, synthesis of LLZO is only the first step towards application in a SSB and ceramic processing is a critical aspect to achieving useful garnet electrolytes. Since LLZO is a hard, brittle ceramic, it is generally processed into functional pieces similar to other technical ceramics i.e., via sintering. Sintering is a thermally activated process whereby a powder compact is densified into a single solid by mass transport between particles in the powder.[125] Where high temperatures generally in excess of 900 °C are required to synthesize LLZO (via SSR), even higher temperatures (generally in excess of 1100 °C for conventional sintering) are generally required to sinter LLZO powder into a dense ceramic electrolyte. In most cases, LLZO powder is compacted using a die into a so-called 'green' or un-sintered pellet, followed by heat treatment to cause the individual compacted particles to coalesce. In simple terms, there are two main solid-state sintering mechanisms: surface diffusion and bulk diffusion.[125] Surface diffusion occurs along the surfaces of individual particles in a powder compact and is the dominant mass transport mechanism at lower temperatures, leading to coalescence of particles via formation of necks between them, but not producing net densification. Bulk diffusion on the other hand, dominates at higher temperatures and results in net solid-state diffusion and mass transport, causing densification as pores are eliminated. Sintering processes are dependent on heating rate, sintering atmosphere, sintering temperature or temperatures in the case of multiple-step sintering, and of course the hold time at a given temperature, among other factors, not to mention pressure-

assisted sintering, liquid-phase sintering, and so forth.[125] Sintering is a highly complex process with many variables that affect the final density, microstructure, and other properties of a sintered material.

In the case of LLZO, the processes involved in sintering are even more complex due to the strong propensity for Li_2O to evaporate at relevant sintering temperatures.[4] For this reason, additional Li-sources, often comprising excess 'mother powder' of the same composition to cover the green LLZO pellet, are placed in the crucible used for sintering (often Al_2O_3[6] although MgO[126] or even Pt[39] crucibles are used to prevent reaction between the crucible and the LLZO pellet) to offset the loss of Li_2O, which eventually results[19] in decomposition of the garnet into Li-deficient pyrochlore type $La_2Zr_2O_7$. Since measurement of ionic conductivity of a given LLZO sample generally requires a densified sample, the reports of sintering of LLZO are nearly as abundant as reports on LLZO in general and are thus too numerous to properly review in this chapter. More advanced sintering techniques such as hot-pressing[68,95,127], spark-plasma sintering[30,128,129], rapid Joule-heating-induced sintering[130] have also been applied to LLZO but generally require more complex furnaces or other equipment.

The aforementioned sintering methods generally target formation of dense, single ceramic bodies in the form of sintered discs or pellets, or sometimes in a bar type geometry. Generally speaking, for simple shapes (such as LLZO pellet samples) forming of the ceramic green body is accomplished using a die set, wherein powder is placed into a die, pressed at a pressure selected to produce a high green body density but not too much residual strain in the powder compact, and then removed for subsequent thermal treatment.[125] This process is a straightforward, brute force ceramic forming technique,

which is commonly used in the laboratory due to its reliability, simplicity, and comparability with the literature. However, practical SSBs require thin electrolytes to maximize the volumetric and mass fraction of active materials, namely the anode and cathode. This motivates employing as thin an electrolyte as possible while maintaining mechanical and electrochemical stability of the battery. While thin film deposition methods focusing primarily on e.g. vacuum deposition of submicrometer films have been discussed already, another class of film forming methods for ceramics are the tape-casting or doctor-blade method.[131,132] The text by Mistler and Twiname[131] and the useful review from Jabbari et al.[132] discuss aspects of the tape-casting method in great detail. In general, tape-casting of ceramic powders involves preparing a slurry of ceramic powder (along with additives such as a binder, dispersant, etc. to impart the desired slurry properties) suspended in a solvent system. Then, the slurry is spread across a substrate using a doctor blade, a device with a narrow, usually adjustable slit, that when moved relative to the substrate dispenses a slurry film of controllable thickness. Then, the slurry dries, leaving a green film or 'tape' composed of the ceramic powder and minimal binder to hold powders into a single body. Finally, this tape may be fired or sintered to produce a dense, thin ceramic. Although less common than conventional ceramic forming methods (due to its high complexity), some LLZO researchers have utilized tape-casting to form thin films of LLZO, including Yi et al.,[23,111] Fu et al.,[9] Hitz et al.,[8] and Ye et al.[133] In order to form stable slurries for casting, small particle sizes are required,[23,111] motivating synthesis or processing methods to produce LLZO powders with small particle sizes. Further extensions of tape-casting such as freeze-tape-casting have also been demonstrated to form LLZO membranes with the desired pore structure.[134,135]

1.5. Applications of LLZO as an Electrolyte in Batteries

To-date, researchers in the field of solid electrolytes in general and LLZO specifically have investigated a variety of battery architectures. As previously mentioned, pure metallic Li is a highly attractive anode due to its high capacity, and its use in secondary batteries is one of the main motivations for use of a solid-electrolyte in the first place.[1,2,5,6,136] In addition to Li-metal, lithium titanate ($Li_4Ti_5O_{12}$, LTO) has some attractive qualities due to its near zero volumetric change upon charging and discharging, which may allow very high power applications, although its theoretical voltage vs Li/Li^+ is high at ~1.55 V and it has relatively low capacity (175 mAh g^{-1}, 600 mAh cm^{-3}).[136] Pfenninger et al. recently demonstrated that LTO may be readily deposited onto a dense LLZO pellet and used to form a half cell with the expected 175 mAh g^{-1} of LTO when using a Li metal counter electrode.[137] In another application, Inada et al. utilized titanium niobate ($TiNb_2O_7$, TNO) as an anode with LLZO as the electrolyte in a half cell configuration, using aerosol deposition of TNO powder to form a thin film.[44] While simply a proof of concept, in this case Ba- and Ta- co-doped LLZO demonstrated high conductivity and electrochemical stability between 0-6 V without deleterious reactions with the TNO film. Other potential high capacity anodes include alloying type materials such as Si, Ge, or Sn, which have very high specific capacity (> 4000 mAh g^{-1} for Si) and low lithiation and delithiation potentials.[136] These materials however exhibit extremely high volumetric changes upon charging and discharging, which usually results in mechanical failure of cells.[136]

On the cathode side, there are also a variety of options being investigated. Current high voltage oxide cathodes like $LiCoO_2$ (LCO) and similar materials like $LiNi_{0.33}Mn_{0.33}Co_{0.33}O_2$ (NMC) and so forth are attractive options due to their widespread use, moderately high specific / volumetric capacity (200-450 mAh g^{-1} or 700-1700 mAh cm^{-3} respectively) and high theoretical cell voltage.[136,138] Using air (oxygen) as the cathode is also an attractive option, and may allow very specific energy (1910-3460 Wh kg^{-1} depending on whether aqueous or non-aqueous electrolytes are used[32]), when coupled to Li-metal as an anode.[2,32] Li-S batteries are another attractive embodiment of Li-metal batteries due to the low cost and abundance of sulfur, and its high theoretical specific capacity (1675 mAh g^{-1}) when used as a cathode.[136] While Li-S batteries have many potential advantages, the issue of polysulfide dissolution and shuttling in liquid electrolytes and resultant low coulombic efficiency has prevented practical application of Li-S chemistry.[136] For this reason, solid electrolytes are expected to be a critical technology to enable successful Li-S batteries in the future. [8,9,136]

There are now many groups targeting full solid-state batteries (or quasi-solid-state batteries in some cases) based on variations of these aforementioned cell designs. For example, Fu et al. demonstrated a Li-S battery using metallic Li as the anode and a composite carbon nanotube-sulfur cathode using LLZO as the electrolyte.[9] In order to increase the contact area between the electrolyte and cathode, a bilayer LLZO structure was fabricated with a dense film in contact with the Li-metal anode, and a porous film deposited on top of the dense film via tape-casting of LLZO and a sacrificial polymer sphere porogen.[9] Finally, a carbon nanotube interlayer was infiltrated into the porous LLZO, and elemental sulfur was melted into the pores to yield an areal loading ~ 7 mg

cm^{-2}. Critically, polysulfide dissolution and shuttling is prevented by use of a solid electrolyte, which addresses a major problem with Li-S batteries based on a liquid electrolyte. For the batteries synthesized, an energy density of 900 Wh kg^{-1} was projected for an optimized cell, although an energy density of ~250 Wh kg^{-1} was calculated for the cells tested. Hitz et al. demonstrated a trilayer LLZO based SSB, with pores generated on both the anode and cathode side of a dense, thin LLZO film. By infiltrating the cathode side with S and the anode side with Li, a SSB with high rate capability of 10 mA cm^{-2} was generated (based on the geometric area rather than actual surface area of the pores, "real" current density was on the order of 0.25 mA cm^{-2}).[8] In this case the actual energy density of the cell was 195 Wh kg^{-1}, which is roughly comparable to current lithium-ion batteries.[8] Potentially, increasing the pore volume and surface area to allow more active material per cm^{-2} could increase this value, but would mostly likely require application of ultrafine LLZO powder with high surface area.

Finsterbusch et al. demonstrated a LLZO based SSB using Li as the anode and LCO as the cathode.[139] Similar to the method used by Fu[9] and Hitz[8], a dense LLZO supporting electrolyte was first prepared, followed by intimate mixing of LLZO and LCO in a 1:1 mass ratio and co-sintering on top of the dense LLZO support.[139] The resultant hybrid cathode-electrolyte layer had a mass loading of 7.1 mg cm^{-2}. Finally, Li foil was pressed against the dense electrolyte to form the anode. These cells exhibited a utilization of 81% of the theoretical cathode capacity, in comparison to only 3% when a bilayered SSB with only a planar interface between LLZO and LCO was used. This crucial result illustrates a major challenge of incorporating a solid electrolyte into a SSB with a solid

cathode or anode, in that an intimate and interpenetrating network is required to utilize the theoretical capacity of the cell.[139]

One remaining challenge with this system is the reactivity of LLZO and LCO at high temperatures, wherein there is a tradeoff between high density and good contact and the formation of interphases, as it is well known that LLZO and LCO can react at high temperatures[139]. From the same group, Tsai et al. reported a process using the same composite garnet-$LiCoO_2$ cathode that seemed to prevent significant interfacial reaction between the electrolyte and electrode materials.[140] However, the volume changes in the cathode component of the composite electrolyte during cycling resulted in micro-cracking phenomena, which ultimately degraded the performance of the battery significantly over only 100 cycles.[140] Vardar et al. observed interfacial reactions and cation interdiffusion beginning to occur as low as 300 °C between LCO and Ta-doped LLZO, with the effect of forming ion-blocking interfaces.[141] One critical factor for preventing or minimizing deleterious interfacial reactions seems to be the presence of atmospheric CO_2, forming Li_2CO_3 and motivating reactions between LCO and LLZO.[141,142] Clearly, the processing temperatures frequently used for synthesis or sintering of LLZO (> 700 °C generally if not much higher) make thermal processing with cathode materials such as LCO difficult, motivating the discovery of even lower temperature synthesis and processing methods.

While some initial examples of SSBs using LLZO exist, there are several substantial challenges which have been observed. Mechanical stability is a challenge since LLZO is quite brittle, and volume changes with anodes or cathodes can result in mechanical failure or performance loss over time in large part due to electromechanical

cycling and mechanical failure. This well-known effect results in loss of good interfacial contact and ‘dead’ material that is no longer accessible even in standard LIBs with porous electrodes infiltrated by a liquid electrolyte,[138] and is further exacerbated when a rigid and brittle solid electrolyte is utilized to fabricate a SSB.[11,143] While it has been demonstrated that successful SSBs using oxide cathodes are possible[139], it remains to be seen whether such architectures can accommodate the cyclic stress involved with many charge and discharge cycles, and whether the charge / discharge rate will be limited to prevent mechanical failure. At least in the cases of Finsterbusch et al. and Tsai et al., the capacity faded relatively quickly, indicating that mechanical stability may yet be a challenge between LLZO and an oxide cathode.[139,140] Anodes comprising silicon or other high capacity alloying compositions can be expected to have even worse problems with cyclic stresses, owing to their extremely large volumetric changes of hundreds of percent upon full lithiation.[136]

1.6. Motivations and Goals of the Research Presented Herein

Li-conducting garnets and particularly LLZO are a promising class of solid electrolytes for solid-state lithium batteries, but as outlined in this chapter, there are still many challenges impeding its application to practical batteries. Many researchers continue to explore these many challenges, but some of the particular challenges regarding synthesis and processing inspired my research interests and pursuits. Methods to produce LLZO with smaller particle size and with lower synthesis temperature or time are a particular focus, beginning with the research presented in **Chapters 3 and 4**, and extending to very low synthesis temperatures in the results presented in **Chapters 5 and 6**. These last results, wherein Ta-doped LLZO can be synthesized at temperatures between 400-550 °C may be one approach to address the interfacial incompatibility / reactivity between cathode materials such as $LiCoO_2$ and LLZO. More broadly, these are the lowest formation temperatures reported for Ta-doped LLZO to-date and represent a significant advancement in synthesis of Li-garnets. Each of the methods presented in **Chapters 3 through 6** are able to produce Li-garnet powders with smaller (in some cases much smaller) particle sizes than can be obtained via conventional SSR unless extensive high energy ball-milling is employed, which may motivate the use of these synthesis methods to produce LLZO powders more directly applicable to scalable ceramic processing methods such as tape-casting. Finally, the effects of synthesis and processing on the ionic conductivity of Li-garnets is an important factor to validate the applicability of novel synthetic methods, which is the focus of **Chapter 7**.

2. EXPERIMENTAL METHODS

This chapter describes the general experimental and characterization methods used throughout this work. Section 2.1 presents the general sintering approach used for preparing dense garnet electrolytes for subsequent measurement of ionic conductivity, activation energy, etc. Section 2.2 describes the main characterization tools used for the research presented in this Dissertation. Specific details of sintering, synthesis, and characterization relevant to each Chapter are outlined in each respective Chapter or the corresponding Appendix where they differ from those described in this Chapter.

2.1. Methods to Sinter LLZO Powders to form Solid Electrolyte Ceramics

In the research presented in this dissertation, pressure-less sintering in air atmosphere is employed at temperatures between 1100-1300 °C. Optimization of sintering conditions was a considerable undertaking, requiring substantial time and effort to obtain well-sintered garnet samples. Discussion of specific sintering methods are contained **in Chapters 3-8** or in corresponding **Appendices**. While the reports of many researchers were beneficial in my understanding of practical strategies to sinter LLZO, the works of Huang et al.[39,41,126,144] were of particular benefit to me personally, and I point the curious reader to them for reference.

In most cases in the literature as well as in each case presented herein, LLZO is sintered either placed on top of or embedded within 'mother powder' either from the same batch of LLZO (in the case of the experiments presented in **Chapter 4**) or of the

same composition but synthesized via SSR. This synthesis process is described here as follows based on prior[145] work: stoichiometric $La(OH)_3$, ZrO_2, and Ta_2O_5 with 20% excess Li_2CO_3 (based on the composition $Li_{6.4}La_3Zr_{1.4}Ta_{0.6}O_{12}$) were used as reagents. The reagents were ball-milled (MSE Supplies benchtop planetary ball-mill, Tucson AZ) in an equivalent mass of 2-propanol using a planetary ball mill. Zirconia jars and milling media were used, and the mill was operated at 700 RPM for 4 h. Subsequently, the milled reagents were collected, and the 2-propanol was evaporated in a fume hood. The powder was transferred to a MgO crucible (Tateho Ozark Technical Ceramics round tray with flanged MgO lid, part # SR3005 for crucible and SF300 for the lid) and calcined once at 1000 °C for 8 h. The synthesis was performed in air. After calcination, the powder was lightly ground with an agate mortar and pestle to de-agglomerate before use.

This aforementioned SSR process for Ta-doped LLZO is commonly used in the works herein, although some variations for synthesis of sacrificial mother powder were employed in some cases. Generally speaking, these sacrificial powders were synthesized in the same way although sometimes lower synthesis temperatures ($900 < T < 1000$ °C) and different reaction times ($8 < t < 12$ h) were used. However, the powders used were determined to be pure or nearly pure Ta-doped LLZO based on XRD and were thus suitable to as a sacrificial mother powder source.

Initial sintering experiments (**Chapter 4**) utilized an Al_2O_3 crucible and lid and did not control Li_2O evaporation as effectively as the more optimized sintering used in **Chapters 3 and 5-8**. Based on many sintering optimization studies, the following general sintering strategy was adopted. For sintering, pellets were either placed on a small bed (10-20 mg) of mother powder to prevent stiction to the substrate (**Scheme 2.1**) and

optionally also covered with some mother powder and placed atop a porous MgO substrate (Tateho Ozark Technical Ceramics, 98.5% MgO grade CTM porous spacer part # B6764sq109-065 or B8755d086-125, or comparable MgO substrate). Additionally, a mixture of mother powder and Li_2O_2 was employed (generally between 3 : 3 : 1 to 6 : 3 : 1 mass ratio of mother powder : pellet(s) : Li_2O_2) and placed below the porous MgO substrate inside of the MgO crucible to provide a Li_2O-rich[39] vapor phase (see **Scheme 2.1a**) during sintering. This use of a mixture of LLZTO and Li_2O_2 inside the sintering crucible was found[146] to be effective for providing a Li_2O vapor source to facilitate sintering while minimizing "wasted" LLZTO mother powder. The crucible was covered with a MgO lid (Tateho Ozark Technical Ceramics) during sintering. For these sintering experiments, the smallest crucibles possible were generally used to minimize evaporation of Li_2O (1" diameter and 0.5" tall crucibles, Tateho Ozark part no. SR1005 and SF100), although early sintering experiments utilized larger crucibles.

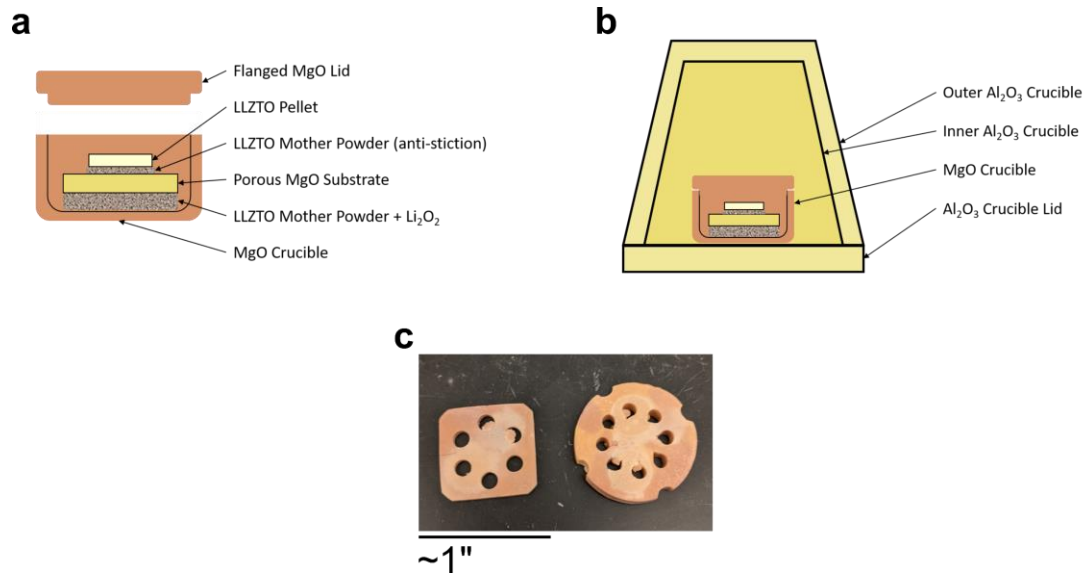

Scheme 2.1. a) arrangement of MgO crucible containing LLZO pellet for sintering and contain Li_2O vapor, **b)** arrangement of MgO sintering crucible situated in nested Al_2O_3 crucibles to contain further Li_2O vapor and limit egress of Li_2O vapor into furnace atmosphere, **c)** two examples of porous MgO substrates upon which to place green LLZO pellets to prevent stiction or adventitious Al-doping.

The entire MgO crucible assembly was then placed on an Al_2O_3 crucible lid and enclosed within inverted larger Al_2O_3 crucibles (Coorstek 100 and 250 mL High Alumina crucibles, part no. 65505 and 65506 respectively) for sintering to contain Li-vapor and prevent / minimize interaction with the furnace heating elements (see **Scheme 2.1b**). Please note that excess Li vapor can cause substantial damage to furnace heating elements over time if not contained adequately. In most cases, sintering was performed in a Lindberg Blue M 1700 °C box furnace with $MoSi_2$ heating elements. Some samples were instead sintered in a Lindberg Blue M 1100 °C tube furnace. In this latter case, the same small MgO crucible arrangement was placed in an Al_2O_3 furnace tube rather than contained in an Al_2O_3 crucible, with the same effect of containing Li_2O vapors and preventing reaction with the furnace elements. The MgO substrates (**Scheme 2.1c**) are

used to prevent adventitious Al-doping of the LLZO pellets during sintering and to provide a generally unreactive substrate. The density of the as-sintered pellets was calculated from the sample geometry (measured using a micrometer) and mass and compared to the theoretical density of $Li_{6.4}La_3Zr_{1.4}Ta_{0.6}O_{12}$ (~5.5 g cm^{-3})[41] or Al- / Ga-doped LLZO (~5.107 g cm^{-3})[16].

Minor variations to this overall sintering method were used as an optimized sintering scheme was being incrementally developed, but the general sintering approach used for most of the sintering experiments in this work and the best samples resulting from them were such that excess Li_2O vapor pressure was provided for the duration of sintering to facilitate effective densification and minimize deleterious Li_2O loss.

2.2. Characterization Techniques Utilized

2.2.1. X-Ray Diffraction

X-ray diffraction (XRD) is one of the most common characterization tools used by materials scientists for characterization of crystalline samples. XRD utilizes x-rays with a wavelength on the order of the lattice spacing of crystalline planes within the sample, which results in diffractive, elastic scattering of x-rays by the periodic structure of the crystal.[147] In a diffraction experiment, the wavelength is ideally restricted to a single wavelength, such as that of Cu Kα radiation at 1.541874 Å. While more generally described by the Laue equations, the Bragg equation (**Equation 2.2.1**) simply describes the scattering angle of x-rays diffracted from a sample as a function of the wavelength (λ) of x-rays employed and the lattice plane spacing (d) of the particular set of planes being excited by x-rays impinging on the sample at a given angle θ. In this formalism, 'n', the order of the reflection, is an integer.

$$n\,\lambda = 2\,d\,\sin(\theta) \qquad (\mathbf{2.2.1})$$

In a simple diffraction experiment using Bragg-Brentano geometry (as in most powder diffractometers), the x-ray source and detector are kept at a fixed radius from the specimen, with the source x-rays incident on the sample at angle θ with corresponding x-rays diffracted from the sample and detected at angle 2θ to generate the diffraction

pattern from which the crystal structure, phase purity, etc. of a sample may be determined.

While the positions of peaks of intensity (or simply 'peaks') corresponding to certain Bragg reflections (i.e. lattice spacings) are simply determined from the Bragg equation, the intensities, peak shapes, and background require more in-depth mathematical treatment. Some of these factors are summarized briefly here, and for more in-depth discussion or treatment the reader is referred to relevant texts such as 'Elements of X-Ray Diffraction' by Cullity and Stock, [147] 'Underneath the Bragg Peaks' by Egami and Billinge,[148] and 'X-ray Diffraction in Crystals, Imperfect Crystals, and Amorphous Bodies' by Guinier,[149] among others.

The intensity of a given reflection is determined by the structure factor F and is a function of the atomic number of atoms comprising a given lattice plane as well as the arrangement within the crystal structure. The breadth or full-width half-maximum (FWHM) of a reflection is related to thermal motion of atoms in the crystal (i.e. the Debye-Waller factor),[147–149] the size of crystalline domains within the sample (as described by the Scherrer equation),[147,149] and by the degree of crystalline (dis)order[149] within the sample. The background underneath the Bragg peaks results from various effects including diffuse scattering from thermal disorder and amorphous or poorly ordered materials. One major limitation of Bragg diffraction is the inability to readily characterize amorphous materials due to the propensity[149] to exaggerate the signals arising from periodicity in the sample. Similarly, the structure of nanocrystalline samples is difficult due to the significant peak broadening arising from the limited size of crystalline domains.[150] These factors motivate use of other characterization techniques to

understand the structure of non-crystalline, nanocrystalline, or disordered materials, as will be discussed in the next section. For the works presented in this document, XRD data was acquired using either a Siemens D-5000 diffractometer with Cu Kα radiation (or in a few cases Co Kα radiation followed by shifting the pattern to match the peak positions that would result from the more standard Cu kα radiation), a Bruker D-8 diffractometer with Cu Kα radiation, a Panalytical X'Pert diffractometer with Cu Kα radiation, or a Panalytical Aeris diffractometer with Cu Kα radiation.

2.2.2. X-Ray Total-Scattering (Pair-Distribution-Function Analysis)

In addition to Bragg scattering based on x-ray diffraction from crystalline, periodic substances, other x-ray scattering signals are also collected in an x-ray scattering experiment that do not originate from diffraction of incident x-rays from the periodic lattice. This so-called total-scattering experiment produces a dataset that, given sufficient reciprocal space resolution, can produce a real-space function that gives information about the arrangement of atoms or structure on the angstrom-level of amorphous, poorly crystalline, or nanocrystalline materials in addition to the information and signals arising from ordered or crystalline materials. This method is called pair-distribution function (PDF) analysis and allows real-space crystallography or structural analysis of materials.[148] Peaks of intensity in a PDF correspond to interatomic distances, with intensity correlated to the atomic number of the specific atoms forming an atomic pair as well as the number of pairs. Robust models of x-ray scattering can be applied to simulate PDF data for a given crystal structure or structural model, and fit experimental data to

understand the phase fraction of compounds in the sample as well as provide insight into local order or disorder, crystallinity, and even crystallite size.[148,150–153] Generally, a PDF experiment requires a high energy, monochromatic x-ray source, most commonly at a synchrotron beamline (although PDF measurements can also be accomplished via neutron scattering potentially with comparable resolution). X-ray PDF measurements presented in this work were obtained using the Diamond Light Source (United Kingdom) dedicated PDF synchrotron beamline I15-I using 76 keV x-rays (λ = 0.161669 Å). In order to generate a PDF from total scattering data, PDFgetx3[154] in the xPDFsuite[152] software package was used. The total x-ray scattering intensity as a function of scattering vector $Q = 4\pi \sin\theta / \lambda$, *I(Q)* was first corrected to obtain coherent scattering, $I_c(Q)$, and subsequently transformed into the structure function, *S(Q)* according to **Equation 2.2.2** [154]:

$$S(Q) = \frac{I_c(Q) - \langle f(Q)^2 \rangle + \langle f(Q) \rangle^2}{\langle f(Q) \rangle^2} \qquad (\mathbf{2.2.2})$$

In **Equation 2.2.2**, *f(Q)* is the atomic scattering factor averaged over all atom types in the sample (as indicated by angle brackets). Then the real-space PDF, *G(r)* is obtained from the sine Fourier transform of *S(Q)* as in **Equation 2.2.3**:

$$G(r) = \frac{2}{\pi} \int_{Q_{min}}^{Q_{max}} Q[S(Q) - 1] \sin(Qr)\, dQ \qquad (\mathbf{2.2.3})$$

Specific parameters used for generating PDFs from total scattering data in **Chapters 6 and 7** are included in the corresponding **Appendices D and E**. Processing and refinement of PDF data in **Chapters 6 and 7** using PDFgetx3[154] and PDFgui[151] software packages is discussed also in the corresponding **Appendices D and E**.

2.2.3. Scanning, Transmission, Scanning Transmission, and Analytical Electron Microscopy Techniques

Electron microscopy is one of the most powerful tools for analysis and characterization of materials at resolutions unmatched by other imaging techniques. Since electrons, like photons used in optical microscopy, exhibit both particle and wave behavior, accelerating electrons to high velocities (under vacuum to prevent scattering from gas molecules) and therefore high energies allows the wavelength of an electron beam to be tuned. Since electrons are massive (unlike photons), their corresponding wavelengths (for 300 keV electrons the wavelength is ~ 0.0196 Å) can be extremely small, allowing orders of magnitude higher resolution than conventional light microscopy, and specifically in the case of transmission electron microscopy (TEM) atomic-scale resolution.[155,156] In general, electrons are generated from a source such as a tungsten filament, lanthanum hexaboride, or in most modern microscopes, a tungsten field-emission gun (FEG). These electrons are extracted and accelerated to the desired accelerating voltage and subsequently focused using electromagnetic optics based on the application.

For scanning electron microscopy (SEM), the electron beam is focused to a small point and scanned (rastered) across the desired area of a sample, generating many signals of interest. Among these signals are secondary electrons (SE) arising from the surface and near-surface inelastic scattering from the sample, backscattered electrons (BSE) arising from elastic scattering that possess high atomic number (Z) contrast (i.e. brighter contrast for regions of sample with higher average atomic number), characteristic x-rays, and others.[155] For the research presented in this work, either a FEI XL-30 or FEI Nova 200 SEM was used, primarily for imaging with secondary and backscattered electrons and for x-ray analysis using energy dispersive x-ray spectroscopy (EDX / EDS, referred to as EDS throughout this work).

In transmission electron microscopy, either a parallel (TEM) or focused (STEM) electron beam impinges on and is transmitted through the sample to form an image in the case of TEM or rastered to generate an image in the case of scanning TEM (STEM). In either case, the sample of interest must be thin enough to be transparent to electrons. Generally, much higher accelerating voltages (100-300 kV) are used in TEM (compared to < 30 kV in SEM), which imparts higher resolution and less electron scattering (i.e. better electron transparency). [156] Various contrast mechanisms including amplitude-contrast, diffraction-contrast, and phase-contrast generate a wide variety of images containing rich information in a TEM measurement and will not be discussed in detail here. Rather, the reader is pointed to texts such as Transmission Electron Microscopy: A Textbook for Materials Science,[156] or other comprehensive texts for theory of image formation and so forth. In addition to the capability to generate images with sub-angstrom resolution in under the correct conditions, many other relevant analytical signals are

generated by the interaction of the electron beam with the sample, including characteristic x-rays (EDS), inelastically scattering electrons (electron energy loss spectroscopy, EELS), diffracted electrons, which can be measured in an electron diffraction (ED) experiment via e.g. selected-area electron diffraction (SAED), incoherently scattered electrons such as measured in STEM via high-angle annular dark field (HAADF) STEM imaging, among others.[156] For the research presented herein, several microscopes were used including a Philips CM-200 TEM (200 kV), a FEI Titan aberration-corrected TEM (300 kV), and a JEOL ARM200F aberration-corrected STEM (200 kV) to collected images and perform analytical TEM to acquire electron diffraction, EDS, and EELS data.

Of the various analytical signals produced in an electron microscope, characteristic x-rays as measured using EDS are employed extensively in the works presented in this Dissertation, and as such more discussion is warranted. An electron beam impinging on a sample will transfer kinetic energy to electrons within a material, causing them to be emitted from the sample, leaving an ionized atom.[155] The subsequent relaxation of outer orbital electrons to empty inner orbital levels can result in emission of an x-ray with an energy characteristic of that particular electronic transition.[155] The specific electronic transitions possible for a given element are based on the number of electrons (i.e. atomic number, Z) and specific selection rules.[155] Therefore, the x-rays emitted from a given atom are an analytical fingerprint, which allows qualitative and in some cases quantitative analysis of the composition of materials. The former is much more straightforward, as the presence of a set of x-ray peaks at specific energies are readily attributable to a specific element. The latter however, can be quite challenging,

requiring precise experimental conditions and often standard reference materials.[155,156] Due to the challenges associated with quantitative EDS (especially when comparing data obtained for a range of sample types and by different instruments), a different approach was utilized for the research presented in **Chapter 7**, wherein simulated EDS spectra are used to approximate the composition of Ta-doped LLZO powders and ceramics based on the ratio of Ta M and Zr L x-ray lines for samples in the $Li_{7-x}La_3Zr_{2-x}Ta_xO_{12}$ ($0.2 < x < 1$) solid-solution. This method is mentioned here and discussed extensively in **Chapter 7** and **Appendix E**.

2.2.4. Electrochemical Impedance Spectroscopy

Electrochemical impedance spectroscopy (EIS) is frequently used to understand a variety of electrochemical systems including ion conducting solids.[83,157] In an EIS measurement, most commonly an alternating voltage (potentiostatic EIS, PEIS) is applied to the sample system. The frequency of the driving signal is varied over the desired range in order to determine the frequency response of the sample system. The impedance measured at a given frequency is related to various physicochemical processes in the sample and can be modeled using an equivalent circuit based on the physical processes occurring in the sample system to understand these processes. Commonly, the impedance in the complex plane is plotted (i.e. the real and imaginary components of impedance are plotted on the abscissa and ordinate respectively, in the complex plane such as in a Nyquist plot) and analyzed in this way.[83,157] A depiction of a typical Nyquist plot for a solid-electrolyte is shown in **Figure 2.1**. Many systems including standard liquid

electrochemical cells, conventional LIBs, and solid-electrolytes can be understood using EIS.[157] In the work presented in this dissertation, the primary use of EIS is to understand the magnitude and frequency of impedance in garnet solid-electrolyte samples in order to understand the Li-ion diffusion processes in a given sample and determine the bulk and total ionic conductivity of the sample, and in some cases the magnitude of interfacial impedance. Acquisition of EIS spectra was performed using a Biologic SP-200 potentiostat in PEIS mode, generally at frequencies between 7 MHz and 1 Hz.

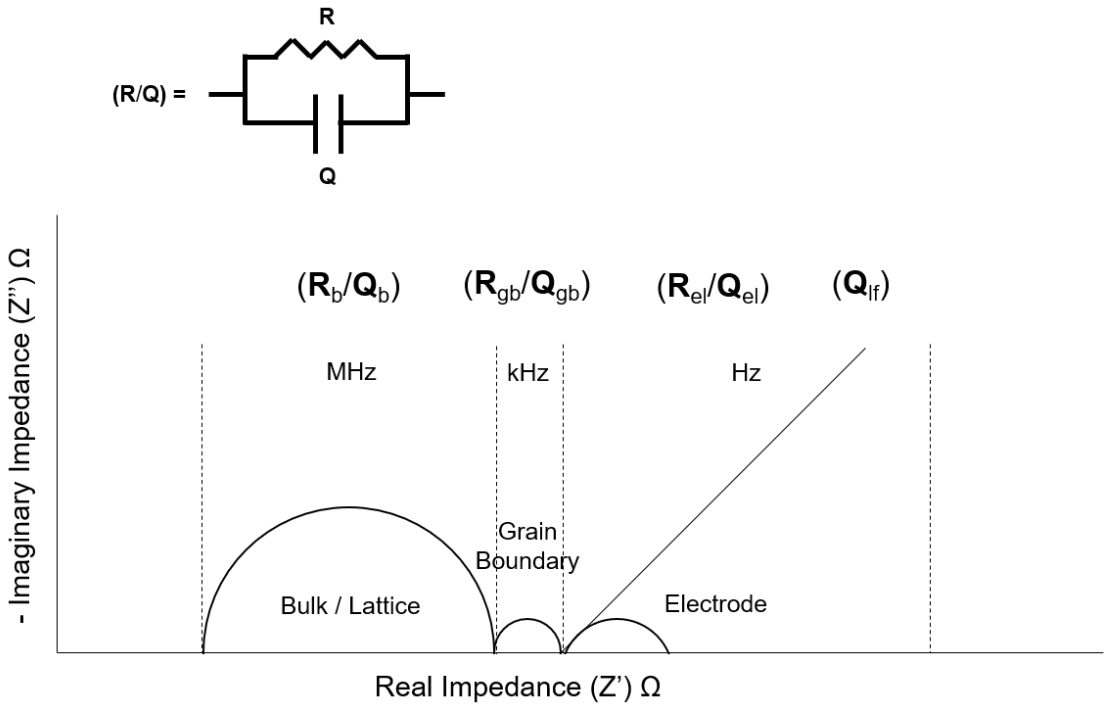

Figure 2.1. graphical representation of a typical Nyquist plot for a solid-electrolyte, where a high frequency (MHz) semicircle arising from bulk or lattice impedance, a middle frequency (kHz) range semicircle arising from grain boundary impedance, and a low frequency (Hz) range semicircle or tail (depending on whether ion conducting or ion blocking electrodes are used respectively) arising from electrode impedance are depicted. The convention adopted by Nyquist plots has the negative of the imaginary impedance (-Z'') plotted on the ordinate vs. real impedance (Z') on the abscissa. In this case, **R** = resistor and **Q** = constant phase element (capacitive), and the convention (**R**/**Q**) indicates parallel resistor and constant phase element, and ($\mathbf{R}_b/\mathbf{Q}_b$)($\mathbf{R}_{gb}/\mathbf{Q}_{gb}$) indicates that the bulk and grain boundary impedances are in series.

In order to acquire EIS data, the sample must be prepared properly with electrodes to interface between the sample and the potentiostat. Before application of electrodes, densified garnet electrolytes were polished to planarize and produce a uniform disc

geometry from which the relative density and conductivity can be easily determined. SiC polishing paper of increasing grit number (increasing fineness) beginning with 240 grit and ending with 2000 grit was employed. For graphite blocking electrodes, generally 240 and 400 grit polishing were done without further polishing to aid in the abrasion of graphite and application onto the ceramic surface. EIS measurements were accomplished using either ion blocking electrodes such as Au or graphite[63], or ion conducting electrodes based on Li-metal or alloys of Li and Sn (specifically the 20 wt% Sn-Li alloy demonstrated by Wang et al.[65]). While Au electrodes are used frequently in the literature and were used in early experiments in this work, it was found that graphite electrodes produced lower impedance. This is attributable to the fact that application of Au electrodes could not be performed without air exposure (as there was no sputter coater readily available in an inert atmosphere environment), which results in formation of high impedance Li_2CO_3. In contrast, graphite could be readily applied immediately after polishing, minimizing the time during which high impedance surface species can form. Application of graphite electrodes was performed by a 'drawing' method based on the work of Shao et al.[63] For Sn-Li alloy electrodes, first Sn and Li metals (Li-foil scraped with a spatula beforehand to remove surface contaminants) were weighed in the correct ratio (20 wt% Sn) in a stainless steel crucible in an Ar-filled glovebox. Then, they were melted at 250 °C in order to form the alloy. This alloy may be reused many times. Then, both sides of a 2000 grit polished LLZO pellet are contacted with the molten Sn-Li alloy for 30 – 60 seconds (with mild rubbing of the pellet in the molten alloy to ensure that any surface contaminants weren't sticking to the pellet) to result in a well-adhered film (**Figure 2.2a**). This process is repeated for each side of the pellet. If necessary, any alloy

that is stuck to the sides of the pellet can be removed via polishing to ensure that a short circuit condition is prevented. Then, the LLZO sample is placed in a sealed pouch cell (foil poly bag sealed with an impulse sealer) with strips of copper foil attached to the Sn-Li electrodes on each side as current collectors such that part of the foil extended out of the sealed poly bag in order to allow electrical connection to the sample outside of an inert atmosphere. Copper tape is then attached to the copper foils to make more mechanically robust connections before an EIS measurement. A photograph of this arrangement can be seen in **Figure 2.2b**.

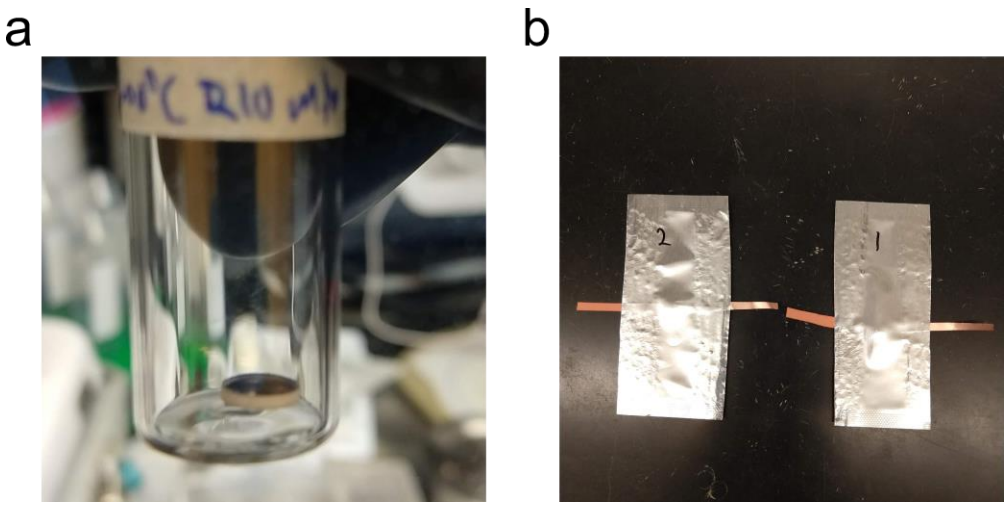

Figure 2.2. photographs of **a)** Ta-doped LLZO pellet coated with Sn-Li alloy electrode in vial, **b)** pouch cell containing LLZO pellets with Sn-Li alloy electrodes and Cu foil as a current collector / feedthrough to allow electrical connection to potentiostat outside of glovebox.

Determination of pertinent physical quantities from EIS requires analysis of the complex impedance and fitting to an equivalent circuit model that represents the physical processes occurring in the sample.[83] In the nomenclature used, '**R**' is a resistor and '**Q**' is

a constant phase element, which is a capacitive element with an arbitrary phase shift and units of F $s^{(a-1)}$, where a is a constant phase exponent where $0 < a < 1$.[157] For a = 1, an ideal capacitor with purely imaginary impedance results. [157] In practical samples, a constant phase element therefore has some combination of real and imaginary impedance. While there are various approaches to fitting EIS data, for the experiments presented in this document, generally the circuit $(\mathbf{R}_b/\mathbf{Q}_b)(\mathbf{R}_{gb}/\mathbf{Q}_{gb})(\mathbf{R}_{el}/\mathbf{Q}_{el})(\mathbf{Q}_{lf})$ or a variation of it is used for fitting, where 'b,' 'gb,' 'el,' and 'lf' are 'bulk,' 'grain boundary,' 'electrode,' and 'low-frequency' respectively, based on the approach of Tenhaeff et al.[158] (among other researchers). Each of the aforementioned physical processes modeled by R/Q circuit elements occur in a different frequency range, generally allowing distinction between them.[158] Bulk or lattice Li-ion conduction in LLZO generally has a characteristic frequency in the MHz range, while grain boundary conduction has frequencies generally in the range of 10-100 kHz. [158] Electrode characteristic frequencies are generally below 10 kHz. [158]

It is often difficult to resolve grain boundary impedance in LLZO at room temperature when ion-blocking electrodes such as Au or graphite are used, as generally the total contribution of the grain boundaries to impedance is low in LLZO.[82,158] Therefore in many EIS analyses with blocking electrodes, the circuit $(\mathbf{R}_{tot}/\mathbf{Q}_{tot})(\mathbf{Q}_{el})$ or $(\mathbf{R}_b/\mathbf{Q}_b)(\mathbf{Q}_{el})$ is used instead, where the R_{tot} is considered approximately equal to R_b (unless another semicircle is clearly visible). To fit EIS data, the Z-Fit tool in EC-Lab software from Biologic was used. Once the circuit is fit, pertinent quantities such as the bulk, grain boundary, and interfacial impedances can be determined (depending on the sample and type of electrodes used), and the ionic conductivity calculated based on the

sample geometry and impedance. For example, the total ionic conductivity of a garnet sample is calculated based on **Equation 2.2.4**:

$$\sigma = \frac{t}{R_{tot}A} \qquad (2.2.4)$$

Where R_{tot} is (R_b + R_{gb}), t is the specimen thickness, and A is the specimen surface area.

Another electrochemical quantity of interest is the activation energy ($E_{a,}$ generally reported in units of eV atom^{-1}) of Li-ion conduction. In Li-garnets and other solid-electrolytes, Li-ion conduction follows an Arrhenius relationship as shown in **Equation 2.2.5**:

$$\sigma \propto e^{\frac{-E_a}{k_b T}} \qquad (2.2.5)$$

Where T is the absolute temperature (K) and k_b is the Boltzmann constant.

The temperature dependence of ionic conductivity was investigated in many cases for various samples presented in this work, generally at various temperatures between 273-343 K in order to determine E_a based on the Arrhenius equation (**Equation 2.2.5**). Once σ is determined over a range of temperatures, a linear regression of ln (σ) vs. T^{-1} can be performed to determine the value of E_a based on the slope of the line.

All E_a measurements were performed on samples with Sn-Li electrodes (i.e. sealed in poly bags under inert atmosphere but measured outside of a glovebox). Some E_a measurements were attempted using graphite electrodes as well, but slight non-linearity was observed in the Arrhenius plots for higher temperatures, which were attributed to a temperature dependent change in contact pressure. However, this effect was not further explored as similar issues were not observed for Sn-Li alloy electrodes. For temperatures above room temperature, a temperature-controlled oven (Thermo Scientific HeraTherm) with a thermostat was used. For measurements at 273 K, the sealed pouch containing the LLZTO pellet-electrode assembly was placed in a polymer bag, which was in turn immersed in an ice bath (EMD Millipore NanoPure system used to provide pure water). By virtue of immersion in the ice-water bath, air was removed from the polymer bag providing good thermal contact between the cold bath and the sealed LLZTO pellet-electrode assembly. For measurements at a new temperature, at least 10 minutes were given for thermal equilibration after the temperature readout on the oven thermostat or ice bath thermocouple reached the desired temperature.

3. NON-AQUEOUS POLYMER COMBUSTION SYNTHESIS OF CUBIC LITHIUM LANTHANUM ZIRCONATE

3.1. Introduction

The high thermal energy cost of SSR for synthesis of LLZO has motivated many researchers to use sol-gel / combustion methods as an alternative, lower temperature synthesis method. Many of these methods are well-suited to producing nanosized LLZO including electrospinning, templating, and flame-spray pyrolysis as discussed in **Chapter 1.3**. That said, many such methods are also limited in terms of material throughput, and often require a complex experimental apparatus especially in the case of electrospinning or flame-spray pyrolysis. Finally, irreproducibility can be an issue when highly oxidizing nitrate precursors are used.[96]

These issues of low throughput, irreproducibility, and complexity motivated adoption of a potentially more versatile combustion strategy, known as the 'polymer sol-gel method' or simply the 'polymer method.' In this approach, a solution of metal precursors and a polymer are simply dissolved together, dried, and combusted to produce oxide powders.[89] This has the effect of homogeneously distributing precursors and forming a uniform 'fuel' mixture in one step, unlike the aforementioned procedures. An aqueous polymer method for LLZO was recently reported using a polyvinyl alcohol-based hydrogel as matrix for the LLZO nitrate precursors.[105] Herein, a unique non-aqueous polymer (NAP) method is employed to synthesize nanopowders of LLZO. Additionally, two aqueous combustion synthesis methods, both based on metal nitrates but with different carbon sources, are described and contrasted to the non-aqueous

method. In all cases, c-LLZO can be obtained at reasonably low temperatures between 700-800 °C. Ta-doped LLZO (LLZTO) nanopowders obtained from the NAP method are consolidated using simple pressureless sintering, demonstrating both high density and high ionic conductivity. These results show that the NAP combustion route is a promising method to obtain LLZO nanopowder, which is more straightforward than other template-based combustion syntheses, less limited in terms of throughput, and allows more controllable combustion compared to conventional nitrate-based combustion methods.

3.2. Experimental

The synthesis of LLZO using the non-aqueous polymer (NAP) method was performed using lanthanum, lithium, and zirconium acetylacetonate reagents ('acac') as precursors (and optionally tantalum(V) ethoxide as a dopant source). Propionic acid (PA), poly(vinylpyrrolidone) (PVP), and dicloromethane (DCM) were used as solvent, polymer, and co-solvent, respectively. For comparison, LLZO was also prepared from aqueous solutions using tannic acid (TA) or poly(vinylalcohol) (PVA) and nitrate salt precursors. For brevity, the aqueous processes using PVA and TA are referred to as 'PVA' and 'TA.' Combustion of the mixtures was performed in air between 600 – 800 °C. Pellets were prepared by conventional uniaxial pressing using as-synthesized calcined nanopowders or by mixing nanopowders with 5 wt% anhydrous LiOH. The pellets were embedded in mother powder as shown in **Figure A1** and sintered at 1100 °C for 6 – 15 h or 1200 °C for 2 – 12 h. For preliminary characterization, pellets were contacted with graphite[63] electrodes and ionic conductivity measurements were performed using

electrochemical impedance spectroscopy at 25 °C. Subsequently, lithium electrodes comprising a 20 wt% (~1.5 mol%) Sn-Li alloy[65] were applied for temperature dependent ionic conductivity measurements. More detailed descriptions of the experimental procedures can be found in **Appendix A**.

The general synthesis procedure for the non-aqueous polymer sol-gel method is outlined in **Scheme 3.1**, with the aqueous synthesis methods following a similar flow as described in **Table A1**. In both the aqueous and NAP methods, reagents are initially dissolved in a solvent system (water or PA with DCM) to result in molecular mixing of precursors. Then, an organic component (PVA, PVP, or TA) is added to serve as fuel and maintain homogeneous distribution of the precursors after solvent removal. Finally, the mixture (optionally pre-dried) is calcined, which initially results in conversion of the organic material to a carbonized matrix, followed by complete burnout of the carbon and formation of oxide nanocrystals. In all three cases, under the correct calcination conditions, undoped c-LLZO is obtained.

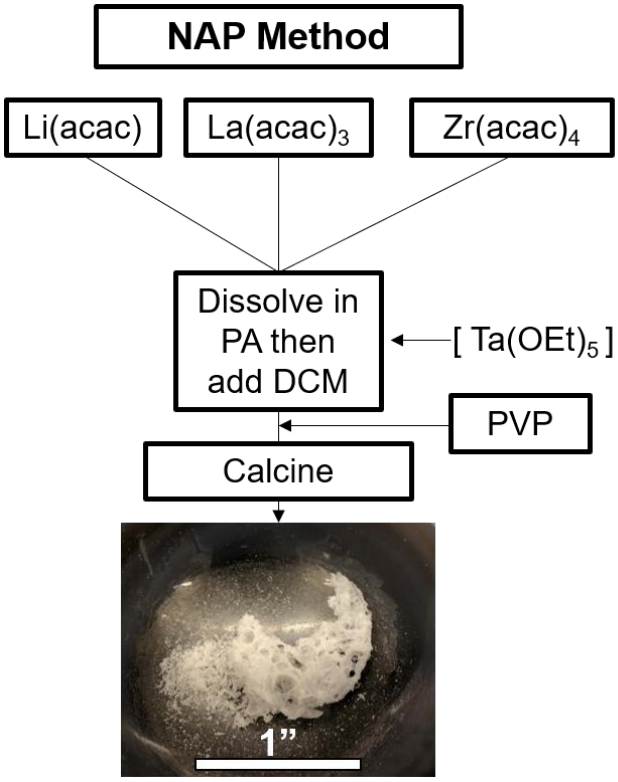

Scheme 3.1. Synthesis procedure for non-aqueous polymer combustion process for LLZO; bottom: photograph of LLZO powder in an agate mortar showing foam-like morphology of the powders after calcination.

3.3. Results and Discussion

3.3.1. Synthesis of LLZO

To elucidate the thermal decomposition process in the NAP method, a dried film of the precursor was characterized by thermogravimetric and differential thermal analysis (TGA/DTA) in air from room temperature (RT) to 800 °C (**Figure 3.1**). During heating from RT to 400 °C (region 1), a slight mass increase was observed (most likely due to uptake of moisture or chemical addition of oxygen due to thermal oxidation of the

polymer), followed by a steady mass loss with two small exothermic peaks. This most likely originates from the decomposition of organic ligands (i.e., acetylacetonate and propionate)[159]. Region 2 is marked by a sharp mass loss beginning at around 400 °C with a brief plateau at 500 °C, followed by another sharp loss between 500 – 600 °C. The first exothermic process can be attributed to the oxidative decomposition of the pyrrolidone (C_5H_9NO) groups of the polymer with conversion of the remaining organic matter to carbon, and the second exotherm to the complete thermal oxidation of the remaining carbon to CO_2.[160] Finally, region 3 is believed to correspond to the formation and growth of LLZO particles.

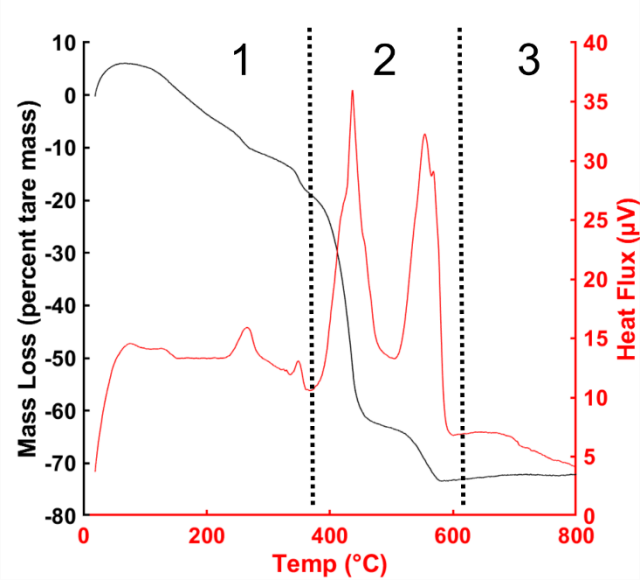

Figure 3.1. TGA/DTA analysis of dried NAP precursor, showing % mass loss (black) as a function of temperature and heat flux (red) coinciding with mass loss (exothermic processes pointing upwards).

X-ray diffraction (XRD) patterns for a subset of synthesis conditions used to prepare undoped LLZO using the PVA, TA, and NAP methods are shown in **Figure A2**. In all three methods, $La_2Zr_2O_7$ (LZO) is observed for incomplete reactions, while the

tetragonal phase (t-LLZO) begins to form when excessive calcination time is employed. This is in line with previous observations, where the cubic phase is observed in undoped LLZO nanowires, but extended calcination causes particle growth and concomitant appearance of t-LLZO[100]. Reducing the size of LLZO to nanometric dimensions has been demonstrated[100] to produce undoped cubic LLZO (c-LLZO, space group $Ia\bar{3}d$)[6], whereas the thermodynamically favorable but poorly conducting tetragonal phase (t-LLZO, space group $I4_1/acd$)[17] is formed in bulk LLZO in the absence of aliovalent dopants. This effect was also observed incidentally in several reports[92,98,102,161], though not discussed in detail, and is hypothesized to originate from a size-stabilization effect of c-LLZO in undoped nanostructures[100].

The calcination conditions and products for the NAP cases are summarized in **Table 3.1**, with corresponding XRD patterns in **Figure A2**. Based on the TGA/DTA analysis, for one set of experiments (NAP-1, NAP-2, NAP-3), a 2 h hold at 400 °C was introduced to controllably carbonize but not completely burn away the organic components before ramping to the final hold temperature, since PVP converts to carbon in air at roughly 400 °C [160]. Pure-phase c-LLZO can be obtained after calcination for 4 h at 700 °C (after the 400 °C hold) or 0.5 h at 800 °C (no intermediate hold), but precise control over the reaction conditions is crucial for obtaining cubic LLZO without addition of extrinsic dopants.

Table 3.1. Summary of NAP method synthesis conditions leading to incomplete and complete formation of undoped c-LLZO. ([a] held at 400 °C for 2 h before final hold temperature, [b] 2x heating rate compared to other samples, LZO = $La_2Zr_2O_7$)

Sample	Hold Temperature (°C)	Time (h)	Result
NAP-1	700[a]	2	Mixture of LZO and c-LLZO
NAP-2	700[a]	4	Undoped c-LLZO
NAP-3	750[a]	2	Mixture of c-LLZO and t-LLZO
NAP-4	800[b]	0.5	Undoped c-LLZO
NAP-5	800[b]	1	Mixture of c-LLZO and t-LLZO

While specific conditions required to obtain undoped c-LLZO differ somewhat between each of the three methods, all follow the same general progression, with c-LLZO observed under conditions at which nanosized powders are formed with minor to no impurity phases based on XRD analysis. Representative XRD patterns (**Figure 3.2a**), SEM (**Figure 3.2b-d**), and TEM images (**Figure 3.2e-g**) for c-LLZO powders prepared from these methods are shown in **Figure 3.2**. It should be reiterated that no extrinsic dopants were added to the precursor solutions, implicating a size-dependency on the formation of c-LLZO as outlined previously. This is corroborated by the fact that in each of the micrographs in **Figure 3.2**, most feature sizes observed are smaller than 1 μm, even though some sintering between primary particles is observed. In **Figure 3.2f,g**, a thin flake-like particle is seen, with a roughly 3 nm thick amorphous surface layer, which corresponds to the Li_2CO_3 layer that is known[52,59] to form on LLZO upon exposure to air. The small thickness of the surface Li_2CO_3 layer indicates that despite the large amount of organic components used in this synthesis procedure, the excess CO_2 formed as a result of their combustion does not have a deleterious effect in excess Li_2CO_3 formation.

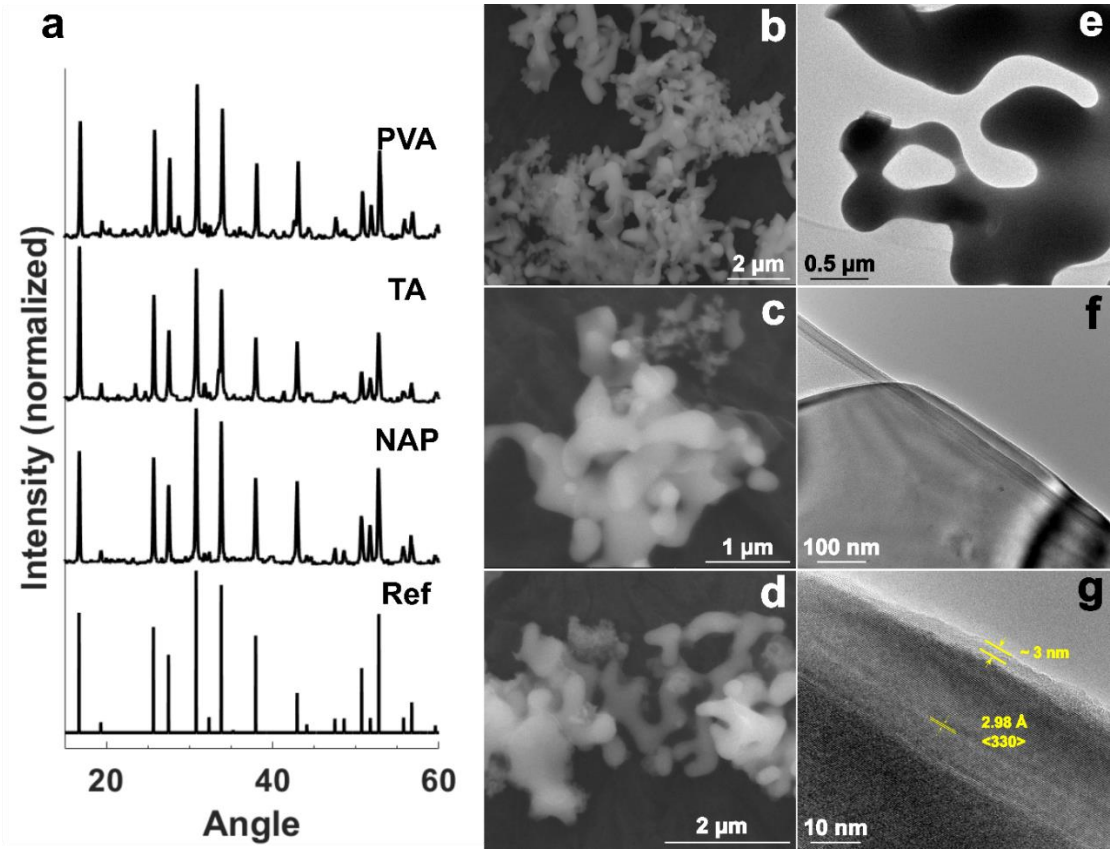

Figure 3.2. **a**) XRD patterns corresponding to as-synthesized powders from the PVA, TA, and NAP methods, with c-LLZO reference (from Geiger et al.[16]); SEM images of powders from **b**) PVA, **c**) TA, and **d**) NAP method. The calcination parameters used were 800 °C for 1.5 h for PVA, 700 °C for 1.5 h for TA, and 800 °C for 0.5 h for NAP. **e**) TEM image of NAP ligament particles, **f**) TEM image of flake-like NAP particle, **g**) HREM image of flake-like particle in (**e**) with <330> lattice fringes visible and ~3 nm amorphous surface layer of Li_2CO_3.

It is worth noting that in the case of both the aqueous methods, drying the precursor at relatively low temperatures (130 – 150 °C) resulted in conversion of the dried precursor to a dark brown material that had evidently partially combusted. In fact, when temperatures above ~130 °C were used to dry the precursors, actual combustion was sometimes observed, most likely due to initial decomposition of some of the nitrates, initiating a self-propagating reaction that is well known to occur in similar combustion-

type syntheses[89]. Additionally, it was observed that the amount of precursor combusted in one synthesis run played a substantial role in the phase purity of the resultant material. For example, in one larger scale synthesis, once the onset of combustion occurred, the reaction was so energetic that it caused the furnace door to come open, most likely due to rapid evolution of gases. Such observations have been described elsewhere[96] as well. Clearly, the heat released during combustion of the organic material and metal nitrates can be expected to change the local temperature in the crucible due to a self-propagating combustion, distinct from the set temperature of the furnace[96]. This somewhat uncontrolled reaction may also be responsible for the noticeable impurity phases seen in the XRD patterns (**Figure 3.2a)** for material prepared from the PVA and TA methods. A similar issue was seen with nanocellulose templated LLZO using the same type of nitrate precursors.[102]

However, this was less of a problem for the NAP method, which did not rely on highly reactive nitrates, and thus further investigations focused on material synthesized by this method. A variant NAP process using acetic acid instead of PA was also attempted, but this resulted in hydrolysis of the sol in a matter of minutes after reagents were mixed. In contrast, use of PA resulted in highly stable sols that could be stored for several months in ambient atmosphere without observable precipitation or degradation. This is believed to arise from formation of propionate complexes, which are somewhat more hydrophobic than acetates, and provide better steric hindrance against hydrolysis for the otherwise reactive metalorganic species (in particular, tantalum ethoxide) used.

3.3.2. Synthesis and formation mechanism of LLZTO via NAP Method

Since grain coarsening of undoped c-LLZO causes its transformation to t-LLZO, Ta-doped LLZO (LLZTO) of nominal composition $Li_{6.4}La_3Zr_{1.4}Ta_{0.6}O_{12}$ was prepared via NAP (see **Appendix A**) to preserve the highly conductive cubic phase during pellet sintering. After minor optimization of the synthesis parameters, it was determined that phase-pure LLZTO could be obtained at 700 °C in 3.5 h, with the reaction time evidently decreased slightly by Ta-doping. This may be due to LLZTO being a more energetically favorable phase than c-LLZO, as corroborated by computational studies[162]. For preparation of larger batches of nanopowder, a direct ramp and 4 h hold at 700 °C was used to ensure that the excess of carbon was fully removed. Representative SEM images and an XRD pattern of LLZTO used in this study are shown in **Figure 3.3** and an EDS map in **Figure A3** indicates uniform distribution of the Ta dopant. These results show that the NAP method may be easily extended to include dopants while maintaining the same morphology and phase purity of undoped c-LLZO.

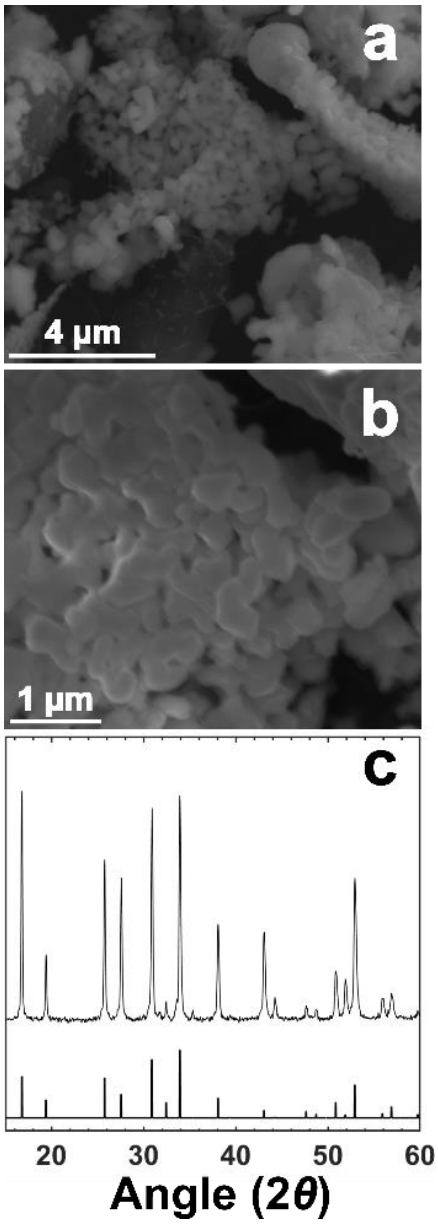

Figure 3.3. **a**) Representative SEM image of as-synthesized LLZTO from the NAP method, **b**) higher magnification image from (**a**), **c**) representative XRD pattern of as-synthesized LLZTO from the NAP method with reference (Logéat et al.[48])

In order to more clearly understand the formation mechanism of nanosized particles via the polymer method, some of the LLZTO precursor solution was heated to 400 °C for 2 h in air to mimic the formation of the carbon material that is generated prior

to formation of LLZTO. High-angle annular dark field (HAADF) scanning transmission electron microscopy (STEM) was performed on the partially combusted samples, with electron energy loss spectroscopy (EELS) and energy dispersive spectroscopy (EDS) spectral images acquired simultaneously and shown in **Figure 3.4**.

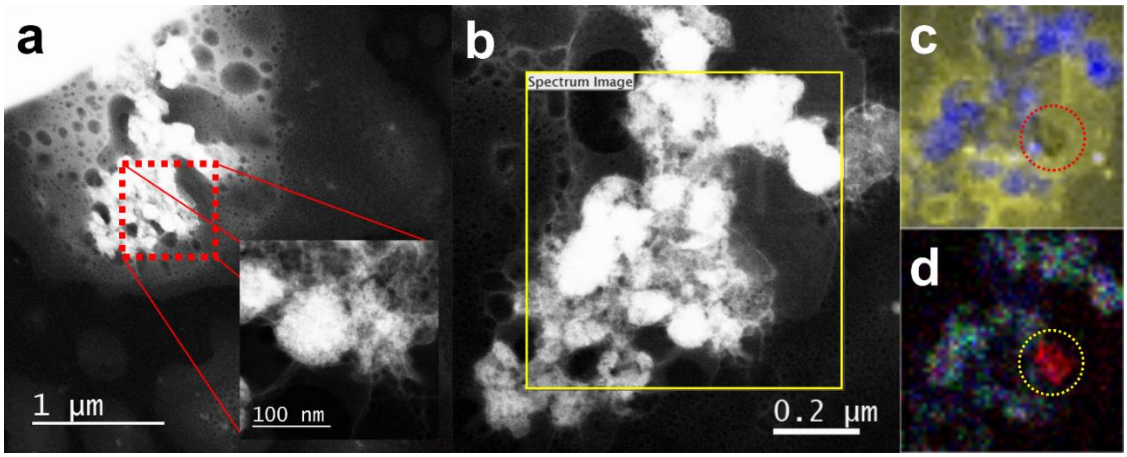

Figure 3.4. HAADF-STEM spectral image analysis of carbonized NAP precursor powder, **a**) survey HAADF-STEM image (higher magnification image in inset), **b**) HAADF-STEM image with region of interest shown as a yellow box, **c**) STEM-EELS map of region of interest in (**b**) showing map of integrated C K-edge (284 eV) signal in yellow and La $M_{4,5}$-edges (849 and 832 eV respectively) signal in blue, and **d**) STEM-EDS map of region of interest in (**b**) showing map of integrated signal from La L-peak (~ 4.65 keV) in blue, Ta M-peak (~ 1.7 keV) in red, and Zr L-peak (~ 2 keV) in green.

In the HAADF-STEM image in **Figure 3.4a**, a cluster of particles with high contrast can be seen embedded in a foam-like material with much lower contrast. This type of contrast difference in HAADF imaging is to be expected between a high atomic number (high-Z material) and a low-Z material, alluding to the presence of partially formed oxides dispersed within a carbon matrix. A higher magnification image in **Figure 3.4a** (inset) shows that at least some of the particles are evidently ensembles or

aggregates of ultrafine particles. **Figure 3.4b** shows another HAADF-STEM image corresponding to the spectral images in **Figure 3.4c-d**, with the region of interest outlined as a yellow box. To determine the identity of the materials, a STEM-EELS map (**Figure 3.4c**, example EELS spectrum in **Figure A4**) and a STEM-EDS map (**Figure 3.4d**) were simultaneously acquired, allowing for chemical imaging of carbon, zirconium, lanthanum, and tantalum. The blue regions in **Figure 3.4c** correspond to signal from the La-$M_{4,5}$ edge signal, which originates exclusively from the high Z-contrast particles in **Figure 3.4a**. The C K-edge signal (yellow) originates from the surrounding matrix, confirming that during intermediate stages of combustion, precursors begin to form nanosized particles within a foamy carbon matrix. This is further corroborated by the STEM-EDS map in **Figure 3.4d**, showing the coinciding signals from La, Zr, and Ta (blue, green, and red respectively). An exception is one Ta-rich region (outlined with a yellow dotted line), which evidently appears as a separate phase as no La or Zr signals are observed. Signal from the N K-peak is markedly absent from the EDS spectra (**Figure A5**) of the carbon material shown in **Figure 3.4**, corroborating the assignment of the first exothermic peak in region 2 of **Figure 3.1** as complete decomposition of PVP (i.e. removal of nitrogen-containing pyrrolidone groups) to form a pure carbon phase when the temperature is held at 400 °C.

The presence of oxide particles in this carbonaceous matrix indicates that the foam forms *in situ* and acts as a template that physically disperses and restricts contact and sintering between individual LLZO particles as they begin to form. The evolution of LLZO from the polymer sol-gel solution is shown schematically in **Scheme 3.2**, showing the uniform polymer sol converting to a transient carbon foam embedded with distributed

oxide particles, and finally the resultant LLZO particle network. This process has some notable advantages over other similar templating methods. The ability to template LLZO without requiring pre-made fibers is one benefit to this polymer sol-gel method. Further, the long-term stability of the precursor solution and ability to produce larger amounts of material in shorter times relative to templating methods are significant advantages.

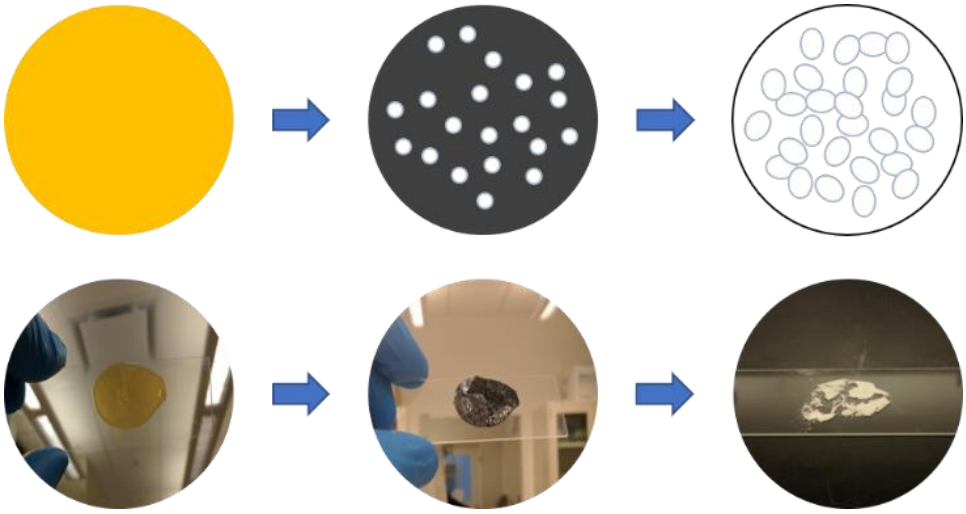

Scheme 3.2. Hypothesized process of formation of nanosized LLZO from polymer sol-gel solutions with corresponding photographs of the as-made yellow polymer sol, partially combusted oxidic particles embedded inside carbon foam matrix, and white LLZO powders after full calcination.

3.3.3. Densification and ionic conductivity measurements

Both undoped and Ta-doped LLZO powders prepared using the NAP method were pressed and sintered at various temperatures for ionic conductivity measurements via electrochemical impedance spectroscopy (EIS). However, good impedance spectra for the undoped c-LLZO pellet could not be obtained due to the low pellet densities obtained at sintering temperatures (i.e. 600 °C) at which the cubic phase was maintained

(see **Figure A6-A7**). Sintering the undoped LLZO powder at 1100 °C caused the expected transformation to t-LLZO. LLZTO, however, was easily densified at 1100 and 1200 °C as can be seen from highly dense grain structures seen in SEM fracture surface images (**Figure 3.5a,b**). Ionic conductivity and relative density values from sintering at 1200 and 1100 °C for various times are shown in **Figure 3.5c,d**, respectively. Nyquist plots (**Figure A8)** were characterized by a single depressed partial semi-circle, which is common for EIS measurements performed on LLZO pellets at room temperature. Representative XRD patterns of pellets sintered at 1100 and 1200 °C are shown in **Figure A9**. The addition of some excess lithium (5% anhydrous LiOH by weight) was employed before pressing and sintering the LLZTO pellets at 1200 °C under mother powder to offset the volatilization of lithium at high temperature, which is known to result in low ionic conductivity or decomposition of the LLZO lattice[19,161]. LiOH was chosen over Li_2CO_3 as it melts at a lower temperature and was thus expected to uniformly wet the LLZTO powder and thus more uniformly offset Li-volatilization.

Based on measured ionic conductivity and density results from pellets sintered at 1200 °C (**Figure 3.5a,c**), it can be seen that the highest pellet density and ionic conductivity do not occur under the same sintering conditions, and that reasonably high ionic conductivity only occurs for one sintering condition (4 h). This indicates that, despite the added LiOH and mother powder covering the pellets, Li loss likely results in lower ionic conductivity for sintering conditions that provide high density. Huang et al. recently reported the importance of maintaining a Li_2O-rich vapor phase during sintering of LLZO to obtain high densities and ionic conductivity.[39] From our results, it appears that simple addition of LiOH to pellets and use of mother powder is insufficient for

sintering at 1200 °C. Loss of Li at high temperatures may also induce oxygen vacancy formation, which can also lower the conductivity in Ta-doped LLZO.[163] In another case, a small increase in Li content of 4% in the LLZO was also reported to result in 120% increase in ionic conductivity,[37] which implies conversely that sintering for slightly too long may result in enough deviation from optimal Li content through Li-volatility to drastically reduce conductivity. Finally, it was shown in studies of Li diffusion by muon-spin relaxation and quasi-elastic neutron scattering that the number of mobile Li^+ species is the primary factor determining ionic conductivity in garnets,[164] indicating that Li-loss that it not severe enough to decompose[19] LLZO outright may still drastically lower ionic conductivity.

Therefore, in order to minimize the negative effects of Li volatility, pellets were also sintered at a lower temperature of 1100 °C for slightly longer times in smaller volume MgO crucibles (a photograph of this setup can be found in **Figure A1b**). In this case, rather than adding excess LiOH to the powder, the LLZTO nanopowder was pressed as-synthesized and covered with a mixture containing mother powder and Li_2O_2, which decomposes to form Li_2O beginning at approximately 250 °C.[165] By providing excess Li_2O and utilizing a lower sintering temperature, higher ionic conductivities and higher relative densities were achieved over a wide range of sintering times. The fact that this LLZTO powder is nanosized likely also plays a role[103] in allowing high densities to be achieved via pressureless sintering at the relatively low temperature of 1100 °C. Similarly high densities were also reported at low sintering temperatures for flame-spray pyrolysis LLZO nanopowders.[23,111] Multiple pellets were sintered for 6, 9, 12, and 15 h at 1100 °C to assess replicability, with results (minima and maxima of conductivity and

density) presented in **Table A2**. Ionic conductivity and density values for pellets sintered at 1100 °C are plotted in **Figure 3.5d** (with averaged values from multiple pellets shown for 6, 9, 12, and 15 h sintering times). Pellets sintered at 1200 and 1100 °C both exhibit transgranular fracture, indicating strong grain cohesion, although the samples sintered at 1100 °C display intergranular fracture as well (**Figure 3.5b)**.

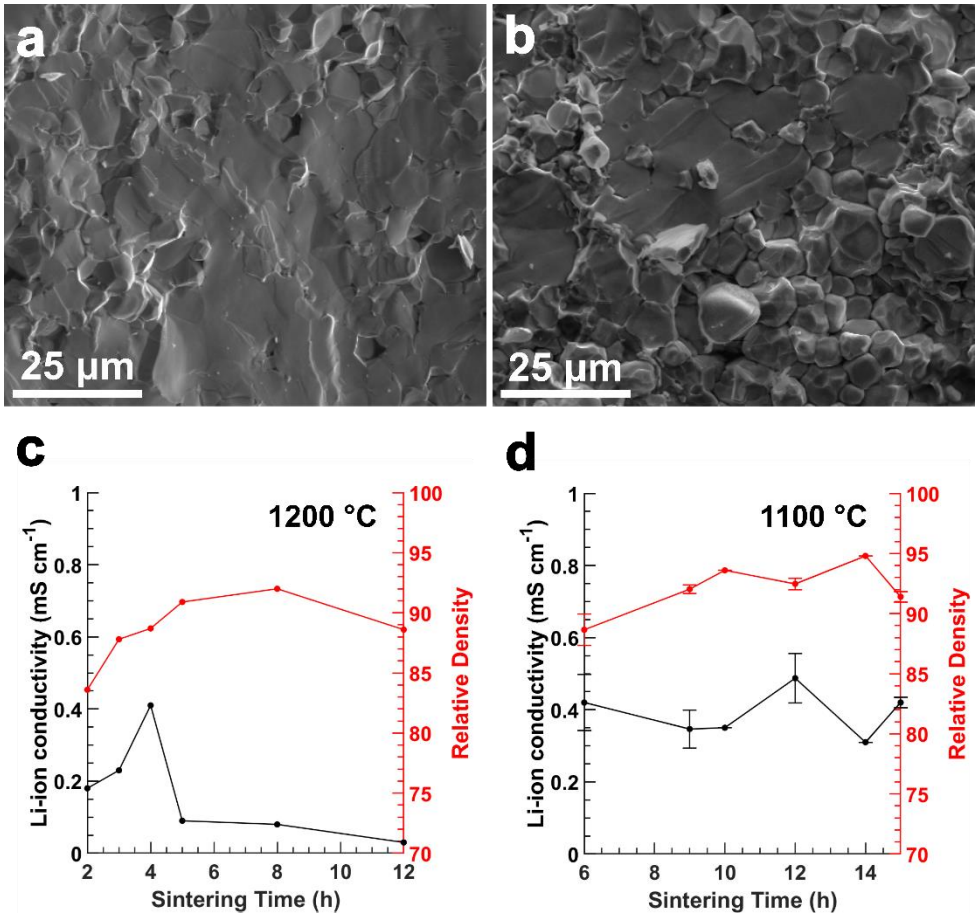

Figure 3.5. a) SEM fracture surface image of a pellet sintered at 1200 °C, **b**) SEM fracture surface image of a pellet sintered at 1100 °C, **c**) total ionic conductivity and relative density of pellets sintered at 1200 °C for 2-12 h, **d**) total ionic conductivity and relative density of pellets sintered at 1100 °C for 6-15 h (average values of conductivity and density from multiple pellets sintered at 6, 9, 12, and 15 h with error bars equal to the standard deviation)

The temperature dependence of ionic conductivity was investigated for some of the pellets sintered at 1100 °C in order to determine the activation energy and was calculated by performing EIS measurements at several temperatures between 25-70 °C and taking a linear fit of ln (σ) (S cm^{-1}) vs. 1/T (K^{-1}). EIS spectra used for these calculations are shown in **Figure 3.6**, with the resultant Arrhenius plots shown in **Figure A10**. Based on the slopes of the linear fits, the activation energies for these LLZTO pellets vary between 0.34 and 0.42 eV, corresponding well to other values in the literature (see **Table 3.2**).

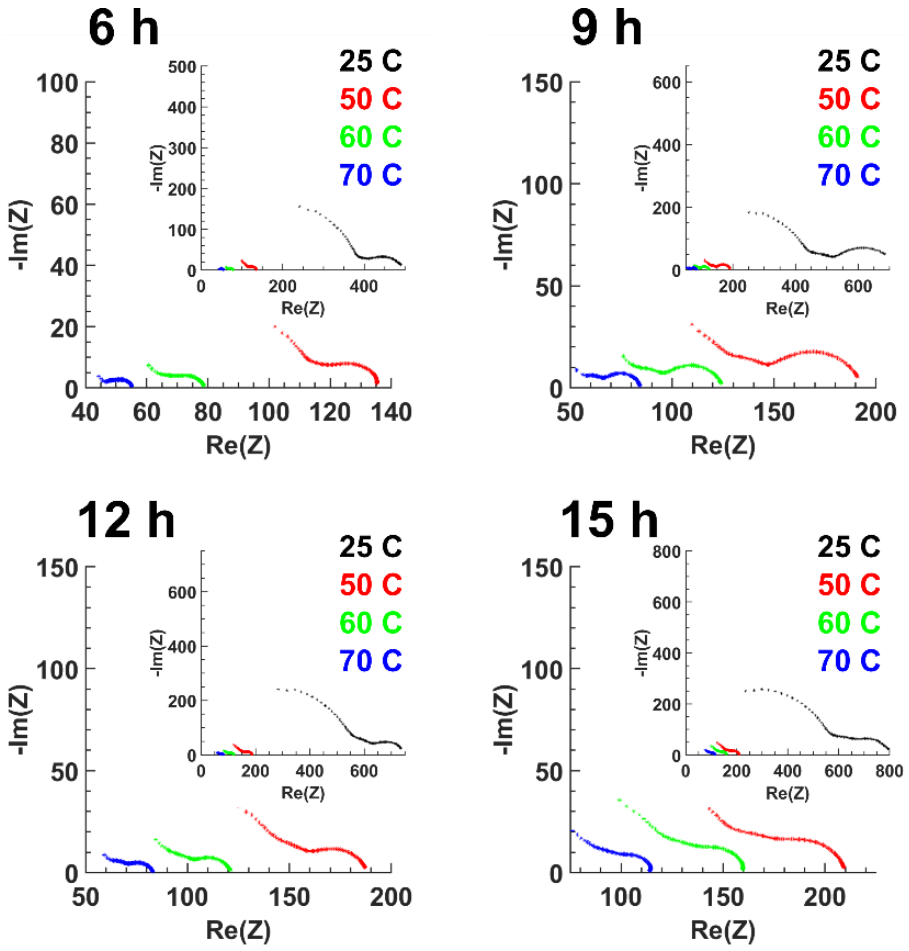

Figure 3.6. Temperature dependent EIS spectra of LLZTO pellets sintered at 1100 °C for 6, 9, 12, and 15 h

Table 3.2 contains a comparison of various synthesis methods targeting nanosized LLZO based on sol-gel, combustion, and other novel synthetic methods from the literature, with synthesis conditions and performance metrics for comparison to the NAP method. From these results, it is evident that the NAP method can yield nanopowders that result in high ionic conductivity comparable to or surpassing other methods by simple pressureless sintering in air, which could be improved further with optimization of the pellet sintering process or use of advanced sintering techniques such as hot pressing. Additionally, the use of a lower sintering temperature and Li_2O_2 to increase the Li_2O vapor pressure during

sintering allow high density and conductivity to be obtained over a wide range of sintering times, even at a relatively short sintering time of 6 h, while also reducing the amount of mother powder needed. The small particle size of the LLZTO nanopowder likely also contributes to higher density at this lower sintering temperature. These benefits, along with the observation that the NAP method enables greater control over combustion conditions compared to the conventional nitrate-based methods outlined above make this a promising synthetic approach for obtaining LLZO nanopowders of potentially many compositions, allowing lower synthesis and sintering temperatures of garnet solid electrolytes.

Table 3.2. Comparison of sol-gel, combustion, and co-precipitation type synthesis methods for Al-doped (ALLZO), Ga-doped (GLLZO), and Ta-doped ($Li_{6.4}La_3Zr_{1.4}Ta_{0.6}O_{12}$ unless noted, LLZTO) LLZO from various works in the literature. Note that an EIS spectrum corresponding to the highest conductivity samples prepared in this work (1100 °C, 12 h) is shown in **Figure A12**.

Type of LLZO	Synthesis Technique	Synthesis Conditions		Pellet Sintering Conditions		Sintered Pellet Properties			Reference
		Time (h)	Temperature (°C)	Time (h)	Temperature (°C)	Density (%)	RT Total Ionic Conductivity (mS cm^{-1})	Activation Energy (eV)	
ALLZO	Sol-gel	4	600-800	1	1000	96	0.40[#]	0.41	Sakamoto et al.[95]
ALLZO	Co-precipitation	10	850	20	1150	> 90	0.20	0.25	Shao et al.[166]
ALLZO	Co-precipitation	6	850	1	1000	57	0.06[+]	0.58	Langer et al.[167]
ALLZO	Nitrate-Glycine Combustion	6	750	6	1200	95	0.51[†]	0.29	Dhivya et al.[168]
ALLZO	Co-precipitation	6	900	0.05	1000	96.5	0.33[‡]	0.32	Zhang et al.[169]
ALLZO	Flame-Spray Pyrolysis	N/A	N/A	1	1080	94	0.2	0.35	Yi et al.[111]
GLLZO	Flame-Spray Pyrolysis	N/A	N/A	0.3	1130	95	1.3	0.28	Yi et al.[23]
GLLZO	Nitrate Combustion	10-15	650	6	950	76	0.24	0.32	Afyon et al.[22]
LLZTO	Co-precipitation	8	750	6	1125	NR	0.20	NR	Chen et al.[31]
LLZTO	Sol-gel	2	900	0.33	1000	88	0.05[#]	0.43	El-Shinawi et al.[35]
LLZTO	Sol-gel[*]	12	900	36	1180	96	0.45	0.529	Ishiguro et al.[32]
LLZTO	Sol-gel[≠]	4	950	4	1100	NR	0.21	NR	Yoon et al.[93]
LLZTO	Sol-gel[≠]	4	900	1	1100	92	0.48[#]	NR	Kim et al.[26]
LLZTO	**NAP method**	**4**	**700**	**6-15**	**1100**	**90.5-93.6**	**0.24-0.67**	**0.34-0.42**	**This Work**

NR – not reported
N/A – not applicable
- consolidated using hot-pressing
+ - measured at 80 °C
† - measured at 30 °C
‡ - consolidated using field-assisted sintering
≠ - $Li_{6.5}La_3Zr_{1.5}Ta_{0.5}O_{12}$
* - $Li_{6.3}La_3Zr_{1.3}Ta_{0.7}O_{12}$

3.4. Conclusions

In summary, a novel combustion synthesis route to obtain nanosized LLZO is presented. Three distinct synthesis methods were employed to investigate the effect of the type of metal precursor, solvent system, and organic fuel. Both aqueous methods using metal nitrate precursors were effective for preparing LLZO, but demonstrated a strong propensity towards runaway combustion, which is commonly observed in such combustion syntheses. On the other hand, the non-aqueous method using metalorganic precursors ameliorated this issue, enabling relatively better reproducibility and control over synthesis conditions. The combination of molecular mixing of precursors throughout an organic medium synergizes with the formation of a carbonaceous foam during intermediate stages of combustion, which acts as an *in situ* sacrificial template, with the effect of segregating pockets of reagents throughout, thus physically restricting particle size growth as the oxides are forming. Elucidation of the formation of this transient carbonaceous foam was performed via electron microscopy and illustrates the mechanism by which this combustion synthesis results in nanosized LLZO. All three methods enabled formation of nanosized, undoped c-LLZO under the correct calcination conditions. Ta-doped LLZO was also easily synthesized by the non-aqueous route, demonstrating high total ionic conductivity of 0.24-0.67 mS cm^{-1} after simple pressureless sintering at 1100 °C in air for between 6-15 h, with an activation energy of 0.34-0.42 eV. The polymer combustion route described herein is a promising alternative synthesis route to controlled preparation of nanosized LLZO, utilizing less reactive

reagents and demonstrating lower complexity compared to many other synthesis routes targeting nanosized LLZO.

4. SYNTHESIS OF LITHIUM LANTHANUM ZIRCONATE IN MOLTEN LICL-KCL

4.1. Introduction

While Li-conducting garnets such as LLZO are generally synthesized via solid-state reaction (SSR), for practical applications, the ability to synthesize LLZO at lower temperatures, in less time, and in forms other than bulk powders would be highly advantageous. Such methods are discussed at length in **Chapter 1.3**, including sol-gel, combustion, and even thin film deposition methods. While many such methods are successful, in general they do not confer an easily scalable method to form LLZO, given the typically high cost for sol-gel precursors (e.g. metal alkoxides) and large amounts of 'sacrificial' reagents such as excess solvents (alcohols, glycols, etc.), combustible material (nanocellulose, polymers, or 'Pechini method' type synthesis), or high vacuum equipment (for ALD, CVD, etc).

Among the various means to prepare nanocrystalline ceramics, molten salt synthesis (MSS) (sometimes known as "salt melt synthesis" or the "molten salt method"), is a common method to obtain various-sized particles of ceramics from generally inexpensive precursors at temperatures or times lower than those required in SSR.[119,122,170–176] In MSS, precursors usually consisting of metal oxides or metal salts are mixed intimately with a salt (or salt mixture, often a eutectic), followed by heat treatment above the melting point of the salt(s) to provide the thermodynamic driving force for dissolution of the precursors and to promote the formation of the desired crystalline phase.[119] Although the MSS method has been utilized for quite some time to synthesize

nanostructured oxides[119], it has only been recently applied to the synthesis of LLZO. Reddy et al. utilized a eutectic mixture of lithium nitrate ($LiNO_3$) and lithium chloride (LiCl) as the molten medium, with lanthanum oxide, zirconium tetrachloride, and tantalum oxide as precursors for the synthesis of tantalum-doped LLZO (LLZTO) between 700-900 °C.[122] Aggregates of micrometer-sized, irregularly faceted crystals of LLZTO were obtained using this method. The resultant materials exhibited a maximum ionic conductivity value of 0.78×10^{-5} S cm^{-1} at room temperature, in contrast to the roughly 100x higher conductivity generally reported for LLZTO prepared using SSR.[32,80,36] The low ionic conductivity in the particles prepared using this MSS method was attributed to the post-synthesis, aqueous washing step used to remove the eutectic salt medium, which led to an exchange of Li^+ with protons[30].

The main focus of this Chapter is synthesis of LLZO in a eutectic mixture of lithium chloride and potassium chloride (59:41 mol% LiCl:KCl) to further develop the use of MSS to obtain LLZO powders in large quantities, and examine the thermodynamic and kinetic factors affecting the formation of LLZO in this medium. Initial experiments that replicated the method of Reddy et al.[122] are also presented, showing that Al-doped LLZO cannot be obtained using the same $LiNO_3$-LiCl reaction medium, and noting that most of the salts are evidently evaporated during synthesis. In contrast, in addition to forming c-LLZO without the requirement of extrinsic dopants, aluminum-doped (ALLZO) and gallium-doped (GLLZO) LLZO powders were also easily synthesized using MSS in the LiCl-KCl reaction medium. The role of proton exchange and hydration on the sinterability of the as-synthesized powders was also investigated. In the case of ALLZO and GLLZO powders synthesized via MSS, ceramic pellets with reasonably high

density and conductivities are obtained, and that the proton exchange can be reversed through the incorporation of LiOH prior to pellet sintering.

4.2. Experimental

4.2.1. Materials and Reagents

All reagents used are of ACS grade or higher and used as-received. Lithium chloride (LiCl), potassium chloride (KCl), lithium nitrate ($LiNO_3$), zirconium oxynitrate ($ZrO(NO_3)_2$) hydrate, aluminum nitrate ($Al(NO_3)_3$) nonahydrate, and gallium nitrate ($Ga(NO_3)_3$) hydrate were obtained from Sigma-Aldrich. Lanthanum nitrate ($La(NO_3)_3$) hexahydrate was obtained from Alfa Aesar.

4.2.2. Preparation of LLZO Salt Precursor Mixtures

To prepare the $LiNO_3$-LiCl salt mixture, $LiNO_3$ and LiCl were mixed in a molar ratio of 88 mol % $LiNO_3$ and 12 mol % LiCl by grinding with a mortar and pestle. Then, $La(NO_3)_3$, $ZrO(NO_3)_2$, and optionally $Al(NO_3)_3$ were added and ground again with a mortar and pestle to mix thoroughly. To prepare the chloride salt mixture, 59 mol% LiCl and 41 mol% KCl were mixed followed by grinding thoroughly with a mortar and pestle. The LLZO nitrate precursors were prepared by mixing $LiNO_3$, $La(NO_3)_3$, and $ZrO(NO_3)_2$ in a 7:3:2 molar ratio and grinding thoroughly with a mortar and pestle. In the case of ALLZO, Al^{3+} from $Al(NO_3)_3$ was used as a substitutional dopant for Li^+ to introduce the critical level of Al-doping (*i.e.* greater than 0.204)[19] to stabilize the cubic phase of LLZO, resulting in a nominal formula of $Li_{6.28}Al_{0.24}La_3Zr_2O_{12}$. Similarly, in the case of GLLZO, $Ga(NO_3)_3$ was used to introduce a critical level of Ga-doping[13], resulting in a nominal formula of $Li_{6.25}Ga_{0.25}La_3Zr_2O_{12}$.

4.2.3. Molten Salt Synthesis of LLZO

For the initial synthesis experiments in $LiNO_3$-LiCl, the salt mixture and reagent mixture (1:1 ratio by mass) were mixed thoroughly by hand using a mortar and pestle. Then the mixture was placed in an alumina crucible and heated to 800 °C for 1 h. Before synthesis in eutectic LiCl-KCl, the salt mixture and the nitrate precursor salt mixture were mixed by grinding thoroughly with a mortar and pestle and then added to alumina crucibles. The pre-mixed chloride salts and precursor salts were mixed in a 1:1 ratio by mass, with total mass between 2 – 4 g for exploratory syntheses, and up to 50 g for producing large batches for densification and ionic conductivity studies. The crucibles were covered with alumina lids to mitigate the evaporation of salts at high temperatures. Since the LiCl-KCl salt mixture melts at 352 °C[119], temperatures between 500 – 900 °C were readily accessible for experimentation to determine optimal reaction conditions. In general, the mixtures were heated at a rate of 5 °C/min (Thermo Scientific Lindberg Blue M), held for various times (between 1 – 6 h), and cooled naturally to room temperature in the furnace.

After the synthesis, ultrapure water (>18 MOhm cm) was added to the cooled crucibles and the suspension was ultrasonicated using an immersion probe (Cole-Parmer 500 W Ultrasonic Processor) to rapidly dissolve the salts and generate a slurry of powder. Subsequently, the slurry was vacuum filtered using poly(vinylidene fluoride) membranes (0.22 µm pore size, DuraPore, EMD corporation) and washed with at least 150 mL of water followed by 50 mL of methanol (BDH, HPLC grade) to facilitate fast drying. Finally, the filter membranes along with the wet powder cakes were placed in an oven at

50 °C and dried in air. After drying, the powders were removed from the filter membranes and lightly ground with a mortar and pestle.

4.2.4. Ceramic Pellet Preparation

LLZO pellets were consolidated from the as-synthesized powders via uniaxial cold-pressing (SpecAc Atlas 15T Manual Hydraulic Press) using a 6 mm stainless steel die. Before pressing, powders were crushed using a mortar and pestle followed by vibratory ball-milling (SPEX Corporation, 8000M) for 5 minutes to help mitigate agglomeration of particles. Optionally, 3% or 10% (by mass) LiOH was added. Pellets were pressed using 2 metric tons of force for 5 minutes.

All pressed green pellets were sintered at 1100 °C for between 6 – 18 hours. For sintering, pellets were placed on a bed of mother powder and covered with additional mother powder to offset lithium loss. All pellets were supported on a MgO plate that was placed inside of an alumina crucible (CoorsTek) in order to prevent both adventitious aluminum doping and sticking of the LLZO pellets to the crucible.[81] Further, 100 – 200 mg of lithium carbonate were also placed within the alumina crucible, adjacent to the pellets, to generate a lithium-rich vapor-phase during sintering. All crucibles were covered with an alumina lid (CoorsTek) during sintering. A representative photograph of this arrangement can be seen in **Figure B1**. The density of the pellets was calculated from the sample geometry and mass and compared to the theoretical density of Al- and Ga-doped LLZO (5.107 g cm^{-3})[16,23,81].

4.2.5. Materials Characterization

X-ray diffraction (XRD) was performed using a Siemens D5000 powder diffractometer with CuK_{α} radiation for phase identification. The reference pattern for c-LLZO ($Ia\bar{3}d$) was generated according to the structure reported by Geiger et. al[16].

The sample morphology was examined using an FEI XL30 scanning electron microscope (SEM) equipped with an EDAX system, or an FEI Nova 200 dual-beam SEM-FIB with a Thermo Scientific solid state energy dispersive spectrometer. Transmission electron microscopy (TEM) was performed using an FEI Titan Environmental TEM operated at 300 kV. To prepare TEM samples, the LLZO powder was ultrasonically suspended in methanol. A holey carbon TEM grid (Pacific Grid Tech) was then briefly immersed into the aforementioned suspension. Crystalmaker Single Crystal™ software was used to simulate the selected area diffraction pattern (SADP) of c-LLZO based on the structure from Geiger et al[16].

4.2.6. Ionic Conductivity Measurements

After sintering, the dense pellets were polished using 400 grit alumina polishing films (Agilent) until a smooth, uniform surface was obtained. Metal contacts were applied by sputter coating a ~10 nm Au film onto the polished surfaces. Symmetric cells with the Au electrodes were analyzed via electrochemical impedance spectroscopy (EIS) using a BioLogic SP200 potentiostat. Impedance spectra were recorded from 7 MHz to 1 kHz at room temperature and fit (see discussions in **Chapter 2.2.4** and **Appendix B**) using the Z fit analysis tool in the BioLogic EC-lab software.

4.3. Results and Discussion

4.3.1. Characterization and Discussion of Formation Mechanism

In the method reported by Reddy et al., a eutectic mixture of $LiNO_3$ and LiCl (88:12 mol%, mp ~280°C) was used to synthesize LLZTO between 700-800 °C.[122] While effective for preparing LLZO, the products obtained in this method had two undesirable properties. First, the pellets formed from these powders had uncharacteristically low Li^+ ionic conductivity, as previously mentioned. This is likely explained by the well-known Li^+/proton-exchange effect that is noted when LLZO is exposed to water or moist air, which has a negative effect on conductivity.[52,53,55] Secondly, the morphology of the as-synthesized powders was somewhat irregular, whereas MSS commonly produces more uniform powders. The latter is likely explained as follows: due to the boiling and/or decomposition of $LiNO_3$ at around 600 °C[123], there is a high possibility that some, if not much, of the nitrate portion of the medium evaporates under conditions (i.e., temperatures between 700 – 800 °C) that form LLZTO. The evaporation of a substantial portion of the reaction medium could have a deleterious effect on the uniformity and morphology of the resultant powders. Initial explorations of MSS for LLZO herein attempted to form undoped and Al-doped LLZO using this same $LiNO_3$-LiCl eutectic medium. At a reaction temperature of 800 °C for 1 h without added dopants, t-LLZO forms, confirming the applicability of this method to undoped LLZO (**Figure B2**). However, addition of a critical doping level of Al (via $Al(NO_3)_3$) resulted in formation of t-LLZO rather than cubic ALLZO, as shown in **Figure B2**. Further, some $LaAlO_3$ forms, indicating that in this medium and under these conditions, Al does not readily incorporate into the garnet

lattice to form cubic LLZO. It is believed that the decomposition of $LiNO_3$ and the small proportion of LiCl (only 12 mol % of salt mixture) both contribute to the inability to easily dissolve Al-species due to evaporation / decomposition of $LiNO_3$ and insufficient liquid LiCl to facilitate liquid-phase diffusion, preventing facile incorporation into the garnet structure. It may also be the case that under these synthesis conditions, $LaAlO_3$ or other Al-containing phases are more thermodynamically favorable than Al-doped LLZO.

To mitigate this challenge, an approach utilizing less volatile salt species, specifically a eutectic mixture of LiCl-KCl[119] (59:41 mol%, mp ~ 352 °C; LiCl: bp ~ 1382 °C, KCl: bp ~ 1420 °C, compared to ~ 600 °C for $LiNO_3$[123]), is used. In this case, since the molten chloride medium contains no innate oxygen source (besides the slow diffusion of atmospheric oxygen), precursors that can provide reactive oxygen species are required. Therefore, a stoichiometric mixture of $LiNO_3$, $La(NO_3)_3$, and $ZrO(NO_3)_2$ was chosen to provide reactive oxoanions while also forming a completely homogeneous salt melt from which to precipitate fine oxide powders. Although LiCl may provide the Li^+ needed to form LLZO, $LiNO_3$ was also added in order to ensure that enough reactive oxygen species could be generated upon decomposition of the NO_3^- anion (**Equation 4.1**) to react with all metal cations:

$$NO_3^- \rightarrow NO_2^- + O^- \qquad (\mathbf{4.1})$$

In short, the excess $LiNO_3$ ensures that more than enough oxygen is provided to the system to generate stoichiometric LLZO. In contrast to Reddy and coworkers' use of oxides for some of the precursors, all salt precursors were chosen herein so that potential concentration gradients due to dissolution and diffusion of the metal oxides were ideally

eliminated. This is to aid the formation of a smaller particle size distribution and ensure initial homogeneity of all species in the reaction mixture.

A large design space was investigated to elucidate some of the thermodynamic and kinetic factors involved in formation of LLZO in this system and is summarized in **Table B1** and **Figure B3**. Selected XRD patterns showing the phases present using different reaction temperatures (500 – 900 °C) and 3-hour reaction time are displayed in **Figure 4.1a**.

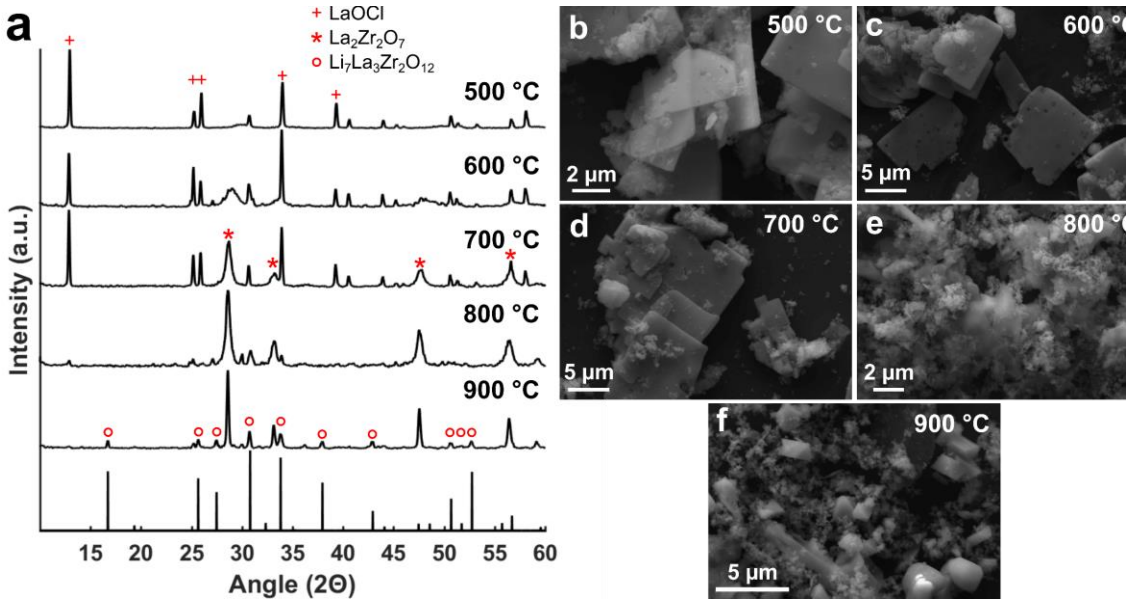

Figure 4.1. Formation Process of LLZO using different reaction temperatures (500 – 900 ^{o}C) and 3 hr hold times. (**a**) XRD patterns (c-LLZO reference structure from Geiger et al.[16] on bottom); (**b-f**) respective SEM images showing morphology of materials synthesized at various temperatures

When using a MSS reaction temperature of 500 °C, the only crystalline phase formed is lanthanum oxychloride (LaOCl), presenting as large plates with edge lengths on the order of several micrometers and thicknesses below several hundred nanometers

(**Figure 4.1b**). This is unsurprising, as MSS was used to synthesize LaOCl plates by Huang et. al at temperatures between 300-800 °C in molten LiCl-KCl eutectic.[177] Interestingly, no obvious evidence of crystalline zirconium containing phases was observed at 500 °C, indicating that most likely all of the La existed in the form of LaOCl. That said, several very broad features in the baseline of the XRD pattern from the reaction conducted at 500 °C coincide with $La_2Zr_2O_7$ (LZO) peak positions, which may indicate that LZO is beginning to form even at this temperature. LZO is a known intermediate phase in LLZO sol-gel based syntheses and converts to LLZO upon reaction with additional Li[100,102]. Increasing the reaction temperature to 600 °C results in the formation of ultrafine (as indicated by extremely wide XRD peaks) LZO nanocrystals in addition to LaOCl plates (**Figure 4.1c**). At a reaction temperature of 700 °C, both phases still coexist (**Figure 4.1d**), with the LZO reflections becoming somewhat sharper in the XRD patterns, indicating crystallite growth and/or an increasing degree of crystallization. As the temperature increases to 800 °C, the majority of LaOCl is consumed in favor of LZO, presenting as ultrafine particles (**Figure 4.1e**). Interestingly, the LaOCl obtained at 800 °C by Huang et al.[177] presented in the form of nanoplates of similar morphology to our materials, indicating that the thermodynamic driving force in our case is the energetic favorability of another phase (*i.e.*, LZO or LLZO) rather than the instability/solubility of LaOCl at 800 °C. This is suggested by the fact that nearly all LaOCl is gone at 800 °C and no LaOCl exists at 900 °C, with the implication that above a threshold temperature between 800 – 900 °C, all LaOCl has re-dissolved, providing soluble La-species necessary to form LLZO from nanocrystalline LZO. At 900 °C, a mixture of LZO and

LLZO forms in 3 hr (**Figure 4.1f**), and both very fine powders as well as and highly faceted particles with side lengths between 0.5 and 2 μm can be seen.

Phase pure c-LLZO was obtained using a reaction time of 6 hr at 900 °C (**Table B1**). Optimization of the reaction time also resulted in phase pure c-LLZO in 4 hr at 900 °C (**Figure 4.2**), indicating that all LZO present after 3 hr at 900 °C converts within 1 hr to LLZO. As seen in **Figure 4.2**, LLZO particles formed in this 4 hr reaction present either as faceted discrete particles (**Figure 4.2b,c**), or as spheroidal particles that may result from fusion of individual particles that come into contact in the melt (**Figure 4.2a**). Of note, the ability to synthesize faceted, submicron single crystals of LLZO may allow further investigation into the size-stabilization effect of undoped c-LLZO investigated by Yang et al.[100] and Gordon et al.[102] Based on the substantially larger size of the LLZO particles relative to the LZO nanocrystals, it is likely that an Ostwald ripening or similar process occurs, in which some LZO nuclei convert to LLZO while nearby nuclei below a size threshold are consumed in favor of larger LLZO particles. A fragmented (from high energy ball-milling) crystal of LLZO is shown in the HRTEM image in **Figure 4.2d**, with electron diffraction patterns shown in **Figure 4.2e** (measured) and **Figure 4.2f** (simulated based on data from Geiger et al.[16]). Observation of clear lattice fringes corresponding to the $(0\bar{2}2)$ plane along with reflections corresponding solely to the [133] zone-axis diffraction pattern of LLZO indicate that at least some of the formed LLZO particles are single crystalline. This taken in conjunction with the observed faceted particles may further allude to an Ostwald ripening process.

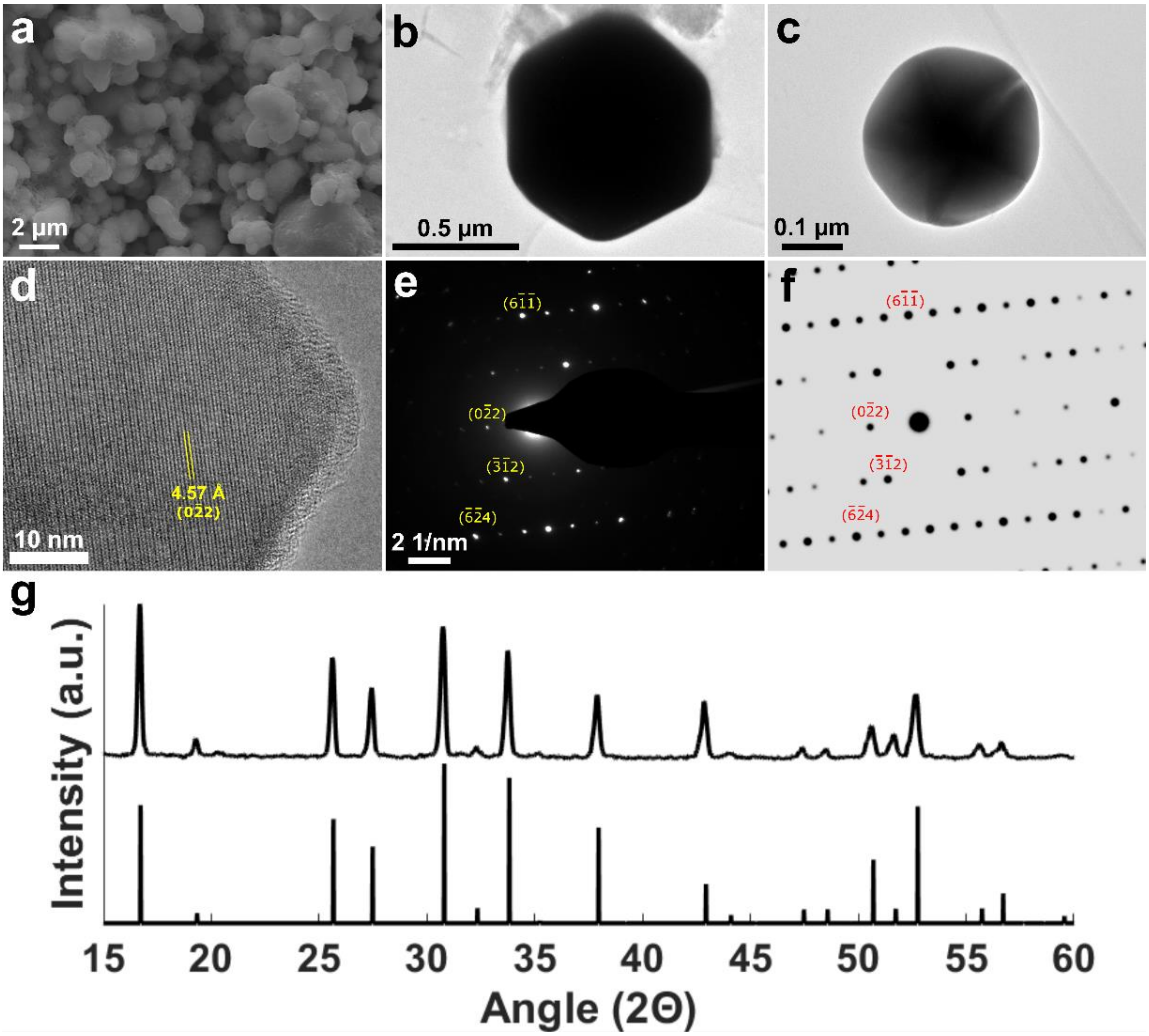

Figure 4.2. Phase pure c-LLZO powders synthesized via MSS: (**a**) SEM image of undoped c-LLZO with particle sizes between 0.3 – 3 µm, showing textured surfaces, (**b,c**) TEM images showing faceted particles of undoped c-LLZO, (**d**) HRTEM image of particle edge from ball-milled (i.e. fractured) powder in (133) zone-axis orientation, (0$\bar{2}$2) lattice spacing noted (**e**) parallel-beam nanodiffraction pattern of (**d**), (**f**) simulated (133) zone-axis SADP of c-LLZO using Crystalmaker Single Crystal software, based on reference pattern generated according to Geiger et al[16], (**g**) powder XRD pattern (15 - 60°) of c-LLZO with reference pattern (Geiger et al.)[16]

In short, as the temperature and/or reaction time increase, the otherwise stable LaOCl begins to dissolve to form ultra-fine LZO nanocrystals, followed by complete dissolution of LaOCl and formation of c-LLZO at 900 °C. This process is depicted in **Scheme 4.1**. Under optimized conditions wherein pure c-LLZO is obtained with a smaller particle size distribution (5 °C/min ramp to 900 °C, 4 hour hold), phase-pure c-LLZO can be obtained without added extrinsic dopants. In this case, phase-pure c-LLZO particles with sizes primarily ranging from ~0.3 – 3 µm were obtained, with a mean and median particle size of 1.06 µm and 0.806 µm, respectively (**Figure B4**). This is consistent with prior observations of nanostructured LLZO[100,102], wherein c-LLZO formation is preferred in smaller particles. Further, in all cases of these exploratory MSS experiments, no dopants were added, suggesting that the particle/crystallite size of the LLZO formed under these conditions was below a critical threshold for size-stabilization.

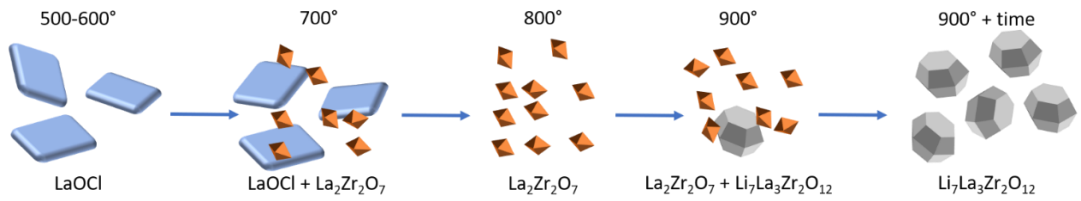

Scheme 4.1. Overall process of formation of c-LLZO in eutectic LiCl:KCl

In addition, Al-doped and Ga-doped LLZO (ALLZO and GLLZO respectively) are easily obtained by addition of either $Al(NO_3)_3$ or $Ga(NO_3)_3$ to the salt precursor mixture. In each case, c-LLZO was obtained using the same reaction conditions as those used to obtain c-LLZO without added dopants, indicating that this method may be easily

extended to incorporate dopants. Representative SEM images of the as-synthesized doped powders and XRD patterns are depicted in **Figure 4.3** (a-inset and c-inset) and **Figure 4.4b,e**, respectively. In addition, energy-dispersive X-ray spectroscopy (EDS) maps taken of these large batches of ALLZO (**Figure B5**) and GLLZO (**Figure B6**) indicated that the dopants are uniformly distributed throughout the as-synthesized powders. Large batches (~5 – 10 g) of the Al-doped, and Ga-doped LLZO were synthesized for subsequent densification studies and ionic conductivity measurements.

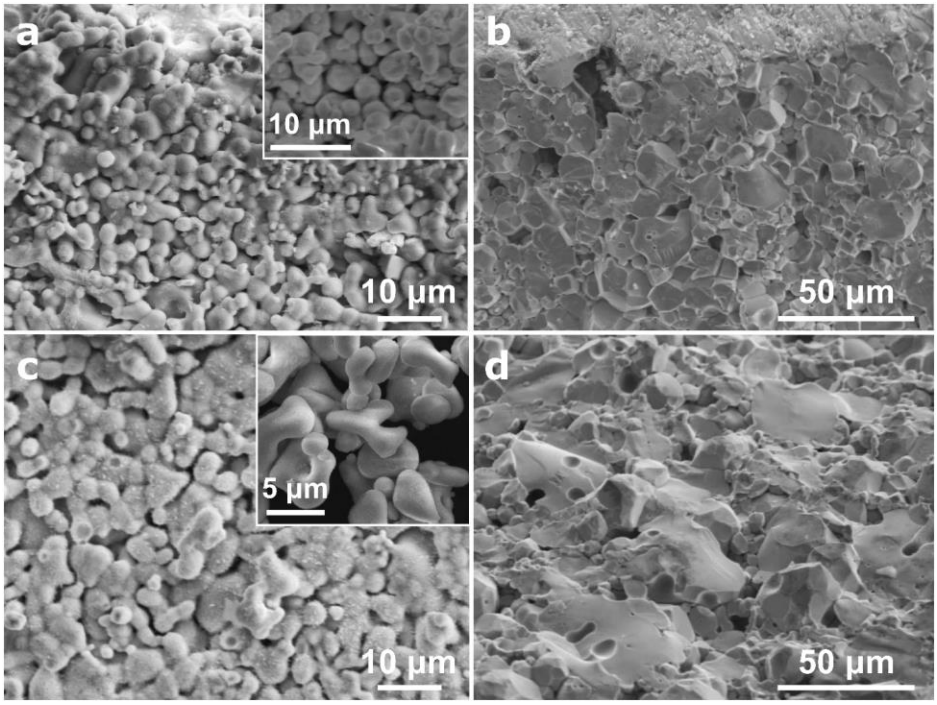

Figure 4.3. SEM images of fracture surfaces of (**a**) ALLZO pellet sintered without added LiOH for 18 hr; (**a inset**) as-synthesized ALLZO powder; (**b**) ALLZO pellet sintered with 10% excess LiOH for 18 hr, (**c**) GLLZO pellet sintered without added LiOH for 18 hr; (**c inset**) as-synthesized GLLZO powder, (**d**) GLLZO pellet sintered with 10% excess LiOH for 12 hr

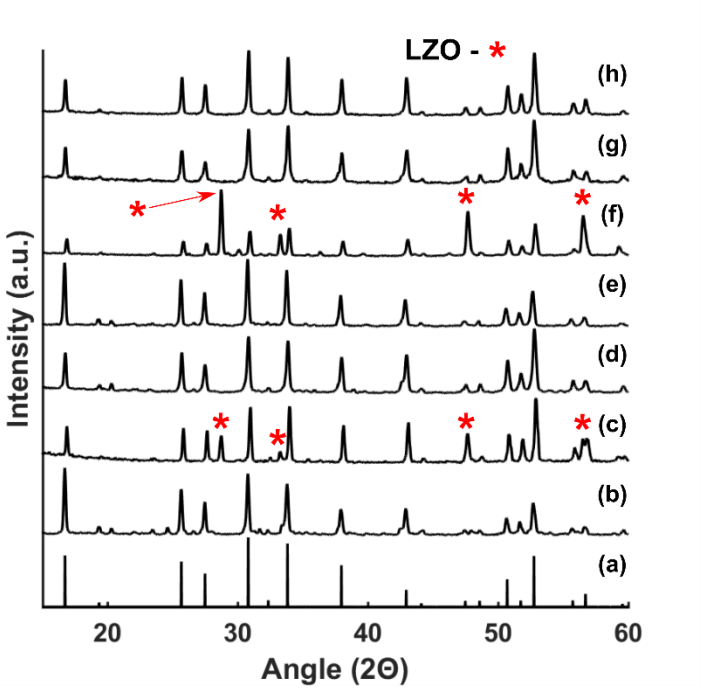

Figure 4.4. Comparison of XRD patterns of (**a**) c-LLZO reference pattern (from Geiger et al.)[16], (**b**) as-synthesized ALLZO powder, (**c**) ALLZO pellet without added LiOH sintered for 18 hr, (**d**) ALLZO pellet sintered with 10% excess LiOH for 18 hr, (**e**) as-synthesized GLLZO powder, (**f**) GLLZO pellet without added LiOH sintered for 18 hr, (**g**) GLLZO pellet sintered with 10% excess LiOH for 12 hr, (**h**) GLLZO pellet sintered with 3% excess LiOH for 6 hr. *LZO = $La_2Zr_2O_7$

4.3.2. Densification and Conductivity of Sintered Powders

Pellets formed using the as-synthesized powders generally had quite poor properties. In general, the resultant densities were less than 50% of the theoretical density of c-LLZO, and XRD patterns of the pellets indicated some decomposition of LLZO to LZO (see **Figure 4.4c**,**f**), which is known to occur when LLZO becomes too Li-deficient.[92,129,178,179] Additionally, attempts to polish these pellets resulted in rapid abrasion of powder from the pellets, indicating that little to no sintering had occurred,

even when heating at 1100 °C for 18 hours. Because of this, only very noisy EIS spectra (not shown) could be obtained, with very large values of impedance. This phenomenon was observed in the undoped, Al-doped, and Ga-doped LLZO, and may be explained by the substantial hydration that most probably occurs during washing of the powders due to formation of Li_2CO_3. Cheng et al. and Sharafi et al. have demonstrated computationally that exposure to moisture and subsequent Li_2CO_3 formation is thermodynamically favorable at room temperature.[53,55] This may occur via a proton exchange pathway[55] or by simple removal of Li^+ from the lattice, creating Li-deficient LLZO via formation of LiOH and subsequent reaction with CO_2 to form Li_2CO_3[53]. Hydration, proton-exchange, and doping with CO_2 have been demonstrated to separately displace Li^+ from LLZTO by Wang and Lai, with deleterious effects on conductivity.[54] In these cases and in the study by Larraz et al.[52], only gaseous H_2O was discussed, and it can be assumed that liquid H_2O (used to wash the as-synthesized powders) will have a stronger propensity to induce protonation/hydration. Indeed, Shimonishi et al. demonstrated that upon exposure to several aqueous solutions, LLZO pellets show both a change in morphology and substantially reduced conductivity.[97] This strongly implies that the as-synthesized powders produced herein and by Reddy et al.[122] are negatively affected by exposure to water during washing.

In order to confirm whether hydration is the cause of the poor pellet properties, 3% or 10% (by mass) LiOH was added to the as-synthesized powder, followed by ball-milling for 5 minutes to intimately mix the powders and then subsequent pressing and sintering. LiOH (mp ~ 462 °C) easily forms an alkaline flux during sintering that should

readily reverse proton exchange if present, with the formation of water vapor, according to **Equation 4.2**:

$$LiOH\ (l) + Li_{(7-x)}H_xLa_3Zr_2O_{12} \rightarrow Li_7La_3Zr_2O_{12} + xH_2O\ (g) \qquad (\mathbf{4.2})$$

In the case of powders with added LiOH, reasonably well-densified pellets (84-86% of theoretical density) were obtained unlike those prepared from only as-synthesized powder. All the Nyquist plots for the well-densified ALLZO and GLLZO pellets displayed a tail at low frequencies, corresponding to the impedance at the electrodes, and a partial, slightly depressed semicircle at high frequencies attributed to the bulk conductivity (**Figure 4.5**). A second semicircle arising from the grain boundary resistance was not noticeable, which is often the case for LLZO pellets measured at room temperature. More importantly, fitting of the impedance data **(Table B2)** showed that these pellets had ionic conductivities between 0.230 mS cm^{-1} and 0.371 mS cm^{-1} (**Table 4.1**). This indicates that proton exchange was reversed, as it is well known that the proton-exchanged, "low-temperature cubic LLZO" has poor ionic conductivity.[52,57]

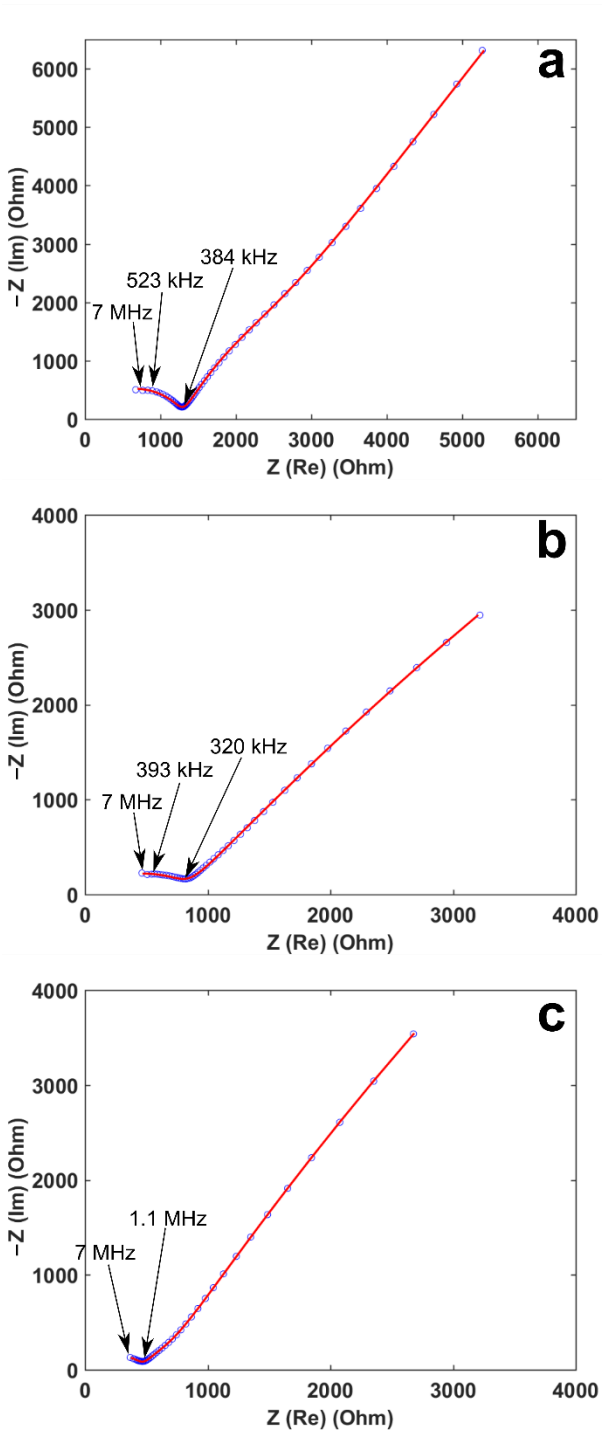

Figure 4.5. EIS spectra (measured between 7 MHz and 1 kHz) of (**a**) ALLZO pellet (sintered with 10% LiOH for 18 hr) and (**b,c**) GLLZO pellets (sintered with 10% LiOH for 12 hr and 3% LiOH for 6 hr respectively); the experimental data are plotted as circles and the solid line are the fit data.

Table 4.1. Comparison of pellet density and room temperature total ionic conductivity for Al and Ga-doped LLZO prepared using different synthesis methods.

Type of LLZO	Synthesis Method (Pellet Sintering Conditions)	Relative Density	Ionic Conductivity (mS . cm^{-1})	Reference
Al-doped LLZO	Molten salt [as-synthesized] (1100 °C, 18 h)	< 50%	n/a	This work
	Molten salt + 10 wt% LiOH (1100 °C, 18 h)	84%	0.230	This work
	Solid state reaction (1300 °C, 1 h)	Not reported	0.31	Ref[20]
	Sol-gel (1100 °C, 1 h under 40 MPa)	96%	0.4	Ref[95]
	Flame-spray (1090 °C, 1 h)	94%	0.2	Ref[111]
Ga-doped LLZO	Molten salt [as-synthesized] (1100 °C, 18 h)	< 50%	n/a	This work
	Molten salt + 3 wt% LiOH (1100 °C, 6 h)	84%	0.371	This work
	Molten salt + 10 wt% LiOH (1100 °C, 12 h)	86%	0.323	This work
	Solid state reaction (1000 °C, 1 h under 40 MPa)	91%	0.35	Ref[13]
	Sol-gel (950 °C, 6 h)	76 - 80%	0.24	Ref[22]
	Flame-spray (1130 °C, 0.3 h)	95%	1.3	Ref[23]

The fracture surfaces for the ALLZO (**Fig. 4.3a,b**) and GLLZO (**Fig. 4.3c,d**) pellets were characterized using SEM. **Figure 4.3a**,**c** confirm that for both ALLZO and GLLZO pellets prepared without added LiOH, little sintering had occurred, as the particle morphology is nearly the same as that of the as-synthesized powders (shown in the insets). Only slight coalescence of the particles can be seen, with little reduction of void space or porosity. In contrast, **Figure 4.3b**,**d** illustrate significant sintering and grain coarsening, with predominantly transgranular fracture observed, indicating substantially improved mechanical properties. However, spheroidal voids within grains as well as larger intergranular voids are observed in the well-densified samples. There are several possible explanations for this observation: first, it may be that the sintering time and/or

temperature are not yet optimized for these powders, and it is entirely plausible that the reactions that occur when hydration is reversed cause some different behavior during sintering relative to conventionally synthesized powders. Second, a relatively large amount of LiOH was added, which while necessary to reverse protonation, may also result in residual voids after the excess LiOH evaporates during sintering. EDS maps of the fracture surfaces of ALLZO and GLLZO are shown in **Figure B7** and **Figure B8** respectively, indicating that the distribution of dopants is still uniform, although it is possible that some Al-rich phases are present in the ALLZO case.

The density and ionic conductivity of our materials are slightly lower than the best ALLZO and GLLZO pellets prepared from powders synthesized using other methods (**Table 4.1**). That said, the conductivity values are within the expected values for c-LLZO, and in the case of ALLZO, our material exhibited higher conductivity than that of Yi et al.[111] even though it has noticeably lower density. Similarly, our GLLZO has higher conductivity than that prepared by Wolfenstein et al.[13], despite the lower density, and both conductivity and density compare favorably with GLLZO prepared via combustion synthesis by Afyon et al[22]. Taken in context, these initial results indicate that c-LLZO prepared via MSS can be processed in such a way to produce expected behavior as long as hydration can be reversed. While other researchers have demonstrated substantially higher conductivity for GLLZO (e.g. Yi et al.)[23], the relatively low density and clear existence of non-optimized sintering as shown in **Figure 4.3** indicate that under fully optimized conditions, the materials synthesized here could have better dopant incorporation, higher density and improved conductivity comparable to some of the more successful methods shown in **Table 4.1**.

4.3.3. Discussion of Densification and the Effect of Protonation/Hydration

As hydration is the most likely explanation for the low conductivity of the Ta-doped LLZO prepared via MSS by Reddy and coworkers[122], the facile ability to reverse hydration/proton exchange demonstrated here is an important result to motivate further exploration of MSS for the synthesis of LLZO. Recently, Yi et al. reported that hydration in the case of ALLZO and GLLZO powders synthesized via flame-spray pyrolysis actually aided in the densification of LLZO.[23] They theorize that hydration introduces additional mechanisms for densification, which operate in addition to conventional surface and bulk diffusion during sintering.[23] While Yi et al.'s result is in clear contrast to these findings at first glance, the results may be reconciled as follows: in the case of flame-made powders with high specific surface areas, substantial hydration is unsurprising, especially when these powders are ball milled for an extended time in air. However, all or nearly all of the Li^+ from the LLZO lattice that is displaced by either H^+/H_2O or reaction with CO_2 is still present as surface Li_2CO_3. In the case of MSS, the process of washing with a large volume of water to remove the salt media likely results in the gradual dissolution and removal of any LiOH or Li_2CO_3 that forms as a consequence of proton exchange from the as-synthesized powders. Since these MSS LLZO powders are washed using a vacuum filtration apparatus, repeated additions of ultrapure water are used, shifting the equilibrium for the Li^+/H^+ exchange reaction further toward removal of Li^+ and resulting in a net effect of lowering the stoichiometric level of Li, since some amount of the surface Li-species will dissolve and be washed away during each repeated washing step. The conversion of LLZO to LZO in the pellets sintered without added

LiOH, as illustrated in **Figure 4.4c**,**f**, further corroborates this explanation. Based on the evidence presented, the addition of LiOH is critical to reverse hydration and allow dense LLZO with high conductivity to be obtained. The use of non-aqueous solvents such as lower alcohols (e.g. methanol) for washing may be a worthwhile investigation in future studies. Finally, while the method of Reddy et al.[122] produced LLZTO with low ionic conductivity, it is highly likely that re-incorporation of a Li-source such as LiOH would have enabled their material as well to achieve higher ionic conductivity more characteristic of LLZTO.

Molten salt synthesis has not been extensively investigated for the preparation of LLZO until recently. Here, it is shown that MSS can provide particular benefits to the synthesis of LLZO, including lower reaction temperatures than those used in solid state reaction (and often in less time), less expensive precursors than those used in sol-gel methods, and a straightforward synthesis route that enables the rapid preparation of fine crystalline powders in a short time. The ability to easily synthesize fine, non-agglomerated powders of LLZO via MSS may be a critical step to widespread utilization of LLZO as a solid electrolyte. Since ball-milling has limitations to particle size reduction[23], these more uniform and fine powders may enable roll-to-roll processing of electrolyte materials e.g. by tape-casting such as demonstrated by Yi et al.[23,111], (which requires a stable slurry of fine powder) and thus better incorporation into practical battery production methods. This factor in particular overcomes one of the primary challenges of using a brittle, crystalline ceramic as an electrolyte. Finally, on a lab scale alone, tens of grams of uniform c-LLZO can be easily obtained in a matter of hours using a single small

furnace, indicating that this synthesis approach may confer a new easily scalable method of LLZO production, necessary for implementation in future solid-state LIBs.

4.4. Conclusions

Undoped, aluminum-doped, and gallium-doped c-LLZO were successfully synthesized using a novel molten salt synthesis route. As the reaction temperature increases from 500 °C to 900 °C, LaOCl is formed followed by initial formation of ultrafine LZO nanocrystals, and finally fine LLZO powders at 900 °C in 4 hours. Well-dispersed, fine (submicron to few micron) powders were obtained under optimized conditions. The hydration/proton exchange resulting from the unavoidable washing step involved in molten salt synthesis was also observed here, and a simple solution via addition of LiOH before pellet sintering is presented. Well-densified pellets were obtained with Li-ion conductivity values ranging from 0.230 to 0.371 mS cm^{-1} using simple uniaxial pressing followed by sintering at 1100 °C, indicating that under further optimized conditions, these powders will result in ceramic electrolytes with excellent properties. Finally, the ease with which fine powders can be obtained with this method may be a crucial step towards realistic processing of LLZO for scalable solid-state LIBs.

5. REDUCTION IN FORMATION TEMPERATURE OF TA-DOPED LITHIUM LANTHANUM ZIRCONATE BY APPLICATION OF LUX-FLOOD BASIC MOLTEN SALT SYNTHESIS

5.1. Introduction

As shown in **Chapter 4**, molten salt synthesis (MSS) is a versatile synthetic strategy for the preparation of oxides at temperatures and times lower than those required for SSR, with better control over particle size and morphology.[119,120] It was recently demonstrated that submicron LLZO particles can be prepared with MSS using a LiCl-KCl eutectic mixture as solvent, although a reaction temperature of 900 °C was still required to obtain phase-pure LLZO.[161] One strategy for reducing the reaction temperature for oxide formation in MSS is by utilizing more basic melt components such as oxobases (e.g. $LiNO_3$, LiOH).[119] Acidity and basicity for oxides are described in the Lux-Flood acid-base theory, wherein a base is an O^{2-} donor (e.g. $Li_2O \rightarrow 2\ Li^+ + O^{2-}$) and an acid is an O^{2-} acceptor (e.g. $SiO_2 + O^{2-} \rightarrow SiO_3^{2-}$).[180,181] A basicity index analogous to pH can be defined in this way based on the concentration of O^{2-} in the melt ($pO^{2-} = -\log([O^{2-}])$, related to the concentration and nature of bases used. The ability of more basic molten salts to liberate more O^{2-} at lower temperatures results in a shift in acid-base equilibrium, which favors the precipitation of oxide phases[119], thereby providing a stronger thermodynamic driving force for oxide formation. For example, $Li_4Ti_5O_{12}$ (LTO) can be synthesized in molten LiCl-KCl at 800 °C,[182] whereas utilization of a Lux-Flood basic molten salt medium based on the ternary $LiNO_3$-LiOH-Li_2O_2 system enables

formation of LTO at temperatures as low as 300 °C.[172] For comparison, LTO synthesized via SSR requires temperatures between 800-1000 °C.[172] Other examples of MSS of oxides in the literature have noted a similar effect, wherein increased basicity of the melt components (*e.g.*, use of nitrite over nitrate salts) can confer a greater decrease in formation temperature of a given oxide.[183]

Herein, this effect is leveraged for preparation of Ta-doped LLZO (LLZTO, nominal composition $Li_{6.4}La_3Zr_{1.4}Ta_{0.6}O_{12}$), which is known to possess exceptionally high conductivity among Li-garnets.[38] Doping of LLZO with Ta is advantageous as Ta resides on the Zr-sites in the garnet structure, and therefore does not disrupt or impede Li-diffusion on the Li sublattice like other dopants such as Al or Ga.[27] Additionally, Ta-doping provides better electrochemical stability compared to other Zr-site dopants such as Nb.[26] For synthesis of LLZTO, several molten salt media of increasing basicity were employed by successively increasing the proportion of oxobases in the melt, beginning with eutectic LiCl-KCl (from now on referred to as the "chloride" melt), progressing to a mixture of LiCl and LiOH (which we call the "mixed" melt), and finally ternary mixture of oxobases consisting of $LiNO_3$-Li_2O_2-LiOH (which we call the "highly basic" or HB melt). It is shown that the formation temperature of LLZTO can be successively reduced by increasing the basicity of the melt, and the morphology and particle size of the resultant material can also be controlled by the nature of the salt medium utilized.

5.2. Experimental

5.2.2. Materials Synthesis and Processing

Several molten salt media of varying Lux-Flood basicity were employed for synthesis of LLZTO of composition $Li_{6.4}La_3Zr_{1.4}Ta_{0.6}O_{12}$. These reaction media include eutectic LiCl-KCl, LiCl-LiOH in a 1:1 ratio by mass, and a ternary mixture of $LiNO_3$-LiOH-Li_2O_2 with variable composition. The general workflow for the various MSS methods described in this Chapter are shown in **Scheme 5.1**. Sacrificial LLZTO powder was also synthesized via SSR to provide a Li_2O-rich vapor phase during sintering. Sintering of LLZTO pellets from various molten salt powders was performed in MgO crucibles with sacrificial SSR LLZTO powder and in some cases Li_2O_2 to ensure sufficient Li_2O vapor pressure. Detailed descriptions of the synthetic and sintering procedures are contained in **Appendix C**.

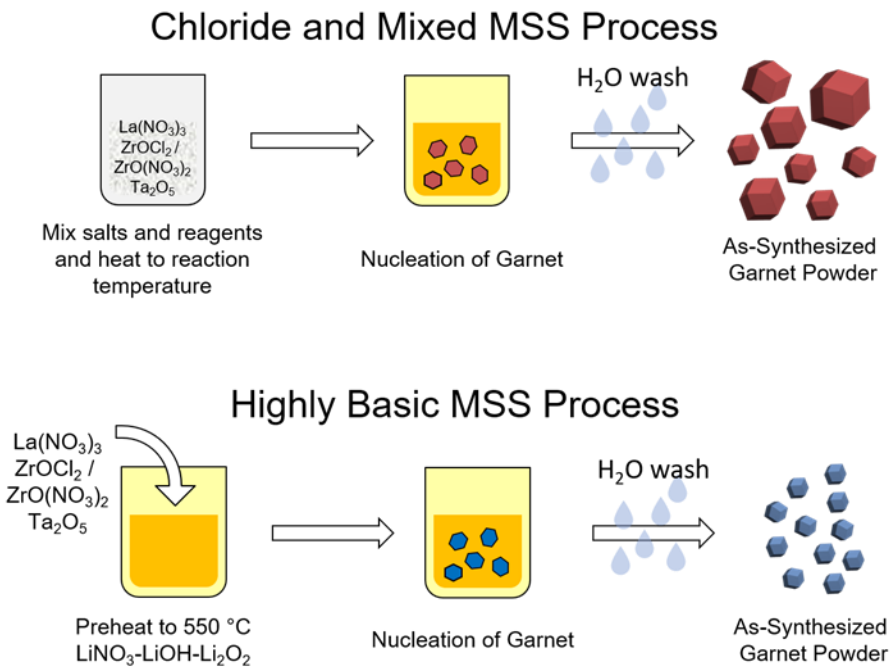

Scheme 5.1. General synthetic process for molten salt synthesis (MSS) of LLZO garnet using the chloride-MSS (LiCl-KCl), mixed-MSS (LiCl-LiOH), and HB-MSS ($LiNO_3$-Li_2O_2-LiOH) salt media used in this work. For the chloride and mixed-MSS, the salts and reagents are mixed together before heat treatment followed by a standard temperature ramp in the furnace. For the HB-MSS, the lower synthesis temperature allows a 'reagent feeding' method to be employed, where the salts are preheated to the reaction temperature and the reagents are subsequently added. This approach initiates the reaction at the desired reaction temperature, rather than relying on a slow furnace ramp to the desired reaction temperature.

5.2.2. Materials Characterization

X-ray diffraction (XRD) was performed using either a Siemens D-5000 or a Bruker D-8 powder diffractometer with CuK_α radiation for crystalline phase identification. The reference pattern for c-LLZO ($Ia\bar{3}d$) was generated according to the structure reported by Logeat *et al.*[48] The sample morphology was examined using a FEI XL30 scanning electron microscope (SEM) equipped with an EDAX system for energy

dispersive spectroscopy (EDS). To minimize charging, a carbon film was deposited on the samples before imaging using a thermal evaporator type carbon coater.

Transmission electron microscopy (TEM) was performed using an aberration corrected (CEOS image corrector) FEI Titan Environmental TEM operated at 300 kV. For high-resolution aberration corrected TEM imaging, aberrations were corrected to yield an imaging resolution better than 1 angstrom, and negative spherical aberration imaging (Cs ~ -13 μm) was employed to yield bright contrast at the positions of atom columns. Electron diffraction (ED) patterns were obtained using a third condenser lens to allow formation of a submicrometer diameter parallel beam rather than using a selected area aperture. To prepare TEM samples, the LLZO powder was ultrasonically suspended in HPLC-grade methanol. A holey carbon TEM grid (Pacific Grid Tech) was then briefly immersed into the aforementioned suspension. Finally, the grid was dried at elevated temperature (*e.g.,* 100 °C) in air to fully remove methanol.

Detailed descriptions of the procedures used for electrochemical measurements are in **Chapter 2.2.4** and **Appendix C**.

5.3. Results and Discussion

5.3.1. Synthesis of $Li_{6.4}La_3Zr_{1.4}Ta_{0.6}O_{12}$ in various molten salt media

To understand the formation process of LLZTO in the various MSS reactions, a series of syntheses were performed at different temperatures. In all cases, phase-pure LLZTO can be prepared under the appropriate experimental conditions (**Figure 5.1**). Initial attempts at forming cubic Al-doped LLZO and Ga-doped LLZO in the basic media were unsuccessful (*i.e.*, resulting in tetragonal LLZO), likely due to the poor solubility of Al_2O_3 or Ga_2O_3. Therefore, LLZTO was the focus of further study. In the case of MSS in the LiCl-KCl medium, the formation process of undoped LLZO was described previously, with lanthanum oxychloride (LaOCl) forming at 500 °C followed by formation of pyrochlore type lanthanum zirconate ($La_2Zr_2O_7$) beginning at 600 °C and finally LLZO at 900 °C.[161] Interestingly, LLZTO with a Ta-doping level of 0.6 moles per formula unit (PFU) forms at only 850 °C (**Figure C1**), 50 °C lower than that needed to synthesize undoped LLZO in the same melt. This seems to indicate that Ta-doping results in a more energetically favorable phase than undoped LLZO, which is corroborated by calculations from Miara *et al.*,[162] wherein increasing the Ta-content from 0 to 2 mol PFU results in a decrease of the decomposition energy, implying a more stable cubic garnet phase.

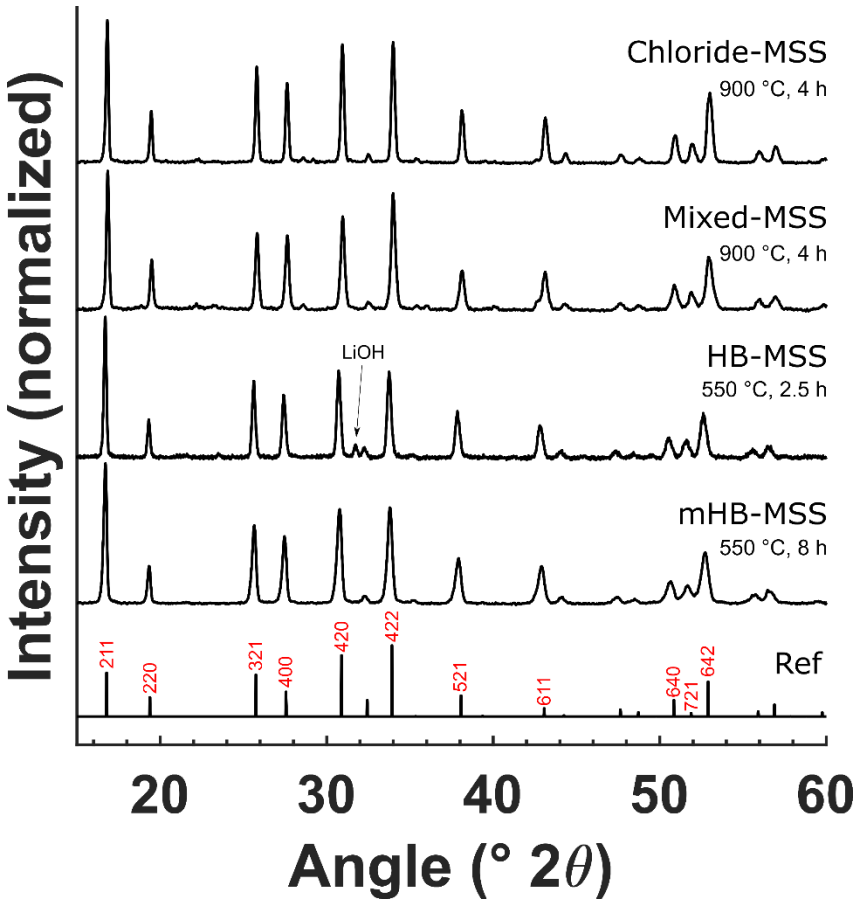

Figure 5.1. XRD patterns of LLZTO synthesized using molten salt synthesis (MSS) in the chloride (900 °C 4 h), mixed (900 °C, 4 h), HB (550 °C, 2.5 h), and modified HB (550 °C, 8 h) melts; reference pattern produced according to Logeat *et al.*[48] with major reflections labeled with (red) corresponding Miller indices. LiOH present in the HB-MSS sample is due to the large amount of salts used to form the melt and some residue after washing.

XRD patterns for LLZTO syntheses in the mixed and HB melts are shown in **Figure C2**. In both media, phase-pure garnet powders can be obtained under the appropriate experimental conditions. In the case of MSS in the mixed halide/hydroxide melt, similar to the pure chloride melt, LaOCl and LZO intermediates form before LLZO; the increased basicity of LiOH, however, allows formation of LLZTO at only 700 °C

(**Figure C2a**). The morphology of these intermediates is the same as previously reported[161] and can be seen in **Figure C3a**.

On the other hand, LLZTO can form at much lower temperatures using the highly basic, ternary salt medium. Due to the $LiNO_3$ present in this mixture, the maximum feasible reaction temperature is ~600 °C, as $LiNO_3$ decomposes[123] above this temperature. One advantage of the low synthesis temperature in HB-MSS is the ability to add reagents ('reagent feeding') to the melted salts, essentially 'starting' the reaction at the desired temperature rather than requiring a slow temperature ramp. This distinction is depicted in **Scheme 5.1** above. However, the high viscosity of the paste-like mixture below 550 °C made uniform addition of reagents challenging. Nonetheless, synthesis at 450 °C was attempted and $La(OH)_3$, $LiTaO_3$, and a small amount of LLZTO were observed in the XRD pattern of the products (**Figure C2b**). Curiously, no other intermediate Zr-containing phases such as $La_2Zr_2O_7$ or ZrO_2 were observed, which may indicate that Zr is sequestered in amorphous intermediates. The morphology of the intermediates from the HB synthesis at 450 °C is shown in **Figure C3b**.

Due to the lower viscosity of the melt at 550 °C, most experiments using HB-MSS were conducted at this temperature. A time-dependent study (**Figure C2b**) showed that initially, $La(OH)_3$ is the main crystalline phase formed, but it eventually reacts and a small amount of $LiTaO_3$, La_2O_3 and LLZTO are formed after 1 h at 550 °C. Phase pure LLZTO is obtained using reaction times of 2.5 – 4 h at 550 °C. Some reactions were performed at 550 °C for 4 h without either $LiNO_3$ or LiOH and both resulted in incomplete formation of LLZTO (**Figure C2b**). Based on these results, we conclude that all three flux components are important to efficiently form LLZTO in the case of HB-

MSS. There appears to be a synergistic effect of these three components that results in the effectiveness of the HB-MSS method, wherein the relatively low melting point of $LiNO_3$ (~ 264 °C)[123] helps to reduce the melting point of the mixture, LiOH acts as a solvent with versatile acidic or basic properties,[184] and Li_2O_2 acts as a base, liberating reactive oxygen species as it decomposes[165] starting around 250 °C, while also forming reactive Li_2O.

Representative scanning electron microscopy (SEM) images of LLZTO prepared from each method are shown in **Figure 5.2a-c**. The particle size range of the LLZTO powders synthesized in the halide melt (**Figure 5.2a**) corresponds well with that of undoped, Al-doped, and Ga-doped LLZO synthesized in the same melt previously by our group,[161] although the size distribution is slightly larger, possibly due to the energetic favorability of forming LLZTO compared to other forms of LLZO as discussed previously. In contrast, LLZTO synthesized in the mixed melt (**Figure 5.2b**) presents as substantially larger faceted particles with sizes ranging from 10 – 40 μm, implying that single crystal growth is favored. LLZTO synthesized in the highly basic medium (**Figure 5.2c**) generally has the smallest particle size, with the primary particle size ranging from 200 – 500 nm (though many individual nuclei are fused together) up to about 2 μm for a small number of particles. These results indicate a complex interrelationship between melt basicity and the solvent properties (e.g. chlorides vs. oxosalts) of the melt and resultant particle size.

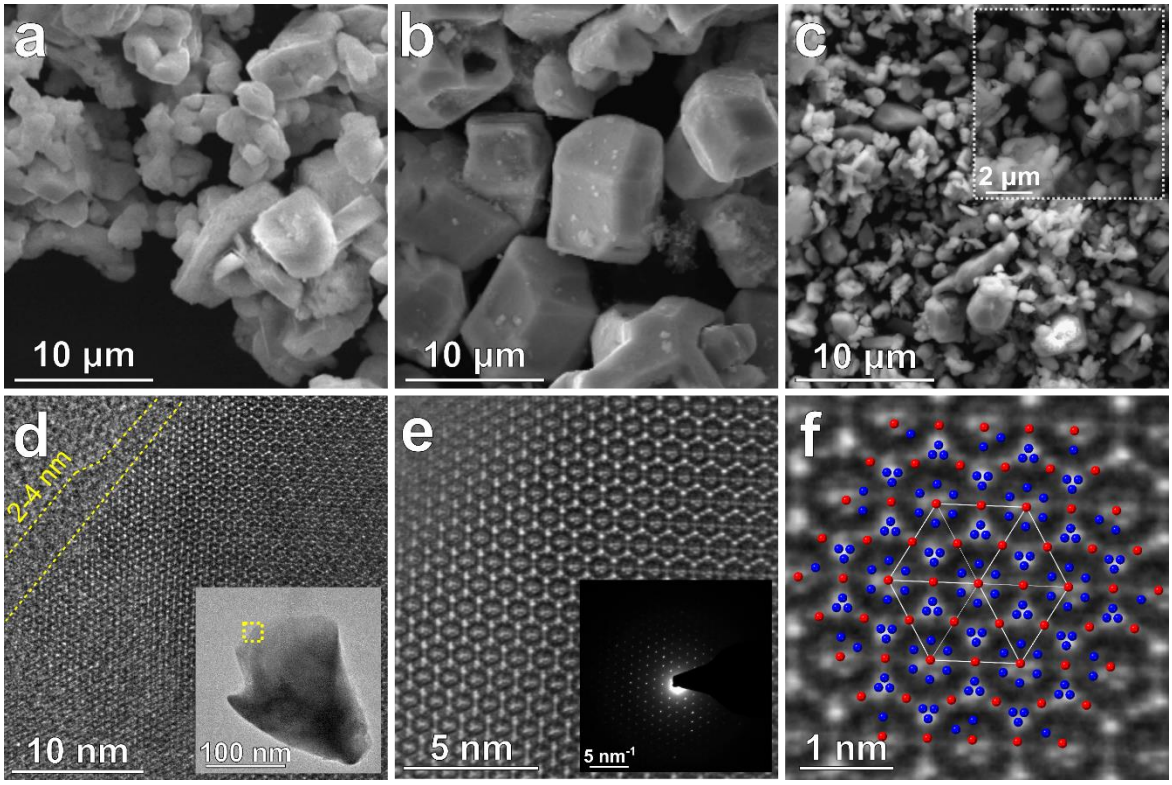

Figure 5.2. Representative SEM images of LLZTO powders synthesized using MSS in the **a)** chloride melt at 850 °C (higher magnification in inset); **b)** mixed melt at 700 °C; **c)** and highly basic melt at 550 °C (higher magnification in inset), and TEM images of particle from highly basic melt **d)** phase contrast image of particle on carbon film with low magnification image in inset, with 2 – 4 nm surface Li_2CO_3 layer indicated by dashed yellow lines showing characteristic amorphous structure distinct from underlying holey carbon grid, **e)** Wiener filtered phase contrast image of particle in (**d**) with nanoprobe electron diffraction pattern in inset showing (111) crystal symmetry, and **f)** zoom of (**e**) with LLZTO (111) crystal structure overlaid with La (blue) and Zr/Ta (red) atoms shown generated using CrystalMaker software based on structure from Logeat et al.[48]

Although the presence of a substantial amount of LiOH seems to favor the formation of large particles in the mixed medium, the addition of $LiNO_3$ and Li_2O_2 seems to promote formation of small LLZTO particles in the HB medium despite the large amount of LiOH in the melt. Further, the HB melt can be seen to slowly bubble at 550

°C, most likely due to the decomposition of Li_2O_2 and subsequent liberation of O_2 gas,[165] which may in turn provide a sort of innate mixing that helps to more uniformly nucleate particles of LLZTO and distribute dissolved species. This innate mixing likely complements the reagent feeding method used for HB-MSS where reagents are added to the pre-heated melt, which is known to result in a smaller particle size distribution under comparable synthesis conditions.[185] The small particle size produced by the HB-MSS method allows for facile high-resolution TEM (HRTEM) imaging. **Figure 5.2d** shows a HRTEM image of a LLZTO particle synthesized using HB-MSS, with a lower magnification image shown in the inset. A layer 2 – 4 nm thick is observed on the particle surface, which is attributed to the surface Li_2CO_3 layer that forms when LLZO is exposed to ambient atmosphere.[59] A higher magnification image (Wiener-filtered to improve clarity) is in **Figure 5.2e**, with a corresponding (111) electron diffraction pattern in the inset. Finally, **Figure 5.2f** shows a zoomed image of **Figure 5.2e** with the LLZTO (111) crystal structure overlaid. These results indicate that primary particles synthesized from the HB-MSS method are single crystals.

The formation pathway of LLZTO in each of these synthesis methods is depicted graphically in **Scheme 5.2**. The trend of increasing Lux-Flood basicity and reduced garnet formation temperature is clear in the progression from the chloride, mixed, and highly basic molten salt media. The formation of crystalline LLZTO at only 550 °C using HB-MSS is particularly interesting, and to our knowledge is the lowest formation temperature for this garnet material reported to date. By comparison, SSR for LLZTO generally requires at least a single calcination at 900 °C for 8 h, although the majority of examples use higher temperatures, longer reaction times, and/or even multiple reaction

steps (see **Table 5.1** for comparison of experimental conditions for LLZTO using various methods).

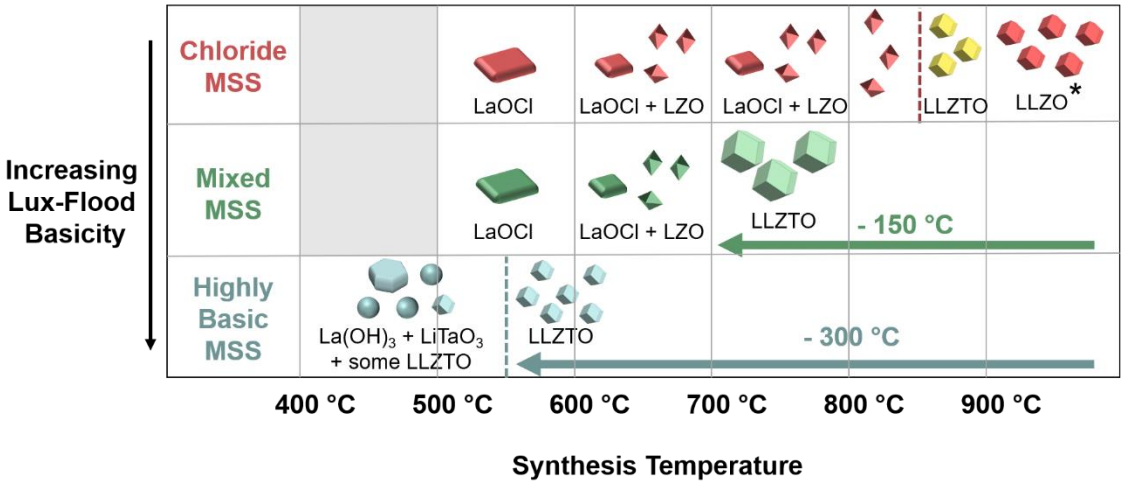

Scheme 5.2. Depiction of products formed at different reaction temperatures for LLZO (* indicates undoped, from ref.[161]) and LLZTO synthesized using chloride (LiCl-KCl), mixed (LiCl-LiOH), and highly basic ($LiNO_3$-LiOH-Li_2O_2) MSS methods. Note the trend of decreased garnet formation temperature as the Lux-Flood basicity of the salt medium increases.

To further decrease the viscosity of the HB-MSS medium and promote a smaller particle size distribution, a modified version of the HB melt was also investigated (which we call mHB-MSS), wherein a higher ratio of $LiNO_3$ and LiOH to Li_2O_2 was used (as described in **Appendix C**) to reduce viscosity and allow better intermixing of reagents and diffusion of solutes. In this case, reactions were performed at 550 °C for 4, 8, and 24 h to understand the particle size evolution of LLZTO in this medium (XRD patterns shown in **Figure C4** and SEM images in **Figure C5**). After 4 h of reaction, many ultrafine nuclei are observed along with some larger particles on the order of one micron

in size. After 8 h, the particle sizes are generally slightly smaller than the conventional HB-MSS method (particle size distributions for LLZTO from HB and mHB-MSS are compared in **Figure C6**) but less agglomerated, indicating that the mHB-MSS method improves mixing and particle dispersity despite the much longer reaction time, which is attributable to the lower viscosity of the mHB melt. Even for a reaction time of 24 h, the particle sizes do not increase substantially, but rather agglomeration of the primary particles increases. Finally, the improved melt properties of the mHB-MSS approach allow a lower ratio of salts to reagents of only 1.7 : 1 (compared to 5 : 1 for the HB-MSS method) by mass, substantially reducing waste.

5.3.2. Ionic conductivity of LLZTO synthesized from various MSS methods

The LLZTO powders prepared from the different MSS methods were sintered at 1200 ^{o}C for various times to identify the optimized conditions, which are shown in **Table 5.2**. The relative density of the pellet sintered from LLZTO powder prepared from the chloride melt was roughly 88%, which is similar to our previous results for Al and Ga-doped LLZO synthesized using MSS in the same melt.[161] Before sintering, the LLZTO from the chloride and mixed MSS syntheses were ball-milled to improve sinterability while the as-synthesized powders from HB-MSS were already highly sinterable due to the smaller particle sizes. The density and ionic conductivity of mHB-MSS LLZTO was largely unaffected by ball-milling (see **Figure C7a,b** and **Table C1**). The relative density of the pellets from the mixed MSS was substantially lower (78.5%) while those for the HB methods were much higher (93.4% for HB and 91.1% for ball-milled mHB). It is not

clear why powders synthesized using the chloride and mixed MSS had low pellet densities, as after ball-milling the particle size distribution was comparable to that seen in the as-synthesized LLZTO particles from HB-MSS. It is hypothesized that the post-synthesis washing step with water may have introduced a larger degree of proton exchange, which is known to have a deleterious effect on sinterability,[122,161] for LLZTO synthesized in chloride and mixed MSS. The large starting particle sizes of the LLZTO from the mixed melts may also have a negative effect on sinterability even after ball-milling.

Table 5.1. Comparison of properties of the LLZO prepared using molten salt synthesis. The bulk (where measurable using Sn-Li electrodes, σ_{bulk}) and total ionic conductivity (σ_{tot}) were measured at 25 °C and have units mS cm^{-1}. (LLZTO = $Li_{6.4}La_3Zr_{1.4}Ta_{0.6}O_{12}$, ALLZO = $Al_{0.24}Li_{6.28}La_3Zr_2O_{12}$, GLLZO = $Ga_{0.25}Li_{6.25}La_3Zr_2O_{12,}$ NM – not measured, G – σ_{tot} measured using graphite electrodes, Au – σ_{tot} measured using sputtered gold electrodes)

Molten Salt Medium	Type of LLZO	Synthesis Conditions		Sintering Conditions		Pellet Properties			Ref.
		Temp. (°C)	Time (h)	Temp.(°C)	Time (h)	Relative Density (%)	σ_{bulk}	σ_{tot}	
Highly Basic	LLZTO	550	2.5	1200	3	93.4	**0.38**	**0.35**	This work
Modified Highly Basic	LLZTO	550	8	1200	4	91.1	**0.73**	**0.61**	This Work
Mixed	LLZTO	900	4	1200	2	78.5	NM	**0.45**^{G}	This work
Chloride	LLZTO	900	4	1200	4	87.9	**0.61**	**0.46**	This work
	ALLZO	900	4	1100	18	84	NM	**0.23**^{Au}	Weller et al.[161]
	GLLZO	900	4	1100	6	84	NM	**0.37**^{Au}	Weller et al.[161]

The room temperature bulk and total ionic conductivity and activation energies for lithium conduction of selected LLZTO samples from each of these MSS methods were determined (**Table C1** and **Table C2** show parameters used to calculate density and

ionic conductivity). Due to the poor sinterability of the pellet from the mixed-MSS, only the total ionic conductivity was assessed (**Figure C7c**, fracture surface image shown in **Figure C7d**). Impedance spectra used for determining room temperature ionic conductivity of the LLZTO from HB, mHB, and chloride-MSS are plotted in **Figure 5.3a** with the characteristic frequencies of notable spectral features shown. Contributions from the bulk and grain boundary impedances along with calculated spectra from circuit fitting of these spectra are shown in **Figure C8**. From the results shown in **Table 5.1**, it is clear that the LLZTO from mHB-MSS displayed the highest total and bulk ionic conductivities from the MSS methods studied. An Arrhenius plot derived from the temperature dependence of ionic conductivity for HB, mHB, and chloride-MSS in shown in **Figure 5.3b**, with impedance spectra measured at various temperatures shown in **Figure C9**. In all three cases, the activation energies are between approximately 0.39-0.4 eV $atom^{-1}$, corresponding well with values reported in the literature (**Table 5.2**). The differences in ionic conductivity between the HB, mHB, and chloride-MSS samples can be explained by a combination of grain boundary impedance (see **Table C2**) and difference in pre-exponential factor (mostly likely charge carrier concentration, which is known[10] to dominate in LLZO) since their activation energies are nearly identical.

Table 5.2. Properties of the Ta-doped LLZO prepared by MSS herein compared with relevant literature results ($Li_{7-x}La_3Zr_{2-x}Ta_xO_{12}$, where x = 0.6 unless otherwise noted and total ionic conductivity (σ_{tot}) measured at 25 °C unless otherwise noted)

Synthesis Method	Synthesis Conditions		Sintering Conditions		Pellet Properties			Reference
	Temp. (°C)	Time (h)	Temp. (°C)	Time (h)	Relative Density (%)	σ_{tot} (mS cm^{-1})	E_a (eV)	
HB-MSS	550	2.5	1200	3	93.4	0.35	0.390	Weller et al.[145]
Modified HB-MSS	550	8	1200	4	91.1	0.61	0.402	Weller et al.[145]
Mixed MSS	900	4	1200	2	78.5	0.47	-	Weller et al.[145]
Chloride MSS$^{\neq}$	900	4	1200	4	87.9	0.46	0.396	Weller et al.[145]
SSR*	900	2x10	1130	36	94.1	0.28^{b}	NR	Wang et al.[34]
SSR*	900	2x10	1100	36	92.5	0.63^{d}	0.36	Wang et al.[34]
SSR$^{\neq,*}$	950	2x6	1250	6	93.9	0.42	0.43	Huang et al.[40]
SSR$^{\neq,*}$	950	2x6	1280/1180	0.33/5	97	0.74	0.42-0.45	Huang et al.[41]
SSR$^{\neq}$	900	12	1180	12	91	0.33	0.53	Yi et al.[33]
SSR	900	6	1200	24	84	0.15‡	0.40	Janani et al.[43]
SSR*	1x at 850 / 2x at 1000	3x20	1150	5	92.7	0.71^{†,c}	0.42	Tsai et al.[28]
SSR*	900	NR	1140	16	NR	1.0†	0.35	Li et al.[38]
Co-precipitation	900	3-4	1050^{hp}	1	97.1	0.39^{a}	0.45	Thompson et al.[37]
Co-precipitation	900	3-4	1050^{hp}	1	97.8	0.82^{b}	0.43	Thompson et al.[37]
Solution-combustion synthesis	750	8	1125	6	NR	0.2	NR	Chen et al.[31]
Sol-gel	950	4	1100	4	89	0.14-0.21^{b}	NR	Yoon et al.[93]
Sol-gel	900	2	1000^{hp}	0.33	88	0.05	0.43	El-shinawi et al.[35]
Polymer combustion	700	4	1100	12	93.6	0.67	0.42	Weller et al.[146]
FZ Single Crystal Growth	850	60	FZ	FZ	100	~ 1.0	0.39-0.47	Kataoka et al.[51]

‡ – σ_{tot} measured at 33 °C; † – Al_2O_3 added as sintering aid; a – x = 0.75; b – x = 0.5; c – x = 0.4; d – x = 0.3; hp – consolidated via hot-pressing;
≠ – high energy ball milling (e.g. planetary milling, attrition milling, etc.) of LLZTO to reduce particle size
** – repeated grinding and heating steps (e.g. 2x10 = 2 calcination steps each for 10 hours)*
NR – not reported
FZ – grown by floating zone single crystal growth method, sintering not applicable

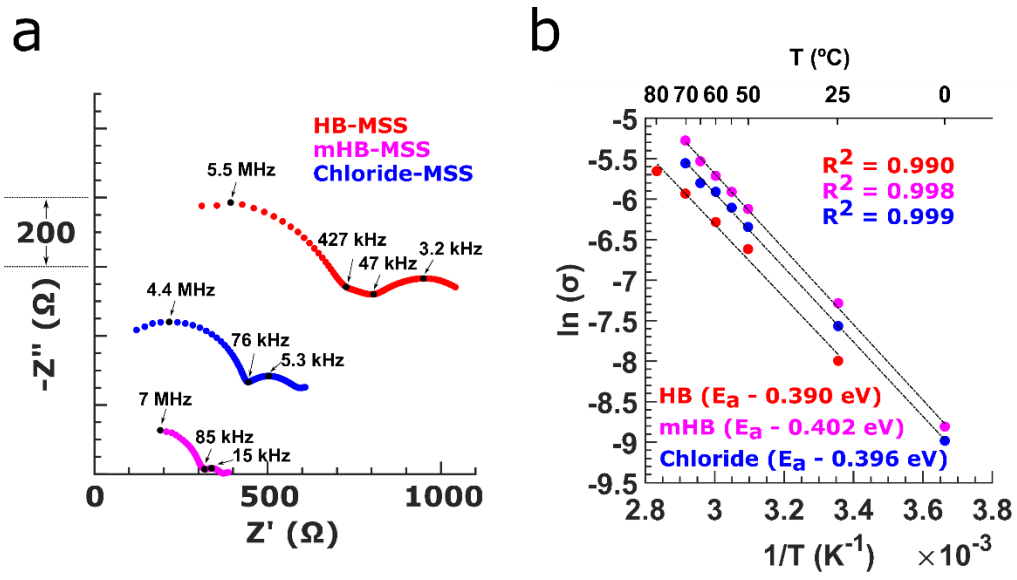

Figure 5.3. **(a)** Room temperature Nyquist plots (7 MHz to 1 Hz) obtained using Sn-Li alloy electrodes for HB-MSS, mHB-MSS, and chloride-MSS pellets, with frequencies of pertinent features noted (note: spectra are offset, -Z" axis scale of 200 Ω between each major tick), **(b)** Arrhenius plot of ln(σ) (S cm^{-1}) vs T^{-1} (K^{-1}) for the same LLZTO pellets in (**a**) used to determine activation energy; fit quality quality (R^2) and calculated E_a (eV at $^{-1}$) values are shown (see **Figure C9** for EIS spectra used to determine temperature dependence of ionic conductivity for each sample).

LLZTO pellets consolidated from HB and mHB MSS powder seem to be highly sinterable based on the high pellet densities (**Table 5.1**). Fracture surface images of HB, mHB, and chloride-MSS pellets are shown in **Figure 5.4**. In all cases, a dense microstructure and a large degree of transgranular fracture is observed, indicating good grain cohesion despite the somewhat lower pellet density for the chloride-MSS LLZTO. Inspection of **Figure 5.4** shows that the grain size (where it can be reasonably estimated from well-separated grains) appears to range between 2-10 μm, with some larger grains present, indicating substantial grain coarsening.

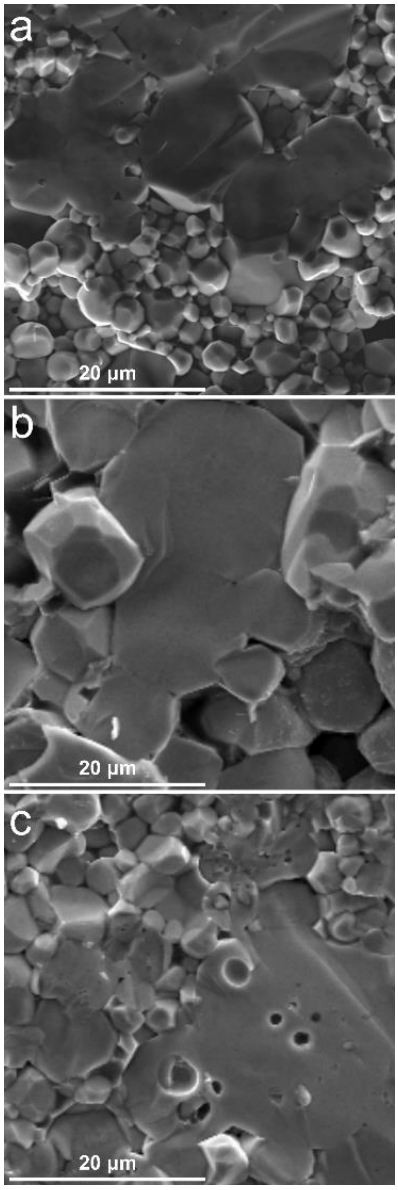

Figure 5.4. SEM fracture surface images of **(a)** an HB-MSS pellet, **(b)** an mHB-MSS pellet, **(c)** a chloride-MSS pellet

The improved sinterability of the HB and mHB-MSS materials compared to the other MSS media may result from less severe proton-exchange due to the high basicity of the salt medium used in the synthesis, producing an alkaline aqueous solution during washing, which has been shown to substantially reverse proton-exchange.[186] However,

the HB-MSS LLZTO has noticeably lower total ionic conductivity (0.35 mS cm^{-1}) than mHB-MSS LLZTO, comparable to that observed in the chloride and mixed melts, despite the much higher pellet densities. Further analysis of an HB-MSS pellet (sintered at 1300 °C to achieve a density higher than 95%) was performed using backscatter electron (BSE) imaging and EDS of the pellet fracture surface (**Figure C10**). The BSE images reveal regions of substantially different contrast, and EDS spectra reveal high Ta-content in the brighter grains, indicating the presence of elemental inhomogeneity in the pellet despite the high sintering temperature. For comparison, BSE images of the mHB and chloride-MSS pellets (**Figure C10**) do not display noticeable contrast differences, indicating more uniform composition between grains. It is possible that the lower ionic conductivity of the HB-MSS LLZTO may be related to this elemental inhomogeneity in the final dense ceramic pellets, which may produce non-optimal lithium conduction in a large subset of the grains in the dense ceramic. To date only Thompson et al. have observed elemental inhomogeneity in LLZTO with the aid of high-resolution synchrotron XRD[10]. The origins of elemental inhomogeneity in LLZTO from MSS and how to mitigate it are the focus **Chapter 7** of this dissertation. However, despite its presence and apparent effect on Li-ion conduction, the ionic conductivity of the HB LLZTO described herein still compares favorably with much of the literature (see **Table 5.2**) and indicates that reasonably good performance can be attained with a synthesis temperature that is drastically lower than those in conventional synthesis methods. More importantly, the mHB-MSS method utilizing a lower fraction of Li_2O_2 in the salt melt can produce sintered LLZTO pellets with higher ionic conductivity (0.61 mS cm^{-1}), indicating that this novel MSS method using a high Lux-Flood basicity medium enables formation of

LLZTO at only 550 °C, with high ionic conductivity and relative density. Finally, the lower ratio of salts to reagents indicates that the mHB-MSS method may be comparably scalable to SSR despite the increased complexity due to the benefit of the substantially reduced synthesis temperature.

5.4. Conclusion

In conclusion, Ta-doped LLZO (LLZTO) of nominal composition $Li_{6.4}La_3Zr_{1.4}Ta_{0.6}O_{12}$ is obtained via molten salt synthesis (MSS) using several different salt media with different Lux-Flood basicity. Using a highly basic melt containing $LiNO_3$, LiOH, and Li_2O_2, the formation temperature of LLZTO decreases to only 550 °C, to our knowledge the lowest synthesis temperature for crystalline LLZTO reported to date, yielding a novel route towards synthesis temperatures that are considerably lower than conventional solid-state reactions (SSR) or other lower temperature synthetic routes such as sol-gel or combustion. Further, by tuning the solution properties of the highly basic melt, small particle sizes and a low degree of agglomeration are obtained using synthesis at 550 ^oC for 8 h, which upon sintering at 1200 ^oC for 4 h results in pellets with relative density of 91.1% and a high bulk and total ionic conductivity of 0.73 and 0.61 mS cm^{-1} respectively. Finally, the presence of elemental inhomogeneity within LLZTO pellets even after sintering at high temperatures is an interesting result that has implications for processing of garnets using Ta-doping; this effect is discussed in detail in **Chapter 7**.

6. PYROCHLORE NANOCRYSTALS AS VERSATILE QUASI-SINGLE-SOURCE PRECURSORS TO LITHIUM CONDUCTING GARNETS

6.1. Introduction

One common feature of LLZO synthesis is the nearly ubiquitous presence of pyrochlore type lanthanum zirconate ($La_2Zr_2O_7$, LZO) as an intermediate phase before garnet formation, signalling incomplete reaction.[22,95,99,146,161,187] Its presence after extended calcination or sintering of LLZO indicates decomposition of the garnet structure due to evaporation of Li at high temperatures.[19] LZO beneficially contains the majority of the non-Li components of LLZO in a single crystalline phase. For this reason, some researchers have used it as a LLZO precursor. In one case, LLZO was synthesized from Li_2CO_3, $La(OH)_3$, and $La_2Zr_2O_7$,[188] but still required a temperature of 800 °C and only formed the low-conductivity[17] tetragonal ($I4_1/acd$) phase of garnet due to the absence of dopants needed to stablize the high-conductivity[1] cubic ($Ia\bar{3}d$) phase. Deviannapoorani *et al*. used $La_2Zr_2O_7$ along with mixtures of nominal composition Li_7LaO_5 or $Li_{6.28}Al_{0.24}LaO_5$ to synthesize undoped and Al-doped cubic LLZO, but the resulting products were not phase-pure even with calcination at 1200 °C, which may have led to their lower ionic conductivity compared to LLZO synthesized using conventional precursors.[187] Most likely, the challenge in using LZO as a precursor for garnet synthesis is due in part to the difference in La : Zr stoichiometry between LZO and LLZO (1 : 1 and 3 : 2 moles per formula unit, respectively). One option to resolve this challenge is to

obtain a La-excess pyrochlore phase that can also incorporate the dopants needed to stabilize the cubic garnet phase.

Pyrochlore-structured oxides generally display a high degree of flexibility in composition and substituents.[189] Pyrochlores adopt the general formula $A_2B_2O_6X$, where A = di- or trivalent cations, B = tetra- or pentavalent cations, and X = O^{2-}, OH^- or F^-.[189] The ease with which chemical substitutions can occur in pyrochlores is leveraged in this work, where it is demonstrated that the synthesis of ultrafine, nanocrystalline, multiply-doped LZO as a precursor for obtaining doped LLZO. Herein, $La_{2+y}Zr_{2-x-y}Ta_xO_{7+(x-y)/2}$ nanocrystals are synthesized with various amounts of Ta and excess La. The pyrochlore $La_{2.4}Zr_{1.12}Ta_{0.48}O_{7.04}$ (corresponding to a mole ratio of La : Zr : Ta = 3 : 1.4 : 0.6) is prepared and utilized as a quasi-single-source-precursor for the garnet ($Li_{6.4}La_3Zr_{1.4}Ta_{0.6}O_{12}$), requiring only a lithium source for the transformation. These pyrochlores can convert to garnets at reaction temperatures as low as 400 °C using molten salt synthesis (MSS) in a highly basic flux. Additionally, densified garnet ceramics can be formed directly from pyrochlore powders via *in situ* reactive sintering with LiOH.

6.2. Results and Discussion

The synthesis of pyrochlore nanocrystals was adapted from the molten hydroxide method[190,191] used for complex oxides. Several syntheses were performed at 400 °C (see **Appendix D**) to determine the feasibility of the extensive doping required to convert LZO to LLZO with only the addition of a Li-source. **Figure 6.1a** shows synchrotron X-

ray diffraction (XRD) patterns of La-doped LZO, Ta-doped LZO, and La/Ta co-doped LZO of increasing doping levels. The broad features in the XRD data are due to the small crystallite[147] size of these pyrochlores. These results show that phase-pure Ta-doped pyrochlore of nominal composition $La_2Zr_{1.5}Ta_{0.5}O_{7.25}$ could be prepared without any noticeable impurities, indicating that Ta readily incorporates into LZO using this method. For La-doped LZO, a small amount of $La(OH)_3$ was observed in the XRD pattern, suggesting that fully doping LZO to a ratio of 3 La : 2 Zr is not feasible in this synthetic medium. Minor $La(OH)_3$ (also likely nanocrystalline based on the breadth of the Bragg peaks observed in **Figure 6.1a**), was also observed in co-doped LZO of nominal compositions $La_{2.2}Zr_{1.575}Ta_{0.225}O_{7.0125}$ and $La_{2.4}Zr_{1.12}Ta_{0.48}O_{7.04}$. Synchrotron X-ray pair distribution function (PDF) analysis (**Figure 6.1b**) of the $La_{2.4}Zr_{1.12}Ta_{0.48}O_{7.04}$ sample showed a better fit to the pyrochlore ($Fd\bar{3}m$) rather than the defect fluorite ($Fm\bar{3}m$) structure.[192] The PDF refinement also indicates that, besides minor amounts of $La(OH)_3$ (~ 9 wt%), all other constituents, including Ta and the rest of the excess La, are contained in a single pyrochlore phase. Transmission electron microscopy (TEM) characterization confirmed that the pyrochlore particles are on the order of 10 – 20 nm in size and highly crystalline (**Figure 6.1c-d**). **Figure 6.1e** shows a high-angle annular dark-field scanning transmission electron microscopy (HAADF-STEM) image of these pyrochlores with a composite energy dispersive X-ray spectroscopy (STEM-EDS) composition map and elemental maps for La, Zr, and Ta (see **Figure D1** for average EDS spectrum), demonstrating good uniformity of each species in the pyrochlores. A high resolution HAADF-STEM image (**Figure 6.1f**) also confirms the high crystallinity of these pyrochlores.

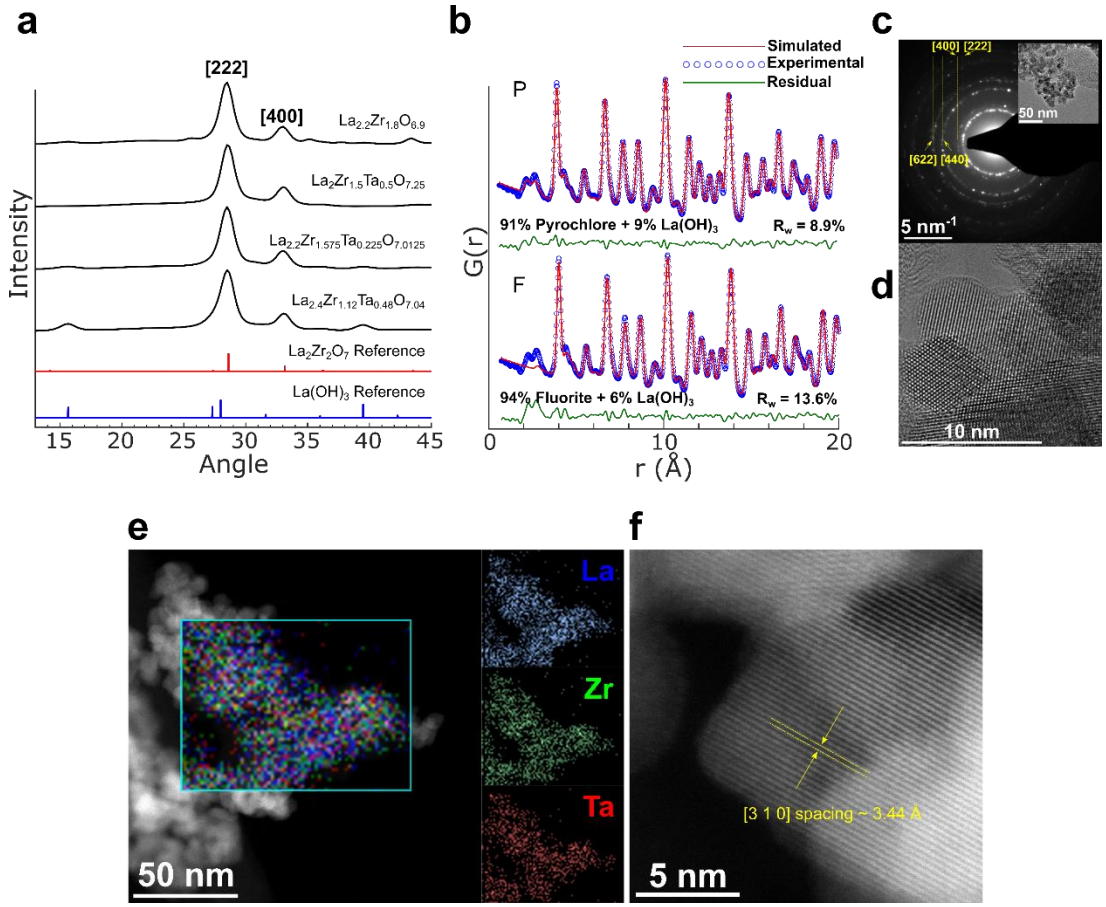

Figure 6.1. **Characterization of pyrochlore precursors. (a)** Synchrotron XRD patterns of La/Ta co-doped LZO pyrochlores synthesized in molten hydroxides; **(b)** Synchrotron X-ray PDF analysis of $La_{2.4}Zr_{1.12}Ta_{0.48}O_{7.04}$ showing the structure is a better fit to pyrochlore vs. defect fluorite with minimal $La(OH)_3$ as a secondary phase; **(c)** TEM electron diffraction ring pattern with major pyrochlore reflections indicated (low magnification TEM image in inset) and corresponding **(d)** high resolution TEM image of $La_2Zr_{1.5}Ta_{0.5}O_{7.25}$ nanocrystals; **(e)** HAADF-STEM image of $La_{2.4}Zr_{1.12}Ta_{0.48}O_{7.04}$ pyrochlores with EDS map from the region outlined in cyan showing distribution of La, Zr, and Ta throughout the nanocrystals; **(f)** high resolution HAADF-STEM image of pyrochlores in (**e**).

These results show that the $La_{2.4}Zr_{1.12}Ta_{0.48}O_{7.04}$ pyrochlores contain the necessary La, Zr, and Ta to be used as quasi-single-source precursors for the synthesis of garnets of composition $Li_{6.4}La_3Zr_{1.4}Ta_{0.6}O_{12}$ (LLZTO). To obtain LLZTO particles, a ternary mixture of $LiNO_3$-LiOH-Li_2O_2 was used as the reaction medium in which to synthesize the garnet from the pyrochlores via MSS. This ternary mixture is characterized by high Lux-Flood basicity,[180,181] which is expected to enable a low oxide formation temperature[119,183] while also serving as the lithium source for the reaction, and also has the advantage of mitigating[145] proton-exchange in the as-synthesized powder compared to neutral molten salt media such as eutectic LiCl-KCl. The reaction time (1 – 5 h), temperature (400 – 550 °C), and ratio of Li_2O_2 : LiOH ([0, 0.5, or 1] : 3.2) in the melt were varied to understand the minimum conditions (time, temperature, amount of Li_2O_2) that enable garnet formation from the pyrochlores (see **Appendix D** for detailed procedures, **Figure D2** for XRD patterns, **Table D1** for specific experimental conditions used). These experiments reveal that pyrochlore nanocrystals convert to garnet crystals at temperatures as low as 400 °C in 5 h, which to-date is the lowest Li-garnet synthesis temperature to be reported. For comparison, previous work showed that garnet synthesis in neutral LiCl-KCl molten salts required a reaction temperature of 850[145] or 900[161] °C. Full conversion of the pyrochlore precursor to the garnet phase was observed with increased reaction time, temperature, or Lux-Flood basicity of the melt (*i.e.*, increased amounts of Li_2O_2 for a fixed ratio of $LiNO_3$/LiOH of 1.1 : 3.2). The minimum conditions in which phase-pure garnet were obtained at each temperature are summarized in **Table 6.1**.

Table 6.1. Experimental MSS conditions (minimum time for a given temperature and salt molar ratio) that lead to phase-pure $Li_{6.4}La_3Zr_{1.4}Ta_{0.6}O_{12}$ garnet from $La_{2.4}Zr_{1.12}Ta_{0.48}O_{7.04}$ pyrochlore quasi-single-source precursors.

Reaction Temperature (°C)	Reaction Time (h)	Molten Salt Composition $LiNO_3$: LiOH : Li_2O_2 molar ratio
400	5	1.1 : 3.2 : 1
450	3	1.1 : 3.2 : 1
500	3	1.1 : 3.2 : 0.5
	1	1.1 : 3.2 : 1
550	3	1.1 : 3.2 : 0.5
	1	1.1 : 3.2 : 1
	4*	1.1 : 3.2 : 1

** - garnet synthesized from individual reagents rather than doped pyrochlores*

Interestingly, it appears that the Lux-Flood basicity of Li_2O_2 is not the sole driving force for the reduced garnet formation temperature using this method, as a comparable melt with Na_2O_2 replacing Li_2O_2 did not result in garnet formation (see **Figure D2c**). This indicates that the Li_2O_2 likely first decomposes into reactive Li_2O,[165] which in turn promotes formation of the garnet phase at low temperatures, indicating a potentially broader use of Li_2O_2 as a reactive Li-source for LLZO synthesis. Indeed, the primary difference between low (0.5 moles) and high (1 moles) Li_2O_2 compositions in **Table 6.1** is that generally less reaction time is required for higher Li_2O_2 content, indicating that Li_2O_2 modulates the reactivity / reaction rate. These results also indicate that garnet synthesis from pyrochlores is kinetically faster than using conventional reagents. For comparison, garnet of the same composition was synthesized from

$La(NO_3)_3$, $ZrOCl_2$, and Ta_2O_5 using MSS in the same melt; phase-pure garnet was obtained at 550 °C in 4 hours as in previous work[145] (**Figure D3**). With the pyrochlore reagents, phase-pure garnet adopting the high-conductivity cubic ($Ia\bar{3}d$)[1] structure formed in the same melt composition at 550 °C with only 1 h of reaction time (**Figure 6.2a** and **Table 6.1**). It is believed that the presence of all major cationic components (La, Zr, and Ta) other than Li as well as the high surface area of the pyrochlore nanocrystals enable this rapid conversion to the garnet phase. These particles are generally submicrometer in size from scanning electron microscopy (SEM) observation (**Figure 6.2b**) and highly crystalline based on TEM analysis (**Figure 6.2c-d**). The HAADF-STEM and EDS analysis (**Figure D4**) also confirmed uniform distribution of La, Zr, and Ta throughout the particles. These results confirm that this approach can enable the preparation of submicron garnet powders from doped pyrochlore nanocrystals. SEM images from a subset of other reaction conditions are shown in **Figure D5**, showing that in general, when only the minimum reaction time required to form garnet is used, the particle size of resultant garnet is comparable to that in **Figure 6.2b** regardless of reaction temperature. For lower synthesis temperatures (e.g. 450 °C, **Figure D5a-d**), increasing the reaction time from 3 to 5 hours does not appreciably increase the particle size with most particles being < 1 μm. However, particle sizes coarsen substantially for longer reaction times at higher temperature (e.g. 500 °C) where primary particles go from mostly < 1 μm for a shorter reaction time of 3 h (**Figure D5e,f**) to mostly > 1 μm for a longer reaction time (**Figure D5g,h**) of 5 h.

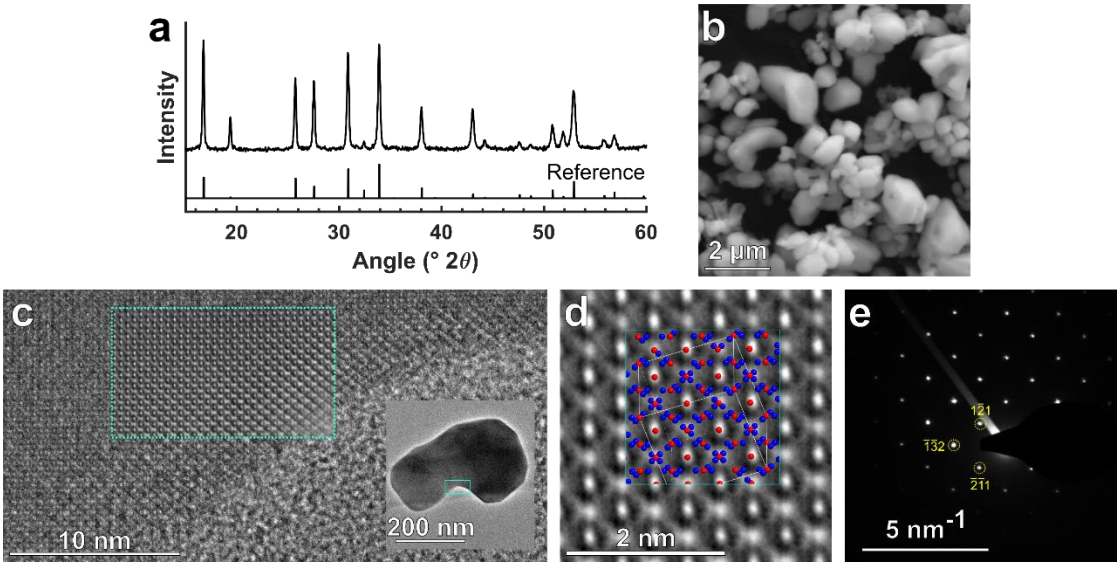

Figure 6.2. Characterization of garnet synthesized from pyrochlore precursors **(a)** XRD pattern of $Li_{6.4}La_3Zr_{1.4}Ta_{0.6}O_{12}$ powder synthesized via MSS from pyrochlores (550 °C 1 h) with reference pattern (Logeat *et al.*)[48], **(b)** SEM image showing primarily submicron, faceted LLZTO crystals, **(c)** HRTEM image of fused LLZTO particle (synthesized at 500 °C for 3 h, low magnification image in inset) in <135> zone-axis orientation and Fourier-filtered image (cyan bordered region) overlaid to remove signal from amorphous carbon grid, **(d)** Fourier-filtered HRTEM image of **(c)** with [135] LLZTO crystal motif overlaid (La: blue, Zr/Ta: red), and **(e)** <135> zone-axis electron diffraction pattern of particle in (**c**) with select reflections indicated.

In addition to the aforementioned $Li_{6.4}La_3Zr_{1.4}Ta_{0.6}O_{12}$ composition, other garnet compositions are also accessible from doped pyrochlores using this method. The oxygen sublattice may be doped with fluorine by using NaF as the dopant during pyrochlore synthesis, resulting in cubic garnet with nominal composition $Li_{6.375}La_3Zr_2O_{11.375}F_{0.625}$ (**Figure D6**). Interestingly, using the same synthesis conditions and slightly less NaF for pyrochlore synthesis resulting in a nominal garnet composition of $Li_{6.5}La_3Zr_2O_{11.5}F_{0.5}$ produced only partially cubic LLZO with some tetragonal distortion (**Figure D7**), possibly indicating that more F^- is required to stabilize cubic LLZO than Ta.

Additionally, a more highly doped garnet of nominal composition $Li_{6.025}La_{2.75}Ca_{0.25}Zr_{1.4}Ta_{0.6}O_{11.375}F_{0.625}$ was formed from pyrochlores co-doped with calcium, tantalum, and fluorine (**Figure D8**). These results show that doping with elements that readily incorporate into the pyrochlore structure,[189,193] such as alkaline earths (*e.g.*, Ca, Sr), lanthanides (*e.g.*, La, Nd), tetra- and pentavalent transition metals (*e.g.*, Ti, Zr, Nb, Ta), and F^- or OH^-, is possible using this approach. The F and Ca/Ta/F doped compositions were investigated as a proof-of-concept for assessing wider applicability of this pyrochlore-to-garnet synthesis method, but further investigation of electrochemical performance was only pursued for Ta-doped garnets.

$Li_{6.4}La_3Zr_{1.4}Ta_{0.6}O_{12}$ garnet powders synthesized from pyrochlores were pressed and sintered at 1200 °C for 2 or 3 h followed by SEM fracture surface imaging and ionic conductivity analysis via electrochemical impedance spectroscopy (EIS) (see **Table D2** for circuit fitting parameters). **Figure 6.3a** shows an SEM fracture surface image of a garnet pellet after conventional sintering, revealing predominately transgranular fracture and large (20 – 50 μm) grains. Additionally, the quasi-single-source feature of the pyrochlore nanocrystals was also exploited for an alternative approach to obtain dense garnet electrolytes. In this case, the pyrochlores were blended with LiOH (10 mol% excess relative to the target garnet stoichiometry of $Li_{6.4}La_3Zr_{1.4}Ta_{0.6}O_{12}$) via ball-milling followed by pressing and sintering. In this reactive sintering approach, the reaction of LiOH with the pyrochlores during high temperature calcination results in simultaneous garnet formation and densification. **Figure 6.3b** shows a fracture surface image of a reactively sintered pellet (1200 °C 3 h) revealing an extremely dense microstructure with small grains on the order of 2 – 5 μm and a relative density of 94.7 %. Nyquist plots of

symmetric cells using 20 wt% (1.5 mol %) Sn-Li alloy[65] electrodes are shown in **Figure 6.3c** for both conventionally and reactively sintered garnets (1200 °C for 2 h, relative densities of 88.0% and 94.1% respectively) possessing room temperature (~ 21 °C) total ionic conductivities of 0.42 and 0.53 mS cm^{-1} respectively, comparable to that obtained from LLZTO prepared using standard SSR and other methods (see **Table D3** for detailed comparisons). No obvious grain boundary impedance is noticeable in the Nyquist plots in **Figure 6.3c**, indicating that the tight grain structure from both sintering methods allows easy intergranular ion conduction. Finally the activation energy of Li-ion conduction was determined from the temperature dependence of ionic conductivity (**Figure 6.3d**, also see **Figure D9** for Nyquist plots at each temperature used to determine ionic conductivity) for each sample to be 0.42 and 0.38 eV per atom for the conventionally and reactivelly sintered garnets respectively. The two processes described here for preparing garnet powders and ceramics from pyrochlores are illustrated schematically in **Figure 6.3e**.

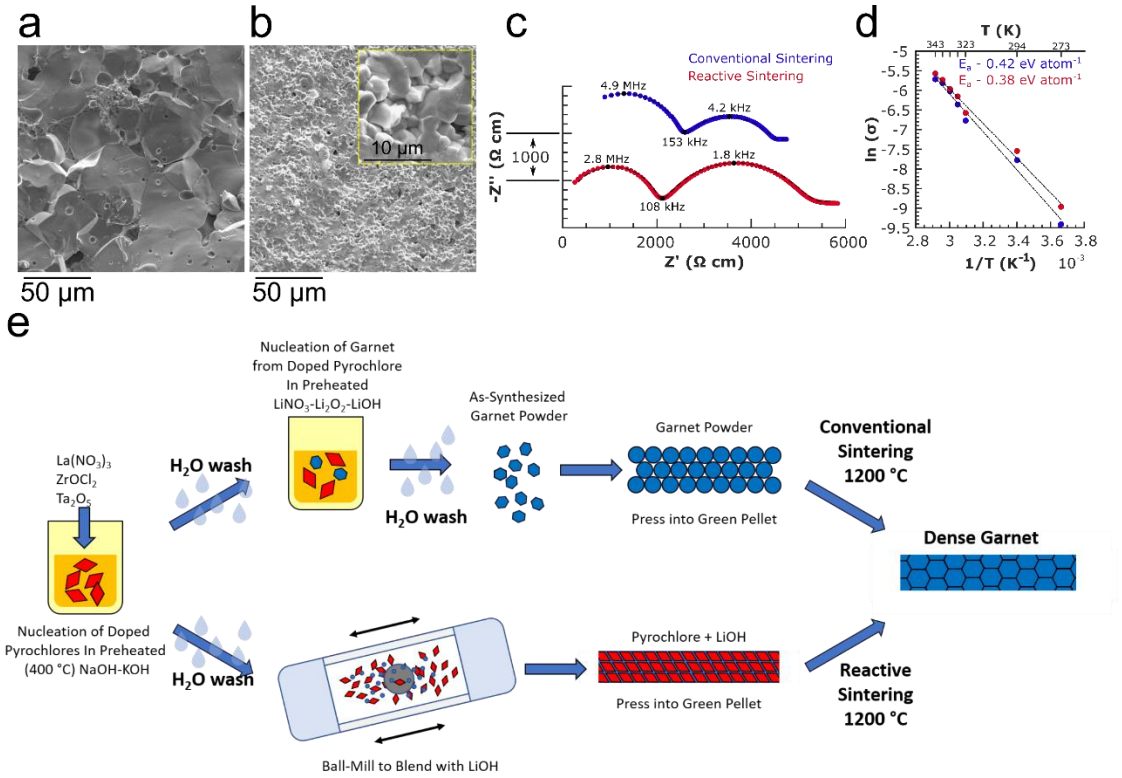

Figure 6.3. Properties of garnet solid electrolytes resulting from the pyrochlore-to-garnet processes **(a)** SEM fracture surface image of a pellet sintered from LLZTO garnet powder synthesized from pyrochlore precursors (1200 °C, 3 h sintering time), **(b)** SEM fracture surface image of a reactively sintered pellet from pyrochlores + LiOH (1200 °C 3 h sintering time, higher magnification image in inset), **(c)** room temperature EIS spectra of conventionally and reactively sintered pellets (1200 °C, 2 h sintering time) with 1.5 mol% Sn-Li alloy electrodes (measured between 7 MHz and 1 Hz, impedance normalized to pellet dimensions, spectra are vertically offset for clarity with vertical axis scale shown), and **(d)** Arrhenius plots of ionic conductivity measured between 273-343 K for samples in (**c**) with activation energies determined to be 0.42 and 0.38 eV per atom for conventional and reactive sintering respectively. **(e)** Graphical depiction of workflow for using MSS to convert pyrochlores to garnets followed by conventional sintering (**top**), and for using *in situ* reactive sintering to form dense garnet ceramics directly from pyrochlores and a Li source such as LiOH (**bottom**).

An XRD pattern of an LLZTO pellet formed from the reactive sintering approach is shown in **Figure D10** confirming that phase-pure garnet can be prepared from the pyrochlore powders directly using *in situ* reactive sintering without requiring an initial

synthesis step. Another benefit to using pyrochlores and LiOH in this way is the inherent stability of both components with water, which eliminates challenges associated with Li^+/H^+ exchange[52,56] and subsequent carbonate formation[52,53,56,59,194] or with using aqueous solutions[40,133,161] for processing garnets. Additionally, the microstructure and high relative density of the reactively sintered LLZTO resembles that of garnet sintered using hot-pressing,[37] spark-plasma sintering,[30] or Joule-heating induced rapid sintering.[130] This indicates that pyrochlore-to-garnet reactive sintering may enable comparable performance and properties without the more complex equipment required for these advanced sintering methods. Furthermore, reactive sintering is more generally applicable to processing of garnet solid-electrolytes in other forms such as thin films, where hot-pressing or spark-plasma sintering are not applicable. I would like to note that since the publication of the contents of this chapter in the literature, a similar method was demonstrated by Hamao et al. wherein a fluorite-structured pyrochlore derivative $La_{2.4}Zr_{1.6}Ta_{0.4}O_7$ was successfully synthesized and converted to garnet-structured $Li_{6.5}La_3Zr_{1.5}Ta_{0.5}O_{12}$.[195] In this case, higher synthesis temperatures were needed for the fluorite precursor (between 800-1100 °C), but conversion to garnet occurred at a comparably low temperature to the pyrochlore to garnet method discussed here, between 400-500 °C, when Li_2O was used as the Li-source.[195] Furthermore, their sintering method produced garnet ceramic with a high conductivity up to 0.94 mS cm^{-1}, indicating that the general approach of using such a quasi-single-source precursor can enable high ionic conductivity under optimized sintering conditions.[195]

6.3. Conclusion

In conclusion, a new synthesis approach is presented wherein doped $La_2Zr_2O_7$ pyrochlore nanocrystals are synthesized with a composition that will result in the correct stoichiometry to form Li-conducting garnets based on $Li_7La_3Zr_2O_{12}$. La and Ta co-doped pyrochlores with a La : Zr : Ta stoichiometry of 3 : 1.4 : 0.6 are demonstrated to readily form garnet type $Li_{6.4}La_3Zr_{1.4}Ta_{0.6}O_{12}$ between 400 – 550 °C in a ternary mixture of molten $LiNO_3$-LiOH-Li_2O_2, with unprecedentedly low reaction temperatures. Pyrochlores can also be used as quasi-single-source precursors and blended with a Li source and reactively sintered in 2 hours at 1200 ℃ to form highly dense, highly conducting garnet ceramics with a microstructure similar to that obtained through advanced sintering techniques, providing a unique and successful approach to dense garnet electrolytes that can be easily extended to more advanced ceramic forming techniques such as tape-casting or additive manufacturing, potentially improving processability of garnet solid-electrolytes for solid-state lithium batteries.

7. OBSERVATION OF ELEMENTAL INHOMOGENEITY AND ITS IMPACT ON IONIC CONDUCTIVITY IN LI-CONDUCTING GARNETS PREPARED WITH DIFFERENT SYNTHESIS METHODS

7.1. Introduction

Most Li-conducting garnets adopt the cubic garnet crystal structure ($Ia\bar{3}d$).[1] However, without extrinsic dopants, LLZO adopts a tetragonal structure ($I4_1/acd$) due to its uniquely high Li-content, which causes a spontaneous ordering of the Li-sublattice.[17,48,196] This thermodynamically favorable (at room temperature) tetragonal phase has lower ionic conductivity (~10^{-6} S cm^{-1} at room temperature) compared to the cubic phase (~10^{-4} to 10^{-3} S cm^{-1}).[1,6,16] For this reason, an aliovalent dopant is needed to introduce Li-vacancies to stabilize the highly conducting cubic phase.[1,4,27,36,37,48] Many doping schemes have been explored, including Al^{3+} [16,27,95] and Ga^{3+} [13,27] to dope the Li sublattice, Nb^{5+} [25,26] and Ta^{5+} [26–43] to dope the Zr sublattice, Ca^{2+} [9,35] and other alkaline earths such as Ba^{2+} [44] to dope the La sublattice (often used in conjunction with another site dopant), and even recently F^- [45–47] to dope the oxygen sublattice. Of the many possible compositions of LLZO, Ta-doped LLZO (LLZTO) with formula $Li_{7-x}La_3Zr_{2-x}Ta_xO_{12}$ ($0.2 < x < 1$) combines good electrochemical stability with lithium metal[26] and high ionic conductivity (> 1 mS cm^{-1})[38,50,51], and by virtue of doping the Zr sites in the garnet structure, does not block sites on the Li-sublattice[27] unlike other dopants such as Al or Ga.

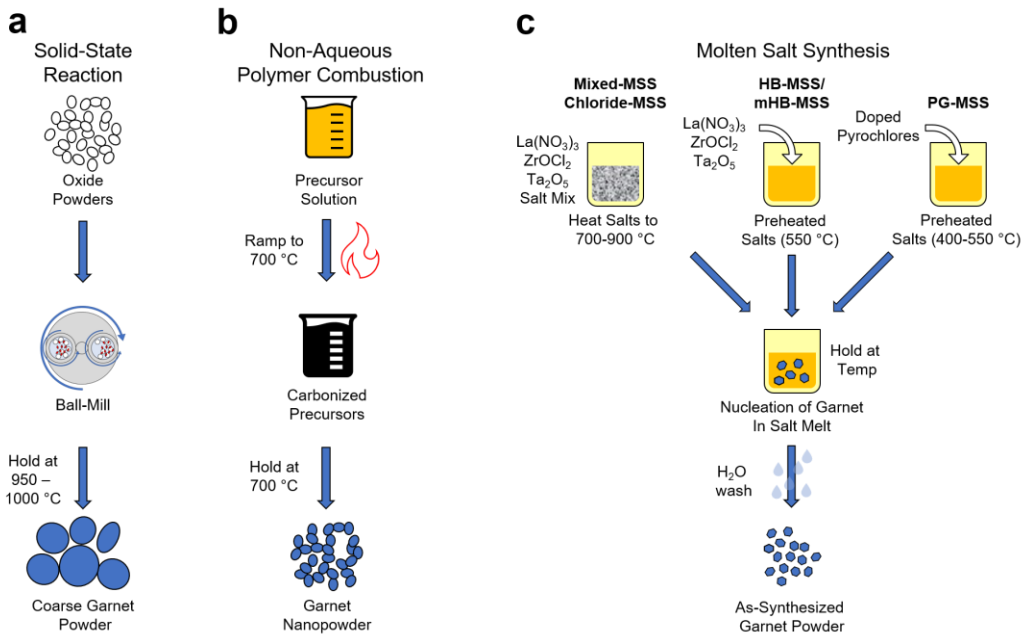

Scheme 7.1. Visual summary of methods to prepare Ta-doped LLZO garnet powders via **a)** solid-state reaction (SSR), **b)** non-aqueous polymer (NAP) combustion synthesis, **c)** molten salt synthesis. In (**c**), three specific embodiments of MSS are shown: for Chloride-MSS or Mixed-MSS, reagents are mixed with salts at room temperature and heated together to the desired hold temperature. For HB-MSS and mHB-MSS (distinguished by differing ratios of $LiNO_3$, Li_2O_2, and LiOH comprising the melt, see **Table 7.1**), the salts are pre-heated to 550 °C and then the reagents are added at temperature. Finally, for PG-MSS, the salts are also pre-heated (400-550 °C) and a mixture of $LiNO_3$ and doped pyrochlore nanocrystals of nominal composition $La_{2.4}Zr_{1.12}Ta_{0.48}O_{7.04}$ are added at temperature. In all cases of MSS, after reaction the melt is cooled, the salts are washed away with water to produce the as-synthesized powder.

The Chan group has devoted substantial efforts to synthesizing nanostructured LLZO using alternative methods to SSR (**Scheme 7.1a**). The variety of synthesis methods has enabled a systematic investigation of the role of synthesis-related parameters, such as reaction temperature and particle size, on the resulting sintering and electrolyte properties of LLZO, the focus of the work reported herein. To this end, the NAP combustion synthesis described in **Chapter 3** based on prior work[146] (**Scheme 7.1b**) was employed. Additionally, various MSS methods described in **Chapters 5 and 6** based on prior work[145,197] (**Scheme 7.1c**) were also utilized.

From these studies, it was found that in each case, garnet electrolytes with high relative density (> 90%) and ionic conductivity (> 0.5 mS cm^{-1}) can be obtained. On the other hand, a range of values of ionic conductivity were observed, with some samples or synthesis methods apparently able to produce electrolytes with higher conductivity. Even between highly similar synthesis methods, differences in ionic conductivity arise. For example, the maximum ionic conductivity of sintered LLZTO obtained from the highly basic MSS (HB-MSS) process depended strongly on the ratios of $LiNO_3$, Li_2O_2, and LiOH comprising the molten salt reaction medium used to synthesize the LLZTO powder, where depending on the composition of the melt, the maximum room temperature total conductivity obtained varied from 0.35 mS cm^{-1}, up to 0.61 mS cm^{-1}.[145] Interestingly, the presence of elemental inhomogeneity, characterized by variation in the local Ta- and Zr-content of individual grains of LLZTO could be observed in one case.[145] Scanning electron microscopy (SEM) backscatter electron (BSE) imaging and x-ray energy dispersive spectroscopy (EDS) revealed the presence of bright grains with higher Ta-content, which were indistinguishable from the surrounding grains in normal

secondary electron images, and the observed deviation in actual local composition was correlated with lower ionic conductivity. The appearance of grains of different composition in sintered LLZTO strongly implies that some variation in composition exists in the as-synthesized powder, which serves as a starting point for analysis. Further, the sinterability and ionic conductivity of LLZTO samples were observed to vary depending on the synthesis method used.[145]

The variability in performance metrics such as ionic conductivity is apparently not limited to these previous samples synthesized by different methods and at different temperatures but is also reflected in the large body of scientific literature on Ta-doped LLZO. Comparison of various results from the literature (see **Table E1)** shows that 1) the 'optimal' Ta-doping level (*i.e.* 'x' in $Li_{7-x}La_3Zr_{2-x}Ta_xO_{12}$) is not agreed-upon in the literature, and 2) that there are considerable differences in maximum total ionic conductivity between the various examples listed. For example, Wang and Lai obtained LLZTO with conductivity between 0.69-0.73 mS cm^{-1} for $0.2 < x < 0.3$.[34] Similarly, Yi *et al.* obtained a high conductivity of ~ 1 mS cm^{-1} for $x = 0.3$.[33] On the other hand, the results of Li *et al.* showed poor ionic conductivity of 0.28 mS cm^{-1} for $x = 0.2$, and high conductivity up to 1 mS cm^{-1} for $x = 0.6$.[38] Finally, single crystals of LLZTO showed ionic conductivities of 1.1 and 1.3 mS cm^{-1} for $x = 0.4$[51] and 0.5[50] respectively. It is unexpected that Ta-doping levels in the range of $0.2 < x < 0.3$ would produce cubic garnets with high conductivity, as the critical Ta-doping amount was demonstrated in one study to be in the range of 0.4 – 0.5 moles per formula unit (PFU).[36] Therefore, one plausible explanation for these differences is the incorporation of Al as co-dopant, either intentionally or adventitiously through contamination from sintering crucibles, into the

Ta-doped garnet phase, which may explain why studies using lower Ta-content still produce cubic garnets with high conductivity. While some researchers intentionally add some Al_2O_3 to LLZTO as a sintering aid[28], the works of Xia *et al.*[198] and Badami *et al.*[124] indicate that Al_2O_3 can also have deleterious effects on conductivity and performance. However, Li *et al.*, also observed some Al incorporation into their garnet electrolytes and still obtained a maximum conductivity at a high Ta content (x = 0.6) rather than at lower levels.[38] Clearly there are many synthesis or processing variables that can affect the performance of Ta-doped LLZO electrolytes besides just the nominal composition.

This work aims to examine some of the synthesis-related factors that may contribute to the differences in performance of garnet electrolytes by systematically characterizing the various LLZTO powder samples discussed herein. SEM, transmission electron microscopy (TEM), or scanning transmission electron microscopy (STEM) with EDS are used to understand the morphology and composition of individual particles, while XRD and in some cases x-ray pair-distribution function (PDF) analysis are used to understand the bulk crystallinity of the samples and for the first time, compare the structural properties of identical LLZTO compositions prepared with vastly different synthetic approaches and temperatures. Then, the effect of elemental inhomogeneity is examined, which is defined as local deviations in actual Zr/Ta mole ratio, as another factor that contributes to variation in ionic conductivity. While other factors such as grain size[67,68] and chemical inhomogeneity arising from impurity phases[199] may also influence electrochemical properties such as critical current density and interfacial impedance, these are not explored in detail in this work. It is shown that the various synthesis and processing-related variables in each of the aforementioned synthesis methods play a role

in these compositional variations, and that even LLZTO synthesized via conventional, high-temperature SSR can exhibit substantial variability in local composition depending on synthesis and sintering parameters. However, by improving reagent mixing and employing LLZTO powder with low agglomeration and small particle size distribution, the compositional uniformity of sintered garnet electrolytes can be improved. The correlation between inhomogeneity present in sintered LLZTO and reduction in ionic conductivity is explored. These results provide evidence that in addition to other variables known to affect the ionic conductivity of garnet electrolytes such as relative density[127] and Li-content[37] (or Li_2O-loss[39]), the compositional homogeneity of the final sintered ceramic can influence the ionic conductivity of solid garnet electrolytes.

7.2. Experimental

Tantalum-doped LLZO (LLZTO) with the nominal composition $Li_{6.4}La_3Zr_{1.4}Ta_{0.6}O_{12}$ was synthesized by the solid-state reaction (SSR) method from Li_2CO_3, $La(OH)_3$, ZrO_2, and Ta_2O_5, as outlined in **Appendix E**. Briefly, two approaches were used for SSR LLZTO: first, a single calcination step at 1000 °C for 8 h was employed (called "1x-SSR_{1000}"). Second, a two-step reaction with two calcination steps at 950 °C for 8 h each (with intermittent ball-milling between calcinations) was employed (called "1x-SSR_{950}" for just the first step and "2x-SSR_{950}" for the full two-step reaction). A slightly lower reaction temperature was used in the second case to reduce Li_2O-evaporation. Further, two sets each of 1x-SSR_{950} and 2x-SSR_{950} were prepared, one using bulk Ta_2O_5 and ZrO_2 and the other using pre-ball-milled Ta_2O_5 and nanosized ZrO_2,

prefixed with ‘B’ to denote bulk precursors (e.g. B-1x-SSR_{950}) and ‘N’ for nanosized precursors (e.g. N-1x-SSR_{950}) as described in **Appendix E**.

Dense LLZTO pellets were obtained via conventional uniaxial pressing followed by pressureless sintering in air between 1100-1200 °C depending on the sample using the same approach reported in previous works.[145,146,197] Details of the sintering conditions are found in **Table E1** and **Appendix E**. Total room temperature ionic conductivity values of pellets with either graphite electrodes[63] or 20 wt % (1.5 mol %) Sn-Li electrodes[65], were determined based on fitting data from electrochemical impedance spectroscopy (EIS) and the sample geometry, as in previous[146] work. The activation energy of Li-ion conduction was likewise measured as in previous[146] work. The relative density of the sintered pellets was determined from the mass and sample geometry and compared to the theoretical value for $Li_{6.4}La_3Zr_{1.4}Ta_{0.6}O_{12}$ of ~ 5.5 g cm^{-3}.[41]

In addition to LLZTO from the SSR method, LLZTO samples of the same nominal composition obtained from molten salt synthesis (MSS)[145], pyrochlore to garnet MSS[197], and non-aqueous polymer (NAP) combustion[146] synthesis in previous works were characterized by the aforementioned characterization techniques for comparison. No new samples were synthesized by these methods for the analysis conducted herein, so the reader is referred to the cited previous works for complete descriptions of the synthesis methods used. For sintered LLZTO samples from MSS or NAP combustion, the relative density, ionic conductivity, and activation energy (where measured) for samples examined herein are reported from previous[145,146,197] works rather than from new samples. In this case, the same samples for which ionic conductivity, activation energy (where measured), and relative density values were reported were further analyzed in this work

as with their respective powders. Sintered pellet samples derived from the various LLZTO powder synthesis methods were chosen from many (generally at least 10) sintering experiments based on the highest ionic conductivity and density, such that sintering could be considered approximately optimized and Li_2O-loss mitigated for further EDS analysis. The exception to this is the PG-MSS sample, for which only a few sintering experiments were performed.

Characterization methods and analyses using x-ray diffraction (XRD), synchrotron x-ray pair distribution function (PDF[151,152,200–202]) analysis, scanning electron microscopy (SEM), transmission electron microscopy (TEM), scanning transmission electron microscopy (STEM), and electrochemical impedance spectroscopy (EIS) are outlined in detail in **Appendix E**. Additionally, methods for approximating composition of powders and pellets using x-ray energy dispersive spectroscopy (EDS) are outlined in **Appendix E**. Briefly, EDS spectra for various compositions of LLZTO ($Li_{7-x}La_3Zr_{2-x}Ta_xO_{12}$, $0.2 < x < 1$) were simulated for appropriate sample geometries and electron beam accelerating voltages (10 kV or 15 kV for SEM, 200 kV for STEM, 200 or 300 kV for TEM) using the NIST DTSA-II software package and used to develop a regression based on the Ta M / Zr L x-ray peak ratio. Then this regression was applied to the experimental EDS data. This approach was chosen in lieu of generating precise standards for each composition amenable to analysis on each of the various instruments used herein or utilizing common standardless analysis. While not aiming to be a true quantitative analysis, this approach rather is intended to allow robust qualitative comparison between the various samples analyzed in this work.

7.3. Results and Discussion

7.3.1. Ionic Conductivity Comparison of $Li_{6.4}La_3Zr_{1.4}Ta_{0.6}O_{12}$ Synthesized by Solid-State Reaction, Combustion, and Molten Salt Synthesis

For comparison with the LLZTO synthesized in previous works via non-aqueous polymer (NAP) combustion synthesis[146], molten salt synthesis (MSS)[145], and pyrochlore to garnet MSS (PG-MSS)[197], LLZTO of the same nominal composition ($Li_{6.4}La_3Zr_{1.4}Ta_{0.6}O_{12}$) was synthesized via conventional solid-state reaction (SSR) and sintered using the same approach in order to produce a standard sample set for comparison. Three types of SSR LLZTO were synthesized to explore the effect of synthesis temperature and degree of mixing of the various reactants on the properties of the resultant material. To examine the effect of repeated milling and calcination steps on the composition, two sample sets of LLZTO were synthesized by calcination at 950 °C for 8 h, one with a single reaction step (1x-SSR_{950}) and the second with intermediate ball-milling before a second calcination (2x-SSR_{950}) at 950 °C for another 8 h. For one set of these SSR samples, pre-ball-milled Ta_2O_5 and nanosized ZrO_2 powders were used to examine the effect of using nanosized reagents. For the other set, bulk Ta_2O_5 and ZrO_2 were used. These samples are prefixed with ‘N’or ‘B’ to denote nanosized and bulk reagents, respectively (e.g. “N-1x-SSR_{950}” and “B-1x-SSR_{950}”). For comparison, LLZTO was also synthesized in a single step from bulk reagents by calcination at 1000 °C for 8 h (1x-SSR_{1000}).

The synthesis conditions for these samples along with the other samples referenced from previous works are summarized in **Table 7.1**, along with the naming nomenclature used to refer to the various samples discussed herein. X-ray diffraction (XRD) patterns of the as-synthesized SSR LLZTO powders (along with relevant MSS and NAP combustion LLZTO powders discussed herein, ordered by increasing synthesis temperature) are shown in **Figure E1** and example SEM images of the as-synthesized SSR LLZTO samples before ball-milling for particle size reduction are shown in **Figure E2a-e**.

Table 7.1. Summary of synthesis methods discussed herein including solid-state reaction, molten salt synthesis, and non-aqueous combustion synthesis for $Li_{6.4}La_3Zr_{1.4}Ta_{0.6}O_{12}$ garnet powders. The room temperature lattice (where measured, $\sigma_{lattice}$) and total (σ_{tot}) ionic conductivity for the specific sintered garnet samples analyzed in this work are given in units of mS cm^{-1}.

Synthesis Method	Shorthand Sample Name	Reagents	Synthesis Parameters	Synthesis Conditions		$\sigma_{lattice}$	σ_{tot}	Ref.
				Temp. (°C)	Time (h)			
Solid-state reaction	N-1x-SSR_{950}	$La(OH)_3$, nano-ZrO_2, Li_2CO_3, ball-milled Ta_2O_5	Shaker mill, (tungsten carbide jar and milling media), calcined in MgO crucible, single reaction	950	1x8	-	-	This Work
Solid-state reaction	N-2x-SSR_{950}	$La(OH)_3$, nano-ZrO_2, Li_2CO_3, ball-milled Ta_2O_5	Shaker mill, (tungsten carbide jar and milling media), calcined in MgO crucible, two reactions with a second milling step between	950	2x8	0.49	0.45	This Work
Solid-state reaction	B-1x-SSR_{950}	$La(OH)_3$, ZrO_2, Li_2CO_3, Ta_2O_5	Shaker mill, (tungsten carbide jar and milling media), calcined in MgO crucible, single reaction	950	1x8	-	-	This Work
Solid-state reaction	B-2x-SSR_{950}	$La(OH)_3$, ZrO_2 , Li_2CO_3, Ta_2O_5	Shaker mill, (tungsten carbide jar and milling media), calcined in MgO crucible, two reactions with a second milling step between	950	2x8	-	-	This Work
Solid-state reaction	1x-SSR_{1000}	$La(OH)_3$, ZrO_2, Li_2CO_3, Ta_2O_5	Planetary mill, (ZrO_2 jar and milling media), calcined in MgO crucible, single reaction	1000	1x8	0.75	0.71	This Work
Non-Aqueous Polymer combustion	NAP	Li(acac), $La(acac)_3$, $Zr(acac)_4$, $Ta(OEt)_5$	Reagents [a)] dissolved in propionic acid and dichloromethane with poly(vinylpyrrolidone) and combusted	700	4	0.61	0.57	Ref.[146]
Highly Basic Molten Salt Synthesis	HB-MSS	$La(NO_3)_3$, $ZrO(NO_3)_2/ZrOCl_2$, Ta_2O_5	Reagents added to molten $LiNO_3$: Li_2O_2 : LiOH (1 : 2 : 2 mole ratio) at synthesis temperature	550	2.5	0.38	0.35	Ref.[145]
Modified Highly Basic Molten Salt Synthesis	mHB-MSS	$La(NO_3)_3$, $ZrO(NO_3)_2/ZrOCl_2$, Ta_2O_5	Reagents added to molten $LiNO_3$: Li_2O_2 : LiOH (1.1 : 1 : 3.2 mole ratio) at synthesis temperature	550	8	0.73	0.61	Ref.[145]
Mixed Molten Salt Synthesis	Mixed-MSS	$La(NO_3)_3$, $ZrO(NO_3)_2/ZrOCl_2$, Ta_2O_5	Reagents ground with LiCl-LiOH (1 : 1 mass ratio) mixture and fired	700/900	1.5/4	-	0.47	Ref.[145]
Chloride Molten Salt Synthesis	Chloride-MSS	$La(NO_3)_3$, $ZrO(NO_3)_2/ZrOCl_2$, Ta_2O_5	Reagents ground with LiCl-KCl eutectic (0.59 : 0.41 mole ratio) mixture and fired	900	4	0.61	0.46	Ref[145]
Pyrochlore-to-Garnet Molten Salt Synthesis	PG-MSS	$La_{2.4}Zr_{1.12}Ta_{0.48}O_{7.04}$ nanocrystals	Reagents added to molten $LiNO_3$: Li_2O_2 : LiOH (1.1 : 1 : 3.2 mole ratio) at synthesis temperature	400	5	-	-	Ref.[197]
Pyrochlore-to-Garnet Molten Salt Synthesis	PG-MSS	$La_{2.4}Zr_{1.12}Ta_{0.48}O_{7.04}$ nanocrystals	Reagents added to molten $LiNO_3$: Li_2O_2 : LiOH (1.1 : 0.5 : 3.2 mole ratio) at synthesis temperature	500	3	-	-	Ref.[197]
Pyrochlore-to-Garnet Molten Salt Synthesis	PG-MSS	$La_{2.4}Zr_{1.12}Ta_{0.48}O_{7.04}$ nanocrystals	Reagents added to molten $LiNO_3$: Li_2O_2 : LiOH (1.1 : 1 : 3.2 mole ratio) at synthesis temperature	550	1	0.42	0.42	Ref.[197]

a) 'acac' – 'acetylacetonate' or '2,4-pentanedionate' ligand;

As a starting point for comparison, the ionic conductivity of SSR LLZTO samples was evaluated. The temperature dependence of ionic conductivity was also evaluated between 273-343 K for one 1x-SSR_{1000} and one 2x-SSR_{950} sample to determine the activation energy of Li-ion conduction, which for each case was 0.41 eV per atom, in line with the literature values presented in **Table E1**. These measurements are presented in **Figure E3a-c**. Additionally, scanning electron microscopy (SEM) fracture surface images of each of these samples are shown in **Figure E2f,g** showing primarily intragranular fracture and high relative density. Nyquist plots used to determine room temperature ionic conductivity for the new samples prepared in this study are shown in **Figure E3** and details used to determine ionic conductivity for these samples are contained in **Table E2**. The synthesis and sintering conditions, relative density, total room temperature ionic conductivity, and (where measured) activation energy of these samples are shown in **Table E1**, along with relevant metrics cited from our previous combustion and MSS specimens. Finally, other examples of performance of Ta-doped LLZO obtained from various synthesis and processing methods from the literature are included in **Table E1** for comparison.

The highest total ionic conductivity obtained from these samples is that of the 1x-SSR_{1000} sample at 0.71 mS cm^{-1}, although the best result from MSS (mHB-MSS)[145] has a comparable total conductivity of 0.61 mS cm^{-1}. However, there are still substantial variations in the total ionic conductivity between these various samples, even of similar relative density, especially when comparing the HB-MSS and 1x-SSR_{1000} (93.4 and 93.0% relative density, respectively) samples, where the 1x-SSR_{1000} sample has more than double the room temperature ionic conductivity. Since all the samples described

herein and in previous works[145,146,197] were sintered in a manner to minimize Li_2O loss using the same approach, the effect of variation of Li-content due to evaporation should be minimal. Further, since many samples were sintered for each method, the samples with the highest room temperature ionic conductivity are considered approximately optimized such that Li_2O-loss is minimal. Therefore, another effect must explain the large discrepancy in performance between these various LLZTO samples.

7.3.2. Observation of Elemental Inhomogeneity in LLZTO Garnet Powders

Beginning with the LLZTO synthesized at low-temperatures (HB-MSS, mHB-MSS, and PG-MSS LLZTO powder), microscopic analysis was performed via S/TEM due to the generally small particle sizes produced by these synthesis methods. Note that all of these powders were synthesized in the same molten salt medium (**Table 7.1**) but with different salt ratios, and in the case of PG-MSS, a different precursor (i.e., doped pyrochlore nanocrystals instead of metal salts/oxidic reagents). **Figure 7.1a,b** shows a low magnification TEM image and corresponding electron diffraction pattern of an HB-MSS fused particle, showing that the approximate minimum dimensions of individual primary particles are on the order of 200-300 nm and that this composite particle is a single crystal. **Figure 7.1c,d** show low magnification TEM images of mHB-MSS particles, and **Figure 7.1e,f** show low magnification high-angle annular dark field STEM images of PG-MSS samples. In each case, the particles are submicrometer but generally have dimensions above 100 nm. Other examples of HB-MSS particles are shown in **Figure E4** with corresponding electron diffraction patterns, indicating that these particles are composed of at most a few fused nuclei.

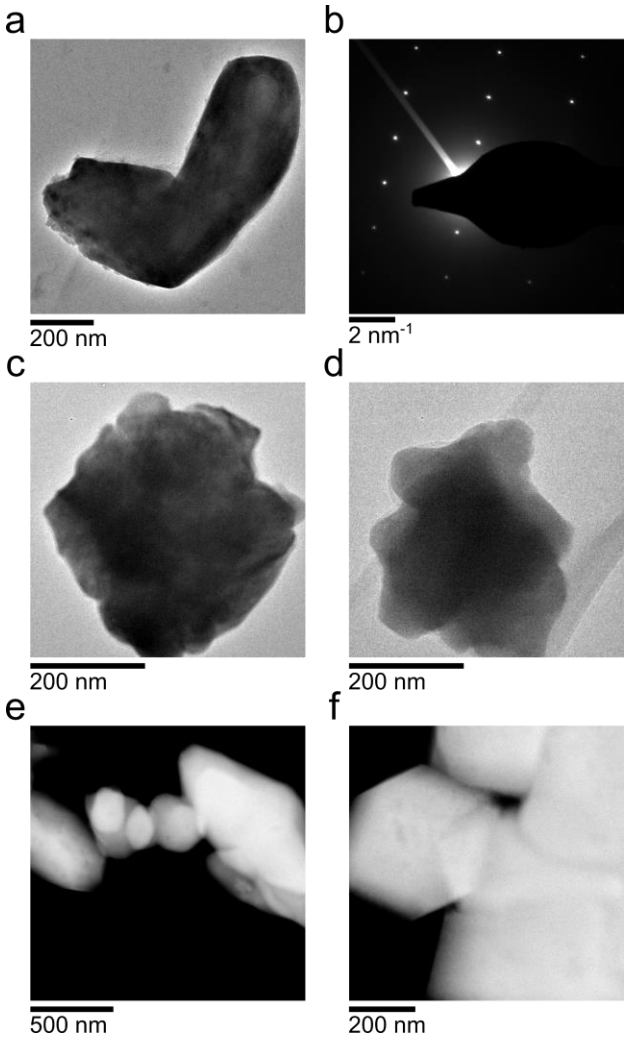

Figure 7.1. **a)** Low magnification TEM image of an HB-MSS particle showing two nodes fused together, **b)** electron diffraction pattern of entire fused particle in (**a**) showing only a single zone-axis diffraction pattern, **c,d)** low magnification TEM images of different mHB-MSS particles, and **e,f)** low magnification STEM images of different PG-MSS particles (in this case synthesized at 500 °C for 3 h) showing various morphologies including spheroid particles and cubic particles.

Additionally, x-ray energy dispersive spectroscopy (EDS) was performed to understand the composition of individual garnet particles from the HB-MSS, mHB-MSS, and PG-MSS methods. Processed EDS spectra (processing methods outlined **Appendix E**) of sets of individual LLZTO particles for these three MSS samples are shown in

Figure 7.2a-c respectively, with Ta M, Zr L, and La L x-ray signals indicated (each spectrum corresponds to one particle/particle agglomerate such as in the examples presented in **Figure 7.1**). All spectra were smoothed, background subtracted via a polynomial fit, and normalized to the highest intensity La L x-ray peak at ~ 4.6 keV. The Ta M and Zr L peaks can be observed to vary considerably on a particle-by-particle basis. To approximately determine the composition of individual particles, EDS spectra of $Li_{7-x}La_3Zr_{2-x}Ta_xO_{12}$ ($0.2 < x < 1$) were simulated and used to generate a regression based on the Ta M to Zr L peak ratio as a function of composition that was applied to the processed experimental EDS spectra (see **Appendix E, Figure E5**). **Figure 7.2j** shows the distribution of peak ratios as a kernel density, showing standard deviations greater than 0.14 moles per formula unit (PFU) in each sample set. Curiously, the HB-MSS sample shows less inhomogeneity than the mHB-MSS sample despite the higher ionic conductivity of the latter sample,[145] which will be discussed further later. Note that the PG-MSS powder examined via STEM was prepared under slightly different conditions as those used to prepare sintered LLZTO for ionic conductivity evaluation (STEM-EDS sample: 500 °C, 3 h reaction time; sintered sample: 550 °C, 1 h reaction time, see **Table 7.1**), but is included to show that variability in composition occurs in LLZTO derived from this method as well. Despite the slightly lower reaction temperature for the PG-MSS sample characterized with EDS compared to the HB-MSS sample (500 vs. 550 °C), the degree of inhomogeneity is comparable, likely due to the better mixing of La, Zr, and Ta afforded by utilizing doped pyrochlores as reagents.

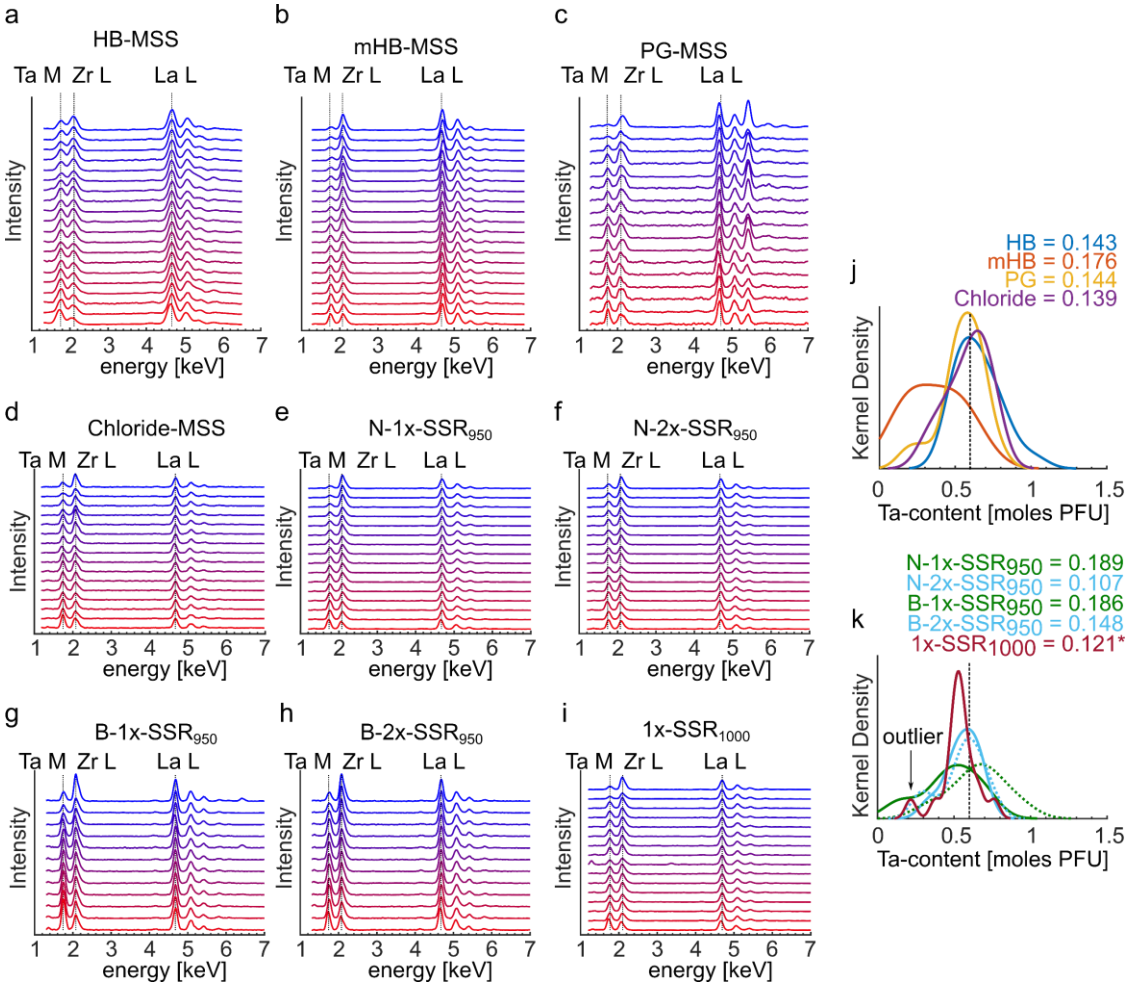

Figure 7.2. Experimental EDS spectra (sorted from lowest Ta signal to highest Ta signal, each spectrum from a single particle or particle agglomerate) from **a)** HB-MSS (TEM-EDS), **b)** mHB-MSS (TEM-EDS), **c)** PG-MSS (STEM-EDS), **d)** Chloride-MSS (SEM-EDS), **e)** N-1x-SSR$_{950}$ (SEM-EDS), **f)** N-2x-SSR$_{950}$ (SEM-EDS), **g)** B-1x-SSR$_{950}$ (SEM-EDS), **h)** B-2x-SSR$_{950}$ (SEM-EDS), **i)** 1x-SSR$_{1000}$ (SEM-EDS). Additionally, the distributions of Ta-content in moles per formula unit (PFU) are plotted as kernel densities for **j)** MSS samples in (**a-d**) and **k)** SSR samples in (**e-i**). Note in (**k**) that the N-SSR samples and B-SSR samples are denoted by solid and dotted lines respectively. The standard deviation in terms of moles Ta per formula unit (PFU) are indicated in (**j,k**) next to each sample name, along with black dotted lines indicating the nominal composition of 0.6 mol PFU. (*if one outlier sample is excluded, the standard deviation of Ta-content for the 1x-SSR$_{1000}$ sample is 0.09 mol PFU).

The same EDS data processing approach discussed above was applied to the SEM-EDS spectra of the chloride-MSS (**Figure 7.2d**) and SSR samples (**Figure 7.2e-i**). Despite the higher SSR reaction temperatures, variation in Ta-content can still be readily observed (**Figure 7.2k**). Furthermore, in the case of both N-1x-SSR_{950} and B-1x-SSR_{950} LLZTO, the standard deviation of Ta-content substantially exceeds that found in the low temperature MSS LLZTO samples. This result is somewhat surprising as the general assumption is that the high reaction temperatures used in SSR will promote enough solid-state diffusion to drive the whole ensemble of reagents to a uniform final product. However, using either a second calcination with an intermediate ball-milling step (for better intermixing of individual atomic species), or a higher calcination temperature appears to result in better compositional uniformity. It is notable that the use of ZrO_2 and Ta_2O_5 with smaller particle sizes (*i.e.*, N-1x-SSR_{950} and N-2x-SSR_{950}) seems to improve compositional homogeneity after the second calcination. In the case of a single higher temperature calcination (1x-SSR_{1000}), the standard deviation of Ta-content is fairly low and has a tight distribution, and if one outlier sample is excluded, an even lower standard deviation than for the N-2x-SSR_{950} sample (0.09 mol Ta PFU vs. 0.107 mol Ta PFU. The SSR procedures used in this work were chosen based on commonly used parameters from the literature (some examples in **Table E1**). This implies that more intensive milling, higher temperatures, and/or longer reactions times may be necessary to ensure compositional uniformity during synthesis than are commonly employed, and as exemplified by the 1x-SSR_{1000} sample, a higher temperature calcination with overall lower reaction time may be a more effective strategy than using a minimal reaction temperature and extended reaction time.

7.3.3. Crystal Structural Characterization of LLZTO Garnet Powders

One clue to the effect of synthesis method on the properties of LLZTO is the observation of peak broadening in the XRD patterns, especially for LLZTO synthesized at lower temperatures (**Figure E1**). Comparing the various XRD patterns from the samples investigated herein reveals that the full-width half-maximum (FWHM) of the Bragg reflections varies considerably (**Figure 7.3**, **Table E3**). Although Scherrer[147,149] broadening is one potential explanation due to the smaller particle sizes of LLZTO prepared by MSS compared to SSR, it generally only occurs for crystallites below ~ 0.2 μm. For the HB-MSS samples, electron diffraction (ED) measurements indicate that most of the particles examined are either single crystals or agglomerates of only a few nuclei and are generally between 0.2-1 μm in size (**Figure E4**). Further, the mixed-MSS powder synthesized at 700 °C in previous work[145] presented as large faceted crystals (most likely single crystals) on the order of tens of microns, but exhibits broadened peaks relative to SSR LLZTO much like the lower temperature MSS samples, indicating that crystallite size effects cannot solely account for peak broadening.

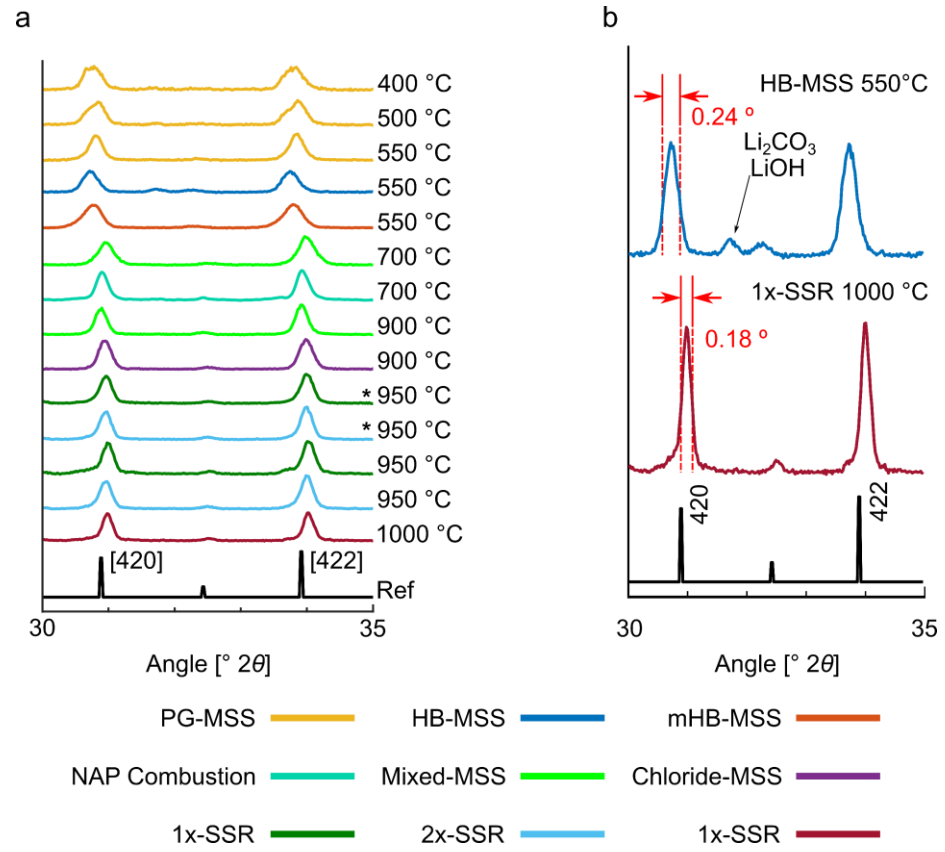

Figure 7.3. X-ray diffraction patterns of LLZTO from **a)** the various powder samples investigated in this work with synthesis temperature indicated reference generated according to the structure in Logéat et al.[48], plotted between 30° < 2θ < 35° (wider scans plotted between 15° < 2θ < 60° in **Figure E1**), and **b)** the HB-MSS and 1x-SSR$_{1000}$ samples to highlight the differences in peak full-width half-maximum (FWHM). There are substantial differences in peak breadth for the reflections noted between different samples, especially when comparing LLZTO synthesized at low vs. high temperatures. (* - indicates N-1x-SSR$_{950}$ and N-2x-SSR$_{950}$ samples, prepared from pre-ball-milled Ta_2O_5 and nanosized ZrO_2 rather than bulk reagents)

Another possible explanation, supported by the compositional variations in the EDS data (**Figure 7.2**) is co-existence of multiple garnet phases with slightly different composition, as the lattice constant of $Li_{7-x}La_3Zr_{2-x}Ta_xO_{12}$ is expected to decrease with increased Ta-content following Vegard's Law.[48] A binary mixture of two LLZTO compositions with deviations of roughly +/- 15% in terms of moles Ta per formula unit

(PFU) has been observed with high-resolution synchrotron XRD[37]. Therefore, it can be expected that if multiple garnet phases with the same crystal structure and only slightly varying lattice parameter coexist in a single sample, Bragg reflections will be observed at approximately the same average positions but with a broadening proportional to the distribution of lattice parameters present. To further understand the origin of the XRD peak broadening, X-ray pair distribution function (PDF) analysis was performed to complement the Bragg diffraction data. Since the PDF is derived from total scattering, its signatures are useful for understand the atomic structure of materials with crystalline defects, small crystallites, and amorphous phases.[150,153] **Figure 7.4** shows PDFs for LLZTO samples synthesized by several MSS methods and SSR, covering a synthesis temperature range of 550-950 °C. While all PDFs share generally similar features, the finer features particularly in the range of $5 < r < 10$ and $18 < r < 22$ Å (indicated by the boxed regions in **Figure 7.4**) of the mixed-MSS, chloride-MSS, and 2x-SSR_{950} samples are much clearer than for the mHB-MSS method. From the calculated partial PDFs (**Figure E6**), the correlations in the 5-10 Å region correspond mostly to the second and third nearest-neighbor La-La distances, with Zr-Zr and Zr-Ta correlations contributing to the shoulder at ~6.5 Å, and correlations between La and Zr/Ta or Ta-Ta / Ta-Zr / Zr-Zr dominating the finer features from ~ 8.5-10 Å. In the region between 18-22 Å, features originating from these same correlations contribute to most of the peaks, which appear to be substantially broadened in the case of mHB-MSS LLZTO synthesized at a lower temperature.

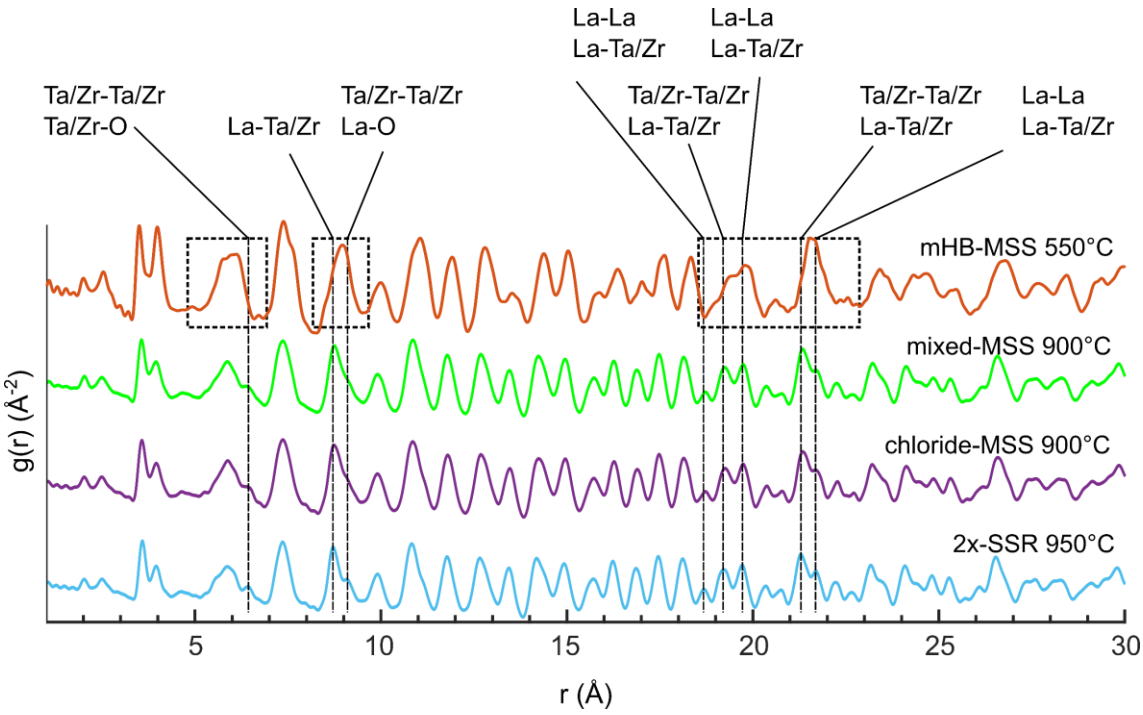

Figure 7.4. Experimental synchrotron X-ray pair distribution function (PDF) plots of various LLZTO samples from a variety of synthetic methods (spanning synthesis temperatures between 550-950 °C) plotted between 1-30 Å, showing that the sharpness of features in the various samples is greatest for samples synthesized at higher temperature.

The PDFs were refined based on the *Ia*$\bar{3}$*d*, $Li_{6.4}La_3Zr_{1.4}Ta_{0.6}O_{12}$ structural model reported by Logéat *et al*.[48] Refinements showed reasonably good fits to the structural model, with goodness of fit, R_w between 14-28% (**Figure E7, Table E4**). Notably, the correlations from 5-10 and 18-22 Å mentioned previously are well fit by the refinement, thus confirming the good crystallinity of the high temperature samples. The mHB-MSS fit is the poorest (R_w ~ 28%), due to the broadening of features relative to other samples. From the EDS analysis in **Figure 7.2**, the N-2x-SSR_{950} sample has relatively low compositional variation and exhibits much more well-defined features (*i.e.* less peak broadening) in the PDF than the other LLZTO samples (particularly the lower temperature MSS sample).

The lower elemental inhomogeneity of the N-2x-SSR_{950} sample and good fit quality from the PDF refinement implies that elemental inhomogeneity *may* be an explanation for the broadening in the PDF data. On the other hand, the fit quality is similar between the N-2x-SSR_{950} and Chloride-MSS samples (~ 14 % difference), but the latter sample has a 30% greater standard deviation in Ta-content (0.139 vs 0.107 moles Ta PFU for chloride-MSS and N-2x-SSR_{950} respectively). Further, the XRD patterns for the various SSR samples shown in **Figure 7.3** are difficult to distinguish based on peak broadening but possess substantially variable Ta-content (**Figure 7.2**), while the HB-MSS, mHB-MSS, and PG-MSS samples have less inhomogeneity than both 1x-SSR_{950} samples (**Figure 7.2**) but have broader XRD peaks (**Figure 7.3**). Finally, the broadening effect in the PDF data is most obviously correlated with the synthesis temperature used, with the best fit resulting from the highest synthesis temperature (950 °C) and the worst fit resulting from the lowest synthesis temperature (550 °C). Therefore, there may also be a different cause for the broadening in the PDF and XRD data, which is unique to the lower synthesis temperatures used for several of the MSS LLZTO samples and is distinct from elemental inhomogeneity.

Another possible explanation for these broadening effects is some form of crystalline defect, namely paracrystalline disorder resulting from crystalline defects that cause deviation from perfect long range order.[149] In a Bragg diffraction experiment, such disorder manifests as an increase in peak FWHM as a function of scattering vector Q (or scattering angle in ° 2θ) on top of other fixed broadening mechanisms such as increased K_α / K_β splitting. To investigate this effect in the LLZTO samples examined herein, the FWHM as a function of Q was determined for several Bragg reflections for the XRD

datasets in **Figure E1**, with the trend of peak FWHM plotted in **Figure 7.5a**. Clearly, different LLZTO samples have substantially different degrees of broadening as a function of Q, indicating that varying degrees of crystalline disorder are present. In **Figure 7.5b**, the peak ΔFWHM (° 2θ) is plotted as a function of synthesis temperature. A clear trend can be observed wherein higher synthesis temperatures result in narrower peaks (**Figure 7.3** and **Table E3**) and less broadening as a function of scattering angle (ΔFWHM). This result is intuitive, as a higher reaction temperature naturally will result in faster solid-state diffusion and easier crystallization. Considering these results, the best explanation of the different degrees of broadening in the PDF data in **Figure 7.4** is also degree of crystalline disorder rather than inhomogeneity. Two samples (circled in **Figure 7.5b**) are exceptions to the general trend of temperature and peak broadening, namely the sample from pyrochlore-to-garnet MSS[197] at 550 °C and from non-aqueous polymer combustion[146] synthesis at 700 °C. In the first case, the containment of La, Zr, and Ta in a single doped pyrochlore phase seems to help reduce diffusion distances and may allow for better crystallinity to be obtained despite the lower synthesis temperature. In the second case, the initial molecular mixing of precursors in solution is expected to have a similar effect. Finally, there is no correlation observed between the elemental inhomogeneity in a powder sample (where measured, see **Figure 7.2**) and the degree of peak broadening in corresponding XRD patterns (**Figure 7.5c**). Therefore, the peak broadening observed in many of the XRD and PDF data can be primarily attributed to the degree of crystalline disorder in the powder sample and is strongly correlated with synthesis temperature, rather than compositional heterogeneity. Conversely, elemental inhomogeneity contributes little to the signals detected in structural characterization methods, as

substantially different degrees of peak broadening occur for samples with comparable levels of inhomogeneity (**Figure 7.5c**, e.g. B-1x-SSR_{950} and mHB-MSS). With this in view, structural characterization, while useful in other respects, is not the best tool to assess uniformity of composition in the $Li_{7-x}La_3Zr_{2-x}Ta_xO_{12}$ system, as variation in composition is difficult to separate from other effects that contribute more to signal variations in Bragg diffraction and even pair-distribution function analysis.

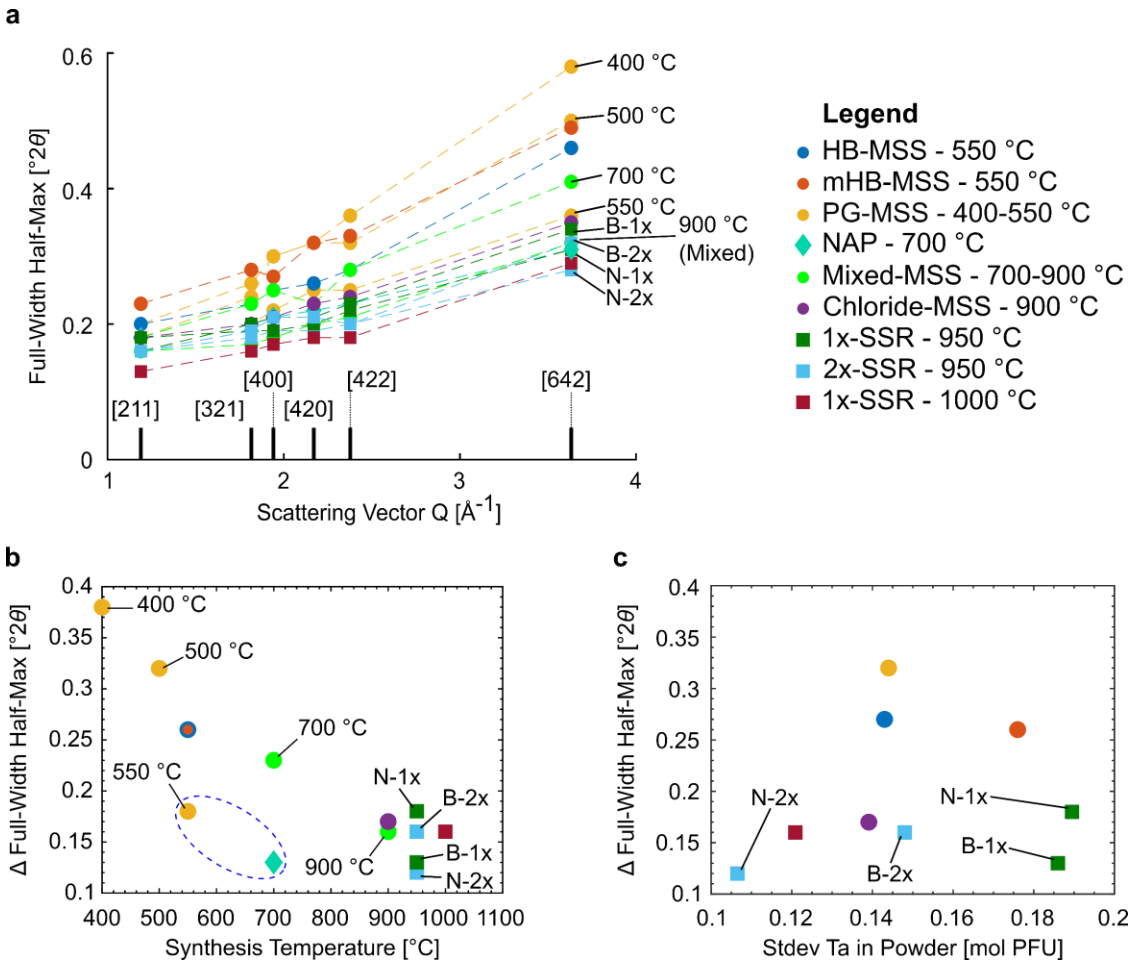

Figure 7.5. **a)** Plot of Bragg reflection full-width half-maximum (FWHM) vs. scattering vector, Q, for several major peaks (indicated on bottom of plot) with synthesis temperature indicated for synthesis methods where multiple synthesis temperatures were used; **b)** change in full-width half-maximum (ΔFWHM, ° 2θ) between garnet [211] and [642] reflections for various MSS, NAP combustion, and SSR LLZTO samples. These data were derived from XRD patterns shown in **Figure E1**; **c)** plot of ΔFWHM versus the standard deviation of Ta-content (moles PFU) in the various powder samples (where measured), with no obvious correlation between compositional variation and Bragg peak broadening.

7.3.4. Observation of Elemental Inhomogeneity in Sintered Garnet Solid Electrolytes

The XRD and PDF results of the LLZTO powders demonstrate that the presence of crystalline disorder is related to the synthesis method and temperature used, with more disorder generally appearing in lower temperature synthesis methods. However, the powders are further densified with high temperature sintering for ionic conductivity measurements, which can also improve the crystallinity. **Figure 7.6** shows XRD patterns of several LLZTO powder samples (low temperature mHB-MSS, high temperature chloride-MSS, and high temperature SSR) before (**Figure 7.6a**) and after (**Figure 7.6b**) sintering at 1200 °C for between 2-4 h. The results show that while the XRD patterns of the as-synthesized powders have varying degrees of peak broadening, the XRD patterns are nearly indistinguishable after sintering. In fact, the ΔFWHM (measured in the same way as powder samples in **Figure 7.5)** for these three sintered samples are 0.08, 0.08, and 0.09 respectively, indicating the MSS powders have not only nearly identical crystallinity, but also slightly better crystallinity than the high temperature SSR powder samples after sintering.

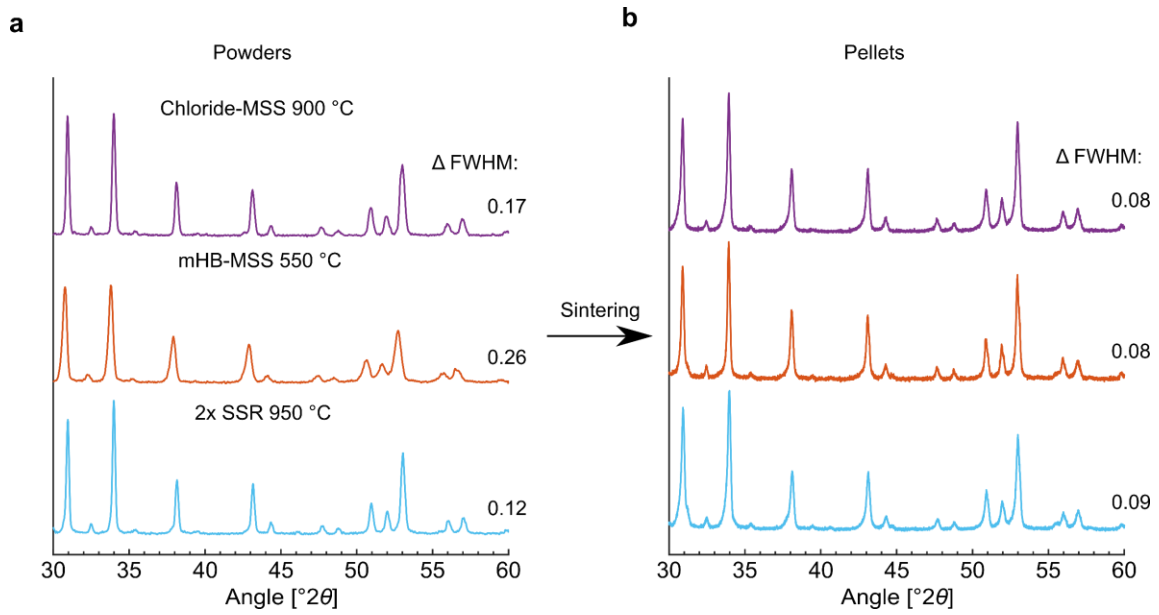

Figure 7.6. X-ray diffraction patterns plotted between 30° < 2θ < 60° of **a)** several garnet powder samples before sintering and **b)** sintered pellets derived from these powders, showing that despite substantially different peak FWHM in the powder, the peak sharpness and shape in the sintered pellets are nearly indistinguishable, with the change in full-width half-maximum (Δ FWHM between LLZTO [211] and [642] reflections) indicated for each sample in (**b**).

To investigate the role of local compositional variations on ionic conductivity, sintered garnet electrolytes were fractured and examined via SEM-EDS and BSE imaging (**Figure 7.7**, results summarized in **Table E5**). Each sample shows variability in the amount of Ta and Zr within different grains or regions of the sintered ceramic, as seen by the variability in the Ta M / Zr L peak ratio in the EDS spectra. In several cases, contrast differences can be clearly seen in the BSE-SEM images, with brighter areas corresponding to regions with higher Ta-content. with brighter areas corresponding to regions with higher Ta-content. Some of the images reveal noticeable contrast differences between neighboring grains (*e.g.* **Figure 7.7e**), but the contrast differences are generally not as stark as in the initial specimen where inhomogeneity was observed in previous

work[145]. This implies that while BSE imaging is useful to reveal significant compositional variability in a garnet electrolyte, the differences in composition between adjacent grains is best detected using localized chemical analysis such as EDS.

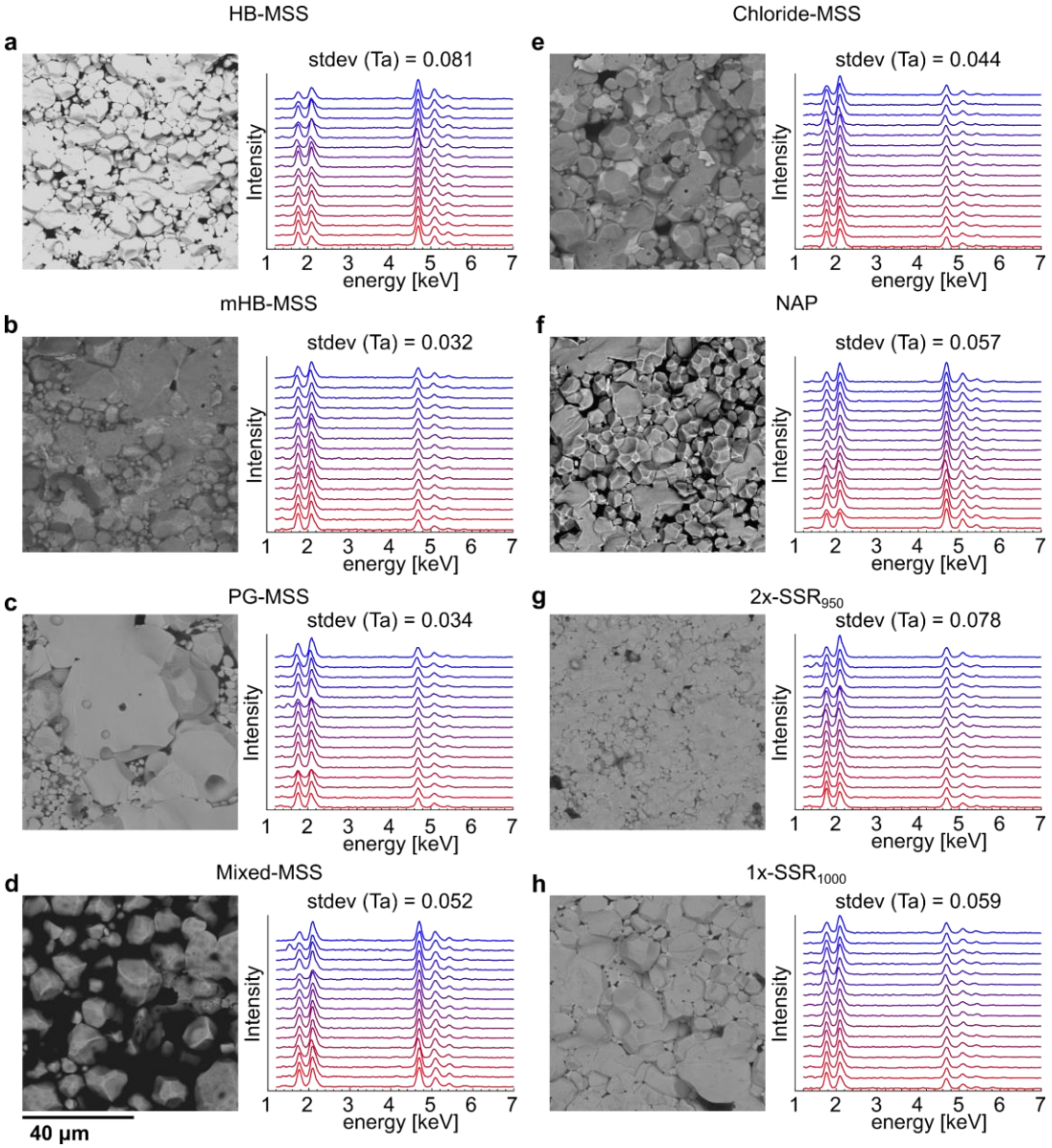

Figure 7.7. BSE-SEM images and EDS spectra of different regions of sintered pellets from LLZTO powders prepared by **a)** HB-MSS, **b)** mHB-MSS, **c)** PG-MSS, **d)** Mixed-MSS, **e)** Chloride-MSS, **f)** NAP, **g)** N-2x-SSR$_{950}$, **h)** 1x-SSR$_{1000}$ sintered at 1200 °C Some of the BSE images had contrast and brightness enhanced to accentuate any differences in contrast between different regions of the image. Note that the darker contrast around grains in (**d**) for the mixed-MSS sample arises from the relatively higher porosity compared to other pellets. The SEM-EDS data for the 1x-SSR$_{1000}$ sample sintered at 1100 °C for 12 h is shown in **Figure E8**. Finally, some Al-signal was observed (~ 1.5 keV for Al K x-ray signal) in the mixed-MSS, 2x-SSR, and PG-MSS, the origin of which is unknown. In each case Al-signal is only observed in a single EDS spectrum.

7.3.5. Correlations Between Sample Processing Parameters and Ionic Conductivity

To better illustrate the effects of various parameters on the ionic conductivity of the different LLZTO samples, **Figure 7.8** presents a summary of the aforementioned analyses investigating the role of synthesis temperature, Ta-distribution in the sintered electrolyte, XRD peak broadening in the as-synthesized powder, and pellet density. While it is possible that some of the variation in ionic conductivity may arise from differences in Li-content (as sintering of Li-garnets can be difficult to perfectly optimize), the sintering methods employed here (specifically to supply excess Li_2O by use of mother powder and Li_2O_2 in an enclosed sintering environment)[146] are based on those shown[39] to minimize or eliminate Li-loss, and for these samples (with the exception of the PG-MSS sample) many pellets were sintered to approximately optimize sintering for each sample type, followed by selecting the sample with the highest ionic conductivity for further analysis. **Figure 7.8a** shows the total ionic conductivity of various LLZTO samples versus synthesis temperature, with no clear trend. Although the pellet density can generally be expected to have some effect on ionic conductivity, there is no strong overall trend for these samples with relative density either (**Figure 7.8b**), most likely since all of the samples possess good intergranular cohesion as evidenced by the predominately transgranular fracture[37,127] seen in **Figure 7.7**. This implies that reasonably high pellet density is a necessary but not sufficient condition to confer high ionic conductivity, which is especially clear when comparing the HB-MSS and 1x-SSR1000 pellets, with nearly identical relative density but a factor of 2 difference in conductivity. The degree of

crystalline disorder in the as-synthesized powders also has no effect on ionic conductivity in the sintered pellets (**Figure 7.8c**).

However, trends emerge when examining the relationship between ionic conductivity and elemental inhomogeneity. The standard deviation of Ta-content in sintered pellets for various LLZTO samples are plotted in **Figure 7.8d**, showing an inverse correlation with the total ionic conductivity. LLZTO prepared by PG-MSS (indicated as a hollow circle) does not fit the general trend as well, which is attributed to the fewer number of pellets prepared and not fully optimized sintering conditions for this sample. However, the relatively low elemental inhomogeneity implies that using pyrochlores as reagents may be advantageous to minimize inhomogeneity in addition to enabling lower synthesis temperature. When considering the effect of inhomogeneity on lattice conductivity (*i.e.* ignoring grain boundary impedance) the trend is even clearer (**Figure 7.8e**). Note the difference in ionic conductivity of the 1x-SSR_{1000} samples sintered at 1100 vs. 1200 °C; despite using the same powder, the two sintering temperatures result in different conductivity for optimized samples, which fits the trend of elemental inhomogeneity well. This may indicate that a shorter sintering operation at a higher temperature may reduce inhomogeneity more effectively than a longer sintering step at a slightly lower temperature. The strong correlation between lattice conductivity and inhomogeneity is particularly good evidence that local compositional variations have a deleterious effect on performance. This is consistent with the fact that the intrinsic Li-ion dynamics in garnet electrolytes are determined largely by Li-content[37] (*i.e.*, composition) and explains why the synthesis temperature or amount of crystalline disorder in the powders, and even the relative density after sintering (so long as

reasonably high density is achieved) have little effect on the performance of garnet solid electrolytes. In short, elemental inhomogeneity is the best explanation for the wide range of ionic conductivities in the various samples discussed herein.

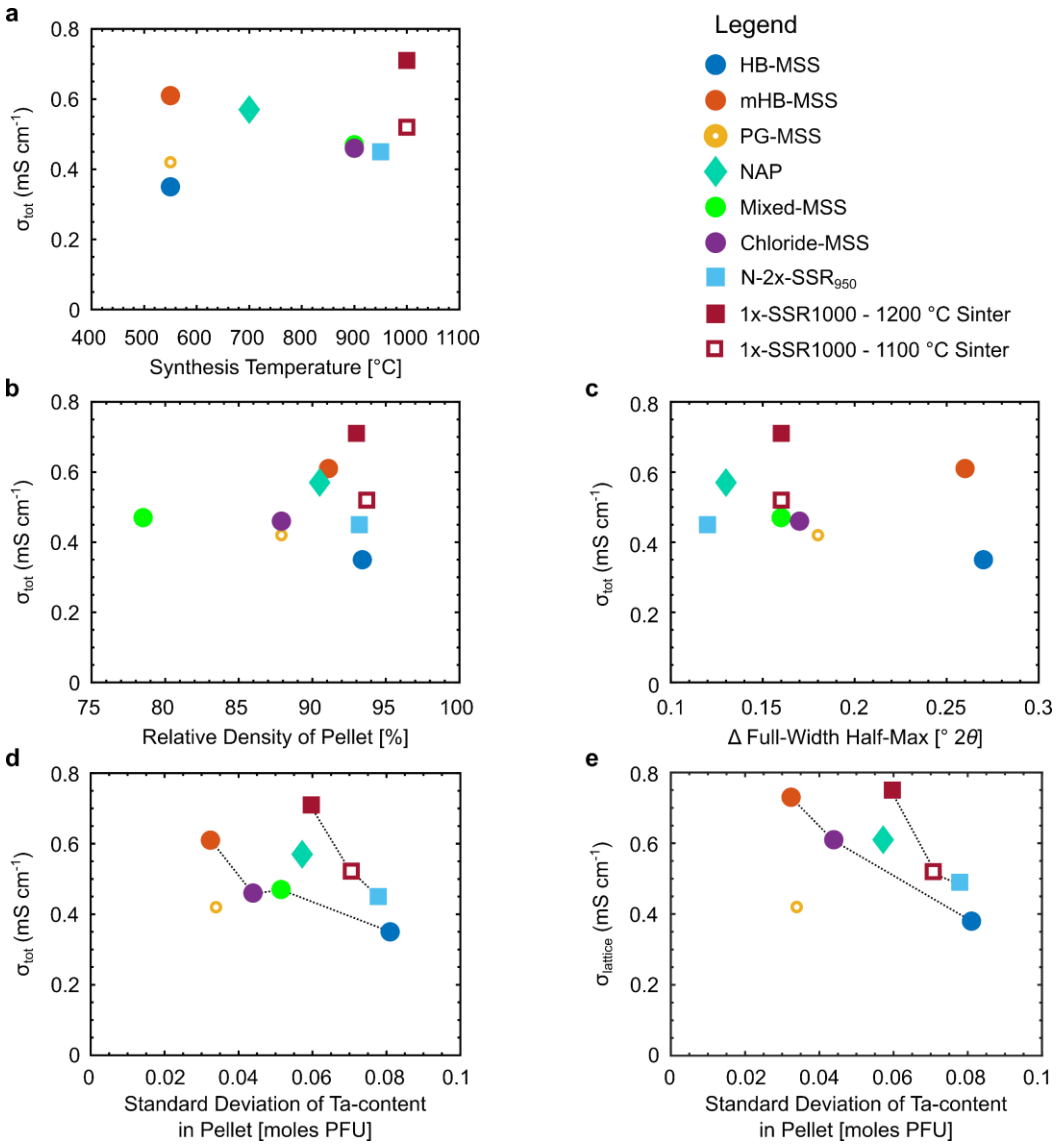

Figure 7.8. Comparison of the effect of various factors on room temperature total ionic conductivity in LLZTO powders studies herein, including **a)** the synthesis temperature used for synthesizing the specific garnet powder, **b)** the relative density of the pellet, **c)** the change in FWHM of Bragg reflections in the powder (as described previously), **d)** the standard deviation of Ta-content residual in the sintered pellet describing elemental inhomogeneity, and **e)** effect of standard deviation of Ta-content residual in the sintered pellet on lattice ionic conductivity in samples where it was measurable. The strongest effect observed is the inverse correlation between total ionic conductivity (**d**) and particularly lattice ionic conductivity (**e**), while the other variables have no obvious correlation with ionic conductivity. Note that the PG-MSS sample is indicated as a hollow circle to denote the lack of extensive sintering optimization relative to other samples. Also note that the hollow maroon square denotes the other 1x-SSR_{1000} sample sintered at 1100 °C rather than 1200 °C (as discussed in **Appendix E, Figure E8**).

Therefore, it is sensible to attribute the main deleterious effect on ionic conductivity to the variability of Ta-content in the sintered pellets as characterized by the magnitude of the standard deviation of Ta-content between various individual crystalline grains in each specimen. Two main reasons for this effect are proposed. First, grains which possess insufficient Ta to fully stabilize the cubic phase will result in non-optimal Li-ion conduction, as the tetragonal phase is known[17] to possess drastically lower ionic conductivity relative to the cubic phase (~0.4-0.5 moles Ta PFU needed at a minimum[36,196]). In this case, striations in fracture surfaces of some LLZTO pellets can be observed (**Figure E9** shows a HB-MSS pellet as an example), which were also observed by Thompson *et al*.[36] and are associated with fracture of a tetragonal (or partially tetragonal) structured garnet ceramic. These striations corroborate the presence of partially tetragonal grains due to local lower Ta-content. Although no obvious evidence of tetragonal LLZO can be observed in the XRD data in **Figure 7.3** and **Figure E1**, it is possible that a small amount is present but not discernable without neutron diffraction as reported previously.[36] Second, grains with too much Ta will have fewer free Li^+ ions as charge carriers, also with the effect of reducing ionic conductivity.[37] Further, since the high ionic conductivity of superionic conductors such as Li-garnets arises not from classical diffusion but rather ensemble motion,[49] it is sensible that maintaining uniformly optimal Li-content (generally between 6-6.5 moles PFU[1,19,37,38]) throughout the solid-electrolyte is crucial to optimizing ion conduction.

7.3.6. Discussion of Relationship Between Thermodynamics and Kinetics of Formation on Elemental Inhomogeneity in Li-Garnets

At this point it is well demonstrated that elemental inhomogeneity can occur in LLZTO nearly irrespective of the synthesis method and is often maintained even after sintering the powders at high temperatures to form densified ceramics. To understand this effect, insight into the thermodynamic stability of LLZTO is important. In the computational study of Miara *et al.*,[162] the $Li_{7-x}La_3Zr_{2-x}Ta_xO_{12}$ solid-solution was shown to be increasingly energetically favorable (specifically, having a lower decomposition energy) for increasing Ta-content. This implies a propensity towards forming Ta-rich garnets at some point during a reaction for synthesis of $Li_{7-x}La_3Zr_{2-x}Ta_xO_{12}$ of a given composition. This energetic trend is supported anecdotally by our previous results showing that LLZTO forms at a slightly lower temperature than undoped cubic phase LLZO (850 °C vs. 900 °C respectively for 4 h synthesis time in the chloride-MSS medium).[145]

Naturally, the minimum free energy condition of the entire ensemble of reagents can be expected to be that resulting from fully intermixed reagents, in this case the phase of nominal composition $Li_{6.4}La_3Zr_{1.4}Ta_{0.6}O_{12}$. However, the formation of other intermediate phases that substantially reduce the overall free energy of the system, especially those that are kinetically easy to form, can complicate the formation process of the target material.[203] In fact, if the intermediates are only slightly less stable than the target material (or in the case of LLZTO grains with higher Ta-content, *more* stable than the uniform nominal composition), the thermal energy required to push the entire

ensemble of reagents to the thermodynamic energy minimum may be quite high. This has been demonstrated in other materials, such as the $Na_{0.67}MO_2$ (M = Co, Mn) system.[203] In this case, most of the net change in free energy of the reagents occurred during formation of metastable intermediates, to the extent that considerably higher reaction temperatures were required to form the equilibrium phase despite its greater energetic favorability.[203] Since the thermodynamic driving force was low, the kinetics of formation were sluggish, implying that kinetics and thermodynamics of forming a given phase from an ensemble of reagents are both critical to understand in order to develop an optimized synthetic approach. Further, since metastable compounds such as LLZO and its doped analogues are generally considered to be entropically stabilized (with the entropy component of the free energy of a system dependent on the temperature)[162], elemental inhomogeneity, if present, may be difficult to ameliorate with low synthesis temperatures. This need for a stronger thermal driving force to promote a sluggish reaction is the most likely explanation for the relatively good compositional uniformity of the LLZTO sample synthesized via solid-state reaction at 1000 °C (1x-SSR_{1000}).

Therefore, for a distribution of composition to occur during formation of LLZTO, it is more likely that Ta-rich garnet phases form first and are maintained due to the locally lower free energy of that subset of reagents. Then, if conditions promoting solid-state diffusion are not maintained for sufficient time, or if the temperature is too low to facilitate solid-state diffusion after the garnet phase forms (as is more likely in the lower temperature MSS methods), the initial distribution of composition is retained even after the synthesis. In the case of SSR (depicted schematically in **Figure 7.9a**), solid-state diffusion is slow[83] and the effective cross-sectional area through which atomic species

can diffuse is limited by the contact area between particles of reagents, which is why higher temperatures are required. In the SSR LLZTO powder samples, use of multiple reaction steps with mixing in between or a higher single reaction temperature can substantially lessen the degree of elemental inhomogeneity. In the case of MSS (depicted schematically in **Figure 7.9b**), dissolution of reagents also plays a role. Since the molten salts act as a high temperature solvent,[119] reagents are more easily distributed during synthesis. For this reason, one would intuitively expect the compositional uniformity of MSS LLZTO to be better than that of SSR. While this is the case in some examples (especially comparing the HB-MSS and chloride-MSS powders to the 1x-SSR_{950} powders), the mechanisms of reagent dissolution and interdiffusion in the melt also bring some added complexity.

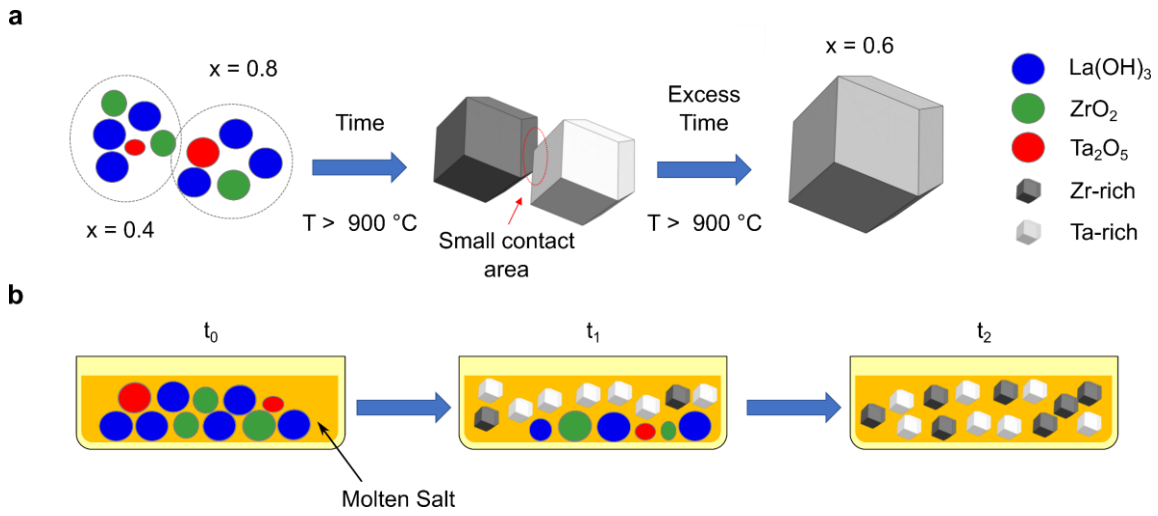

Figure 7.9. Depiction of evolution of reagents to form $Li_{7-x}La_3Zr_{2-x}Ta_xO_{12}$ in **a)** solid-state synthesis of LLZTO showing effect of local compositional variation in reagents being preserved as the garnet phase is formed to produce a distribution of garnet crystals with variable composition, which requires excessive time at high temperatures to result in a uniform composition, and **b)** molten salt synthesis of LLZTO where the higher relative solubility of Ta_2O_5 is hypothesized to result in an initial surplus of dissolved Ta-species and early formation of Ta-rich garnet crystals, followed by slower dissolution of Zr-species and late formation of Zr-rich garnet crystals.

In MSS, there are generally two accepted reaction mechanisms for forming complex oxides: dissolution-precipitation and template-formation.[204,205] In the former, all reagents have sufficient solubility in the chosen salt melt to readily dissolve, interdiffuse, and (in the ideal case) nucleate the desired phase from a uniform, homogeneous solution. In the latter, one or more reagents have limited or no solubility in the chosen melt, resulting in oxide formation by diffusion of the soluble reagents to the insoluble ones and interfacial reaction on the surface of the insoluble reagent. Practically speaking, a mixture of both mechanisms is likely to occur, with one mechanism being favored over the other based on the relative solubilities of all reagents involved. In the case of LLZTO, the reasonably good solubility of La_2O_3[177] and Ta_2O_5[206] in molten salts and the comparably lower solubility of ZrO_2[204], along with the greater energetic favorability of LLZTO with

higher Ta-content, can be expected to act in concert to produce a distribution of garnet particles within the $Li_{7-x}La_3Zr_{2-x}Ta_xO_{12}$ solid-solution. It is hypothesized that this begins with formation of the more energetically favorable, higher Ta-content garnet particles earlier in the reaction followed by higher Zr-content particles later due to these different solubilities. Further, the formation of higher Ta-content particles early in a MSS reaction allows more time for particle coarsening, which explains why the apparent mean composition of the mHB-MSS powder (**Figure 7.2j**) contains less than 0.6 moles of Ta per formula unit. In other words, the smallest particles (likely to be overrepresented on the TEM grid and hence EDS analysis) will tend to be the ones which formed later in the reaction (less energetically favorable), which in turn can be expected to be richer in Zr.

7.3.7. Discussion of Methods to Minimize Deleterious Elemental Inhomogeneity in Li-Garnets

Based on the results presented in **Figure 7.8d,e**, it is clear that elemental inhomogeneity remaining after sintering of Ta-doped LLZO electrolytes has a negative effect on ionic conductivity, and reduces intrinsic *lattice* ionic conductivity and not just total ionic conductivity. Therefore, rather than treating a garnet solid electrolyte as a uniform ionic conductor, a sintered, polycrystalline garnet solid electrolyte may be viewed as an ensemble of crystalline grains presenting individual resistor/capacitor elements both in parallel and in series with potentially different impedances. Grains with Ta-content deviating too far from the optimal value will have increased impedance, causing Li^+ to preferentially flow through adjacent grains with lower impedance. If too

many of these grains exist in a sintered garnet electrolyte, they will block too many of the lower impedance pathways leading to a bottleneck effect. This concept is depicted graphically in **Figure 7.10a**. In such a situation, even a garnet electrolyte with high density, good grain cohesion, low grain boundary impedance, and the correct *average* composition will not possess the expected high ionic conductivity since the proportion of low impedance pathways is too low.

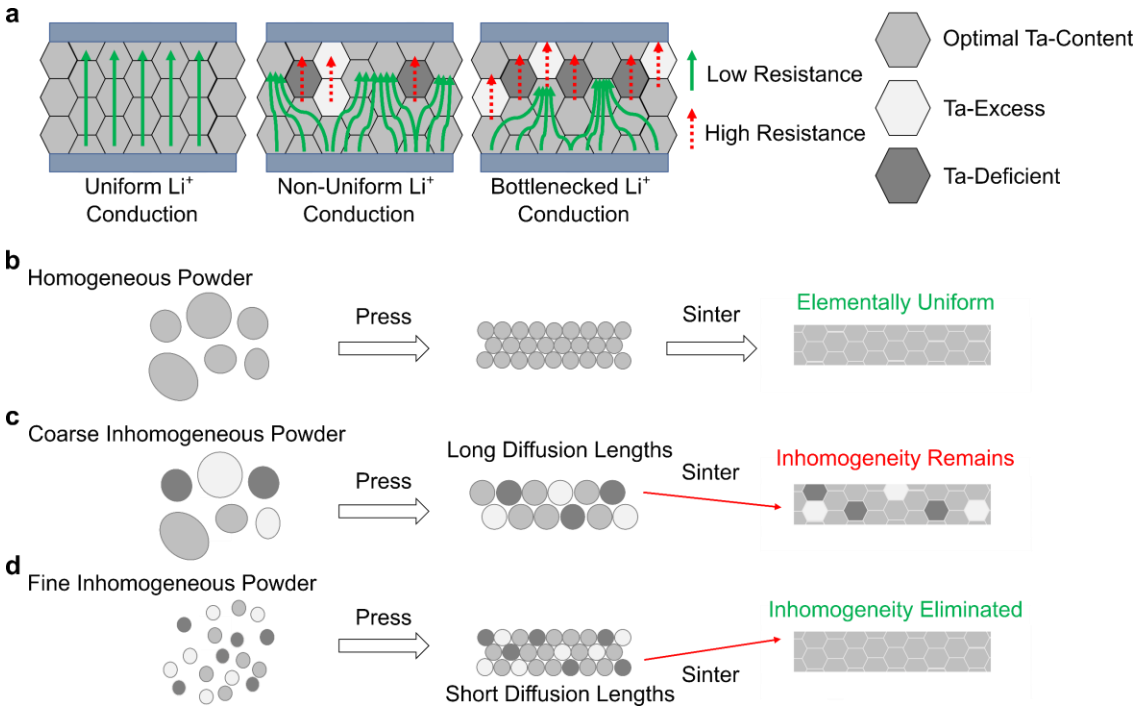

Figure 7.10. a) Graphic depicting hypothesized effects of residual elemental inhomogeneity in sintered garnet electrolytes on Li-ion transport, as well as visualization of hypothesized evolution of elemental inhomogeneity in the case of **b)** beginning with highly homogeneous powder resulting in a compositionally uniform electrolyte, **c)** beginning with inhomogeneous powder with large particle sizes resulting in residual inhomogeneity in the sintered electrolyte, and **d)** beginning with inhomogeneous powder with small particle sizes, which allow solid-state diffusion during sintering to produce a uniform composition after sintering.

Given the ubiquity of local deviations from the target composition in the samples investigated herein, approaches to mitigate it are crucial. The ideal case is to ensure a uniform composition during synthesis (**Figure 7.10b**) so that the sintering step can be optimized simply to minimize porosity and Li-loss. One way to do this is with a brute force approach such as repeated SSR at high synthesis temperatures (e.g. **Table E1**, Wang and Lai[34], Huang et al.[41], Tsai et al.[28]). In the results presented here, utilizing nanosized (*i.e.* pre-ball-milled) reagents (N-1x-SSR and N-2x-SSR) compared to bulk reagents (B-1x-SSR and B-2x-SSR) result in reduced inhomogeneity after two calcinations, as does employing two calcination steps generally (*i.e.* 2x-SSR over 1x-SSR). On the other hand, the 1x-SSR_{1000} sample (sintered at 1200 °C) shows comparable ionic conductivity to samples prepared with the aforementioned methods, implying that a single reaction at a higher temperature may be an attractive strategy to minimize the number of synthesis steps. Another option is single crystal growth from an appropriate melt (e.g. **Table E1**, Kataoka *et al.*[50,51]). While the energy cost of each of these approaches is quite high, they can produce garnet electrolytes with very high ionic conductivity.

A different approach could be to employ high sintering temperatures and long sintering times to allow sufficient solid-state diffusion to homogenize the composition of the electrolyte. Based on Fick's 2nd Law[207], the time needed for a given species to diffuse is proportional to the square of the distance. Hence, as the distance needed to allow full interdiffusion of Zr and Ta increases (based on the particle size of the powder used), the time will increase quadratically. This view is depicted in **Figure 7.10c**, where if particle sizes are large, conventional sintering times may not be long enough to enable solid-state

diffusion to produce a uniform composition after densification. However, since Li-garnets have a strong propensity toward Li_2O loss at the high temperatures necessary for sintering,[19,39] such long sintering strategies require a large amount of sacrificial garnet powder[39,126,208] to continuously provide a high enough Li_2O vapor pressure[39] to allow good densification and maintain a high Li-content[19] in the sintered electrolyte. This makes extended sintering time as a strategy to mitigating elemental inhomogeneity extremely cost prohibitive.

An alternative approach to minimizing elemental inhomogeneity is to ensure that the diffusion lengths between garnet particles during sintering are minimized. A clear illustration of this approach is comparison of the HB-MSS and mHB-MSS LLZTO powders we reported previously.[145] In the HB-MSS method, elemental inhomogeneity present initially in the powder (**Figure 7.2a**) was observed even after sintering at 1300 °C, a temperature notably higher than is generally employed for sintering garnet solid-electrolytes. However, while the mHB-MSS powder has an even greater variation in Ta-content than the HB-MSS powder (**Figure 7.2j, Table E5**), this inhomogeneity is not preserved to as large of an extent in the sintered ceramic (**Figure 7.8, Table E5**). The reason for this apparent contradiction seems to be the markedly smaller particle size distribution of the mHB-MSS powder, with the majority of particles being < 1 μm and less agglomerated than the HB-MSS powder.[145] This smaller particle size distribution allows solid-state diffusion to occur in a shorter amount of time during sintering, resulting in reduced inhomogeneity in the final garnet ceramic (depicted schematically in **Figure 7.10d**).

In the ideal case, the synthesis method chosen to produce garnet powders should be optimized such that no elemental inhomogeneity occurs in the first place. However, this may be difficult to achieve as it will depend on the thermodynamics and kinetics of the various species as well as choice of dopants, synthesis temperature, etc. as discussed previously. Since Ta-rich garnets are more energetically stable than Zr-rich garnets,[162] the driving force for interdiffusion of Ta out of the Ta-rich grains may also be locally reduced depending on the difference in composition between neighboring grains. The combination of a quadratic relationship between grain size and the time needed for interdiffusion and the energetic favorability of Ta-rich grains can further explain the propensity for Ta-rich grains to be preserved even after sintering unless diffusion lengths can be reduced through processing. This result motivates the use of sub-micrometer to nanosized garnet powders. The NAP combustion method is an example of minimizing diffusion distances during synthesis, as the pre-garnet particles that form even before all of the organic species are removed via combustion show relatively uniform elemental distribution, with minor inhomogeneity existing only on small length scales (*i.e.* ~100 nm).[146] For LLZTO prepared by NAP, reasonable uniformity can therefore be expected in the nanopowder despite the low synthesis temperature of 700 °C. Other methods, such as the co-precipitation/co-decomposition type approaches[37] or sol-gel type methods, due to initial molecular mixing of individual atomic species[35,89] may also be effective for this reason.

It is suspected however, that the situation depicted in **Figure 7.10c** is quite common. For one thing, most solid-state reactions are performed at as low of a temperature as possible while still forming the garnet phase, generally around 900

°C.[33,34,38,42,43] Some methods from the literature use multiple calcination steps with grinding between reactions,[28,34,39–41,126] but this is not always the case. Based on the observation of elemental inhomogeneity in the various materials presented here, it is believed that variation in composition most likely also occurs in LLZTO prepared in other examples in the literature but has gone unnoticed. It is suspected that some of the variation in maximum ionic conductivity in the literature may be related to elemental inhomogeneity. Further, the optimum doping level may also be related to the degree of inhomogeneity; if a synthesis method produces garnet powder with a narrow distribution in composition, the optimal doping level determined for that investigation should be closer to the intrinsic optimal doping level for LLZTO, while garnet powder with a wider distribution in composition will have a perceived optimum that minimizes the number of subcritically-doped grains. This is because higher Ta-content (e.g. $Li_6La_3ZrTaO_{12}$) can still provide ionic conductivity up to 0.24 mS cm^{-1},[209] while tetragonal LLZO has much lower conductivity.[17]

Though this study focuses solely on Ta-doped LLZO of a specific nominal composition, there is evidence that other garnet compositions are prone to similar challenges. For example, Hubaud *et al.* observed similar inhomogeneity in Al-doped LLZO with high resolution synchrotron XRD and ^{27}Al nuclear magnetic resonance (NMR) spectroscopy wherein the as-prepared sample was an ensemble of garnets of slightly different Al-content due to the difficulty in incorporating Al into the lattice.[210] In contrast, Posch et al., observed in single-crystalline Al-doped LLZO that the Li-hopping dynamics were quite uniform, where polycrystalline samples of similar composition had a broad range of Li-jump frequencies, which they attribute to a range of Li-content due to

inhomogeneous distribution of Al between particles.[211] In this case, a the narrower range of jump frequencies was correlated to the high uniformity of composition of the garnet single crystal.[211] It was also speculated[211] that regions of a polycrystalline garnet with insufficient Al-doping would hinder long-distance Li-ion motion, a similar conclusion made herein for Ta-doped LLZO. Smetaczek et al. utilized laser ablation inductively-couple plasma optical emission spectroscopy (LA-ICP-OES) to determine the variation in local composition across a sintered Al-doped LLZO electrolyte in conjunction with microcontact electrochemical impedance spectroscopy to demonstrate that the local composition and impedance vary considerably across a single garnet membrane.[212] Badami *et al.* also observed a mix of related garnet phases due to Al-contamination in sintered LLZTO electrolytes.[124] These observations and the results presented here indicate that the relative phase stability of doped garnets and intermediates depend on the dopant type and additives, implying that formation of a distribution of garnets of variable composition is likely a common feature of LLZO synthesis in general, not just Ta-doped LLZO. Indeed, the choice of cationic dopants has a marked effect on the defect energy of LLZO, implying that the thermodynamics of LLZO depend on the dopant type.[213] Regardless of dopant choice or synthetic method, this work demonstrates the importance of understanding the local compositional homogeneity of a garnet solid electrolyte and provides perspective and a strategy to address elemental inhomogeneity. Hopefully, these results will provide tools to help other researchers improve the reproducibility and performance of garnet-type solid electrolytes in the important goal of enabling solid-state lithium batteries.

7.4. Conclusions

In this chapter, synthesis-related effects on the ionic conductivity of lithium-conducting garnets are explored. Using x-ray diffraction and pair distribution function analysis for structural characterization, and chemical characterization via electron microscopy with energy dispersive x-ray spectroscopy, the effects of different synthesis mechanisms and synthesis temperatures in molten salt synthesis, non-aqueous polymer combustion synthesis, and solid-state reaction are explored. Generally, the lower temperature (i.e. 400-700 °C) synthesis methods produce Li-garnet powders with lower crystallinity as evidenced by peak broadening in x-ray diffraction and pair distribution function analysis, but not necessarily reduced ionic conductivity when consolidated into a dense electrolyte since the crystallinity is improved during sintering. On the other hand, elemental inhomogeneity, comprising deviation in composition on a particle-by-particle basis, arises irrespective of the synthesis method and is often preserved in garnet electrolytes even after high temperature sintering. This inhomogeneity arises initially during synthesis most likely due to a mixture of thermodynamic and kinetic factors unique to each synthesis method, and can be significant even in conventional, high-temperature solid-state reaction. Although solid-state reaction is not always effective to ensure perfect uniformity of composition, employing nanosized oxide precursors, repeated calcinations with intermediate ball-milling, or higher synthesis temperatures are all strategies to increase the compositional homogeneity of the resultant LLZTO powder.

The influence of synthesis temperature and relative density on the ionic conductivity of garnet electrolytes is not significant, but there is a noticeable inverse

correlation between ionic conductivity and the degree of elemental inhomogeneity remaining in sintered electrolyte ceramics, especially when considering lattice ionic conductivity over total ionic conductivity. This effect is attributed to non-optimal Li-content as the amount of the Ta-dopant varies on a grain-by-grain basis in sintered LLZTO. However, high ionic conductivity is possible using each of the synthesis methods so long as the inhomogeneity can be eliminated at some point in the overall synthesis and processing scheme, showing that good performance can be achieved in garnet electrolytes formed from garnet powders obtained at very low synthesis temperatures (e.g. 550 °C). This exploration reveals that elemental inhomogeneity is another variable that negatively affects performance in Li-garnets and is difficult to observe with routine characterization methods. Hopefully this work serves as a guide for assessing the extent to which inhomogeneity may be present, as well as provide methods to mitigate it and enable consistently high ionic conductivity in garnet-based solid-state batteries.

8. PROMISING, UNPUBLISHED WORKS

8.1. Introduction

Over the course of my Ph. D. studies, I have performed numerous experiments, many of which bloomed into publications and some of which were either unsuccessful or are as of yet incomplete. This chapter is dedicated to those experiments which show promise for future investigations of LLZO and still would require further work. Many of these experiments are related to optimizing synthesis methods for LLZO or pyrochlores, and while they were not chosen for further exploration in the main chapters of this dissertation, may still be useful for the curious researcher. This chapter is separated into 4 sections, briefly recounting experiments regarding additives to MSS to modify formation temperature and particle size, the synthesis of a new Li-conducting garnet phase $Li_{6.5}La_{1.5}Sr_{1.5}Ta_2O_{12}$, and explorations into molten salt and vapor-phase conversion of pyrochlore thin films and powders to garnets.

8.2. Investigations of Additives in Molten Salt Synthesis of LLZO – Li_2O_2

8.2.1. Introduction and Motivation

After the initial success in applying MSS in eutectic LiCl-KCl[161] to form LLZO, two variations of the method were also explored to reduce the formation temperature and / or produce smaller particle sizes. An early application of Lux-Flood[119,180,181] basic

additives to LLZO synthesis centered on addition of Li_2O_2 as the Li-source to the same LiCl-KCl reaction medium as in **Chapter 4**. Li_2O_2 is a useful and attractive Li-source and may be effectively used as a Li_2O-source without requiring handling under inert atmosphere, as it decomposes[165] to Li_2O beginning around 250 °C as it liberates oxygen. This effect was also utilized to provide Li_2O vapor[39] pressure during sintering in my previous[145,146,197] works, rather than using as much sacrificial LLZO powder.

8.2.2. Experimental Procedure

XRD patterns were acquired with a Siemens D-5000 diffractometer using Cu Kα radiation and SEM images were acquired using a FEI XL30 SEM.

For synthesis of LLZO using Li_2O_2, the same salt composition, reagents, and salt to reagent ratio was used with the addition of various amounts of Li_2O_2 to the salt mixture before heating. For these reactions, a 1:1 ratio of salt to reagents (by mass) was employed using small batches of 4 g salt, 4 g LLZO precursors (metal nitrates as before), and varying amounts of Li_2O_2. All salts and reagents were ground thoroughly by hand in an agate mortar and pestle before being placed in an Al_2O_3 crucible and heated to the desired temperature in a muffle furnace. After synthesis, the salts were washed away and powders collected as reported[161] previously. Experimental details of several syntheses are contained in **Table 8.1**:

Table 8.1. Experimental details for synthesis of undoped and Al-doped LLZO (Sample Number 6) in LiCl-KCl with added Li_2O_2.

Sample Number	Mass Ratio of Li_2O_2 : Reagents	Time (h)	Temperature (°C)	Result
1	0.25	3	900	Mostly t-LLZO
2	0.25	3	600	LaOCl and $La_2Zr_2O_7$
3	0.125	3	700	LaOCl, $La(OH)_3$, $La_2Zr_2O_7$, and some LLZO
4	0.25	3	700	Mostly t-LLZO
5	0.5	3	700	t-LLZO
6	0.5	3	700	$LiAlO_2$, $LaAlO_3$, $La_2Zr_2O_7$, t-LLZO

8.2.3. Results and Conclusions

Where the initial demonstration of undoped, Al-doped, and Ga-doped LLZO formation in eutectic LiCl-KCl required[161] a reaction temperature of 900 °C for 4 h, the experiments presented in **Table 8.1** reveal that undoped t-LLZO can form at lower temperatures depending on the amount of Li_2O_2 added. While 600 °C is still too low of a temperature to form LLZO despite the addition of Li_2O_2 (instead forming LaOCl and $La_2Zr_2O_7$ much like the reaction products at this temperature in the original method outlined in **Chapter 4**), LLZO begins to form at 700 °C in 3 h along with LaOCl, $La(OH)_3$, and $La_2Zr_2O_7$ when a reagent to Li_2O_2 ratio of 0.125 is employed. When this ratio increased to 0.25 or 0.5, t-LLZO is produced as the primary reaction product. Curiously, much like in the initial attempts to form Al-doped LLZO using eutectic $LiNO_3$-LiCl (**Chapter 4**, **Appendix B**), only t-LLZO was obtained in the case of sample 6, despite the addition of $Al(NO_3)_3$ to the reagent mixture to supply a critical doping level of Al. XRD patterns of each of the reactions outlined in **Table 8.1** are shown in **Figure 8.1.**

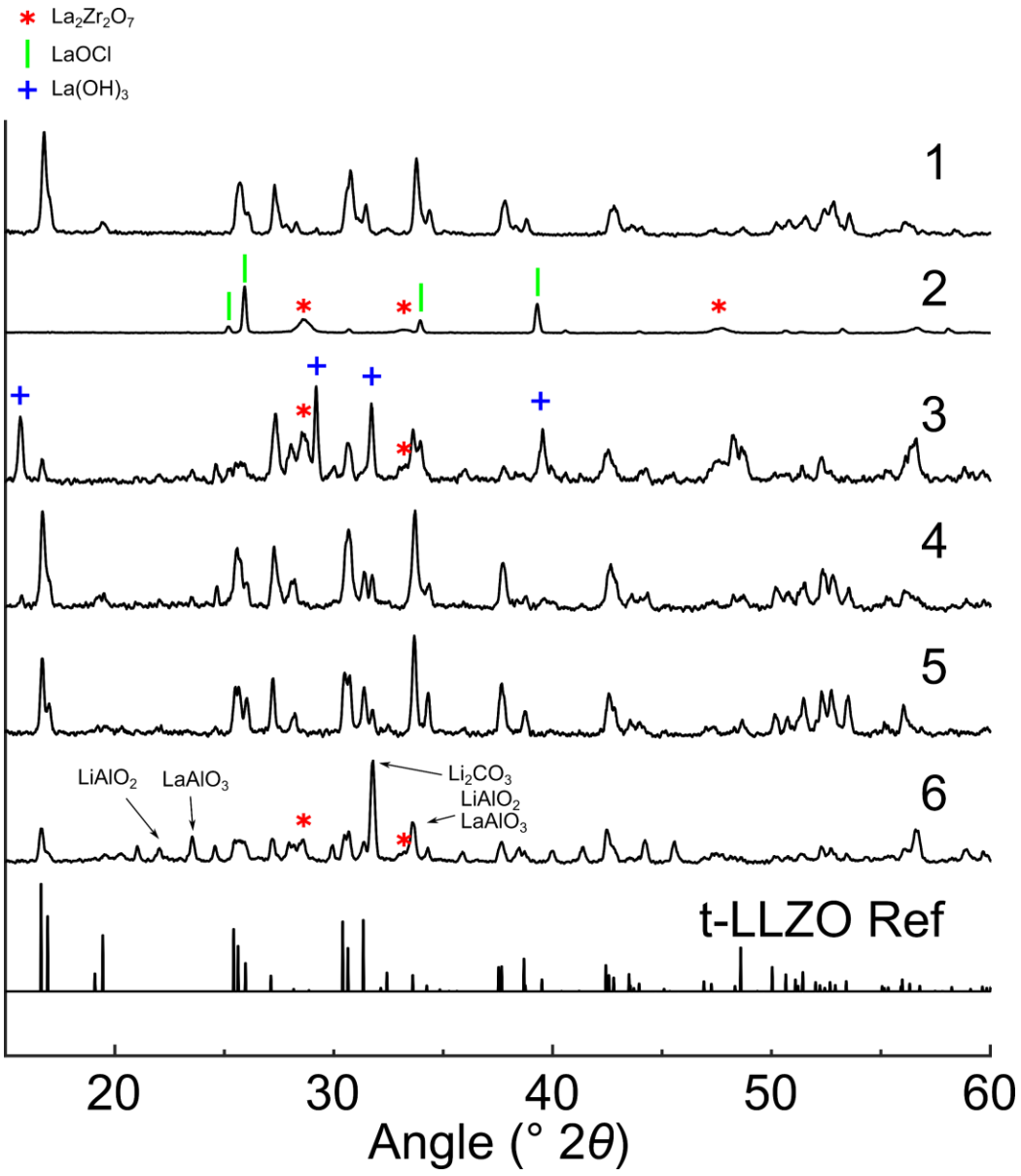

Figure 8.1. XRD patterns of resultant material from synthesis of undoped LLZO in eutectic LiCl-KCl with added with added Li_2O_2. XRD patterns are numbered corresponding to the reaction conditions in **Table 8.1**. Note that in the case of Al-doped LLZO, t-LLZO still forms along with some $La_2Zr_2O_7$ (PDF#00-017-0450), $LiAlO_2$ (ICSD coll. code 92521), and $LaAlO_3$ (ICSD coll. code 23815), indicating that rather than incorporating into the garnet lattice, Al-species form compounds with Li and La. The reference pattern for t-LLZO was generated based on Awaka et al.[17]

In the case of sample 6, cubic ALLZO did not form even though the same reaction conditions (sample 5) could form t-LLZO with little to no observable side products when no dopant sources were added to the reagent mixture. Apparently, under these reaction conditions the Al reacts with Li and La to form $LiAlO_2$ and $LaAlO_3$, as indicated in **Figure 8.1**. This also has the apparent effect of preventing full conversion to t-LLZO as some $La_2Zr_2O_7$ pyrochlore phase is also present. Evidently, the higher basicity imparted to the melt by addition of Li_2O_2 prevents Al from doping the garnet structure. This may be due to greater energetic favorability of $LiAlO_2$ and $LaAlO_3$ over ALLZO or could be due to slow kinetics of forming ALLZO from separate $La_2Zr_2O_7$, $LiAlO_2$, and $LaAlO_3$ phases. Similar problems were observed by Deviannapoorani et al. in their attempts to utilize stoichiometric $La_2Zr_2O_7$ as a reagent for garnet formation.[187] In previous work it was also observed that Al did not seem to readily incorporate into the garnet lattice when using the highly basic molten salt medium.[145] Thus the dopant chemistry in the salt melt clearly must be taken into account to produce garnet depending on desired final composition.

8.3. Investigations of Additives in Molten Salt Synthesis of LLZO – NaF

8.3.1. Introduction and Motivation

In contrast to modulating the basicity of the LiCl-KCl melt with Li_2O_2, some experiments in MSS additives focused on addition of NaF to provide increased solvating[119] power compared to Cl^- by virtue of the smaller and more nucleophilic F^- anion. Since formation of garnet particles in the salt melt requires dissolved La-, Zr-, and Ta-species to all be present before nucleation, it stands to reason that faster dissolution and better solubility of the component oxides (and any intermediate phases such as LaOCl or $La_2Zr_2O_7$ as observed[161] previously) could reduce the necessary reaction temperature or time and also the final particle size. Investigating this hypothesis is the focus of this section.

8.3.2. Experimental Procedure

XRD patterns were acquired with a Siemens D-5000 or a Bruker D-8 diffractometer using Cu Kα radiation and SEM images were acquired using a FEI XL30 SEM.

In these synthesis experiments, Ta-doped LLZO (LLZTO) of target composition $Li_{6.4}La_3Zr_{1.4}Ta_{0.6}O_{12}$ was formed using $LiNO_3$, $La(NO_3)_3$, and $ZrO(NO_3)_2$ nitrates and Ta_2O_5 as reagents. As in previous work[145] (presented in **Chapter 5**) exploring the effect of Lux-Flood[180,181] basicity, rather than a 1 : 1 ratio of LiCl-KCl to reagents, a 3 : 1 ratio was employed. A typical reaction utilized 15 g of eutectic LiCl-KCl and 5 g of

stoichiometric metal nitrates (20% excess $LiNO_3$) and Ta_2O_5. In this set of experiments, some NaF was added to the mixture before thorough grinding with a mortar and pestle. Reactions were carried out in a muffle furnace at 850 °C for 4 h to probe the effect of NaF concentration on phase purity and morphology of the resultant garnet powders. One reaction was performed at 800 °C for 4 h to determine whether addition of NaF lowers the required formation temperature of LLZTO in LiCl-KCl. After synthesis, the salts were washed away and powders collected as reported[161] previously.

Table 8.2. Experimental details for synthesis of Ta-doped LLZO in LiCl-KCl with the addition of NaF.

Sample Number	Mass Ratio of NaF : Reagents	Time (h)	Temperature (°C)	Result
1	0	4	850	LLZTO, larger particles
2	0.04	4	850	LLZTO, smaller uniform particles
3	0.1	4	850	LLZTO, smaller uniform particles
4	0.2	4	850	LLZTO, smaller uniform particles
5	0.4	4	850	LLZTO, LiF, agglomeration
6	0.6	4	850	LLZTO, LiF, agglomeration
7	0.2	4	800	LLZTO

8.3.3. Results and Conclusions

In each synthesis experiment performed here, LLZTO was formed easily, as confirmed by XRD in **Figure 8.2**. For reactions 1-6, the same reaction conditions were employed with the relative amount of NaF added being the only variable to investigate the effect of NaF on LLZTO particle morphology. **Figure 8.3** shows SEM images of particles from reactions 1-6, showing the morphological effects of NaF concentration. With no added NaF, the particles are relatively large and agglomerated, with a wide particle size distribution. However, for small amount of added NaF (NaF : reagent mass

ratio of 0.04, 0.1, and 0.2), the particle size is evidently reduced, with apparently better uniformity and most particles being below ~ 2 μm. However, as the proportion of NaF increases, the particle morphology becomes less regular, with apparently more agglomeration occurring. These results indicated that a small amount of NaF as an additive may be beneficial to improve dissolution and liquid phase diffusion of reagents. It is possible that the reactions employing more NaF proceed faster such that the reaction time used is too long, resulting in too much coarsening of the formed LLZTO nuclei. Further, reaction 7 indicates that 850 °C is higher than necessary to form LLZTO in LiCl-KCl with NaF added, as pure phase LLZTO also forms at only 800 °C in 4 h.

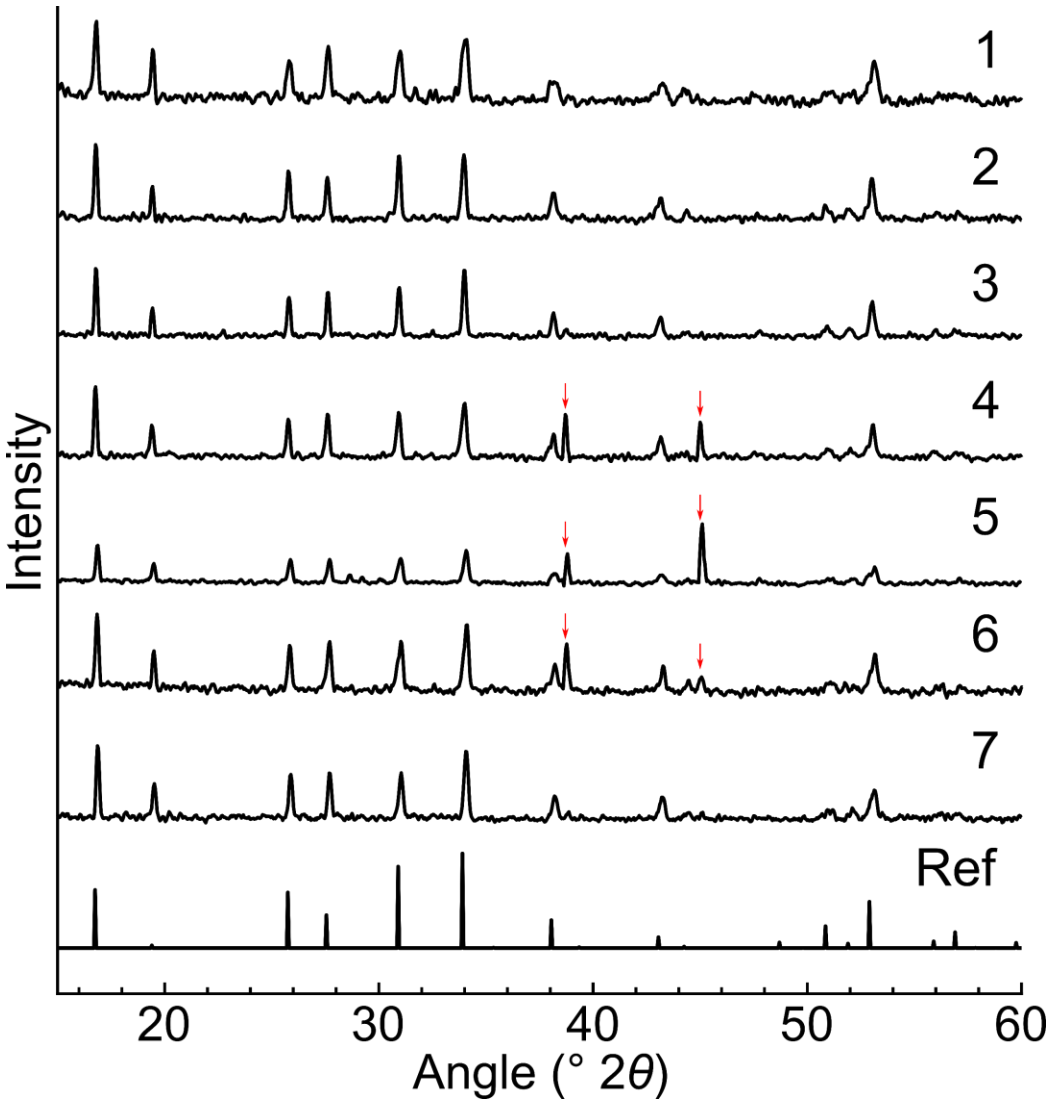

Figure 8.2. XRD patterns of various synthesis conditions applied to form LLZTO in eutectic LiCl-KCl with added NaF. XRD patterns are numbered corresponding to the reaction conditions in **Table 8.2**. In each case, LLZTO is obtained, although in reactions 4 through 6 some LiF is also present (indicated by red arrows): this is believed to be due to ion exchange between NaF and LiCl and the insolubility of LiF in water (used to wash away residual salts). Finally, LLZTO is observed to form at only 800 °C in 4 h with the addition of NaF (NaF to reagents ratio 0.2 : 1 by mass).

It is somewhat curious that the apparent relative intensity of the LiF peaks vary in an unintuitive way in reactions 5 and 6 particularly, where it appears that reaction 5 has more residual LiF despite the lower amount added. The reason for this isn't totally clear,

but may be due to a combination of different solution characteristics when a larger proportion of the melt is NaF (and less exchange between LiCl and NaF that maintains soluble NaF) or potentially a difference in crystallinity of the residual LiF, where more crystalline LiF would result in stronger and sharper Bragg peaks. The relative intensities of the main LiF peaks also vary in an unexpected way between reaction 5 and 6. The source of this variation is of interest but has not been explored in greater detail.

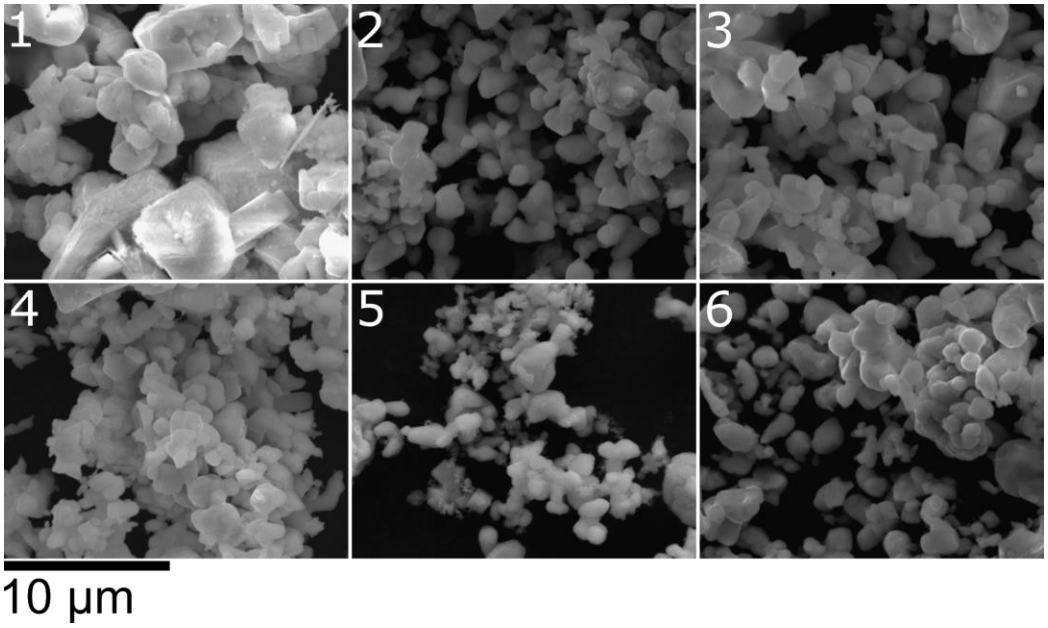

Figure 8.3. SEM images of LLZTO powders obtained in eutectic LiCl-KCl with added NaF, numbered corresponding to the experiments in **Table 8.2**. With no NaF added, the particles are somewhat larger (1) while for small amount of added NaF (2-4) the particle size is apparently reduced and somewhat more uniform. Higher amounts of NaF (5-6) tend to produce more agglomerated particles under the synthesis conditions used.

In conclusion, these few experiments demonstrate a minor modification to the LiCl-KCl eutectic MSS method[161] initially presented in **Chapter 4**, which may prove beneficial to further understand the mechanisms of formation of garnet or other oxide phases, and which allows straightforward modulation of the final particle size. Further, the influence of the F^- anion appears to benefit the formation of LLZTO at a lower temperature than when absent from the LiCl-KCl eutectic, although a conclusive relationship has yet to be developed. It is possible that other minor additives to an otherwise well-behaved 'neutral' salt melt may provide other benefits for synthesis of Li-garnets or other oxides.

8.4. Proof of Concept Synthesis of New Li-Conducting Garnet Phase $Li_{6.5}La_{1.5}Sr_{1.5}Ta_2O_{12}$ (LLSTO) Using Molten Salt Synthesis and Solid-State Reaction

8.4.1. Introduction and Motivation

Although the focus of this research has been on lithium garnets of the zirconate family, there was extensive research into other garnet composition as solid state lithium ion conductors before LLZO was discovered[6] by Murugan et al. Among these lithium garnets are tellurates, niobates, tantalates, and many others as discussed in **Chapter 1**.[1] Generally speaking, these garnets have higher ionic conductivity for higher Li-content, up to the point where the large amount of Li in the Li-7 garnets such as LLZO causes spontaneous ordering of the Li-sublattice, resulting in a cubic to tetragonal transition.[1,17,48] There are many factors that make LLZO and its derivatives a superior Li-ion conductor including the high Li-content (with an optimum in the range of 6.5 moles Li per formula unit, PFU)[37] sufficient number of mobile Li-ions on high energy sites to allow concerted[49] ion diffusion, and a well-optimized bottleneck[49] size for Li-ions. Of interest therefore is whether similar garnets with a comparable Li-content also have high ionic conductivity.

On the other hand, the observation of elemental inhomogeneity (introduced in **Chapter 5** and explored extensively in **Chapter 7**) due to thermodynamic[162] factors (greater energetic favorability of $Li_6La_3ZrTaO_{12}$ compared to cubic $Li_7La_3Zr_2O_{12}$) and kinetic factors (slow solid-state diffusion or differential solubility in molten salts between Ta_2O_5 and ZrO_2), motivates targeting garnet compositions that may have a lower

propensity for elemental inhomogeneity. Since SrO is a basic oxide it is expected that it will have appreciable solubility in molten salts with basic components such as LiOH (as 'like dissolves like' including in molten salts)[119], and was identified as an alternative component to modulate the Li-content in a tantalate garnet, obviating the need for low-solubility ZrO_2 as a component. For these reasons, a new garnet phase with composition $Li_{6.5}La_{1.5}Sr_{1.5}Ta_2O_{12}$ (LLSTO) was synthesized, to test whether it is synthesizable and whether it has comparable ionic conductivity to doped LLZO with a similar Li-content.

8.4.2. Experimental Procedure

XRD patterns were acquired with a Bruker D-8 diffractometer using Cu Kα radiation and SEM images were acquired using a FEI XL30 SEM. EDS spectra were acquired using an EDAX system.

Both MSS in LiCl-LiOH (the same 'mixed-MSS' medium as in previous[145] work) and SSR were utilized as a proof of concept for synthesis of LLSTO. The experimental methods for mixed-MSS and SSR are the same as previously[145] reported with the following modifications. In addition to the normal reagents used ($LiNO_3$, $La(NO_3)_3$, and Ta_2O_5 for MSS or Li_2CO_3, $La(OH)_3$, and Ta_2O_5 for SSR), $SrCO_3$ was synthesized from $SrCl_2$ 6 H_2O as the Sr-source as follows. $SrCl_2$ (Sigma) was first dissolved in de-ionized water (NanoPure system from EMD Millipore) followed by addition of excess Na_2CO_3 (Sigma-Aldrich) under stirring to precipitate insoluble $SrCO_3$. Finally, the precipitate was collected via vacuum filtration and washing with excess de-ionized water to obtain $SrCO_3$. After drying in air (> 100 °C) the $SrCO_3$ was used either for MSS or SSR of

LLSTO. A simulated XRD pattern for the new $Li_{6.5}La_{1.5}Sr_{1.5}Ta_2O_{12}$ phase was generated using VESTA[18] software. Three samples were prepared as outlined in **Table 8.3**. Finally, one sample from Sample 3 was consolidated via sintering at 1200 °C for 4 hours using the same method as in previous[145] work, polished with SiC polishing paper and characterized using EIS (Biologic SP-200) with graphite blocking electrodes between 7 MHz and 1 kHz as described[145] previously (see also **Chapter 2.2.4**).

Table 8.3. Experimental details for synthesis of $Li_{6.5}La_{1.5}Sr_{1.5}Ta_2O_{12}$.

Sample Number	Synthesis Type	Time (h)	Temperature (°C)	Result
1	MSS	8	700	Garnet phase with minor impurity
2	MSS / SSR	12 / 12	700 / 900	Garnet phase with minor impurity
3	SSR	12	900	Nearly pure garnet phase

8.4.3. Results and Conclusions

Several reactions were performed to synthesize LLSTO using MSS, SSR, or MSS with a subsequent calcination step. In all cases, the primary reaction product is a white powder with a garnet crystal structure, as seen in the XRD patterns in **Figure 8.4**. Based on comparison to the simulated XRD pattern, generated using VESTA from a modified CIF file with the theoretical site occupancy of $Li_{6.5}La_{1.5}Sr_{1.5}Ta_2O_{12}$, it is clear that the relative peak intensities from the experimental XRD data match quite well with the simulation. While a full structural refinement was not performed due to the exploratory nature of these experiments, the good correspondence in position and relative intensity of the reflections indicates that LLSTO was successfully formed. In order to test whether this new garnet phase is an ion conductor, some of the sample 3 powder was pressed and

sintered at 1200 °C to form a densified pellet, followed by conventional EIS analysis using graphite blocking electrodes.

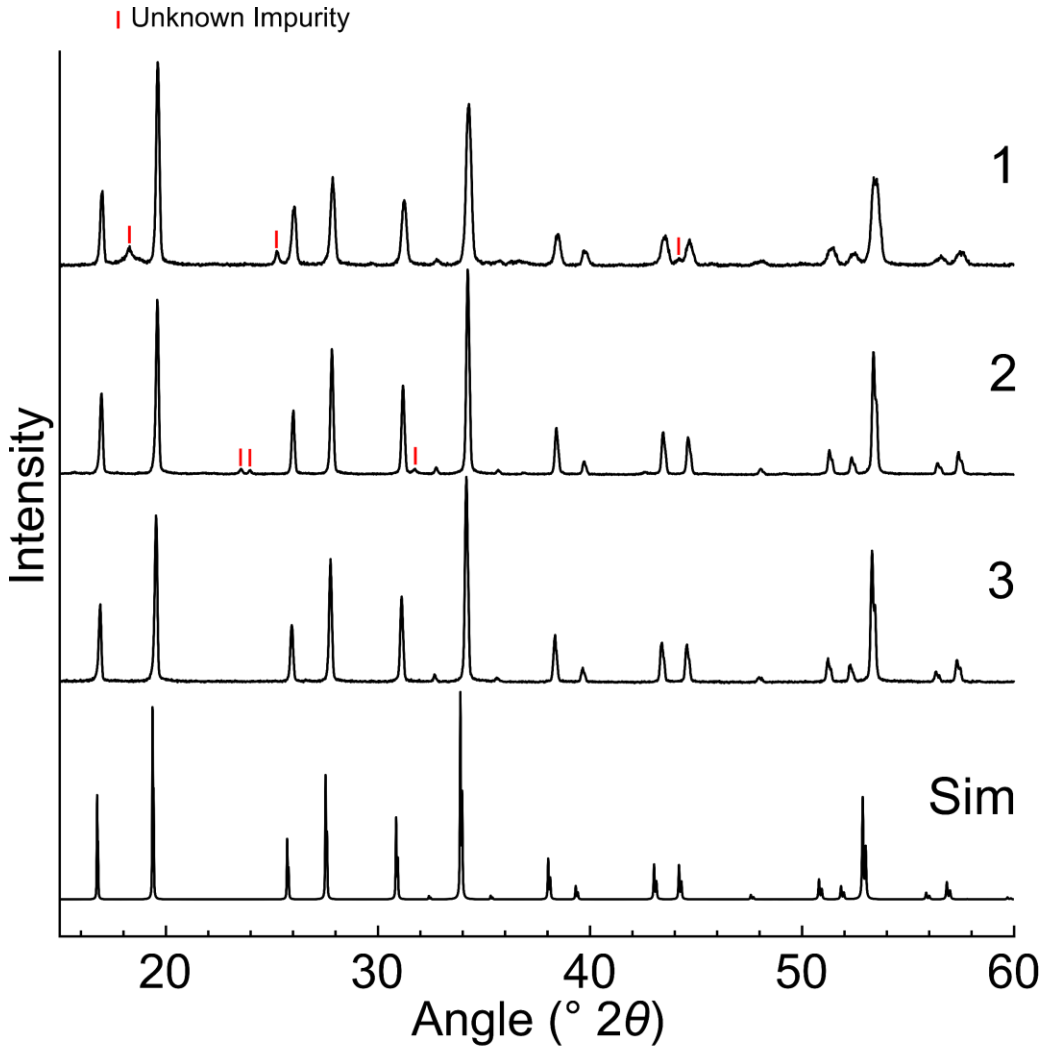

Figure 8.4. XRD patterns of LLSTO samples 1-3 along with a simulated XRD pattern generated using VESTA. Besides minor reflections from an unknown phase, in all three cases a garnet structured phase results. Note that the relative peak intensities of the various Bragg reflections correspond very well to the simulated pattern, indicating that LLSTO was successfully synthesized.

Table 8.4. Circuit fit data for sintered LLSTO pellet used to determine ionic conductivity.

=== Z fit Analysis (02/02/21 10:54) ===	
Equivalent circuit:	
Q1/R1+Q2/R2+Q3	
Q1 = 2.587e30 F.s^(a - 1)	
a1 = 0.591e-9	
R1 = 0.212 5e-3 Ohm	
Q2 = 47.95e-12 F.s^(a - 1)	
a2 = 0.931 4	
R2 = 3 974 Ohm	
Q3 = 1.187e-6 F.s^(a - 1)	
a3 = 0.588 9	
χ^2 / |Z|	0.018

Based on the backscatter electron images in **Figure 8.5a,b**, the pellet is reasonably well sintered but clearly still has a large amount of porosity. The density of the LLSTO pellet as determined from the mass and geometry is ~ 4.77 g cm^{-3}. This implies that further optimization of sintering would be needed to perfectly understand the ionic conductivity of the LLSTO sample. SEM-EDS analysis of the pellet fracture surface (**Figure 8.5c**) shows the expected Ta, Sr, and La signals without obvious other elemental signals, indicating that the sample is relatively pure. Finally, based on EIS analysis (**Figure 8.5d**), the LLSTO pellet is clearly an ion conductor, with bulk Li diffusion occurring in the MHz frequency range as expected[158] for a garnet Li-conductor.

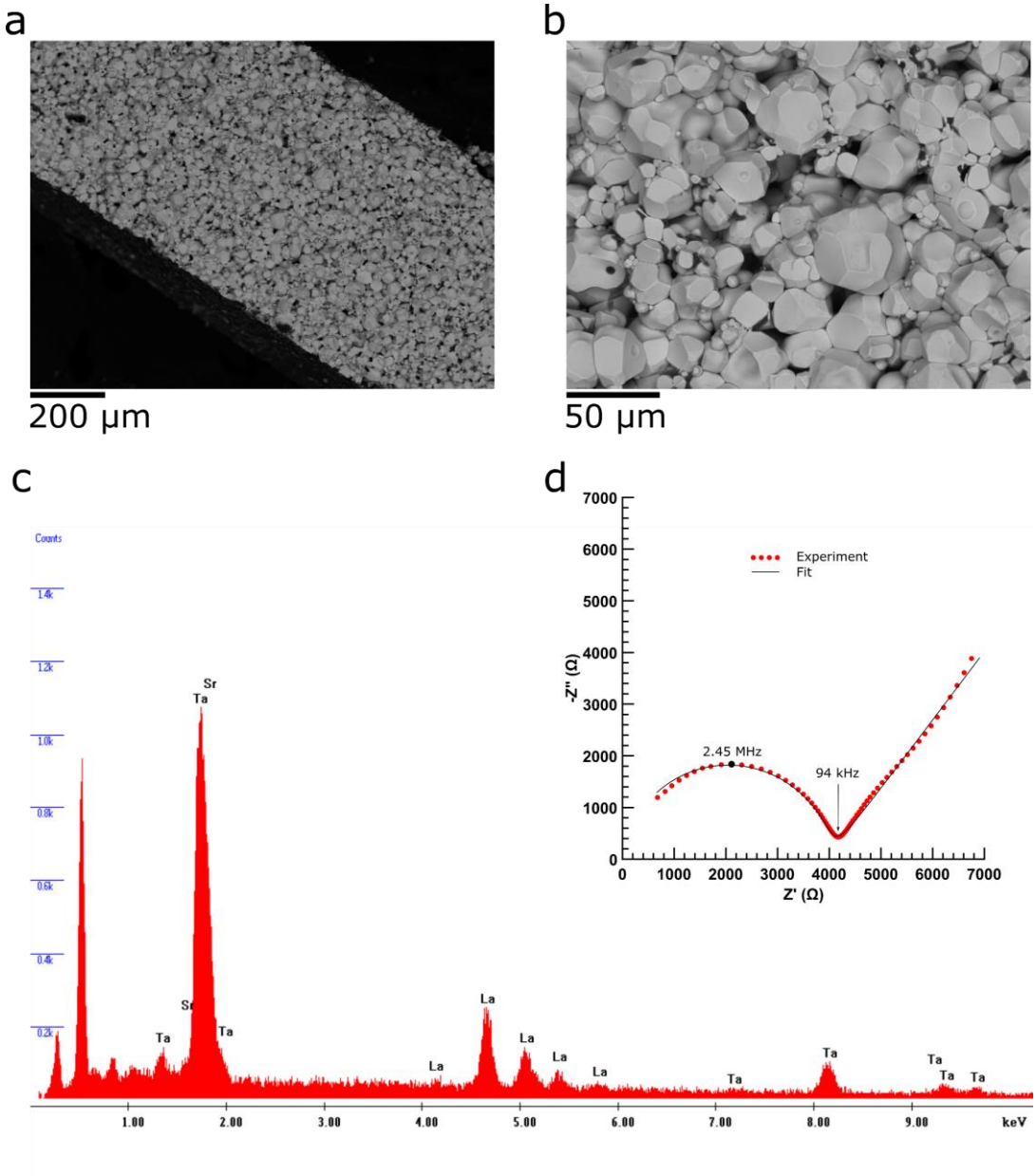

Figure 8.5. **a,b)** backscatter electron (BSE) images of LLSTO pellet fracture surface showing reasonable grain cohesion but also residual porosity, **c)** average EDS spectrum of LLSTO pellet, and **d)** Nyquist plot of EIS spectrum of LLSTO pellet measured with graphite blocking electrodes

The ionic conductivity measured for this sample is somewhat low (~ 5.5 x 10^{-5} S cm^{-1}) at room temperature compared to e.g. LLZTO, but is still reasonably high and

higher than t-LLZO[17] (10^{-6} S cm^{-1}) and other tantalate[1] garnets such as $Li_6La_2BaTa_2O_{12}$ (10^{-6} – 10^{-5} S cm^{-1}). These experiments serve as a proof of concept of the applicability of MSS to a new garnet Li-conducting phase with nominal composition of $Li_{6.5}La_{1.5}Sr_{1.5}Ta_2O_{12}$, which was also synthesized by SSR. It is expected that with proper optimization of sintering that the ionic conductivity could at least be in the range of 10^{-4} S cm^{-1}, potentially comparable to Al-doped LLZO. In fact, some samples of LLZTO from my experiments obtained through non-optimized sintering (i.e. during optimization of sintering conditions) have conductivity values in the range of 10^{-5} to 10^{-4} S cm^{-1}, indicating that the LLSTO composition demonstrated here may be a comparable ionic conductor to zirconate-based Li-garnets.

8.5. Conversion of Doped Pyrochlore Films to Garnet via Interfacial MSS and Vapor Phase Reaction

8.5.1. Introduction and Motivation

Previously, the pyrochlore to garnet synthesis method was explored using doped pyrochlores of nominal composition $La_{2.4}Zr_{1.12}Ta_{0.48}O_{7.04}$ as reagents to form garnet powders via MSS or dense garnet membranes using reactive sintering.[197] In each case, the pyrochlore nanocrystals used readily converted to garnet and retained high ionic conductivity. An exploratory extension of this pyrochlore to garnet method discussed here seeks to use thin films of doped pyrochlore followed by topochemical conversion to garnet as a new route towards thin garnet electrolytes. Various researchers have long sought methods to deposit thin films of LLZO by various methods, including atomic layer deposition (ALD)[114], laser-assisted chemical vapor deposition (LA-CVD)[113], pulsed laser deposition (PLD)[115–117,214], and magnetron[118] sputtering. However, with the recent exception of the work of Buannic et al.,[118] the ionic conductivity of the resultant films is much lower than expected for LLZO. The loss of Li_2O[115–117] under heating to crystallize the as-deposited thin films under dynamic vacuum is a major challenge, and often produces Li-deficient $La_2Zr_2O_7$. The higher ionic conductivity (1.9×10^{-4} S cm^{-1} at room temperature) resultant from the method of Buannic et al., is in large part facilitated by depositing excess Li_2O via a co-sputtering approach. In these thin film based methods, much like in the previously reported pyrochlore to garnet method[197], all necessary reagents are contained in a reasonably dense, uniform phase. This fact inspired the

application of a combination of the knowledge gained through studies on pyrochlore to garnet conversion[197] (outlined in **Chapter 6**), particularly using the high-basic MSS (HB-MSS) mixture, and the versatility of the non-aqueous polymer (NAP) combustion method[146] (outlined in **Chapter 3**). Briefly, doped pyrochlore films can be deposited via spin-coating using a precursor similar to the NAP precursor and converted to garnet using molten salts or even Li_2O vapor, as will be discussed in the following sections.

8.5.2. Experimental Procedure

XRD patterns were acquired with a Panalytical X-Pert or a Panalytical Aeris diffractometer using Cu Kα radiation and SEM images were acquired using a FEI XL30 SEM.

Rather than forming LLZTO, in this case the NAP method was repurposed to form doped pyrochlores of the same composition as the previous pyrochlore to garnet method. Further, the polymer component (polyvinylpyrrolidone) was removed, such that only the mixed metalorganic acetylacetonate-propionate complexes were present upon solvent removal. Otherwise the reagents used ($La(acac)_3$, $Zr(acac)_4$, $Ta(OEt)_5$) (acac = 'acetylacetonate' or '2,4-pentanedionate') and solvents (propionic acid and dichloromethane) and solution preparation method are the same as reported[146] previously, though in one case zirconium n-propoxide was used instead of $Zr(acac)_4$. This precursor solution was then spin-coated (home built spin-coating apparatus, generally 1000-2000 RPM) onto either pieces of Si wafer or thin Al_2O_3 sheets to form uniform films. Si wafers are convenient, nearly perfectly flat substrates and were chosen to explore the geometric

uniformity of resultant thin films, but they are reactive to Li_2O sources. On the other hand, while Al_2O_3 is marginally reactive with Li_2O sources, it is much more stable relative to Si and was thus utilized as a more chemically robust substrate. Finally, a multi-step heat treatment beginning with heating on a hotplate (540 °C set point) and optionally a calcination in a muffle furnace (generally 700-800 °C) was performed to crystallize the film into pyrochlore structured $La_{2.4}Zr_{1.12}Ta_{0.48}O_{7.04}$. Finally, once a pyrochlore film was formed on the desired substrate, one of two pyrochlore to garnet methods were employed. In the first case, various combinations of $LiNO_3$, LiOH, and Li_2O_2 were placed on the film on a hot plate set to 540 °C and allowed to react for the desired time to afford a MSS-based conversion of the pyrochlore film into garnet. In the second case, Li_2O vapors (from heating Li_2O_2 in the crucible environment) were used to convert the pyrochlore film into garnet during heat treatment in an enclosed MgO crucible (750 °C). In one experiment, pyrochlore nanocrystals (synthesized in the same manner as previous[197] work) were converted to garnet powder via the same vapor phase method at 1100 °C for 1 h as a proof of concept.

8.5.3. Results and Conclusions

The NAP-based spin-coating method is quite effective for producing highly uniform thin films. Digital camera images of resultant films on Si (calcined at 540 °C for a few minutes after film deposition) are shown in **Figure 8.6a,b**, with cross-sectional secondary electron and backscatter electron images of a comparable sample in **Figure 8.6c,d**. As can be seen from these SEM images and inferred from the optical inference in

the optical images, these films are of uniform thickness and on the order of ~ 250-300 nm in thickness. This shows that the spin-coating method explored here is generally suitable for making thin, uniform coatings on substrates. Additionally, depending on the calcination temperature, the films convert either to poorly crystalline (540 °C) material with a broad signal in the approximate range of the pyrochlore (222) reflection or nanocrystalline (700 °C) with broad peaks corresponding to the (222) and (400) pyrochlore reflections, as shown in **Figure 8.7**.

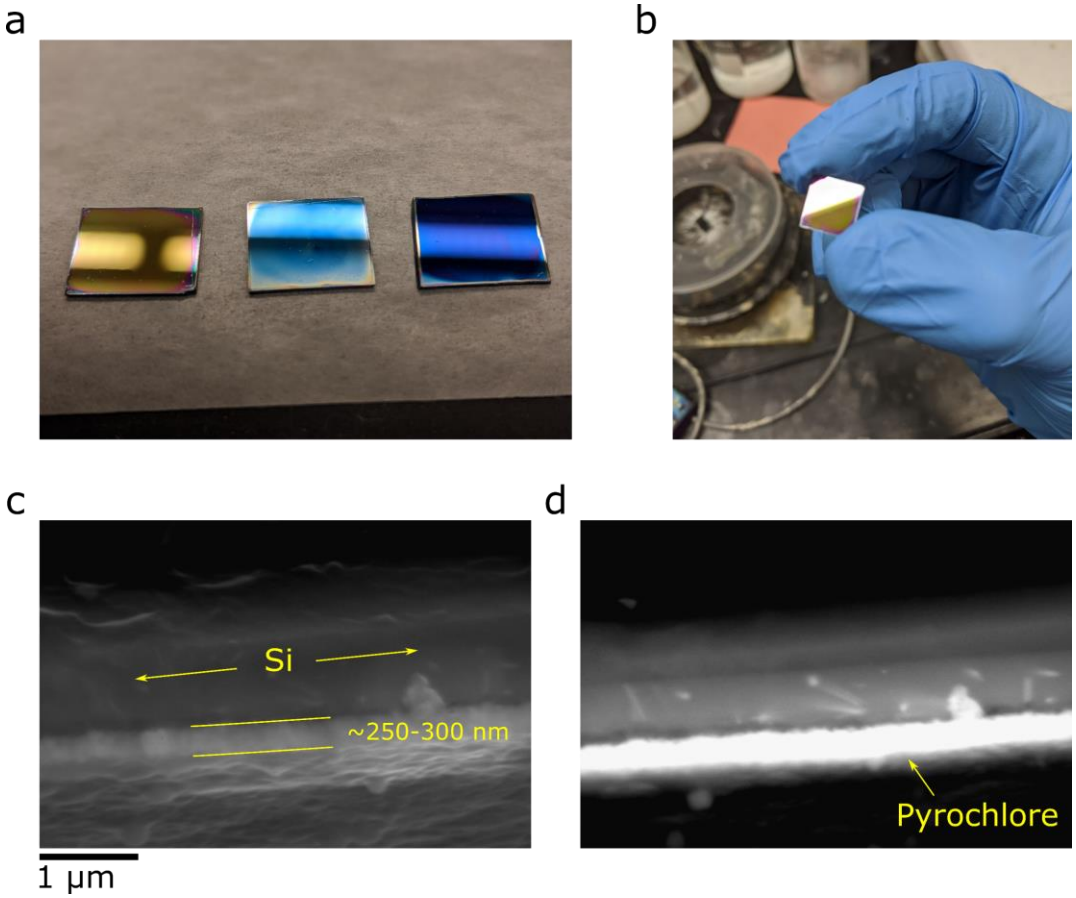

Figure 8.6. Digital camera images of **a)** several spin-coated and calcined (540 °C) films with different numbers of spin-coated layers on Si wafer substrates – the different coloration results from optical interference due to the differing overall thickness, and **b)** one coated substrate, which is seen to be highly reflective, indicating flatness and uniformity of the spin-coated film, cross-sectional **c)** secondary electron and **d)** backscatter electron images of a pyrochlore film deposited on Si and calcined at 750 °C,

showing a thin and uniform layer between 250-300 nm thick for 5 spin-coated layers. This specific sample was also exposed to a mixture of 4:1 (by mass) $LiNO_3$-Li_2O_2 (see also **Figure 8.9**), with the substrate-film interface shown here and the surface shown in **Figure 8.9**.

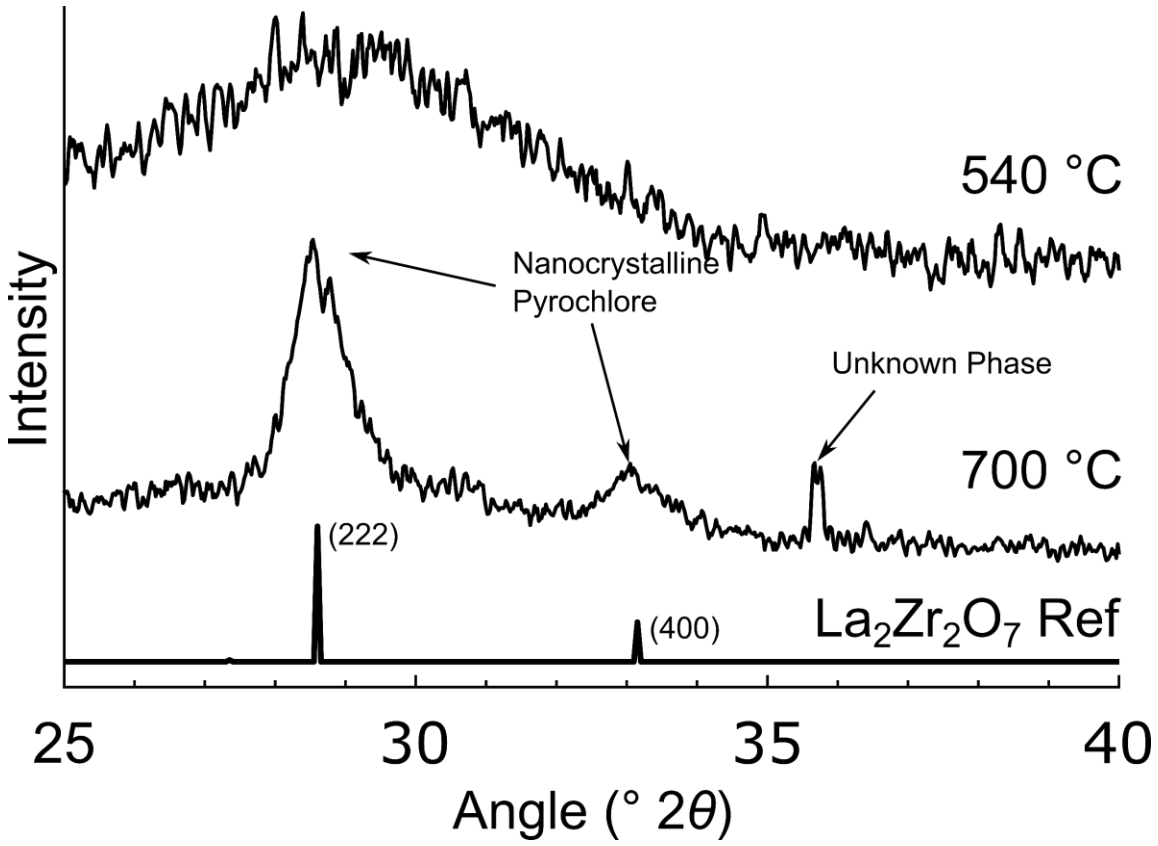

Figure 8.7. XRD patterns of spin-coated pyrochlore films on Si calcined at 540 °C or 700 °C, with reference pattern showing the correspondence to the (222) and (400) pyrochlore (PDF#00-017-0450) reflections.

This uniform, partially crystallized or nanocrystalline pyrochlore film is a useful substrate for subsequent conversion to garnet. Initially, this pyrochlore to garnet conversion was attempted using a highly basic mixture of $LiNO_3$-LiOH-Li_2O_2, much like in previous[197] work using pyrochlore nanocrystals. The results of this experiment are shown in **Figure 8.8**, which presents XRD data of the film on a Si substrate (700 °C calcined pyrochlore film subsequently exposed to molten salts at 540 °C for 12 h).

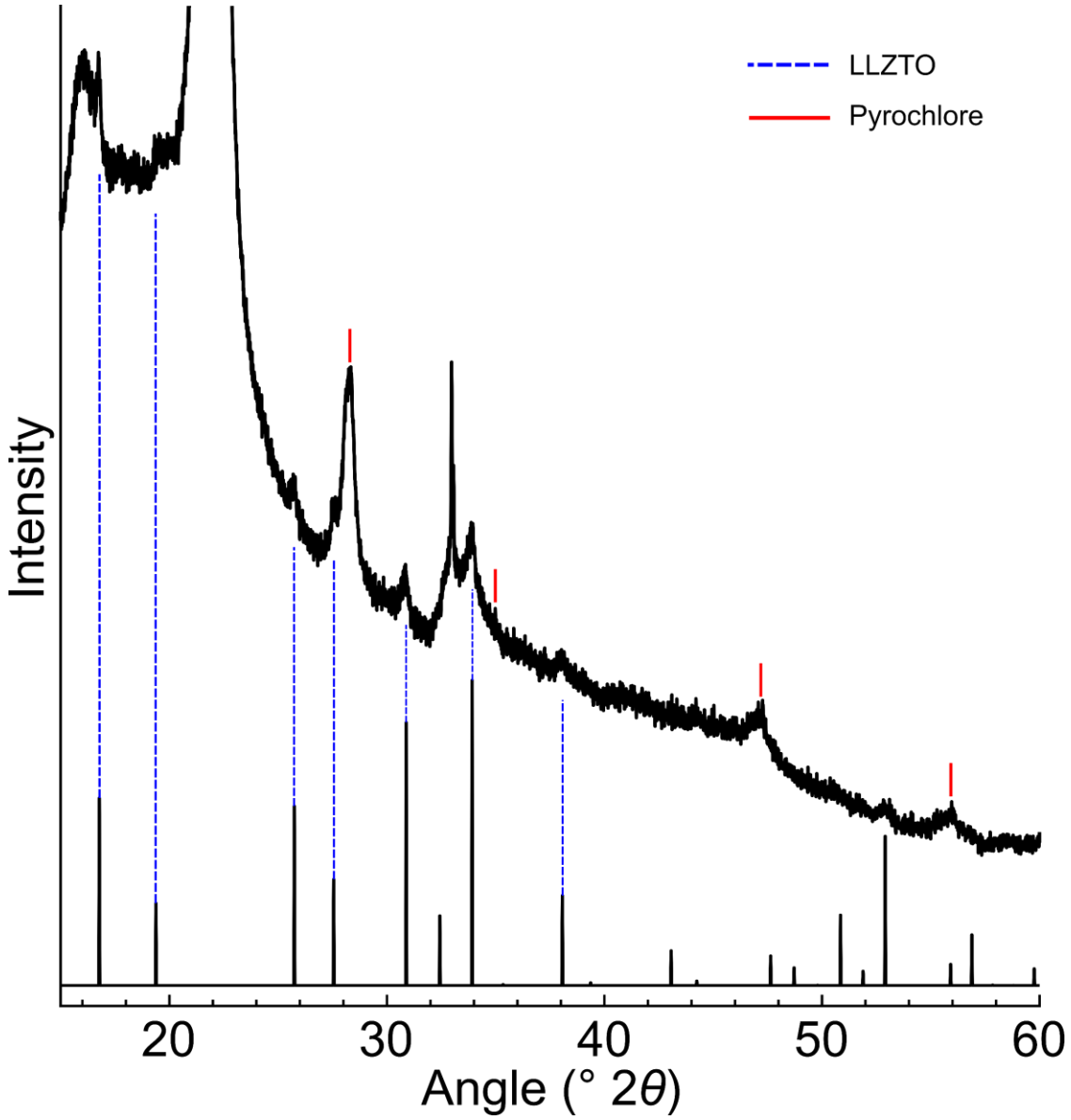

Figure 8.8. XRD pattern of garnet film formed at 540 °C on a hotplate after exposure of a pyrochlore thin film on Si (crystallized at 700 °C) to a highly basic mixture of $LiNO_3$-LiOH-Li_2O_2. Note that only some of the pyrochlore was successfully converted to garnet, but that despite the large signal background from the substrate, Bragg reflections corresponding to garnet can be observed. Reference pattern generated according to Logéat et al.[48]

In addition to the highly basic salt mixture, another similar reaction was performed using just Li_2O_2 and $LiNO_3$ (1:4 mass ratio) placed on the surface in lieu of the ternary salt mixture. Like the ternary salt case, XRD results (**Figure 8.9a**) show that some garnet reflections can be observed in addition to other phases and signal from the substrate.

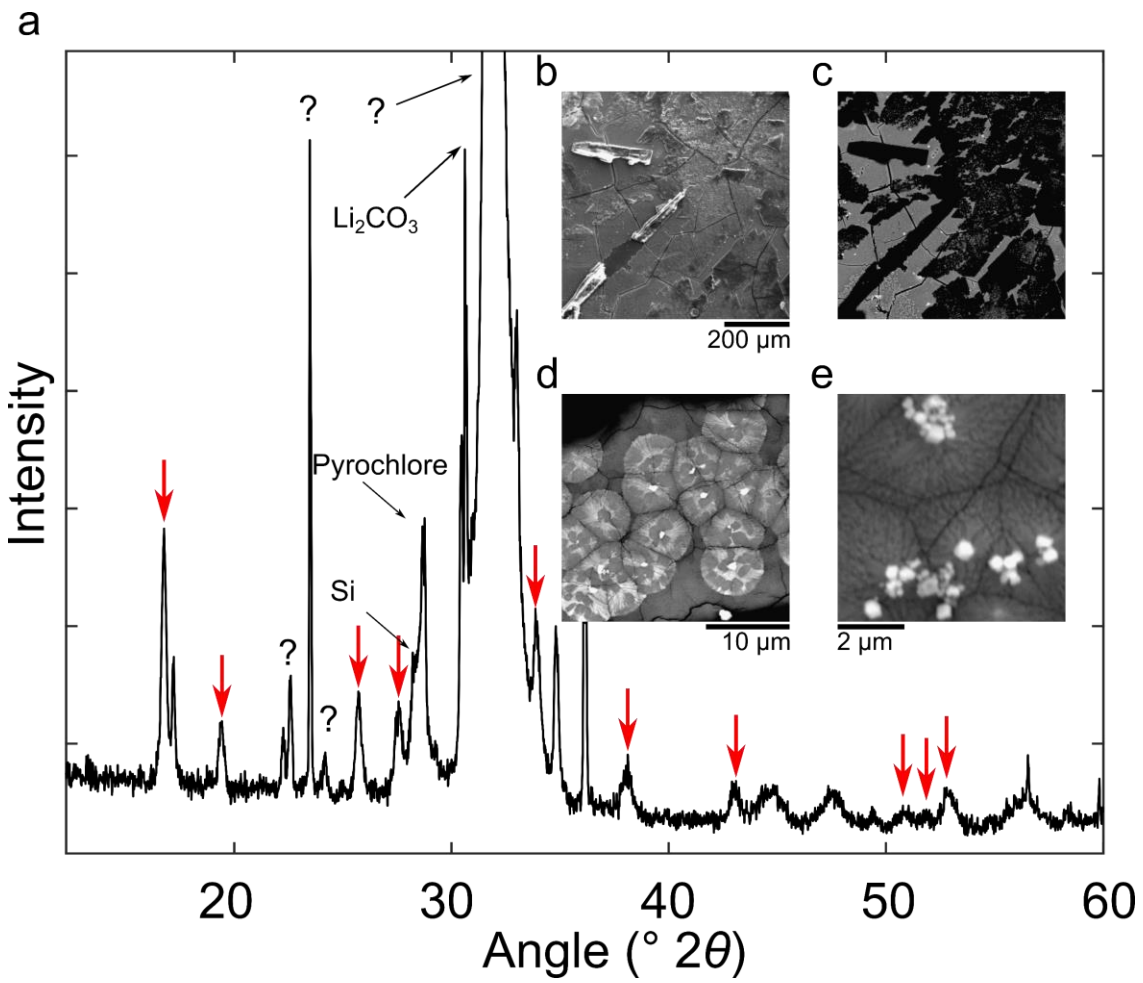

Figure 8.9. **a)** XRD pattern of garnet film formed at 540 °C on a hotplate after exposure of a pyrochlore thin film on Si (crystallized at 700 °C) to a mixture of 4:1 (by mass) $LiNO_3$-Li_2O_2. Bragg reflections corresponding to garnet are indicated with red arrows, and other phases including unknown (possibly $Li_xSi_yO_z$) phases comprising the rest of the signals, **b)** low magnification secondary electron image of the sample from (**a**) showing surface morphology, **c)** BSE image of (**b**) showing substantial contrast differences between the banded features and underlying film, **d)** BSE image of higher Z-contrast feathered structure, and **e)** higher magnification BSE image of (**d**).

The morphology of this sample was also investigated using secondary electron and BSE SEM imaging (**Figure 8.9b-e**). The overall pyrochlore film integrity is reasonably good with some cracks observed on the surface (**Figure 8.9b,c**). However, also observed are large, flat band-like structures with low Z-contrast (**Figure 8.9c**), which are believed to be Li_2CO_3 or another Li-salt due to the dark contrast in the BSE images. Additionally, an unusual morphology of even brighter features on top of the underlying pyrochlore film can be observed (**Figure 8.9d,e**), often comprising a feathered texture sometimes with a discrete particle in the center. Based on the presence of pyrochlore, garnet, and substrate / contaminant signals in the XRD pattern in **Figure 8.9a**, the higher Z-contrast surface features are attributed to garnet, while the more uniform high Z-contrast substrate is believed to be the pyrochlore film. These results indicate that the pyrochlore is reacting to form garnet, but that the morphology changes substantially during this conversion process. These changes are attributed to liquid phase diffusion and dissolution that likely occurs, which facilitates garnet formation but changes the desired film morphology in the process.

Therefore, another strategy was employed inspired by the use of Li_2O_2 to provide Li_2O vapor during sintering. Rather than apply molten salts to the pyrochlore film, Li_2O_2 was placed in the sintering environment to allow a vapor-phase synthesis process. As an initial proof of concept, some pyrochlore nanocrystals (synthesized in the same way as in previous[197] work) were placed on a MgO substrate in an enclosed MgO crucible with excess Li_2O_2 placed to the side in the crucible, followed by heat treatment at 1100 °C for 1 h. This powder was analyzed using XRD and revealed to be nearly phase pure LLZTO with minor residual pyrochlore (**Figure 8.10a**).

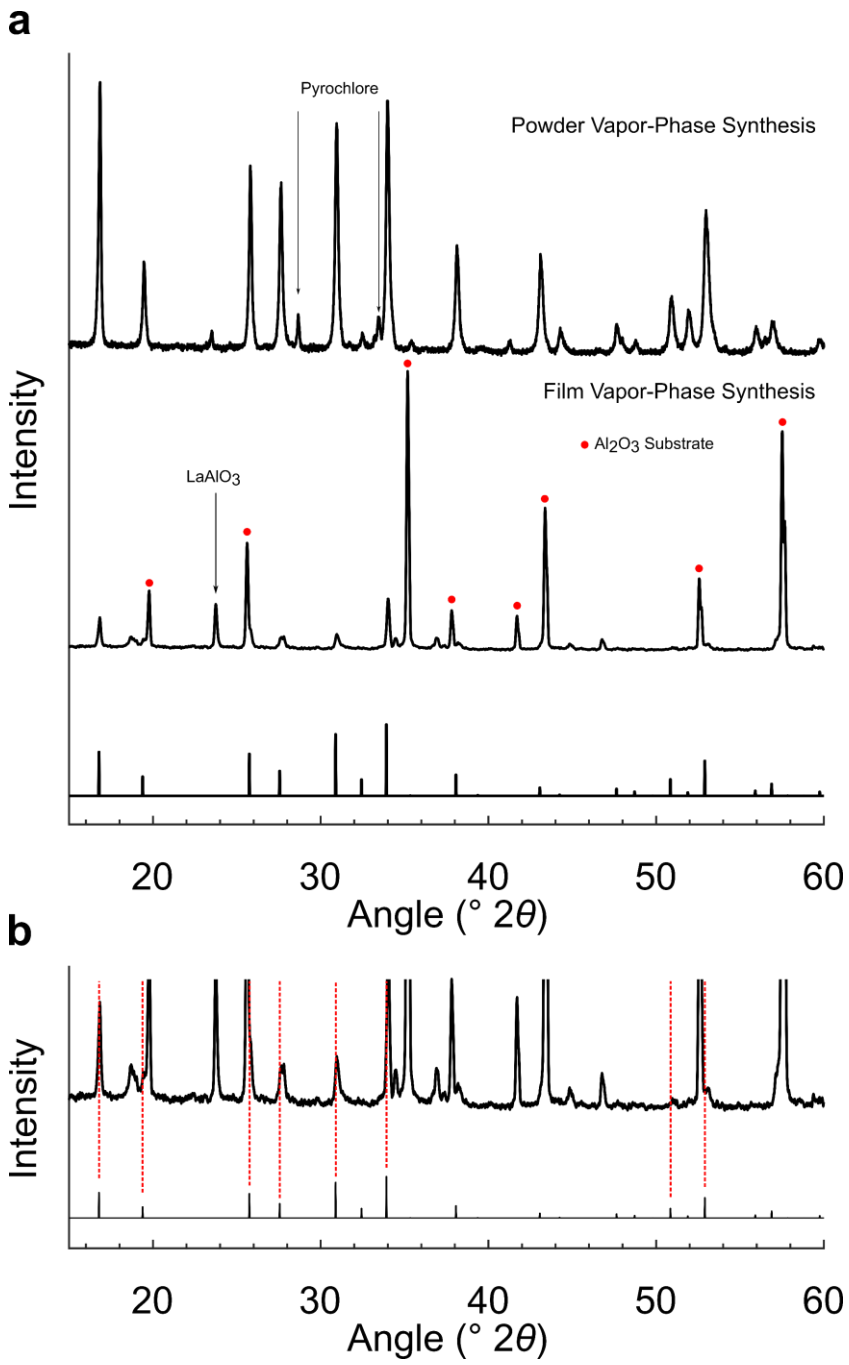

Figure 8.10. **a)** XRD pattern of garnet powder resultant from vapor-phase reaction with Li_2O_2 at 1100 °C for 1 h showing nearly pure LLZTO and of conversion of a pyrochlore thin film on Al_2O_3 to garnet using Li_2O_2 vapor at 750 °C for 4 h, **b)** zoomed XRD of the garnet Bragg reflections with red dotted lines indicating position of garnet reflections. Reference patterns generated based on Logéat et al.[48]

Noting that the appreciable Li_2O vapor pressure at 1100 °C allowed near complete conversion of doped pyrochlores to garnet, a milder heat treatment of 750 °C for 4 h was applied to a pyrochlore thin film on Al_2O_3 (due to its higher chemical stability than Si) using the same approach. In this case (**Figure 8.10a**) some garnet reflections are also apparent in addition to the expected Al_2O_3 Bragg reflections. Due to the much higher signal strength of the Al_2O_3, a zoomed region of the same XRD pattern is shown in **Figure 8.10b**, with the main LLZTO Bragg peaks highlighted using dotted lines to guide the eye. Despite the large difference in overall signal intensity between the Al_2O_3 substrate and the garnet layer, it is clear that no pyrochlore remains (note e.g. the absence of the main pyrochlore (222) peak at ~ 28.6 ° 2θ) and that Bragg reflections from the garnet phase are the other primary set of reflections besides the substrate and $LaAlO_3$.

Finally, the morphology of the pyrochlore-derived garnet powders and films from this vapor phase synthesis approach are shown in **Figure 8.11**. A secondary electron image of the vapor synthesized LLZTO powder (1100 °C 1 h, **Figure 8.10a**) is shown in **Figure 8.11a**, showing particles generally in the 1-10 μm range. The large particle size despite beginning with pyrochlore nanocrystals as reagents is easily explained by the high synthesis temperature. While as of yet not performed, it is expected that a lower reaction temperature could yield smaller garnet particles. The morphology of the vapor phase converted film on Al_2O_3 is shown in **Figure 8.11b-e**.

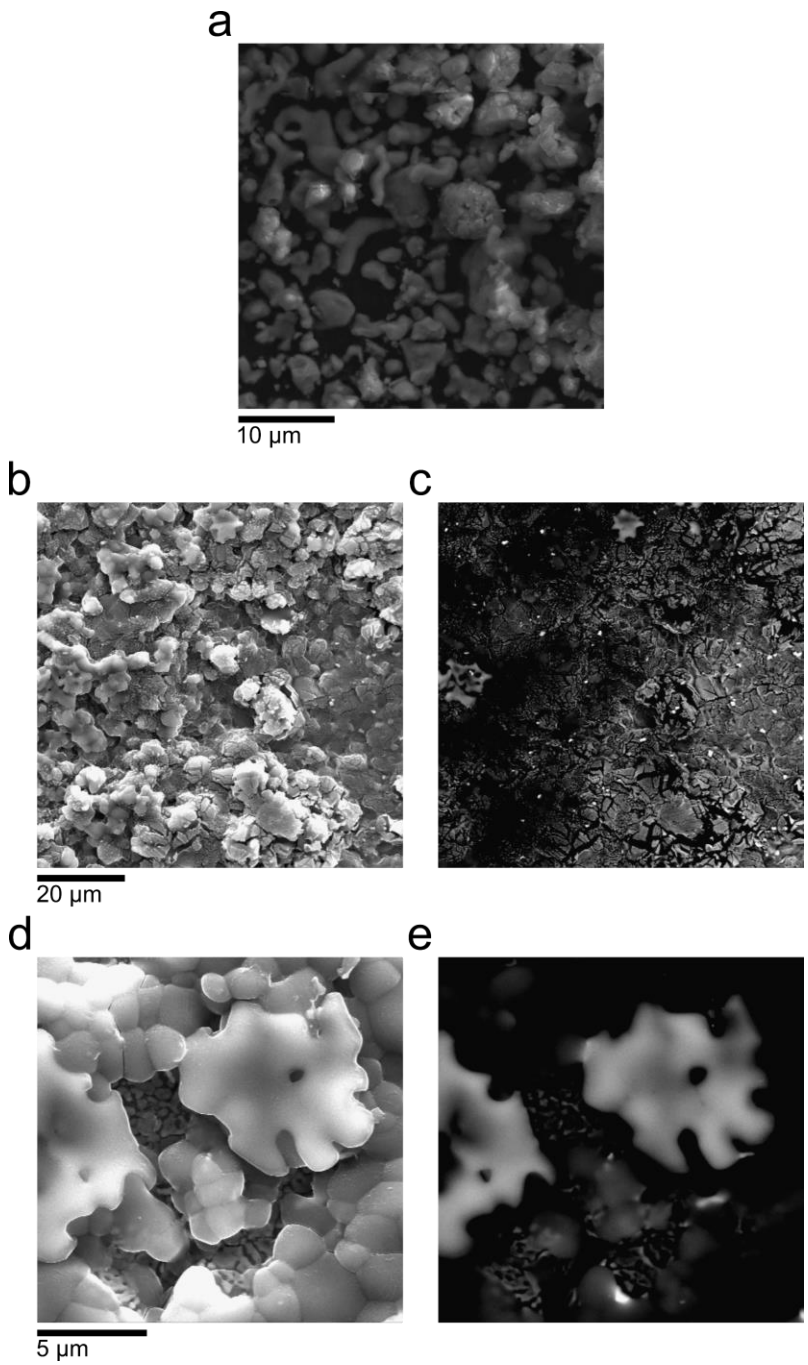

Figure 8.11. **a)** secondary electron image of LLZTO powders derived from vapor phase reaction between doped pyrochlore nanocrystals and Li_2O_2 at 1100 °C for 1 h, low magnification **b)** secondary electron and **c)** BSE SEM images of the garnet film on Al_2O_3, and higher magnification **d)** secondary electron and **e)** BSE SEM images of the same region as (**b,c**), showing morphology of interconnected garnet flake-like features.

In the case of a garnet layer on Al_2O_3, the morphology is primarily composed of 'islands' or 'flakes' of what appear to be interconnected garnet particles on the substrate. The darker regions on **Figure 8.11b,c** are most likely Li-containing surface species such as those observed on the sample coated on Si in **Figure 8.9**. The coverage of the garnet layer is somewhat better than that of the MSS-derived layer on Si, most likely due to the vapor phase vs. liquid phase process used to form the garnet. The contrast in the BSE image in **Figure 8.11e** is somewhat difficult to interpret due to the tiered nature of the layer, which may in turn be due to the natural roughness of the Al_2O_3 substrate itself, but the morphology of the top interconnected particle in **Figure 8.11d** is nearly identical to the lower contrast regions in **Figure 8.11e**, indicating that they are likely the same substance with the image contrast modified by the geometry of signal collection rather than composition. With a smoother Al_2O_3 substrate and tighter control of synthesis temperature and Li_2O partial pressure, these results indicate that more uniform layers of garnet may be accessible using this vapor phase approach.

In conclusion, the pyrochlore to garnet synthesis method was further extended to form garnet films via a topochemical conversion mechanism using either basic molten Li-salts or Li_2O vapor. In both cases, garnet is shown to form although the initial film morphology is better preserved in the vapor phase reaction. These results indicate that further improvements may enable thin (few 100's of nm) garnet layers to be applied to various substrates without requiring vacuum deposition.

8.6. Concluding Remarks

Each of the investigations described in this chapter are the result of experiments that either ultimately led to more promising research pathways, were superseded by more promising research pathways, or were unable to be explored to the extent of publication in the literature due to time or facility access constraints. That said, the curious reader is encouraged to use these experiments and results as a basis for future investigation into Li-garnets or any other pertinent topic. The goal of this chapter is to preserve these results for the record and potential benefit of others in the field.

9. SUMMARY

Lithium lanthanum zirconate (LLZO) garnets are one of the most promising future solid electrolytes for advanced lithium batteries. Despite great interest in this class of materials, there are myriad challenges remaining to enable its practical use. In addition to greater understanding of its fundamental properties, advances in synthesis and processing of LLZO are crucial to reliably obtain LLZO electrolyte membranes with the properties required to produce high performance solid-state Li-batteries and unlock higher energy density. Advanced synthesis methods such as combustion and molten salt synthesis have been employed in this work with this goal in mind.

One major focus herein is on novel synthesis methods to produce Li-garnet powders with inherently small particle size, with the goal of improving the processability of dense garnet electrolytes, specifically by improving sinterability due to small particle size and potentially making preparation of stable slurries for e.g. tape-casting easier also due to smaller particle size. The non-aqueous polymer combustion as well as all molten salt synthesis methods described in this work are able to achieve LLZO powders with small particle size. Another major focus of this work is on reducing the energy cost of synthesis of Li-garnets by these novel synthesis techniques, most successfully demonstrated by using Lux-Flood basic molten salt synthesis, in one case using quasi-single-source precursors, where Li-garnet powders can be obtained at a temperature as low as 400 °C, much lower than has been reported to-date. This so-called pyrochlore to garnet molten salt synthesis is able to produce Ta-doped LLZO with both small particle size and at a very low temperature and may be beneficial for processing of Li-garnets. Moreover, the reactive sintering approach demonstrated using doped pyrochlores with a

lithium source is able to produce highly dense garnet electrolytes with high ionic conductivity, which may unlock a new route towards processing of LLZO in short times and without concern for air or water reactivity / degradation of the garnet powder during processing. An initial investigation of other processing schemes to convert doped pyrochlore powders and thin films into LLZO shows promise as well.

Finally, the unique nature of various synthesis routes was investigated, motivated initially by the discovery of elemental inhomogeneity in samples of Ta-doped LLZO powders. By both structural and elemental characterization of garnet powders and the resulting sintered garnet electrolytes, it was demonstrated that elemental inhomogeneity in the $Li_{7-x}La_3Zr_{2-x}Ta_xO_{12}$ ($0.2 < x < 1$) solid-solution occurs apparently irrespective of the synthesis method used, including solid-state reaction, non-aqueous polymer combustion synthesis, and molten salt synthesis, and that high temperature sintering is not always capable of eliminating composition variations. A new variable that appears to negatively affect ionic conductivity, elemental inhomogeneity, is proposed to explain the differences in ionic conductivity, in addition to well-known variables such as relative density and Li_2O-content (or Li_2O-loss from sintering). However, by employing higher synthesis temperatures or producing small, non-agglomerated garnet powders, elemental inhomogeneity can be eliminated during sintering, implying that the various novel syntheses explored herein are all able to produce garnet electrolytes with high ionic conductivity.

REFERENCES

(1) Thangadurai, V.; Narayanan, S.; Pinzaru, D. Garnet-Type Solid-State Fast Li Ion Conductors for Li Batteries: Critical Review. *Chem. Soc. Rev.* **2014**, *43* (13), 4714–4727.

(2) Xu, W.; Wang, J.; Ding, F.; Chen, X.; Nasybulin, E.; Zhang, Y.; Zhang, J.-G. Lithium Metal Anodes for Rechargeable Batteries. *Energy Environ. Sci.* **2014**, *7* (2), 513–537. https://doi.org/10.1039/C3EE40795K.

(3) Balakrishnan, P. G.; Ramesh, R.; Prem Kumar, T. Safety Mechanisms in Lithium-Ion Batteries. *J. Power Sources* **2006**, *155* (2), 401–414. https://doi.org/10.1016/j.jpowsour.2005.12.002.

(4) Ramakumar, S.; Deviannapoorani, C.; Dhivya, L.; Shankar, L. S.; Murugan, R. Lithium Garnets: Synthesis, Structure, Li^+ Conductivity, Li^+ Dynamics and Applications. *Prog. Mater. Sci.* **2017**, *88*, 325–411. https://doi.org/10.1016/j.pmatsci.2017.04.007.

(5) Knauth, P. Inorganic Solid Li Ion Conductors: An Overview. *Solid State Ionics* **2009**, *180* (14–16), 911–916. https://doi.org/10.1016/j.ssi.2009.03.022.

(6) Murugan, R.; Thangadurai, V.; Weppner, W. Fast Lithium Ion Conduction in Garnet-Type $Li_7La_3Zr_2O_{12}$. *Angew. Chemie - Int. Ed.* **2007**, *46* (41), 7778–7781. https://doi.org/10.1002/anie.200701144.

(7) Albertus, P.; Babinec, S.; Litzelman, S.; Newman, A. Status and Challenges in Enabling the Lithium Metal Electrode for High-Energy and Low-Cost Rechargeable Batteries. *Nat. Energy* **2018**, *3* (1), 16–21. https://doi.org/10.1038/s41560-017-0047-2.

(8) Hitz, G. T.; Mcowen, D. W.; Zhang, L.; Ma, Z.; Fu, Z.; Wen, Y.; Gong, Y.; Dai, J.; Hamann, T. R.; Hu, L.; Wachsman, E. D. High-Rate Lithium Cycling in a Scalable Trilayer Li-Garnet-Electrolyte Architecture. *Mater. Today* **2019**, *22* (2), 50–57. https://doi.org/10.1016/j.mattod.2018.04.004.

(9) Fu, K. (Kelvin); Gong, Y.; Hitz, G. T.; McOwen, D. W.; Li, Y.; Xu, S.; Wen, Y.; Zhang, L.; Wang, C.; Pastel, G.; Dai, J.; Liu, B.; Xie, H.; Yao, Y.; Wachsman, E. D.; Hu, L. Three-Dimensional Bilayer Garnet Solid Electrolyte Based High Energy Density Lithium Metal–Sulfur Batteries. *Energy Environ. Sci.* **2017**, *10* (7), 1568–1575. https://doi.org/10.1039/C7EE01004D.

(10) Bachman, J. C.; Muy, S.; Grimaud, A.; Chang, H. H.; Pour, N.; Lux, S. F.; Paschos, O.; Maglia, F.; Lupart, S.; Lamp, P.; Giordano, L.; Shao-Horn, Y. Inorganic Solid-State Electrolytes for Lithium Batteries: Mechanisms and Properties Governing Ion Conduction. *Chem. Rev.* **2016**, *116* (1), 140–162. https://doi.org/10.1021/acs.chemrev.5b00563.

(11) Kerman, K.; Luntz, A.; Viswanathan, V.; Chiang, Y.-M.; Chen, Z. Review—Practical Challenges Hindering the Development of Solid State Li Ion Batteries. *J. Electrochem. Soc.* **2017**, *164* (7), A1731–A1744. https://doi.org/10.1149/2.1571707jes.

(12) Ohta, S.; Kobayashi, T.; Asaoka, T. High Lithium Ionic Conductivity in the Garnet-Type Oxide $Li_{7-X}La_3(Zr_{2-X}, Nb_X)O_{12}$ (X = 0-2). *J. Power Sources* **2011**, *196* (6), 3342–3345. https://doi.org/10.1016/j.jpowsour.2010.11.089.

(13) Wolfenstine, J.; Ratchford, J.; Rangasamy, E.; Sakamoto, J.; Allen, J. L. Synthesis and High Li-Ion Conductivity of Ga-Stabilized Cubic $Li_7La_3Zr_2O_{12}$. *Mater. Chem. Phys.* **2012**, *134* (2–3), 571–575. https://doi.org/10.1016/j.matchemphys.2012.03.054.

(14) Buschmann, H.; Dolle, J.; Berendts, S.; Kuhn, A.; Bottke, P.; Wilkening, M.; Heitjans, P.; Senyshyn, A.; Ehrenberg, H.; Lotnyk, A.; Duppel, V.; Kienle, L.; Janek, J. Structure and Dynamics of the Fast Lithium Ion Conductor "$Li_7La_3Zr_2O_{12}$." *Phys. Chem. Chem. Phys.* **2011**, *13*, 19378–19392. https://doi.org/10.1039/c1cp22108f.

(15) Wu, J.-F.; Chen, E.-Y.; Yu, Y.; Liu, L.; Wu, Y.; Pang, W. K.; Peterson, V. K.; Guo, X. Gallium-Doped $Li_7La_3Zr_2O_{12}$ Garnet-Type Electrolytes with High Lithium-Ion Conductivity. *ACS Appl. Mater. Interfaces* **2017**, *9* (2), 1542–1552. https://doi.org/10.1021/acsami.6b13902.

(16) Geiger, C. A.; Alekseev, E.; Lazic, B.; Fisch, M.; Armbruster, T.; Langner, R.; Fechtelkord, M.; Kim, N.; Pettke, T.; Weppner, W. Crystal Chemistry and Stability of "$Li_7La_3Zr_2O_{12}$" Garnet: A Fast Lithium-Ion Conductor. *Inorg. Chem.* **2011**, *50* (3), 1089–1097. https://doi.org/10.1021/ic101914e.

(17) Awaka, J.; Kijima, N.; Hayakawa, H.; Akimoto, J. Synthesis and Structure Analysis of Tetragonal $Li_7La_3Zr_2O_{12}$ with the Garnet-Related Type Structure. *J. Solid State Chem.* **2009**, *182* (8), 2046–2052. https://doi.org/10.1016/j.jssc.2009.05.020.

(18) Momma, K.; Izumi, F. VESTA 3 for Three-Dimensional Visualization of Crystal, Volumetric and Morphology Data. *J. Appl. Crystallogr.* **2011**. https://doi.org/10.1107/S0021889811038970.

(19) Rangasamy, E.; Wolfenstine, J.; Sakamoto, J. The Role of Al and Li Concentration on the Formation of Cubic Garnet Solid Electrolyte of Nominal Composition $Li_7La_3Zr_2O_{12}$. *Solid State Ionics* **2012**, *206*, 28–32. https://doi.org/10.1016/j.ssi.2011.10.022.

(20) Matsuda, Y.; Sakamoto, K.; Matsui, M.; Yamamoto, O.; Takeda, Y.; Imanishi, N. Phase Formation of a Garnet-Type Lithium-Ion Conductor $Li_{7-3x}Al_xLa_3Zr_2O_{12}$. *Solid State Ionics* **2015**, *277*, 23–29. https://doi.org/10.1016/j.ssi.2015.04.011.

(21) El Shinawi, H.; Janek, J. Stabilization of Cubic Lithium-Stuffed Garnets of the Type "$Li_7La_3Zr_2O_{12}$" by Addition of Gallium. *J. Power Sources* **2013**, *225*, 13–19. https://doi.org/10.1016/j.jpowsour.2012.09.111.

(22) Afyon, S.; Krumeich, F.; Rupp, J. L. M. A Shortcut to Garnet-Type Fast Li-Ion Conductors for All-Solid State Batteries. *J. Mater. Chem. A* **2015**, *3* (36), 18636–18648. https://doi.org/10.1039/C5TA03239C.

(23) Yi, E.; Wang, W.; Kieffer, J.; Laine, R. M. Key Parameters Governing the Densification of Cubic-$Li_7La_3Zr_2O_{12}$ Li^+ Conductors. *J. Power Sources* **2017**, *352*, 156–164. https://doi.org/10.1016/j.jpowsour.2017.03.126.

(24) Qin, S.; Zhu, X.; Jiang, Y.; Ling, M.; Hu, Z.; Zhu, J. Growth of Self-Textured Ga^{3+} -Substituted $Li_7La_3Zr_2O_{12}$ Ceramics by Solid State Reaction and Their Significant Enhancement in Ionic Conductivity. *Appl. Phys. Lett.* **2018**, *112* (11), 113901. https://doi.org/10.1063/1.5019179.

(25) Huang, M.; Shoji, M.; Shen, Y.; Nan, C. W.; Munakata, H.; Kanamura, K. Preparation and Electrochemical Properties of Zr-Site Substituted $Li_7La_3(Zr_{2-X}M_x)O_{12}$ (M = Ta, Nb) Solid Electrolytes. *J. Power Sources* **2014**, *261*, 206–211. https://doi.org/10.1016/j.jpowsour.2014.03.070.

(26) Kim, Y.; Yoo, A.; Schmidt, R.; Sharafi, A.; Lee, H.; Wolfenstine, J.; Sakamoto, J. Electrochemical Stability of $Li_{6.5}La_3Zr_{1.5}M_{0.5}O_{12}$ (M = Nb or Ta) against Metallic Lithium. *Front. Energy Res.* **2016**, *4*, 1–7. https://doi.org/10.3389/fenrg.2016.00020.

(27) Allen, J. L.; Wolfenstine, J.; Rangasamy, E.; Sakamoto, J. Effect of Substitution (Ta, Al, Ga) on the Conductivity of $Li_7La_3Zr_2O_{12}$. *J. Power Sources* **2012**, *206*, 315–319. https://doi.org/10.1016/j.jpowsour.2012.01.131.

(28) Tsai, C.-L. L.; Roddatis, V.; Chandran, C. V.; Ma, Q.; Uhlenbruck, S.; Bram, M.; Heitjans, P.; Guillon, O.; Tsai, C.-L. L.; Roddatis, V.; Heitjans, P.; Bram, M.; Uhlenbruck, S.; Guillon, O.; Ma, Q. $Li_7La_3Zr_2O_{12}$ Interface Modification for Li Dendrite Prevention. *ACS Appl. Mater. Interfaces* **2016**, *8* (16), 10617–10626. https://doi.org/10.1021/acsami.6b00831.

(29) Hamao, N.; Kataoka, K.; Kijima, N.; Akimoto, J. Synthesis, Crystal Structure and Conductive Properties of Garnet-Type Lithium Ion Conductor Al-Free $Li_{7-X}La_3Zr_{2-X}Ta_xO_{12}$ ($0 < x < 0.6$). *J. Ceram. Soc. Japan* **2016**, *124* (6), 678–683. https://doi.org/10.2109/jcersj2.124.P6-1.

(30) Yamada, H.; Ito, T.; Hongahally Basappa, R. Sintering Mechanisms of High-Performance Garnet-Type Solid Electrolyte Densified by Spark Plasma Sintering. *Electrochim. Acta* **2016**, *222*, 648–656. https://doi.org/10.1016/j.electacta.2016.11.020.

(31) Chen, X.; Cao, T.; Xue, M.; Lv, H.; Li, B.; Zhang, C. Improved Room

Temperature Ionic Conductivity of Ta and Ca Doped $Li_7La_3Zr_2O_{12}$ via a Modified Solution Method. *Solid State Ionics* **2018**, *314*, 92–97. https://doi.org/10.1016/j.ssi.2017.11.027.

(32) Ishiguro, K.; Nemori, H.; Sunahiro, S.; Nakata, Y.; Sudo, R.; Matsui, M.; Takeda, Y.; Yamamoto, O.; Imanishi, N. Ta-Doped $Li_7La_3Zr_2O_{12}$ for Water-Stable Lithium Electrode of Lithium-Air Batteries. *J. Electrochem. Soc.* **2014**, *161* (5), A668–A674. https://doi.org/10.1149/2.013405jes.

(33) Yi, M.; Liu, T.; Wang, X.; Li, J.; Wang, C.; Mo, Y. High Densification and Li-Ion Conductivity of Al-Free $Li_{7-x}La_3Zr_{2-x}Ta_xO_{12}$ Garnet Solid Electrolyte Prepared by Using Ultrafine Powders. *Ceram. Int.* **2019**, *45* (1), 786–792. https://doi.org/10.1016/j.ceramint.2018.09.245.

(34) Wang, Y.; Lai, W. High Ionic Conductivity Lithium Garnet Oxides of $Li_{7-x}La_3Zr_{2-x}Ta_xO_{12}$ Compositions. *Electrochem. Solid-State Lett.* **2012**, *15* (5), A68. https://doi.org/10.1149/2.024205esl.

(35) El-Shinawi, H.; Cussen, E. J.; Corr, S. A. Enhancement of the Lithium Ion Conductivity of Ta-Doped $Li_7La_3Zr_2O_{12}$ by Incorporation of Calcium. *Dalt. Trans.* **2017**, *1*, 9415–9419. https://doi.org/10.1039/C7DT01573A.

(36) Thompson, T.; Wolfenstine, J.; Allen, J. L.; Johannes, M.; Huq, A.; David, I. N.; Sakamoto, J. Tetragonal vs. Cubic Phase Stability in Al - Free Ta Doped $Li_7La_3Zr_2O_{12}$ (LLZO). *J. Mater. Chem. A* **2014**, *2* (33), 13431–13436. https://doi.org/10.1039/c4ta02099e.

(37) Thompson, T.; Sharafi, A.; Johannes, M. D.; Huq, A.; Allen, J. L.; Wolfenstine, J.; Sakamoto, J. A Tale of Two Sites: On Defining the Carrier Concentration in Garnet-Based Ionic Conductors for Advanced Li Batteries. *Adv. Energy Mater.* **2015**, *5* (11), 1–9. https://doi.org/10.1002/aenm.201500096.

(38) Li, Y.; Han, J. T.; Wang, C. A.; Xie, H.; Goodenough, J. B. Optimizing Li^+ Conductivity in a Garnet Framework. *J. Mater. Chem.* **2012**, *22* (30), 15357–15361. https://doi.org/10.1039/c2jm31413d.

(39) Huang, X.; Lu, Y.; Song, Z.; Rui, K.; Wang, Q.; Xiu, T.; Badding, M. E.; Wen, Z. Manipulating Li_2O Atmosphere for Sintering Dense $Li_7La_3Zr_2O_{12}$ Solid Electrolyte. *Energy Storage Mater.* **2019**, *22*, 207–217. https://doi.org/10.1016/j.ensm.2019.01.018.

(40) Huang, X.; Lu, Y.; Jin, J.; Gu, S.; Xiu, T.; Song, Z.; Badding, M. E.; Wen, Z. Method Using Water-Based Solvent to Prepare $Li_7La_3Zr_2O_{12}$ Solid Electrolytes. *ACS Appl. Mater. Interfaces* **2018**, *10* (20), 17147–17155. https://doi.org/10.1021/acsami.8b01961.

(41) Huang, X.; Xiu, T.; Badding, M. E.; Wen, Z. Two-Step Sintering Strategy to Prepare Dense Li-Garnet Electrolyte Ceramics with High Li^+ conductivity. *Ceram.*

Int. **2018**, *44* (5), 5660–5667. https://doi.org/10.1016/j.ceramint.2017.12.217.

(42) Tong, X.; Thangadurai, V.; Wachsman, E. D. Highly Conductive Li Garnets by a Multielement Doping Strategy. *Inorg. Chem.* **2015**, *54* (7), 3600–3607. https://doi.org/10.1021/acs.inorgchem.5b00184.

(43) Janani, N.; Ramakumar, S.; Kannan, S.; Murugan, R. Optimization of Lithium Content and Sintering Aid for Maximized Li^+ Conductivity and Density in Ta-Doped $Li_7La_3Zr_2O_{12}$. *J. Am. Ceram. Soc.* **2015**, *98* (7), 2039–2046. https://doi.org/10.1111/jace.13578.

(44) Inada, R.; Yasuda, S.; Tojo, M.; Tsuritani, K.; Tojo, T.; Sakurai, Y. Development of Lithium-Stuffed Garnet-Type Oxide Solid Electrolytes with High Ionic Conductivity for Application to All-Solid-State Batteries. *Front. Energy Res.* **2016**, *4* (28), 1–12. https://doi.org/10.3389/fenrg.2016.00028.

(45) Cai, LIU; Zhao-Yin, WEN; Kun, R. High Ion Conductivity in Garnet-Type F-Doped $Li_7La_3Zr_2O_{12}$. *J. Inorg. Mater.* **2015**, *30* (9), 995–1000. https://doi.org/10.15541/jim20150163.

(46) Sun, C.; Meng, X.; Fernández-Díaz, M. T.; Alonso, J. A.; Lu, Y. Effects of Fluorine Doping on Structural and Electrochemical Properties of $Li_{6.25}Ga_{0.25}La_3Zr_2O_{12}$ as Electrolytes for Solid-State Lithium Batteries . *ACS Appl. Mater. Interfaces* **2018**, *11* (2), 2042–2049. https://doi.org/10.1021/acsami.8b17656.

(47) Yeandel, S. R.; Chapman, B. J.; Slater, P. R.; Goddard, P. Structure and Lithium-Ion Dynamics in Fluoride-Doped Cubic $Li_7La_3Zr_2O_{12}$ (LLZO) Garnet for Li Solid-State Battery Applications. *J. Phys. Chem. C* **2018**, *122*, 27811–27819. https://doi.org/10.1021/acs.jpcc.8b07704.

(48) Logéat, A.; Köhler, T.; Eisele, U.; Stiaszny, B.; Harzer, A.; Tovar, M.; Senyshyn, A.; Ehrenberg, H.; Kozinsky, B. From Order to Disorder: The Structure of Lithium-Conducting Garnets $Li_{7-x}La_3Ta_xZr_{2-x}O_{12}$ (X=0–2). *Solid State Ionics* **2012**, *206*, 33–38. https://doi.org/10.1016/j.ssi.2011.10.023.

(49) He, X.; Zhu, Y.; Mo, Y. Origin of Fast Ion Diffusion in Super-Ionic Conductors. *Nat. Commun.* **2017**, *8* (May), 1–7. https://doi.org/10.1038/ncomms15893.

(50) Kataoka, K.; Akimoto, J. High Ionic Conductor Member of Garnet-Type Oxide $Li_{6.5}La_3Zr_{1.5}Ta_{0.5}O_{12}$. *ChemElectroChem* **2018**, *5* (18), 2551–2557. https://doi.org/10.1002/celc.201800679.

(51) Kataoka, K.; Akimoto, J. Lithium-Ion Conductivity and Crystal Structure of Garnet-Type Solid Electrolyte $Li_{7-x}La_3Zr_{2-x}Ta_xO_{12}$ Using Single-Crystal. *J. Ceram. Soc. Japan* **2019**, *127* (8), 521–526.

(52) Larraz, G.; Orera, a.; Sanjuán, M. L. Cubic Phases of Garnet-Type $Li_7La_3Zr_2O_{12}$:

The Role of Hydration. *J. Mater. Chem. A* **2013**, *1* (37), 11419. https://doi.org/10.1039/c3ta11996c.

(53) Cheng, L.; Wu, C. H.; Jarry, A.; Chen, W.; Ye, Y.; Zhu, J.; Kostecki, R.; Persson, K.; Guo, J.; Salmeron, M.; Chen, G.; Doeff, M. Interrelationships among Grain Size, Surface Composition, Air Stability, and Interfacial Resistance of Al-Substituted $Li_7La_3Zr_2O_{12}$ Solid Electrolytes. *ACS Appl. Mater. Interfaces* **2015**, *7* (32), 17649–17655. https://doi.org/10.1021/acsami.5b02528.

(54) Wang, Y.; Lai, W. Phase Transition in Lithium Garnet Oxide Ionic Conductors $Li_7La_3Zr_2O_{12}$: The Role of Ta Substitution and H_2O/CO_2 Exposure. *J. Power Sources* **2015**, *275*, 612–620. https://doi.org/10.1016/j.jpowsour.2014.11.062.

(55) Sharafi, A.; Yu, S.; Naguib, M.; Lee, M.; Ma, C.; Meyer, H. M.; Nanda, J.; Chi, M.; Siegel, D. J.; Sakamoto, J. Impact of Air Exposure and Surface Chemistry on Li–$Li_7La_3Zr_2O_{12}$ Interfacial Resistance. *J. Mater. Chem. A* **2017**, *5* (26), 13475–13487. https://doi.org/10.1039/C7TA03162A.

(56) Hofstetter, K.; Samson, A. J.; Narayanan, S.; Thangadurai, V. Present Understanding of the Stability of Li-Stu Ff Ed Garnets with Moisture , Carbon Dioxide , and Metallic Lithium. *J. Power Sources* **2018**, *390* (March), 297–312. https://doi.org/10.1016/j.jpowsour.2018.04.016.

(57) Toda, S.; Ishiguro, K.; Shimonishi, Y.; Hirano, A.; Takeda, Y.; Yamamoto, O.; Imanishi, N. Low Temperature Cubic Garnet-Type CO_2-Doped $Li_7La_3Zr_2O_{12}$. *Solid State Ionics* **2013**, *233*, 102–106. https://doi.org/10.1016/j.ssi.2012.12.007.

(58) Siegel, D. J.; An, K.; Ma, C.; Liu, X.; Sakamoto, J.; Cheng, Y.; Jalarvo, N. H.; Hood, Z. D.; Chen, Y.; Sharafi, A.; Wang, H.; Yu, S.; Chi, M. Elucidating the Mobility of H^+ and Li^+ Ions in $(Li_{6.25-x}H_xAl_{0.25})La_3Zr_2O_{12}$ via Correlative Neutron and Electron Spectroscopy . *Energy Environ. Sci.* **2019**, 945–951. https://doi.org/10.1039/c8ee02981d.

(59) Cheng, L.; Liu, M.; Mehta, A.; Xin, H. L.; Lin, F.; Persson, K. A.; Chen, G.; Crumlin, E. J.; Doeff, M. M. Garnet Electrolyte Surface Degradation and Recovery. *ACS Appl. Energy Mater.* **2018**, *1*, 7244–7252. https://doi.org/10.1021/acsaem.8b01723.

(60) Besli, M. M.; Usubelli, C.; Metzger, M.; Pande, V.; Harry, K.; Nordlund, D.; Sainio, S.; Christensen, J.; Doeff, M. M.; Kuppan, S. Effect of Liquid Electrolyte Soaking on the Interfacial Resistance of $Li_7La_3Zr_2O_{12}$ for All-Solid-State Lithium Batteries. *ACS Appl. Mater. Interfaces* **2020**, *12* (18), 20605–20612. https://doi.org/10.1021/acsami.0c06194.

(61) Ruan, Y.; Lu, Y.; Huang, X.; Su, J.; Sun, C.; Wen, Z. Acid Induced Conversion towards Robust and Lithiophilic Interface for $LiLi_7La_3Zr_2O_{12}$ Solid-State Battery. *J. Mater. Chem.* **2019**, *5*, 14565–14574. https://doi.org/10.1039/c9ta01911a.

(62) Han, X.; Gong, Y.; Fu, K.; He, X.; Hitz, G. T.; Dai, J.; Pearse, A.; Liu, B.; Wang, H.; Rubloff, G.; Mo, Y.; Thangadurai, V.; Wachsman, E. D.; Hu, L. Negating Interfacial Impedance in Garnet-Based Solid-State Li Metal Batteries. *Nat. Mater.* **2017**, *16* (5), 572–579. https://doi.org/10.1038/nmat4821.

(63) Shao, Y.; Wang, H.; Gong, Z.; Wang, D.; Zheng, B.; Zhu, J.; Hu, Y.; Guo, X.; Li, H.; Huang, X.; Yang, Y.; Nan, C.; Chen, L. Drawing a Soft Interface : An Effective Interfacial Modification Strategy for Garnet-Type Solid-State Li Batteries. *ACS Energy Lett.* **2018**, *3*, 1212–1218. https://doi.org/10.1021/acsenergylett.8b00453.

(64) Yang, C.; Xie, H.; Ping, W.; Fu, K.; Liu, B.; Rao, J.; Dai, J.; Wang, C.; Pastel, G.; Hu, L. An Electron/Ion Dual-Conductive Alloy Framework for High-Rate and High-Capacity Solid-State Lithium-Metal Batteries. *Adv. Mater.* **2019**, *31* (3), 1–7. https://doi.org/10.1002/adma.201804815.

(65) Wang, C.; Xie, H.; Zhang, L.; Gong, Y.; Pastel, G.; Dai, J.; Liu, B.; Wachsman, E. D.; Hu, L. Universal Soldering of Lithium and Sodium Alloys on Various Substrates for Batteries. *Adv. Energy Mater.* **2018**, *8* (6), 1701963. https://doi.org/10.1002/aenm.201701963.

(66) Duan, H.; Zheng, H.; Zhou, Y.; Xu, B.; Liu, H. Stability of Garnet-Type Li Ion Conductors: An Overview. *Solid State Ionics* **2017**, 318, 45-53. https://doi.org/10.1016/j.ssi.2017.09.018.

(67) Cheng, L.; Chen, W.; Kunz, M.; Persson, K.; Tamura, N.; Chen, G.; Doeff, M. Effect of Surface Microstructure on Electrochemical Performance of Garnet Solid Electrolytes. *ACS Appl. Mater. Interfaces* **2015**, *7* (3), 2073–2081. https://doi.org/10.1021/am508111r.

(68) Sharafi, A.; Haslam, C. G.; Kerns, R. D.; Wolfenstine, J.; Sakamoto, J. Controlling and Correlating the Effect of Grain Size with the Mechanical and Electrochemical Properties of $Li_7La_3Zr_2O_{12}$ Solid-State Electrolyte. *J. Mater. Chem. A* **2017**, *5*, 21491–21504. https://doi.org/10.1039/C7TA06790A.

(69) Porz, L.; Swamy, T.; Sheldon, B. W.; Rettenwander, D.; Frömling, T.; Thaman, H. L.; Berendts, S.; Uecker, R.; Carter, W. C.; Chiang, Y. M. Mechanism of Lithium Metal Penetration through Inorganic Solid Electrolytes. *Adv. Energy Mater.* **2017**, *1701003*, 1–12. https://doi.org/10.1002/aenm.201701003.

(70) Aguesse, F.; Manalastas, W.; Buannic, L.; Del Amo, J. M. L.; Singh, G.; Llordés, A.; Kilner, J. Investigating the Dendritic Growth during Full Cell Cycling of Garnet Electrolyte in Direct Contact with Li Metal. *ACS Appl. Mater. Interfaces* **2017**, *9* (4), 3808–3816. https://doi.org/10.1021/acsami.6b13925.

(71) Tian, H. K.; Xu, B.; Qi, Y. Computational Study of Lithium Nucleation Tendency in $Li_7La_3Zr_2O_{12}$ (LLZO) and Rational Design of Interlayer Materials to Prevent Lithium Dendrites. *J. Power Sources* **2018**, *392* (March), 79–86.

https://doi.org/10.1016/j.jpowsour.2018.04.098.

(72) Sharafi, A.; Kazyak, E.; Davis, A. L.; Yu, S.; Thompson, T.; Siegel, D. J.; Dasgupta, N. P.; Sakamoto, J. Surface Chemistry Mechanism of Ultra-Low Interfacial Resistance in the Solid-State Electrolyte $Li_7La_3Zr_2O_{12}$. *Chem. Mater.* **2017**, *29* (18), 7961–7968. https://doi.org/10.1021/acs.chemmater.7b03002.

(73) Yu, S.; Schmidt, R. D.; Garcia-Mendez, R.; Herbert, E.; Dudney, N. J.; Wolfenstine, J. B.; Sakamoto, J.; Siegel, D. J. Elastic Properties of the Solid Electrolyte $Li_7La_3Zr_2O_{12}$ (LLZO). *Chem. Mater.* **2016**, *28* (1), 197–206. https://doi.org/10.1021/acs.chemmater.5b03854.

(74) Monroe, C.; Newman, J. The Impact of Elastic Deformation on Deposition Kinetics at Lithium/Polymer Interfaces. *J. Electrochem. Soc.* **2005**, *152* (2), A396. https://doi.org/10.1149/1.1850854.

(75) Masias, A.; Felten, N.; Garcia-Mendez, R.; Wolfenstine, J.; Sakamoto, J. Elastic, Plastic, and Creep Mechanical Properties of Lithium Metal. *J. Mater. Sci.* **2018**. https://doi.org/10.1007/s10853-018-2971-3.

(76) Cheng, E. J.; Sharafi, A.; Sakamoto, J. Intergranular Li Metal Propagation through Polycrystalline $Li_{6.25}Al_{0.25}La_3Zr_2O_{12}$ ceramic Electrolyte. *Electrochim. Acta* **2017**, *223*, 85–91. https://doi.org/10.1016/j.electacta.2016.12.018.

(77) Taylor, N. J.; Stangeland-Molo, S.; Haslam, C. G.; Sharafi, A.; Thompson, T.; Wang, M.; Garcia-Mendez, R.; Sakamoto, J. Demonstration of High Current Densities and Extended Cycling in the Garnet $Li_7La_3Zr_2O_{12}$ solid Electrolyte. *J. Power Sources* **2018**, *396* (June), 314–318. https://doi.org/10.1016/j.jpowsour.2018.06.055.

(78) Swamy, T.; Park, R.; Sheldon, B. W.; Rettenwander, D.; Porz, L.; Berendts, S.; Uecker, R.; Carter, W. C.; Chiang, Y. Lithium Metal Penetration Induced by Electrodeposition through Solid Electrolytes : Example in Single-Crystal $Li_6La_3ZrTaO_{12}$ Garnet. **2018**, *165* (16), 3648–3655. https://doi.org/10.1149/2.1391814jes.

(79) Krauskopf, T.; Hartmann, H.; Zeier, W. G.; Janek, J. Toward a Fundamental Understanding of the Lithium Metal Anode in Solid-State Batteries - An Electrochemo-Mechanical Study on the Garnet-Type Solid Electrolyte $Li_{6.25}Al_{0.25}La_3Zr_2O_{12}$. *ACS Appl. Mater. Interfaces* **2019**, *11* (15), 14463–14477. https://doi.org/10.1021/acsami.9b02537.

(80) Buschmann, H.; Berendts, S.; Mogwitz, B.; Janek, J. Lithium Metal Electrode Kinetics and Ionic Conductivity of the Solid Lithium Ion Conductors "$Li_7La_3Zr_2O_{12}$" and $Li_{7-X}La_3Zr_{2-X}Ta_xO_{12}$ with Garnet-Type Structure. *J. Power Sources* **2012**, *206*, 236–244. https://doi.org/10.1016/j.jpowsour.2012.01.094.

(81) Tsai, C. L.; Dashjav, E.; Hammer, E. M.; Finsterbusch, M.; Tietz, F.; Uhlenbruck,

S.; Buchkremer, H. P. High Conductivity of Mixed Phase Al-Substituted $Li_7La_3Zr_2O_{12}$. *J. Electroceramics* **2015**, *35* (1–4), 25–32. https://doi.org/10.1007/s10832-015-9988-7.

(82) Rettenwander, D.; Redhammer, G.; Preishuber-Pflügl, F.; Cheng, L.; Miara, L.; Wagner, R.; Welzl, A.; Suard, E.; Doeff, M. M.; Wilkening, M.; Fleig, J.; Amthauer, G. Structural and Electrochemical Consequences of Al and Ga Cosubstitution in $Li_7La_3Zr_2O_{12}$ Solid Electrolytes. *Chem. Mater.* **2016**, *28* (7), 2384–2392. https://doi.org/10.1021/acs.chemmater.6b00579.

(83) West, A. *Solid State Chemistry and Its Applications*, First Edit.; John Wiley and Sons: New York, NY, 1984.

(84) Chan, C. K.; Yang, T.; Mark Weller, J. Nanostructured Garnet-Type $Li_7La_3Zr_2O_{12}$: Synthesis, Properties, and Opportunities as Electrolytes for Li-Ion Batteries. *Electrochim. Acta* **2017**, *253*, 268–280. https://doi.org/10.1016/j.electacta.2017.08.130.

(85) Šepelák, V.; Bégin-Colin, S.; Le Caër, G. Transformations in Oxides Induced by High-Energy Ball-Milling. *Dalt. Trans.* **2012**, *41* (39), 11927–11948. https://doi.org/10.1039/c2dt30349c.

(86) Kun, R.; Langer, F.; Delle Piane, M.; Ohno, S.; Zeier, W. G.; Gockeln, M.; Colombi Ciacchi, L.; Busse, M.; Fekete, I. Structural and Computational Assessment of the Influence of Wet-Chemical Post-Processing of the Al-Substituted Cubic $Li_7La_3Zr_2O_{12}$. *ACS Appl. Mater. Interfaces* **2018**, acsami.8b09789. https://doi.org/10.1021/acsami.8b09789.

(87) Huang, X.; Lu, Y.; Jin, J.; Gu, S.; Xiu, T.; Song, Z.; Badding, M. E.; Wen, Z. A Method Using Water-Based Solvent to Prepare $Li_7La_3Zr_2O_{12}$ Solid Electrolytes. *ACS Appl. Mater. Interfaces* **2018**. https://doi.org/10.1021/acsami.8b01961.

(88) C. Brinker; Scherer, G. Sol-Gel Science: The Physics and Chemistry of Sol-Gel Processing. *Advanced Materials*. 1990, p 912. https://doi.org/10.1186/1471-2105-8-444.

(89) Danks, A. E.; Hall, S. R.; Schnepp, Z. The Evolution of 'Sol–Gel' Chemistry as a Technique for Materials Synthesis. *Mater. Horizons* **2016**, *3*, 91–112. https://doi.org/10.1039/C5MH00260E.

(90) Stober, W.; Fink, A. Controlled Growth of Monodispersed Silica Spheres in the Micron Size Range. *J. Colloid Interface Sci.* **1968**, *26*, 62–69. https://doi.org/10.1016/0021-9797(68)90272-5.

(91) Kotobuki, M.; Koishi, M. Preparation of $Li_7La_3Zr_2O_{12}$ Solid Electrolyte via a Sol-Gel Method. *Ceram. Int.* **2014**, *40* (3), 5043–5047. https://doi.org/10.1016/j.ceramint.2013.09.009.

(92) Xie, H.; Li, Y.; Goodenough, J. B. Low-Temperature Synthesis of $Li_7La_3Zr_2O_{12}$ with Cubic Garnet-Type Structure. *Mater. Res. Bull.* **2012**, *47*, 2012. https://doi.org/10.1016/j.materresbull.2012.01.027.

(93) Yoon, S. A.; Oh, N. R.; Yoo, A. R.; Lee, H. G.; Lee, H. C. Preparation and Characterization of Ta-Substituted $Li_7La_3Zr_{2-x}O_{12}$ Garnet Solid Electrolyte by Sol-Gel Processing. *J. Korean Ceram. Soc.* **2017**, *54* (4), 278–284.

(94) Liu, X.; Li, Y.; Yang, T.; Cao, Z.; He, W.; Gao, Y.; Liu, J.; Li, G.; Li, Z. High Lithium Ionic Conductivity in the Garnet-Type Oxide $Li_{7-2x}La_3Zr_{2-x}Mo_xO_{12}$ (x = 0-0 . 3) Ceramics by Sol-Gel Method. *Mater. Lett.* **2017**, *231* (December 2016), 1527–1533. https://doi.org/10.1111/jace.14736.

(95) Sakamoto, J.; Rangasamy, E.; Kim, H.; Kim, Y.; Wolfenstine, J. Synthesis of Nano-Scale Fast Ion Conducting Cubic $Li_7La_3Zr_2O_{12}$. *Nanotechnology* **2013**, *24* (42), 424005. https://doi.org/10.1021/cm201671k.

(96) Wen, W.; Wu, J. M. Nanomaterials via Solution Combustion Synthesis: A Step Nearer to Controllability. *RSC Adv.* **2014**, *4* (101), 58090–58100. https://doi.org/10.1039/c4ra10145f.

(97) Shimonishi, Y.; Toda, A.; Zhang, T.; Hirano, A.; Imanishi, N.; Yamamoto, O.; Takeda, Y. Synthesis of Garnet-Type $Li_{7-X}La_3Zr_2O_{12-1/2x}$ and Its Stability in Aqueous Solutions. *Solid State Ionics* **2011**. https://doi.org/10.1016/j.ssi.2010.12.010.

(98) Kokal, I.; Somer, M.; Notten, P. H. L.; Hintzen, H. T. Sol-Gel Synthesis and Lithium Ion Conductivity of $Li_7La_3Zr_2O_{12}$ with Garnet-Related Type Structure. *Solid State Ionics* **2011**, *185* (1), 42–46. https://doi.org/10.1016/j.ssi.2011.01.002.

(99) Janani, N.; Ramakumar, S.; Dhivya, L.; Deviannapoorani, C.; Saranya, K.; Murugan, R. Synthesis of Cubic $Li_7La_3Zr_2O_{12}$ by Modified Sol-Gel Process. *Ionics (Kiel).* **2011**, *17* (7), 575–580. https://doi.org/10.1007/s11581-011-0611-x.

(100) Yang, T.; Gordon, Z. D.; Li, Y.; Chan, C. K. Nanostructured Garnet-Type Solid Electrolytes for Lithium Batteries: Electrospinning Synthesis of $Li_7La_3Zr_2O_{12}$ Nanowires and Particle Size-Dependent Phase Transformation. *J. Phys. Chem. C* **2015**, *119* (27), 14947–14953. https://doi.org/10.1021/acs.jpcc.5b03589.

(101) Navrotsky, A. Thermochemical Insights into Refractory Ceramic Materials Based on Oxides with Large Tetravalent Cations. *J. Mater. Chem.* **2005**, *15* (19), 1883–1890. https://doi.org/10.1039/b417143h.

(102) Gordon, Z. D.; Yang, T.; Morgado, G. B. G.; Chan, C. K. Preparation of Nano- and Microstructured Garnet $Li_7La_3Zr_2O_{12}$ Solid Electrolytes for Li-Ion Batteries via Cellulose Templating. *ACS Sustain. Chem. Eng.* **2016**, *4* (12), 6391–6398. https://doi.org/10.1021/acssuschemeng.6b01032.

(103) Fang, Z. Z.; Wang, H.; Wang, X.; Kumar, V. Grain Growth during Sintering of Nanosized Particles. *Ceram. Trans.* **2010**, *209* (February), 389–400. https://doi.org/10.1179/174328008X353538.

(104) Zhang, J.; Zhao, N.; Zhang, M.; Li, Y.; Chu, P. K.; Guo, X.; Di, Z.; Wang, X.; Li, H. Flexible and Ion-Conducting Membrane Electrolytes for Solid-State Lithium Batteries: Dispersion of Garnet Nanoparticles in Insulating Polyethylene Oxide. *Nano Energy* **2016**, *28*, 447–454. https://doi.org/10.1016/j.nanoen.2016.09.002.

(105) Bae, J.; Li, Y.; Zhao, F.; Zhou, X.; Ding, Y.; Yu, G. Designing 3D Nanostructured Garnet Frameworks for Enhancing Ionic Conductivity and Flexibility in Composite Polymer Electrolytes for Lithium Batteries. *Energy Storage Mater.* **2018**, *15* (February), 46–52. https://doi.org/10.1016/j.ensm.2018.03.016.

(106) Xie, H.; Yang, C.; Fu, K. (Kelvin); Yao, Y.; Jiang, F.; Hitz, E.; Liu, B.; Wang, S.; Hu, L. Flexible, Scalable, and Highly Conductive Garnet-Polymer Solid Electrolyte Templated by Bacterial Cellulose. *Adv. Energy Mater.* **2018**, *8* (18), 1–7. https://doi.org/10.1002/aenm.201703474.

(107) Yang, T.; Zheng, J.; Cheng, Q.; Hu, Y. Y.; Chan, C. K. Composite Polymer Electrolytes with $Li_7La_3Zr_2O_{12}$ Garnet-Type Nanowires as Ceramic Fillers: Mechanism of Conductivity Enhancement and Role of Doping and Morphology. *ACS Appl. Mater. Interfaces* **2017**, *9* (26), 21773–21780. https://doi.org/10.1021/acsami.7b03806.

(108) Fu, K. (Kelvin); Gong, Y.; Dai, J.; Gong, A.; Han, X.; Yao, Y.; Wang, C.; Wang, Y.; Chen, Y.; Yan, C.; Li, Y.; Wachsman, E. D.; Hu, L. Flexible, Solid-State, Ion-Conducting Membrane with 3D Garnet Nanofiber Networks for Lithium Batteries. *Proc. Natl. Acad. Sci.* **2016**, *113* (26), 7094–7099. https://doi.org/10.1073/pnas.1600422113.

(109) Persano, L.; Camposeo, A.; Tekmen, C.; Pisignano, D. Industrial Upscaling of Electrospinning and Applications of Polymer Nanofibers: A Review. *Macromol. Mater. Eng.* **2013**, *298* (5), 504–520. https://doi.org/10.1002/mame.201200290.

(110) Rosenthal, T.; Weller, J. M.; Chan, C. K.; J. Mark Weller; Chan, C. K. Needleless Electrospinning for High Throughput Production of $Li_7La_3Zr_2O_{12}$ Solid Electrolyte Nanofibers. *Ind. Eng. Chem. Res.* **2019**, *58* (37), 17399–17405. https://doi.org/10.1021/acs.iecr.9b03376.

(111) Yi, E.; Wang, W.; Kieffer, J.; Laine, R. M. Flame Made Nanoparticles Permit Processing of Dense, Flexible, Li^+ Conducting Ceramic Electrolyte Thin Films of Cubic-$Li_7La_3Zr_2O_{12}$ (c-LLZO). *J. Mater. Chem. A* **2016**, *4*, 12947–12954. https://doi.org/10.1039/C6TA04492A.

(112) Bitzer, M.; Van Gestel, T.; Uhlenbruck, S.; Hans-Peter-Buchkremer. Sol-Gel Synthesis of Thin Solid $Li_7La_3Zr_2O_{12}$ Electrolyte Films for Li-Ion Batteries. *Thin Solid Films* **2016**, *615*, 128–134. https://doi.org/10.1016/j.tsf.2016.07.010.

(113) Loho, C.; Djenadic, R.; Bruns, M.; Clemens, O.; Hahn, H. Garnet-Type $Li_7La_3Zr_2O_{12}$ Solid Electrolyte Thin Films Grown by CO_2-Laser Assisted CVD for All-Solid-State Batteries. *J. Electrochem. Soc.* **2017**, *164* (1), A6131–A6139. https://doi.org/10.1149/2.0201701jes.

(114) Kazyak, E.; Chen, K. H.; Wood, K. N.; Davis, A. L.; Thompson, T.; Bielinski, A. R.; Sanchez, A. J.; Wang, X.; Wang, C.; Sakamoto, J.; Dasgupta, N. P. Atomic Layer Deposition of the Solid Electrolyte Garnet $Li_7La_3Zr_2O_{12}$. *Chem. Mater.* **2017**, *29* (8), 3785–3792. https://doi.org/10.1021/acs.chemmater.7b00944.

(115) Garbayo, I.; Struzik, M.; Bowman, W. J.; Pfenninger, R.; Stilp, E.; Rupp, J. L. M. Glass-Type Polyamorphism in Li-Garnet Thin Film Solid State Battery Conductors. *Adv. Energy Mater.* **2018**, *1702265*, 1–14. https://doi.org/10.1002/aenm.201702265.

(116) Rawlence, M.; Garbayo, I.; Buecheler, S.; Rupp, J. L. M. On the Chemical Stability of Post-Lithiated Garnet Al-Stabilized $Li_7La_3Zr_2O_{12}$ Solid State Electrolyte Thin Films. *Nanoscale* **2016**, *8* (31), 14746–14753. https://doi.org/10.1039/C6NR04162K.

(117) Pfenninger, R.; Struzik, M.; Garbayo, I.; Stilp, E.; Rupp, J. L. M. A Low Ride on Processing Temperature for Fast Lithium Conduction in Garnet Solid-State Battery Films. *Nat. Energy* **2019**, *4* (6), 475–483. https://doi.org/10.1038/s41560-019-0384-4.

(118) Buannic, L.; Naviroj, M.; Miller, S. M.; Zagorski, J.; Faber, K. T.; Llordés, A.; Sastre, J.; Priebe, A.; Döbeli, M.; Michler, J.; Tiwari, A. N.; Romanyuk, Y. E. Lithium Garnet $Li_7La_3Zr_2O_{12}$ Electrolyte for All-Solid-State Batteries: Closing the Gap between Bulk and Thin Film Li-Ion Conductivities. *Adv. Mater. Interfaces* **2020**, 2000425. https://doi.org/10.1111/jace.15938.

(119) Liu, X.; Fechler, N.; Antonietti, M. Salt Melt Synthesis of Ceramics, Semiconductors and Carbon Nanostructures. *Chem. Soc. Rev.* **2013**, *42* (21), 8237. https://doi.org/10.1039/C3CS60159E.

(120) Kimura, T. Molten Salt Synthesis of Ceramic Powders. In *Advances in Ceramics - Synthesis and Characterization, Processing and Specific Applications*; Sikalidis, C., Ed.; InTech, 2011; pp 75–100. https://doi.org/DOI: 10.5772/20472.

(121) Awaka, J.; Takashima, A.; Hayakawa, H.; Kijima, N.; Idemoto, Y.; Akimoto, J. Single Crystal Synthesis of Cubic Garnet Related-Type $Li_7La_3Zr_2O_{12}$ by a Self-Flux Method. *Key Eng. Mater.* **2011**, *485*, 99–102. https://doi.org/10.4028/www.scientific.net/KEM.485.99.

(122) Reddy, M. V.; Adams, S. Molten Salt Synthesis and Characterization of Fast Ion Conductor $Li_{6.75}La_3Zr_{1.75}Ta_{0.25}O_{12}$. *J. Solid State Electrochem.* **2017**, *21*, 2921–2928. https://doi.org/10.1007/s10008-017-3615-2.

(123) Patnaik, P. *Handbook of Inorganic Chemicals*, illustrate.; McGraw-Hill: New York, NY, 2003.

(124) Badami, P.; Weller, J. M.; Wahab, A.; Redhammer, G.; Ladenstein, L.; Rettenwander, D.; Wilkening, M.; Chan, C. K.; Kannan, A. N. M. Highly Conductive Garnet-Type Electrolytes : Access to $Li_{6.5}La_3Zr_{1.5}Ta_{0.5}O_{12}$ Prepared by Molten Salt and Solid-State Methods. *ACS Appl. Mater. Interfaces* **2020**, *12* (43), 48580–48590. https://doi.org/10.1021/acsami.0c14056.

(125) German, R. *Sintering: From Empirical Observations to Scientific Principles*; Elsevier: Oxford, UK 2014. https://doi.org/10.1016/C2012-0-00717-X.

(126) Huang, X.; Lu, Y.; Guo, H.; Song, Z.; Xiu, T.; Badding, M. E.; Wen, Z. None-Mother-Powder Method to Prepare Dense Li-Garnet Solid Electrolytes with High Critical Current Density. *ACS Appl. Energy Mater.* **2018**, *1* (10), 5355–5365. https://doi.org/10.1021/acsaem.8b00976.

(127) Kim, Y.; Jo, H.; Allen, J. L.; Choe, H.; Wolfenstine, J.; Sakamoto, J. The Effect of Relative Density on the Mechanical Properties of Hot-Pressed Cubic $Li_7La_3Zr_2O_{12}$. *J. Am. Ceram. Soc.* **2016**, *99* (4), 1367–1374. https://doi.org/10.1111/jace.14084.

(128) Castillo, A.; Charpentier, T.; Rapaud, O.; Pradeilles, N.; Yagoubi, S.; Foy, E.; Moskura, M.; Khodja, H. Bulk Li Mobility Enhancement in Spark Plasma Sintered $Li_{(7-3x)}Al_xLa_3Zr_2O_{12}$ garnet. *Ceram. Int.* **2018**, No. July, 1–7. https://doi.org/10.1016/j.ceramint.2018.07.119.

(129) Baek, S. W.; Lee, J. M.; Kim, T. Y.; Song, M. S.; Park, Y. Garnet Related Lithium Ion Conductor Processed by Spark Plasma Sintering for All Solid State Batteries. *J. Power Sources* **2014**, *249*, 197–206. https://doi.org/10.1016/j.jpowsour.2013.10.089.

(130) Wang, C.; Ping, W.; Bai, Q.; Cui, H.; Hensleigh, R.; Wang, R.; Brozena, A. H.; Xu, Z.; Dai, J.; Pei, Y.; Zheng, C.; Pastel, G.; Gao, J.; Wang, X.; Wang, H.; Zhao, J.; Yang, B.; Rayne, X.; Luo, J.; Mo, Y.; Dunn, B.; Hu, L. A General Method to Synthesize and Sinter Bulk Ceramics in Seconds. *Science.* **2020**, *368*, 521–526. https://doi.org/10.1126/science.aaz7681.

(131) Mistler, R. E.; Twiname, E. R. *Tape Casting: Theory and Practice*; The American Ceramic Society: Westerville, OH, 2000.

(132) Jabbari, M.; Bulatova, R.; Tok, A. I. Y.; Bahl, C. R. H.; Mitsoulis, E.; Hattel, J. H. Ceramic Tape Casting: A Review of Current Methods and Trends with Emphasis on Rheological Behaviour and Flow Analysis. *Mater. Sci. Eng. B Solid-State Mater. Adv. Technol.* **2016**, *212*, 39–61. https://doi.org/10.1016/j.mseb.2016.07.011.

(133) Ye, R.; Tsai, C.; Ihrig, M.; Sevinc, S.; Rosen, M.; Dashjav, E.; Sohn, Y. J.; Figgemeier, E.; Finsterbusch, M. Green Chemistry Electrolyte Separators for

Solid-State Lithium. *Green Chem.* **2020**, *22*, 4952–4962. https://doi.org/10.1039/d0gc01009j.

(134) Shen, H.; Yi, E.; Amores, M.; Cheng, L.; Tamura, N.; Parkinson, D. Y.; Chen, G.; Chen, K.; Doeff, M.; Hao Shen, Eongyu Yi, Marco Amores, Lei Cheng, Nobumichi Tamura, Dilworth Y. Parkinson, Guoying Chen, K. C. and M. D.; All. Oriented Porous LLZO 3D Structures Obtained by Freeze Casting for Battery Applications. *J. Mater. Chem. A* **2019**, *7* (36), 20861–20870. https://doi.org/DOI: 10.1039/c9ta06520b.

(135) Yi, E.; Shen, H.; Heywood, S.; Alvarado, J.; Parkinson, D. Y.; Chen, G.; So, S. W.; Doe, M. M. All-Solid-State Batteries Using Rationally Designed Garnet Electrolyte Frameworks. **2020**. https://doi.org/10.1021/acsaem.9b02101.

(136) Nitta, N.; Wu, F.; Lee, J. T.; Yushin, G. Li-Ion Battery Materials: Present and Future. *Mater. Today* **2015**, *18* (5), 252–264. https://doi.org/10.1016/j.mattod.2014.10.040.

(137) Pfenninger, R.; Afyon, S.; Garbayo, I.; Struzik, M.; Rupp, J. L. M. Lithium Titanate Anode Thin Films for Li-Ion Solid State Battery Based on Garnets. *Adv. Funct. Mater.* **2018**, *1800879*, 1800879. https://doi.org/10.1002/adfm.201800879.

(138) Hausbrand, R.; Cherkashinin, G.; Ehrenberg, H.; Gröting, M.; Albe, K.; Hess, C.; Jaegermann, W. Fundamental Degradation Mechanisms of Layered Oxide Li-Ion Battery Cathode Materials: Methodology, Insights and Novel Approaches. *Mater. Sci. Eng. B Solid-State Mater. Adv. Technol.* **2015**, *192* (C), 3–25. https://doi.org/10.1016/j.mseb.2014.11.014.

(139) Finsterbusch, M.; Danner, T.; Tsai, C.-L. L.; Uhlenbruck, S.; Latz, A.; Guillon, O. High Capacity Garnet-Based All-Solid-State Lithium Batteries: Fabrication and 3D-Microstructure Resolved Modeling. *ACS Appl. Mater. Interfaces* **2018**, *10* (26), 22329–22339. https://doi.org/10.1021/acsami.8b06705.

(140) Tsai, C. L.; Ma, Q.; Dellen, C.; Lobe, S.; Vondahlen, F.; Windmüller, A.; Grüner, D.; Zheng, H.; Uhlenbruck, S.; Finsterbusch, M.; Tietz, F.; Fattakhova-Rohlfing, D.; Buchkremer, H. P.; Guillon, O. A Garnet Structure-Based All-Solid-State Li Battery without Interface Modification: Resolving Incompatibility Issues on Positive Electrodes. *Sustain. Energy Fuels* **2019**, *3* (1), 280–291. https://doi.org/10.1039/c8se00436f.

(141) Vardar, G.; Bowman, W. J.; Lu, Q.; Wang, J.; Chater, R. J.; Aguadero, A.; Seibert, R.; Terry, J.; Hunt, A.; Waluyo, I.; Fong, D. D.; Jarry, A.; Crumlin, E. J.; Hellstrom, S. L.; Chiang, Y.-M.; Yildiz, B. Structure, Chemistry, and Charge Transfer Resistance of the Interface between $Li_7La_3Zr_2O_{12}$ Electrolyte and $LiCoO_2$ Cathode. *Chem. Mater.* **2018**, *30*, 6259–6276. https://doi.org/10.1021/acs.chemmater.8b01713.

(142) Kim, Y.; Kim, D.; Bliem, R.; Vardar, G.; Waluyo, I.; Hunt, A.; Wright, J. T.;

Katsoudas, J. P.; Yildiz, B.; Mn, L.; Cathode, C. O.; Kim, Y.; Kim, D.; Bliem, R.; Vardar, G.; Waluyo, I.; Hunt, A.; Wright, J. T.; Katsoudas, J. P.; Yildiz, B. Thermally Driven Interfacial Degradation between $Li_7La_3Zr_2O_{12}$. *Chem. Mater.* **2020**, *32*, 9531–9541. https://doi.org/10.1021/acs.chemmater.0c02261.

(143) Bucci, G.; Swamy, T.; Chiang, Y.-M.; Carter, W. C. Modeling of Internal Mechanical Failure of All-Solid-State Batteries during Electrochemical Cycling, and Implications for Battery Design. *J. Mater. Chem. A Mater. energy Sustain.* **2017**, *5*, 19422–19430. https://doi.org/10.1039/C7TA03199H.

(144) Huang, X.; Shen, C.; Rui, K.; Jin, J.; Wu, M.; Wu, X.; Wen, Z. Influence of $La_2Zr_2O_7$ Additive on Densification and Li^+ Conductivity for Ta-Doped $Li_7La_3Zr_2O_{12}$ Garnet. *Jom* **2016**, *68* (10), 2593–2600. https://doi.org/10.1007/s11837-016-2065-0.

(145) Weller, J. M.; Chan, C. K. Reduction in Formation Temperature of Ta-Doped Lithium Lanthanum Zirconate by Application of Lux-Flood Basic Molten Salt Synthesis. *ACS Appl. Energy Mater.* **2020**, *3* (7), 6466–6475. https://doi.org/10.1021/acsaem.0c00716.

(146) Weller, J. M.; Whetten, J. A.; Chan, C. K. Non-Aqueous Polymer Combustion Synthesis of Cubic $Li_7La_3Zr_2O_{12}$ Nanopowders. *ACS Appl. Mater. Interfaces* **2020**, *12* (1), 953–962. https://doi.org/10.1021/acsami.9b19981.

(147) B.D. Cullity and S.R. Stock. *Elements of X-Ray Diffraction*; Prentice Hall: Upper Saddle River, NJ, 2001.

(148) Egami, T.; Billinge, S. J. . *Underneath the Bragg Peaks*, 2nd ed.; Pergamon: Oxford, UK 2012. https://doi.org/10.1016/s1369-7021(03)00635-7.

(149) André Guinier. *X-Ray Diffraction in Crystals, Imperfect Crystals, and Amorphous Bodies*; Dover: New York, NY, 1994.

(150) Billinge, S. J. L.; Levin, I. The Problem with Determining Atomic Structure at the Nanoscale. *Science.* **2007**, *316* (5824), 561–565. https://doi.org/10.1126/science.1135080.

(151) Farrow, C. L.; Juhas, P.; Liu, J. W.; Bryndin, D.; Boin, E. S.; Bloch, J.; Proffen, T.; Billinge, S. J. L. PDFfit2 and PDFgui: Computer Programs for Studying Nanostructure in Crystals. *J. Phys. Condens. Matter* **2007**, *19*, 335219. https://doi.org/10.1088/0953-8984/19/33/335219.

(152) Yang, X.; Juhas, P.; Farrow, C. L.; Billinge, S. J. L. XPDFsuite: An End-to-End Software Solution for High Throughput Pair Distribution Function Transformation, Visualization and Analysis. *arXiv:1402.3163 [cond-mat]* **2014**, 1–4.

(153) Billinge, S. J. L.; Kanatzidis, M. G. Beyond Crystallography: The Study of

Disorder, Nanocrystallinity and Crystallographically Challenged Materials with Pair Distribution Functions. *Chem. Commun.* **2004**, *4* (7), 749–760. https://doi.org/10.1039/b309577k.

(154) Juhás, P.; Davis, T.; Farrow, C. L.; Billinge, S. J. L. PDFgetX3: A Rapid and Highly Automatable Program for Processing Powder Diffraction Data into Total Scattering Pair Distribution Functions. *J. Appl. Crystallogr.* **2013**, *46* (2), 560–566. https://doi.org/10.1107/S0021889813005190.

(155) Leng, Y. *Materials Characterization: Introduction to Microscopic and Spectroscopic Methods: Second Edition*; Wiley-VCH: Weinheim, Germany, 2013. https://doi.org/10.1002/9783527670772.

(156) Williams, D. B.; Carter, C. B. *Transmission Electron Microscopy: A Textbook for Materials Science*; 2009. https://doi.org/10.1007/978-0-387-76501-3.

(157) Lasia, A. *Electrochemical Impedance Spectroscopy and Its Applications*; Springer: New York, NY, 2014. 9781461489337. https://doi.org/10.1007/978-1-4614-8933-7.

(158) Tenhaeff, W. E.; Rangasamy, E.; Wang, Y.; Sokolov, A. P.; Wolfenstine, J.; Sakamoto, J.; Dudney, N. J. Resolving the Grain Boundary and Lattice Impedance of Hot-Pressed $Li_7La_3Zr_2O_{12}$ Garnet Electrolytes. *ChemElectroChem* **2014**, *1* (2), 375–378. https://doi.org/10.1002/celc.201300022.

(159) Petit, S.; Morlens, S.; Yu, Z.; Luneau, D.; Pilet, G.; Soubeyroux, J. L.; Odier, P. Synthesis and Thermal Decomposition of a Novel Zirconium Acetato-Propionate Cluster: [Zr12]. *Solid State Sci.* **2011**, *13* (3), 665–670. https://doi.org/10.1016/j.solidstatesciences.2010.12.041.

(160) Kozuka, H.; Takenaka, S. Single-Step Deposition of Gel-Derived Lead Zirconate Titanate Films: Critical Thickness and Gel Film to Ceramic Film Conversion. *Journal of the American Ceramic Society*. 2002, pp 2696–2702.

(161) Weller, J. M.; Whetten, J. A.; Chan, C. K. Synthesis of Fine Cubic $Li_7La_3Zr_2O_{12}$ Powders in Molten LiCl-KCl Eutectic and Facile Densification by Reversal of Li^+/H^+ Exchange. *ACS Appl. Energy Mater.* **2018**, *1* (2), 552–560. https://doi.org/10.1021/acsaem.7b00133.

(162) Miara, L. J.; Ong, S. P.; Mo, Y.; Richards, W. D.; Park, Y.; Lee, J. M.; Lee, H. S.; Ceder, G. Effect of Rb and Ta Doping on the Ionic Conductivity and Stability of the Garnet $Li_{7+2x-y}(La_{3-x}Rb_x)(Zr_{2-y}Ta_y)O_{12}$ ($0 \leq x \leq 0.375$, $0 \leq y \leq 1$) Superionic Conductor: A First Principles Investigation. *Chem. Mater.* **2013**, *25* (15), 3048–3055. https://doi.org/10.1021/cm401232r.

(163) Kubicek, M.; Wachter-Welzl, A.; Rettenwander, D.; Wagner, R.; Berendts, S.; Uecker, R.; Amthauer, G.; Hutter, H.; Fleig, J. Oxygen Vacancies in Fast Lithium-Ion Conducting Garnets. *Chem. Mater.* **2017**, *29* (17), 7189–7196.

https://doi.org/10.1021/acs.chemmater.7b01281.

(164) Nozaki, H.; Harada, M.; Ohta, S.; Watanabe, I.; Miyake, Y.; Ikedo, Y.; Jalarvo, N. H.; Mamontov, E.; Sugiyama, J. Li Diffusive Behavior of Garnet-Type Oxides Studied by Muon-Spin Relaxation and QENS. *Solid State Ionics* **2014**, *262*, 585–588. https://doi.org/10.1016/j.ssi.2013.10.014.

(165) Yao, K. P. C.; Kwabi, D. G.; Quinlan, R. A.; Mansour, A. N.; Grimaud, A.; Lee, Y.; Lu, Y.; Shao-horn, Y. Thermal Stability of Li_2O_2 and Li_2O for Li-Air Batteries : In Situ XRD and XPS Studies. *J. Electrochem. Soc.* **2013**, *160* (6), 824–831. https://doi.org/10.1149/2.069306jes.

(166) Shao, C.; Liu, H.; Yu, Z.; Zheng, Z.; Sun, N.; Diao, C. Structure and Ionic Conductivity of Cubic $Li_7La_3Zr_2O_{12}$ Solid Electrolyte Prepared by Chemical Co-Precipitation Method. *Solid State Ionics* **2016**, *287*, 13–16. https://doi.org/10.1016/j.ssi.2016.01.042.

(167) Langer, F.; Glenneberg, J.; Bardenhagen, I.; Kun, R. Synthesis of Single Phase Cubic Al-Substituted $Li_7La_3Zr_2O_{12}$ by Solid State Lithiation of Mixed Hydroxides. *J. Alloys Compd.* **2015**, *645*, 64–69. https://doi.org/10.1016/j.jallcom.2015.03.209.

(168) Dhivya, L.; Karthik, K.; Ramakumar, S.; Murugan, R.; Karthik, S.; Ramakumar, S.; Murugan, R. Facile Synthesis of High Lithium Ion Conductive Cubic Phase Lithium Garnets for Electrochemical Energy Storage Devices. *RSC Adv.* **2015**, *5* (116), 96042–96051. https://doi.org/10.1039/c5ra18543b.

(169) Zhang, Y.; Cai, J.; Chen, F.; Tu, R.; Shen, Q.; Zhang, X.; Zhang, L. Preparation of Cubic $Li_7La_3Zr_2O_{12}$ Solid Electrolyte Using a Nano-Sized Core-Shell Structured Precursor. *J. Alloys Compd.* **2015**, *644*, 793–798. https://doi.org/10.1016/j.jallcom.2015.05.085.

(170) Zhang, S. Low Temperature Synthesis of Complex Refractory Oxide Powders From Molten Salts. *J. Pakistan Mater. Soc.* **2007**, *1* (2), 49–53.

(171) Wang, X.; Zhu, Y.; Zhang, W. Preparation of Lanthanum Zirconate Nano-Powders by Molten Salts Method. *J. Non. Cryst. Solids* **2010**, *356* (20–22), 1049–1051.

(172) Rahman, M. M.; Wang, J. Z.; Hassan, M. F.; Chou, S.; Wexler, D.; Liu, H. K. Basic Molten Salt Process-A New Route for Synthesis of Nanocrystalline $Li_4Ti_5O_{12}$-TiO_2 Anode Material for Li-Ion Batteries Using Eutectic Mixture of $LiNO_3$-LiOH-Li_2O_2. *J. Power Sources* **2010**, *195* (13), 4297–4303. https://doi.org/10.1016/j.jpowsour.2010.01.073.

(173) Guo, Q.; Li, S.; Wang, H.; Gao, Y.; Li, B. Molten Salt Synthesis of Nano-Sized $Li_4Ti_5O_{12}$ Doped with Fe_2O_3 for Use as Anode Material in the Lithium-Ion Battery. *RSC Adv.* **2014**, *4* (104), 60327–60333. https://doi.org/10.1039/C4RA09813G.

(174) Guo, Q.; Wang, Q.; Chen, G.; Shen, M.; Li, B. Molten Salt Synthesis of Different Ionic Radii Metallic Compounds Doped Lithium Titanate Used in Li-Ion Battery Anodes. **2017**, *58* (3), 383–389.

(175) Huang, Z.; Deng, X.; Liu, J.; Jiao, C. Preparation of $CaZrO_3$ Powders by a Microwave – Assisted Molten Salt Method. *J. Ceram. Soc. Japan* **2016**, *5*, 593–596. https://doi.org/http://dx.doi.org/10.2109/jcersj2.15309.

(176) Zhong, X.; Chen, M.; Zhu, Y.; Zhang, P.; Xu, M.; Li, W. Layered Lithium-Rich Oxide Nanoparticles: Low-Temperature Synthesis in Mixed Molten Salt and Excellent Performance as Cathode of Lithium-Ion Battery. *Ionics.* **2017**, *23*, 1955–1966. https://doi.org/10.1007/s11581-017-2039-4.

(177) Huang, Z.; Zhang, H.; Zhang, S. Growth of Well-Developed LaOCl Microplates by Chloride Salt-Assisted Method. *CrystEngComm* **2017**, *19* (22), 2971–2976. https://doi.org/10.1039/C7CE00549K.

(178) Deviannapoorani, C.; Dhivya, L.; Ramakumar, S.; Murugan, R. Synthesis of Garnet Structured $Li_{7+x}La_3Y_xZr_{2-x}O_{12}$ (x = 0-0.4) by Modified Sol-Gel Method. *J. Sol-Gel Sci. Technol.* **2012**, *64* (2), 510–514. https://doi.org/10.1007/s10971-012-2874-8.

(179) Huang, M.; Liu, T.; Deng, Y.; Geng, H.; Shen, Y.; Lin, Y.; Nan, C.-W. Effect of Sintering Temperature on Structure and Ionic Conductivity of $Li_{7-x}La_3Zr_2O_{12-0.5x}$ (X=0.5~0.7) Ceramics. *Solid State Ionics* **2011**, *204–205*, 41–45. https://doi.org/10.1016/j.ssi.2011.10.003.

(180) Lux, H. "Säuren" Und "Basen" Im Schmelzfluss: Die Bestimmung Der Sauerstoffionen-Konzentration. *Z. Elektrochem.* **1939**, *45*, 303.

(181) Flood, H.; Förland, T. The Acidic and Basic Properties of Oxides. *Acta Chem. Scand*. 1947, pp 592–604. https://doi.org/10.3891/acta.chem.scand.01-0592.

(182) Guo, Qingjun, Wang Qiang, Chen, Gang, Xu, Hongkie, Wu, Jiayu, Li, B. Molten Salt Synthesis of Transition Metal Oxides Doped $Li_4Ti_5O_{12}$ as Anode Material of Li-Ion Battery. *ECS Trans.* **2016**, *72* (9), 11–23. https://doi.org/10.1149/07209.0011ecst.

(183) Du, Y.; Inman, D. Preparation of Zirconia Powders from Molten Nitrites and Nitrates. *J. Mater. Sci.* **1996**, *31*, 5505–5511. https://doi.org/10.1007/BF01159324.

(184) Claes, P.; Peeters, G.; Glibert, J. Chemical and Electrochemical Behavior in Molten Alkali Hydroxides: III. Chemistry of Tin (II) and (IV) in the NaOH-KOH Eutectic Mixture and in Pure NaOH. *J. Electrochem. Soc.* **1989**, *136* (9), 2599–2603. https://doi.org/10.1149/1.2097501.

(185) Vradman, L.; Friedland, E.; Zana, J.; Vidruk-Nehemya, R.; Herskowitz, M. Molten Salt Synthesis of $LaCoO_3$ Perovskite. *J. Mater. Sci.* **2017**, *52* (19), 11383–11390.

https://doi.org/10.1007/s10853-017-1332-y.

(186) Cheng, M.; Rangasamy, E.; Liang, C.; Sakamoto, J.; More, K. L.; Chi, M. Excellent Stability of a Lithium-Ion-Conducting Solid Electrolyte upon Reversible Li^+/H^+ Exchange in Aqueous Solutions. *Angew. Chemie - Int. Ed.* **2015**, *54* (1), 129–133. https://doi.org/10.1002/anie.201408124.

(187) Deviannapoorani, C.; Ramakumar, S.; Janani, N.; Murugan, R. Synthesis of Lithium Garnets from $La_2Zr_2O_7$ Pyrochlore. *Solid State Ionics* **2015**, *283*, 123–130. https://doi.org/10.1016/j.ssi.2015.10.006.

(188) Kimura, T.; Yamada, Y.; Yamamoto, K.; Matsuda, T.; Nomura, H.; Hirayama, T. Rapid Low-Temperature Synthesis of Tetragonal Single-Phase $Li_7La_3Zr_2O_{12}$. *J. Am. Ceram. Soc.* **2017**, *100* (4), 1313–1319. https://doi.org/10.1111/jace.14633.

(189) Subramanian, M. A.; Aravamudan, G.; Rao, G. V. S. Oxide Pyrochlores - A Review. *Prog. Solid State Chem.* **1983**, *15*, 55–143.

(190) Liu, H.; Hu, C.; Wang, Z. L. Composite-Hydroxide-Mediated Approach for the Synthesis of Nanostructures of Complex Functional-Oxides. *Nano Lett.* **2006**, *6* (7), 1535–1540. https://doi.org/10.1021/nl061253e.

(191) Jin, H.; Huang, D.; Gao, Q.; Li, L.; Wang, N.; Wang, Y.; Hou, S. Synthesis of Lanthanum Zirconium Oxide Nanomaterials through Composite-Hydroxide-Mediated Approach. *Mater. Res. Bull.* **2012**, *47* (1), 51–53. https://doi.org/10.1016/j.materresbull.2011.10.005.

(192) Paul, B.; Singh, K.; Jaroń, T.; Roy, A.; Chowdhury, A. Structural Properties and the Fluorite-Pyrochlore Phase Transition in $La_2Zr_2O_7$: The Role of Oxygen to Induce Local Disordered States. *J. Alloys Compd.* **2016**, *686*, 130–136. https://doi.org/10.1016/j.jallcom.2016.05.347.

(193) Yaroshevskii, A. A.; Bagdasarov, Y. A. Geochemical Diversity of Minerals of the Pyrochlore Group. *Geochemistry Int.* **2008**, *46* (12), 1245–1266. https://doi.org/10.1134/S0016702908120045.

(194) Huo, H.; Luo, J.; Thangadurai, V.; Guo, X.; Nan, C. W.; Sun, X. Li_2CO_3: A Critical Issue for Developing Solid Garnet Batteries. *ACS Energy Lett.* **2020**, *5* (1), 252–262. https://doi.org/10.1021/acsenergylett.9b02401.

(195) Hamao, N.; Hamamoto, K.; Taguchi, N.; Tanaka, S.; Akimoto, J. Synthesis and Crystal Structure of Fluorite-Type $La_{2.4}Zr_{1.2}Ta_{0.4}O_7$: A Precursor Oxide for Low Temperature Formation of Garnet-Type $Li_{6.5}La_3Zr_{1.5}Ta_{0.5}O_{12}$. *Solid State Ionics* **2020**, *357* (April), 115460. https://doi.org/10.1016/j.ssi.2020.115460.

(196) Bernstein, N.; Johannes, M. D.; Hoang, K. Origin of the Structural Phase Transition in $Li_7La_3Zr_2O_{12}$. *Phys. Rev. Lett.* **2012**, *109* (205702), 1–5. https://doi.org/10.1103/PhysRevLett.109.205702.

(197) Weller, J. M.; Chan, C. K. Pyrochlore Nanocrystals as Versatile Quasi-Single-Source Precursors to Lithium Conducting Garnets. *J. Mater. Chem. A* **2020**, *8*, 17405–17410. https://doi.org/10.1039/d0ta05842d.

(198) Xia, W.; Xu, B.; Duan, H.; Guo, Y.; Kang, H.; Li, H.; Liu, H. Ionic Conductivity and Air Stability of Al-Doped $Li_7La_3Zr_2O_{12}$ Sintered in Alumina and Pt Crucibles. *ACS Appl. Mater. Interfaces* **2016**, *8* (8), 5335–5342. https://doi.org/10.1021/acsami.5b12186.

(199) Brugge, R. H.; Pesci, F. M.; Cavallaro, A.; Sole, C.; Isaacs, M. A.; Kerherve, G.; Weatherup, R. S.; Aguadero, A. The Origin of Chemical Inhomogeneity in Garnet Electrolytes and Its Impact on the Electrochemical Performance. *J. Mater. Chem. A* **2020**, *8* (28), 14265–14276. https://doi.org/10.1039/d0ta04974c.

(200) Toby, B. H.; Von Dreele, R. B. GSAS-II: The Genesis of a Modern Open-Source All Purpose Crystallography Software Package. *J. Appl. Crystallogr.* **2013**, *46* (2), 544–549. https://doi.org/10.1107/S0021889813003531.

(201) Soper, A. *GudrunN and GudrunX, Tech. Rep. RAL-TR13, Rutherford Appleton Laboratory*; 2012.

(202) Keen, D. A. A Comparison of Various Commonly Used Correlation Functions for Describing Total Scattering. *J. Appl. Crystallogr.* **2001**, *34* (2), 172–177. https://doi.org/10.1107/S0021889800019993.

(203) Bianchini, M.; Wang, J.; Clément, R. J.; Ouyang, B.; Xiao, P.; Kitchaev, D.; Shi, T.; Zhang, Y.; Wang, Y.; Kim, H.; Zhang, M.; Bai, J.; Wang, F.; Sun, W.; Ceder, G. The Interplay between Thermodynamics and Kinetics in the Solid-State Synthesis of Layered Oxides. *Nat. Mater.* **2020**, *19*, 1088–1095. https://doi.org/10.1038/s41563-020-0688-6.

(204) Li, Z.; Lee, W. E. Low-Temperature Synthesis of $CaZrO_3$ Powder from Molten Salts. *J. Am. Ceram. Soc.* **2007**, *368*, 364–368. https://doi.org/10.1111/j.1551-2916.2006.01383.x.

(205) Geselbracht, M. J.; Noailles, L. D.; Ngo, L. T.; Pikul, J. H.; Walton, R. I.; Cowell, E. S.; Millange, F.; O'Hare, D. Probing Molten Salt Flux Reactions Using Time-Resolved in Situ High-Temperature Powder X-Ray Diffraction: A New Synthesis Route to the Mixed-Valence $NaTi_2O_4$. *Chem. Mater.* **2004**, *16* (6), 1153–1159. https://doi.org/10.1021/cm034770w.

(206) Li, A. D.; Kong, J. Z.; Zhai, H. F.; Cheng, J. B.; Li, H.; Wu, D. Synthesis, Characterization, and Applications of Water-Soluble Tantalum Carboxylate Precursors via a Flux Method. *J. Am. Ceram. Soc.* **2009**, *92* (9), 1959–1965. https://doi.org/10.1111/j.1551-2916.2009.03162.x.

(207) Porter, D. A.; Easterling, K. E.; Sherif, M. Y. *Phase Transformations in Metals and Alloys, Third Edition*, 3rd Edition; Taylor & Francis: New York, NY, 2009.

(208) Huang, X.; Song, Z.; Xiu, T.; Badding, M. E.; Wen, Z. Searching for Low-Cost Li_xMO_y Compounds for Compensating Li-Loss in Sintering of Li-Garnet Solid Electrolyte. *J. Mater.* **2018**, *5* (2), 221–228. https://doi.org/10.1016/j.jmat.2018.09.004.

(209) Li, Y.; Wang, C. A.; Xie, H.; Cheng, J.; Goodenough, J. B. High Lithium Ion Conduction in Garnet-Type $Li_6La_3ZrTaO_{12}$. *Electrochem. commun.* **2011**, *13* (12), 1289–1292. https://doi.org/10.1016/j.elecom.2011.07.008.

(210) Hubaud, A. A.; Schroeder, D. J.; Key, B.; Ingram, B. J.; Dogan, F.; Vaughey, J. T. Low Temperature Stabilization of Cubic $(Li_{7-X}Al_{x/3})La_3Zr_2O_{12}$: Role of Aluminum during Formation. *J. Mater. Chem. A* **2013**, *1*, 8813–8818. https://doi.org/10.1039/c3ta11338h.

(211) Posch, P.; Lunghammer, S.; Berendts, S.; Ganschow, S.; Redhammer, G. J.; Wilkening, A.; Lerch, M.; Gadermaier, B.; Rettenwander, D.; Wilkening, H. M. R. Ion Dynamics in Al-Stabilized $Li_7La_3Zr_2O_{12}$ Single Crystals – Macroscopic Transport and the Elementary Steps of Ion Hopping. *Energy Storage Mater.* **2020**, *24* (March 2019), 220–228. https://doi.org/10.1016/j.ensm.2019.08.017.

(212) Smetaczek, S.; Wachter-Welzl, A.; Wagner, R.; Rettenwander, D.; Amthauer, G.; Andrejs, L.; Taibl, S.; Limbeck, A.; Fleig, J. Local Li-Ion Conductivity Changes within Al Stabilized $Li_7La_3Zr_2O_{12}$ and Their Relationship to Three-Dimensional Variations of the Bulk Composition. *J. Mater. Chem. A* **2019**, *7*, 6818–6831. https://doi.org/10.1039/C9TA00356H.

(213) Miara, L. J.; Richards, W. D.; Wang, Y. E.; Ceder, G. First-Principles Studies on Cation Dopants and Electrolyte|Cathode Interphases for Lithium Garnets. *Chem. Mater.* **2015**, *27* (11), 4040–4047. https://doi.org/10.1021/acs.chemmater.5b01023.

(214) Saccoccio, M.; Yu, J.; Lu, Z.; Kwok, S. C. T.; Wang, J.; Yeung, K. K.; Yuen, M. M. F.; Ciucci, F. Low Temperature Pulsed Laser Deposition of Garnet $Li_{6.4}La_3Zr_{1.4}Ta_{0.6}O_{12}$ films as All Solid-State Lithium Battery Electrolytes. *J. Power Sources* **2017**, *365*, 43–52. https://doi.org/10.1016/j.jpowsour.2017.08.020.

(215) Hovden, R.; Cueva, P.; Mundy, J. A.; Muller, D. A. The Open-Source Cornell Spectrum Imager. *Micros. Today* **2013**, *21* (01), 40–44. https://doi.org/10.1017/S1551929512000995.

(216) Đorđević, V.; Antić, Ž.; Nikolić, M. G.; Dramićanin, M. D. Comparative Structural and Photoluminescent Study of Eu^{3+}-Doped La_2O_3 and $La(OH)_3$ nanocrystalline Powders. *J. Phys. Chem. Solids* **2014**, *75* (2), 276–282. https://doi.org/10.1016/j.jpcs.2013.10.004.

(217) Inada, R.; Kusakabe, K.; Tanaka, T.; Kudo, S.; Sakurai, Y. Synthesis and Properties of Al-Free $Li_{7-x}La_3Zr_{2-x}Ta_xO_{12}$ Garnet Related Oxides. *Solid State Ionics* **2014**, *262*, 568–572. https://doi.org/10.1016/j.ssi.2013.09.008.

(218) Dhivya, L.; Murugan, R. Effect of Simultaneous Substitution of Y and Ta on the Stabilization of Cubic Phase , Microstructure , and Li^+ Conductivity of $Li_7La_3Zr_2O_{12}$ Lithium Garnet. *ACS Appl. Mater. Interfaces* **2014**, *6*, 17606–17615. https://doi.org/10.1021/am503731h.

(219) Persson, K. Materials Data on $LiLaO_2$ (SG:14) by Materials Project, doi:10.17188/1290550, mp-756544 https://materialsproject.org/materials/mp-756544/. https://doi.org/doi:10.17188/1290550.

(220) Shannon, R. D.; Prewitt, C. T. Effective Ionic Radii in Oxides and Fluorides. *Acta Crystallogr. Sect. B Struct. Crystallogr. Cryst. Chem.* **1969**, *25* (5), 925–946. https://doi.org/10.1107/s0567740869003220.

(221) Rosenblatt, M.; Davis, R. A.; Lii, K.-S.; Politis, D. N. Remarks on Some Nonparametric Estimates of a Density Function. *Ann. Math. Stat.* **1956**, *27* (3), 832–837. https://doi.org/10.1007/978-1-4419-8339-8_13.

(222) Parzen, E. On the Estimation of Probability Density Functions and Mode. *Ann. Math. Stat.* **1962**, *33*, 1065–1076.

(223) Cao, R.; Cuevas, A.; González Manteiga, W. A Comparative Study of Several Smoothing Methods in Density Estimation. *Comput. Stat. Data Anal.* **1994**, *17* (2), 153–176. https://doi.org/10.1016/0167-9473(92)00066-Z.

(224) Bowman, A. W.; Azzalani, A. *Applied Smoothing Techniques for Data Analysis*; Oxford University Press Inc.: New York, 1997.

APPENDIX A

SUPPORTING INFORMATION FOR CHAPTER 3

A.1. Experimental Methods

A.1.1. Reagents and Chemicals

Lanthanum(III) 2,4-pentanedionate (2,4-pentanedionate = acetylacetonate, 'acac') hydrate ('$La(acac)_3$'); lithium 2,4-pentanedionate ('Li(acac)'); zirconium(IV) 2,4-pentanedionate ('$Zr(acac)_4$'); propionic acid ('PA'); and lanthanum(III) nitrate hexahydrate ($La(NO_3)_3 \cdot 6H_2O$) were procured from Alfa Aesar and were of ACS grade purity or higher. Poly(vinylpyrrolidone) (PVP) with average molecular weight of 1.3 MDa; tannic acid; poly(vinylalcohol) (PVA) with average molecular weight 89,000 to 98,000 Da; 99+% tantalum(V) ethoxide ($Ta(OEt)_5$); lithium nitrate; zirconium(IV) oxynitrate hydrate ($ZrO(NO_3)_2 \cdot xH_2O$); and ACS grade anhydrous dichloromethane ('DCM') were procured from Sigma-Aldrich. The $La(acac)_3$ precursor was dried at elevated temperature (e.g. 105 °C) in vacuo to remove water of hydration.

A.1.2. Preparation of LLZO Precursor Solutions

For preparation of an aqueous polymer sol-gel solution, the Li nitrate, La nitrate, and Zr oxynitrate compounds were dissolved in de-ionized water in a molar ratio of 10.5 : 3 : 2 to result in 50% excess (by mole) Li content. The molecular weight of the Zr precursor was assumed to be 325 g/mol, corresponding to $ZrO(NO_3)_2 \sim 5.2\ H_2O$, which is consistent with previous[99] reports. Optionally, a small amount of nitric or acetic acid can be added to aid dissolution of the zirconium salt. Subsequently, PVA was added to the dissolved nitrates solution and dissolved via stirring at elevated temperature (e.g. above 80 °C) on a standard hot plate to result in a viscous sol with a mass ratio of 18.75 : 2.25 : 1 of water to metal salts to polymer.

In the case of the tannic acid (TA) chelation complex, a 0.1 M aqueous TA solution was first prepared. Separately, the Li nitrate, La nitrate, and Zr oxynitrate compounds were dissolved in deionized water in a mole ratio of 10.5 : 3 : 2. A small amount of nitric acid or acetic acid may be used in this case as well to aid dissolution of the Zr precursor. The total concentration of metal nitrates was kept to 0.1 M. Subsequently, the 0.1 M TA solution was added slowly under stirring to an equal volume of the metal nitrate solution to result in a tan, milky suspension with substantially increased viscosity (final solution has a 1:1 molar ratio of tannic acid to metal nitrates). After stirring to ensure uniformity for 30 minutes, the stir bar was removed, and the suspension was slowly evaporated at elevated temperature (80 – 120 °C) in a standard laboratory oven to result in a flaky, brittle precursor.

For preparation of the non-aqueous polymer sol-gel solution, Li(acac), $La(acac)_3$, and $Zr(acac)_4$ (mole ratio 10.5 : 3 : 2) were dissolved in PA. Subsequently, the acac-PA solution was heated to boiling on a standard hot plate (b.p. of PA is 141.2 °C) under stirring, removed from heat as soon as boiling of the solvent had started, and cooled to room temperature. Once cooled, DCM was added as a hydrophobic co-solvent followed by the addition of PVP. For Ta-doped LLZO, some of the $Zr(acac)_4$ was replaced by tantalum(V) ethoxide, added dropwise to the PA solution under stirring, to result in a nominal molar ratio of 10.5 : 3 : 1.4 : 0.6 for Li : La : Zr : Ta. The resultant sol-gel solution contained a ratio of approximately 11 : 8.3 : 1 : 1 of PA : DCM : PVP : precursors by mass. For increased throughput, the amount of precursors and PVP could be doubled with no appreciable difference in as-synthesized product.

The amounts and volumes used in typical experiments for each of the above methods are shown in **Table A1**.

A.1.3. Synthesis of LLZO Nanopowders

In the case of the aqueous PVA sol and the TA-based slurry, the precursor solution was dried at elevated temperature (80 °C < T < 120 °C) in order to obtain a flaky, brittle precursor material, which is easily crushed to form a reactive precursor powder. In this step, it is important to use a mild drying temperature to prevent the onset of rapid decomposition of the nitrates and subsequent combustion. The dried and crushed precursor powder was then subjected to calcination in air at temperatures between 600 – 800 °C for 0 – 4 h inside a muffle or tube furnace. In general, a ramp rate of 10 °C min^{-1} was employed unless otherwise noted. The authors would like to encourage caution in using this process, as the combustion of nitrates can rapidly produce large amounts of heat. It was observed in one case that if more than ~100 mL of the PVA-nitrate solutions were dried and combusted in a small crucible, a rapid reaction occurred such that the gas evolution caused the furnace door to come open. ***This is essentially an explosion, and while relatively mild, caution is still warranted in combusting nitrate-fuel mixtures.*** Similar care should be taken with the TA-nitrate solutions.

In the case of the non-aqueous sol, the solution may be poured into an alumina crucible (e.g. 25 mL of solution into a 100 mL crucible) and directly subjected to calcination in a muffle furnace, as the drying of the solvent occurs quickly at low temperatures without any significant boiling or splashing of the solution so long as the crucible is not too full. In this case, calcination was performed at temperatures between 700 – 800 °C for 0 – 4 h with a heating rate of 5 °C min^{-1} unless otherwise noted.

In these three procedures, after cooling naturally to room temperature in the furnace, the result was a white to off-white fluffy 'foam' of nanopowder under optimized conditions, which was then removed from the crucible and gently ground with an agate mortar and pestle. Very little force is required to crush the powder, which flows easily after grinding to de-agglomerate particles. As a final note, it has been observed that the internal volume of the furnace used has a role on the combustion process, where a smaller furnace volume may result in incomplete reaction. The authors believe that this is due to an insufficient amount of oxygen to fully combust the organic material if no airflow is present to remove carbon dioxide and replenish the oxygen, though detailed understanding of this phenomenon is outside of the scope of this work.

A.1.4. Materials Characterization

X-ray diffraction (XRD) on the as-calcined samples was performed using a Bruker D-8 X-ray diffractometer or a Siemens D-5000 X-ray diffractometer with CuK_{α} radiation for phase identification. The reference pattern for c-LLZO ($Ia\bar{3}d$) was generated according to Logéat[48] while the pattern from t-LLZO was obtained from Awaka[17] et al.

The sample morphology was examined using a FEI XL30 scanning electron microscope (SEM) or a FEI Nova 200 Dual Beam instrument with a Thermo Scientific solid-state X-ray detector for energy dispersive spectroscopy (EDS). Thermogravimetric / differential thermal analysis was performed using a Labsys Evo TGA/DTA in air. Transmission electron microscopy (TEM) was performed using a Philips CM 200 microscope operated at 200 kV. Scanning transmission electron microscopy (STEM) was performed using a probe corrected JEOL ARM200 STEM operated at 200 kV, equipped with a high solid angle windowless JEOL X-Ray detector and a Gatan Enfinium dual channel camera for performing electron energy loss spectroscopy (EELS). To prepare S/TEM samples, the LLZO powder or crushed precursor powder was ultrasonically suspended in methanol followed by brief immersion of a holey carbon grid (Pacific Grid Tech) in the aforementioned suspension. In the case of precursor material carbonized at 400 °C, the brittle black material was ball milled in a vibratory mill (SPEX 8000M) with isopropanol for 5 minutes to break the material into submicrometer particles. Subsequently, the suspension was applied to a copper TEM grid as described above.

Processing of EELS and EDS data was performed from raw data files (Gatan Digital Micrograph .dm3 file type) using the Cornell Spectrum Imager[215] plugin in ImageJ, optionally with further data processing performed using Matlab. Spectrum images were obtained and processed in the conventional manner by obtaining an EELS map, followed by several iterations of background removal (power law fit) to isolate the carbon K, oxygen K, and lanthanum M signals respectively. Then, the desired peak areas

were obtained via integration, and the integrated peak intensity for each EELS spectrum was mapped to each pixel in the EELS map to obtain a composite spectral image. The general workflow for EELS data processing is exemplified in **Figure A4**.

A.1.5. Pellet Preparation

Ceramic pellets of LLZO were prepared from undoped and tantalum-doped LLZO (LLZTO) nanopowders using uniaxial pressing (SpecAc manual hydraulic press). For pellets sintered at 1200 °C, 5 wt% anhydrous LiOH was added to the powder and ball-milled for 10 min (SPEX 8000M vibratory mill) in order to uniformly mix the LiOH and LLZO powder. Then, 100 – 150 mg of the desired powder was weighed and placed in a 7 mm stainless steel die and pressed at ~500 MPa using a SpecAc manual hydraulic press. Green pellets were then carefully placed on a small amount of mother powder on a sintered MgO plate, covered in more mother powder, and finally placed in a MgO crucible and covered with a MgO lid, as shown in **Figure A1a**. Use of MgO eliminates the possibility of adventitious doping by the conventionally used Al_2O_3 crucibles, providing an unreactive surface to prevent pellets and mother powder from sticking as described by Tsai et al.[81] Initially, pellets were sintered in air at 1200 °C for various times between 2-12 h, with a ramp rate of 3.33 °C min^{-1}. The sintered pellets were allowed to cool naturally to room temperature, then were removed from the crucibles and immediately polished with 400 grit SiC polishing paper to remove any adhered mother powder and generate a smooth surface. In some cases, pellets were stored in an argon-filled glovebox prior to polishing.

In order to better control the volatility of Li_2O during sintering, sintering experiments at 1100 °C were also performed (in air), which utilized a smaller MgO crucible arrangement as shown in **Figure A1b** and described in **Chapter 2.1**. In this case, the as-synthesized powder was pressed as-is (i.e. no added LiOH) into 7mm green pellets using 125 MPa of pressure. Then, pellets were embedded into a mixture of mother powder and lithium peroxide (Li_2O_2). The ratio of pellet mass ($\mathbf{m}_P$) to mother powder mass ($\mathbf{m}_{MP}$) to Li_2O_2 mass ($\mathbf{m}_{Li2O2}$) used for sintering is $\mathbf{m}_P$:$\mathbf{m}_{MP}$:$\mathbf{m}_{Li2O2}$ = **3:6:1**. The rationale for use of mother powder and Li_2O_2 is to minimize the amount of LLZO used as a sacrificial lithium source during sintering by using some Li_2O_2, while still providing a Li_2O vapor source, as maintaining Li_2O vapor pressure during sintering was shown by Huang et al.[39] to be crucial to allow good densification of LLZO. Li_2O_2 was chosen over other Li-sources such as LiOH or Li_2CO_3 since these become molten and may thus have unexpected effects on sintering, where Li_2O_2 simply decomposes to Li_2O, which has a higher melting point than the sintering temperatures used. The specific 3:6:1 ratio with some Li_2O_2 used herein was found to result in similarly effective sintering as using a

much higher ratio of mother powder ($\mathbf{m}_P$:$\mathbf{m}_{MP}$ of 1:4 to 1:5), and is able to do so with much less wasted and costly mother powder.

A.1.6. Ionic Conductivity Measurements

Polished pellets were manually coated with a graphite film by a 'drawing' method using a soft graphite rod akin to the method of Shao et al.[63] immediately after polishing as described in **Chapter 2.2.4**.

Fitting of electrochemical impedance spectra was performed using EC-Lab v.11.10 software from Biologic. Generally, impedance spectra with graphite electrodes were fit to an equivalent circuit of ($\mathbf{R}_{tot}$/$\mathbf{Q}_{tot}$)($\mathbf{Q}_{el}$) where 'tot' and 'el' are the LLZO total (bulk + grain boundary) components and electrode interface, respectively[168]. The use of this circuit was justified by the inability to resolve a second semi-circle arising from a separate grain boundary contribution. The ionic conductivity, σ (S cm^{-1}), was determined from the R_{tot} values, the pellet thickness (t), and the pellet cross-sectional area (A) per **Equation 2.2.4**.

For temperature dependent ionic conductivity measurements, pellets with Sn-Li alloy electrodes were prepared as described in **Chapter 2.2.4**.[65] Use of Li electrodes allowed resolving bulk and grain boundary impedances at room temperature, so for these EIS spectra, the circuit ($\mathbf{R}_{bulk}$/$\mathbf{Q}_{bulk}$)($\mathbf{R}_{gb}$/$\mathbf{Q}_{gb}$)($\mathbf{R}_{el}$/$\mathbf{Q}_{el}$) was used for fitting. Additionally, the temperature dependence of ionic conductivity was investigated for some pellets with Sn-Li electrodes between 25 and 70 °C in order to determine the activation energy of ion conduction (E_a) based on the Arrhenius equation (**Equation 2.2.5**). A linear regression of ln (σ) vs. T^{-1} was performed to determine the value of E_a for a subset of NAP LLZTO pellets sintered at 1100 °C for 6, 9, 12, and 15 h.

It was observed that EIS spectra became more difficult to fit in some cases for spectra acquired at higher temperatures. When fits were difficult to perform, the inflection points in the EIS spectra corresponding to the bulk and grain boundary impedance were used to approximate the impedance instead of a conventional Z-Fit routine. The impedance at the inflection point in an EIS spectrum and that calculated from a fitting routine correspond quite well (~ 1-2% difference) when Li electrodes are used, as can be seen in **Figure A11**. This method of approximating impedance has also been utilized by Huang et al.[39] Finally, it should be noted that the impedance values determined from EIS using graphite blocking electrodes correlate very well with the total impedance (bulk + grain boundary) determined from EIS using the Sn-Li electrode, indicating that the impedance measured with blocking electrodes is the total impedance rather than the bulk impedance of an LLZO pellet.

A.1.7. Processing of electron energy loss and x-ray spectra

As described in section A.1.4 above, electron energy loss spectral (EELS) datasets were processed from raw files (Gatan Digital Micrograph .dm3 file type) using the free Cornell Spectrum Imager[215] plugin in ImageJ. Spectrum images were obtained and processed in the conventional manner by obtaining an EELS map, followed by several iterations of background removal (power law fit) to isolate the carbon K, oxygen K, and lanthanum M edge(s) respectively, as shown in the EELS spectrum series below. Then, the desired peak areas were obtained via integration, and the integrated peak intensity for each EELS spectrum was mapped to each pixel in the EELS map to obtain a composite spectral image. Since the O K-edge map overlaps almost completely with the La-M map, the O K-edge map is omitted in favor of mapping the La signal in **Figure 3.4**. The energy dispersive x-ray spectra were processed by simple integration of the relevant peaks, as there was negligible background. The average EDS spectrum from the EDS map in **Figure 3.4** is shown in **Figure A5**.

A.2. Supporting Tables

Table A1. Quantities of reagents used in typical syntheses of LLZO using the aqueous and non-aqueous polymer methods.

Method	**Metal Precursors**	**Organic**	**Solvent**
PVA	0.7245 g $LiNO_3$ 1.299 g $La(NO_3)_3 \cdot 6H_2O$ 0.642 g $ZrO(NO_3)_2 \cdot 5H_2O$	6 g PVA	50 mL Water
TA	0.234 g $LiNO_3$ 0.42 g $La(NO_3)_3 \cdot 6H_2O$ 0.207 g $ZrO(NO_3)_2 \cdot 5H_2O$	50 mL of 0.1 M TA	50 mL Water
NAP (undoped LLZO)	1.02 g Li(acac) 1.31 g $La(acac)_3$ 0.975 g $Zr(acac)_4$	3.32 g PVP	27.7 mL PA 27.7 mL DCM
NAP (LLZTO)	1.02 g Li(acac) 1.31 g $La(acac)_3$ 0.683 g $Zr(acac)_4$ 0.156 mL $Ta(OEt)_5$	3.32 g PVP	27.7 mL PA 27.7 mL DCM

Table A2. Tabulated pellet data for NAP LLZTO pellets sintered at 1100 for 6, 9, 12, and 15 h used for calculating activation energy. Table including sintering conditions, relative density, ionic conductivity (bulk or total specified), and type of electrode used. Additionally, since multiple pellets were sintered at their various conditions, the minimum and maximum values of total ionic conductivity and relative density are also noted (*italics*). Note that the value of σ calculated from EIS spectra with graphite electrodes corresponds well to the σ_{tot} value calculated from EIS spectra with Sn-Li electrodes (**bolded**). The 1100 °C 12 h pellet with the highest ionic conductivity has a corresponding EIS spectrum in **Figure A12**.

Sintering Conditions	**Ionic Conductivity (mS cm^{-1})**				**Relative Density (%)**	**Min-Max Density (%)**	**E_a (eV)**
	σ_{tot} (graphite)	**σ_{bulk} (SnLi)**	**σ_{tot} (SnLi)**	**Min-max (σ)**			
1100 °C, 6 h	**0.53**	0.61	**0.57**	*0.31-0.53*	90.5	*86.8-90.5*	0.398
1100 °C, 9 h	**0.45**	0.53	**0.45**	*0.24-0.45*	91.4	*91.4-92.8*	0.389
1100 °C, 12 h	**0.45**	0.51	**0.45**	*0.34-0.67*	91.9	*91.5-93.6*	0.42
1100 °C, 15 h	**0.44**	0.49	**0.42**	*0.40-0.44*	92.0	*90.8-92*	0.342

A.3. Supporting Figures

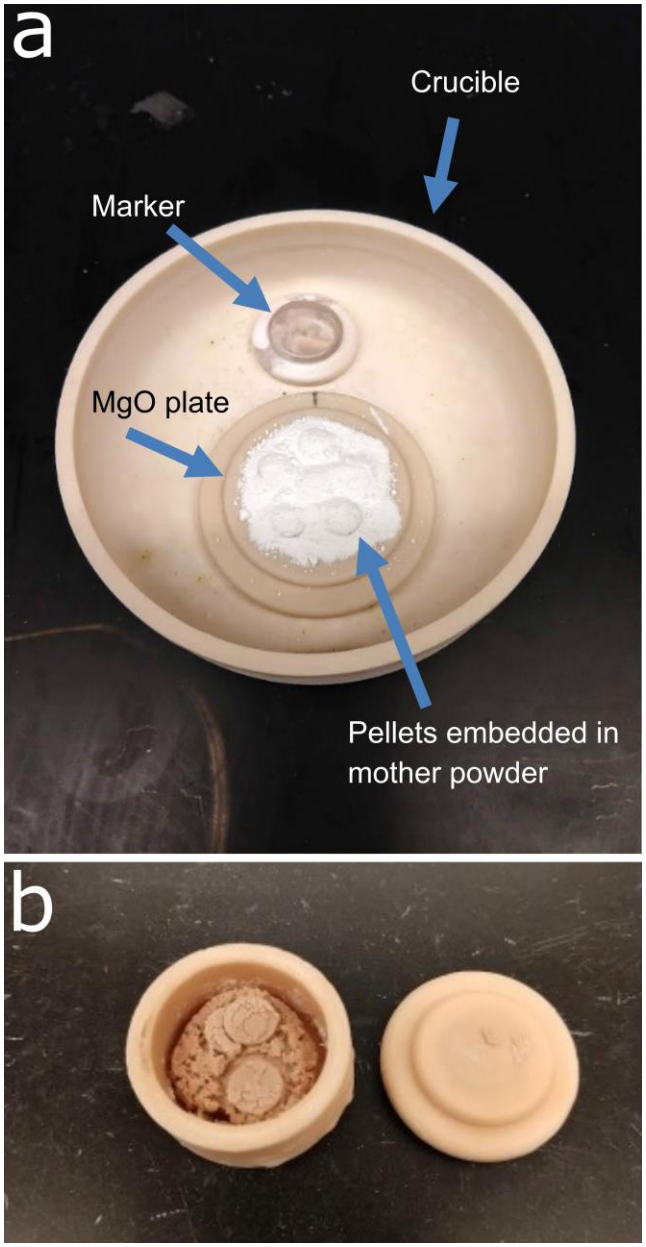

Figure A1. **a**) Photograph of typical pellet configuration for sintering at 1200 °C, in this case using a MgO crucible and MgO plate. Several pellets are laid on a bed of white mother powder, with another layer of mother powder covering the tops of the pellets. A small MgO piece is also placed in the crucible to serve as a marker for keeping track the orientation of the pellets, **b**) small MgO crucible for sintering at 1100 °C and minimizing crucible volume to increase Li_2O vapor pressure, with sintered pellets sitting atop a MgO plate – sintered mother powder can be seen under, around, and on top of the pellets, which is easily removed before polishing

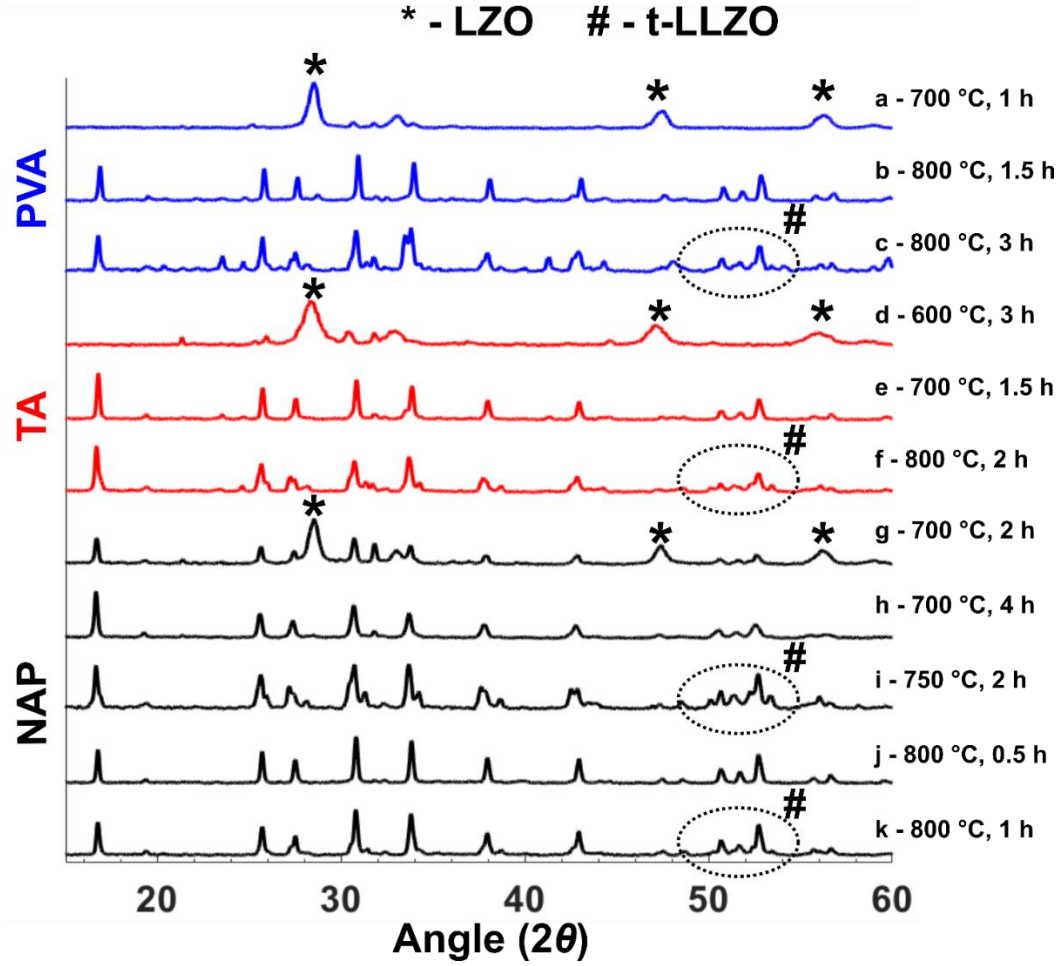

Figure A2. XRD patterns of products obtained using PVA (a-c), TA (d-f), and NAP (g-k, corresponding to samples NAP-1 through NAP-5, respectively) methods with calcination parameters used. The presence of t-LLZO in some samples is shown with a dotted outline and identified by the presence of peak splitting (i.e. the presence of clearly separated peaks or marked broadening of peaks relative to the pure cubic phase of LLZO). The XRD patterns corresponding to the NAP samples in Table 1 are shown here: At 700 °C for 2 h (NAP-1, **Figure A2g**), a mixture of LZO and c-LLZO forms, converting completely to c-LLZO with a 4 h hold time at 700 °C (NAP-2, **Figure A2h**). However, increasing the calcination temperature by just 50 °C to 750 °C results in the onset of formation of t-LLZO in 2 h (NAP-3, **Figure A2i**). Short reaction times at 800 °C were also investigated, using a direct ramp with no intermediate hold temperature, revealing that pure c-LLZO forms in only 0.5 h at 800 °C (NAP-4, **Figure A2j**), with the onset of t-LLZO formation occurring after 1 h (NAP-5, **Figure A2k**).

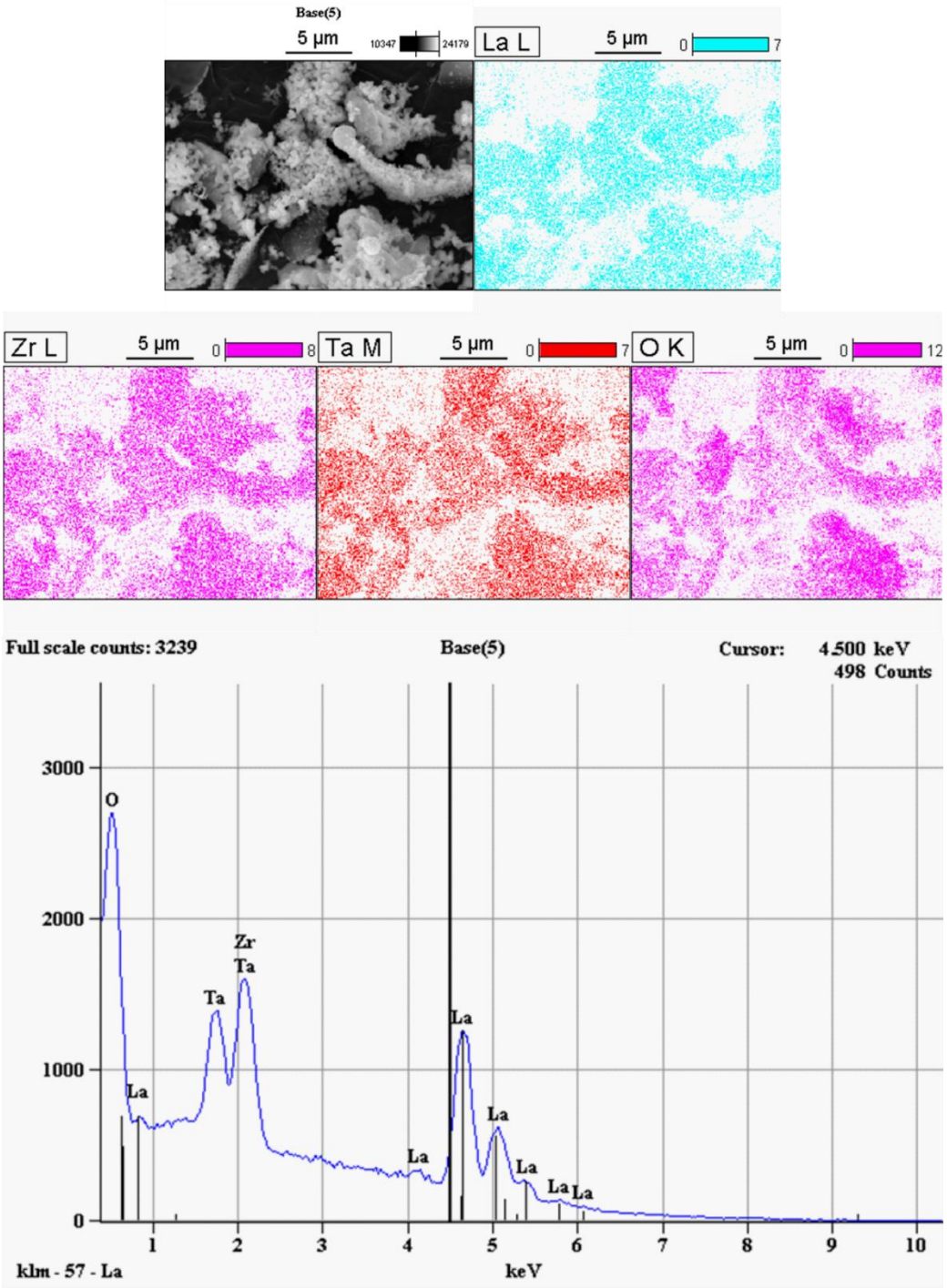

Figure A3. EDS maps and spectrum of LLZTO nanopowder

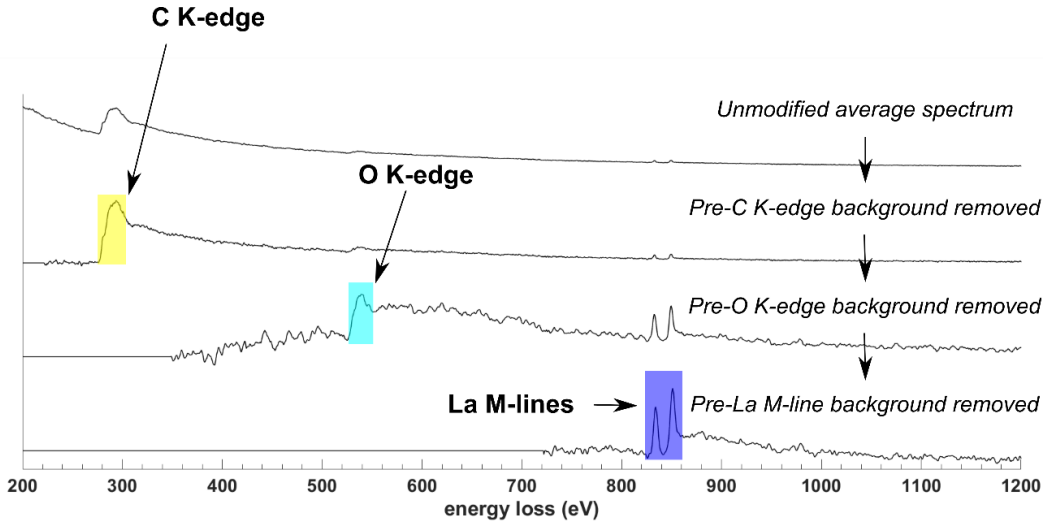

Figure A4. Example of workflow for EELS spectrum processing, using the average of all EELS spectra from the spectral image shown in **Figure 3.4**: the background is removed from the raw data (top) before the first edge (carbon K-edge), to result in the second EELS spectrum and enable integration of the carbon K EELS signal (yellow shaded area). Subsequently, the background is removed from the second spectrum before the O K-edge, followed by integration of the teal shaded area for the O K-edge. Finally, the background is removed from the third spectrum to allow integration of the La M-lines (blue shaded area).

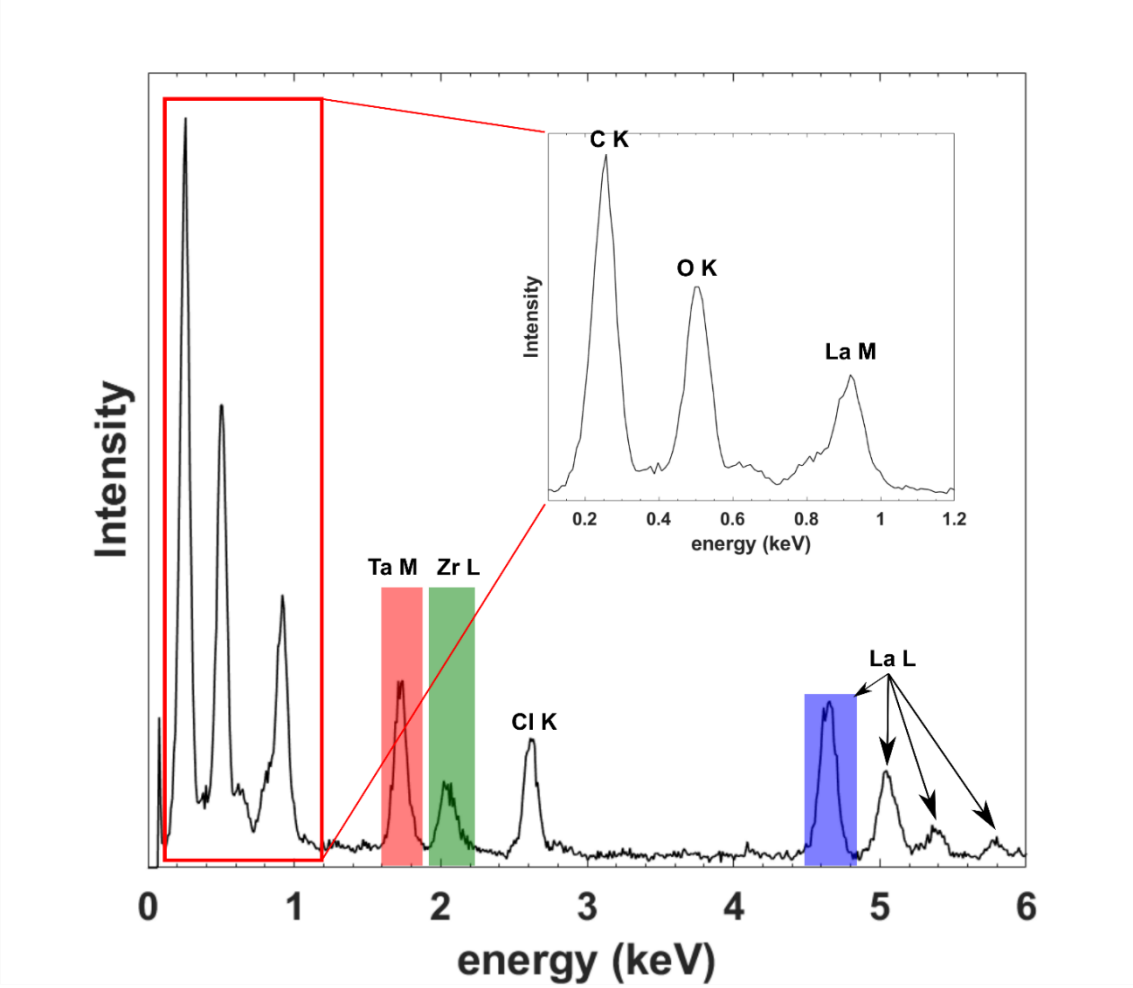

Figure A5. Average EDS spectrum of EDS map in **Figure 3.4**, with integrated peak areas for Ta M, Zr L, and La L peaks (red, green, and blue shaded regions respectively) shown. Note the evident presence of some Cl contamination, the source of which is unknown but assumed to be residual adsorbed material from the ball milling jar used to prepare the TEM sample. Also note the absence of the N K peak (expected at 0.392 keV), indicating full decomposition of the pyrrolidone groups from PVP when carbonized at 400 °C.

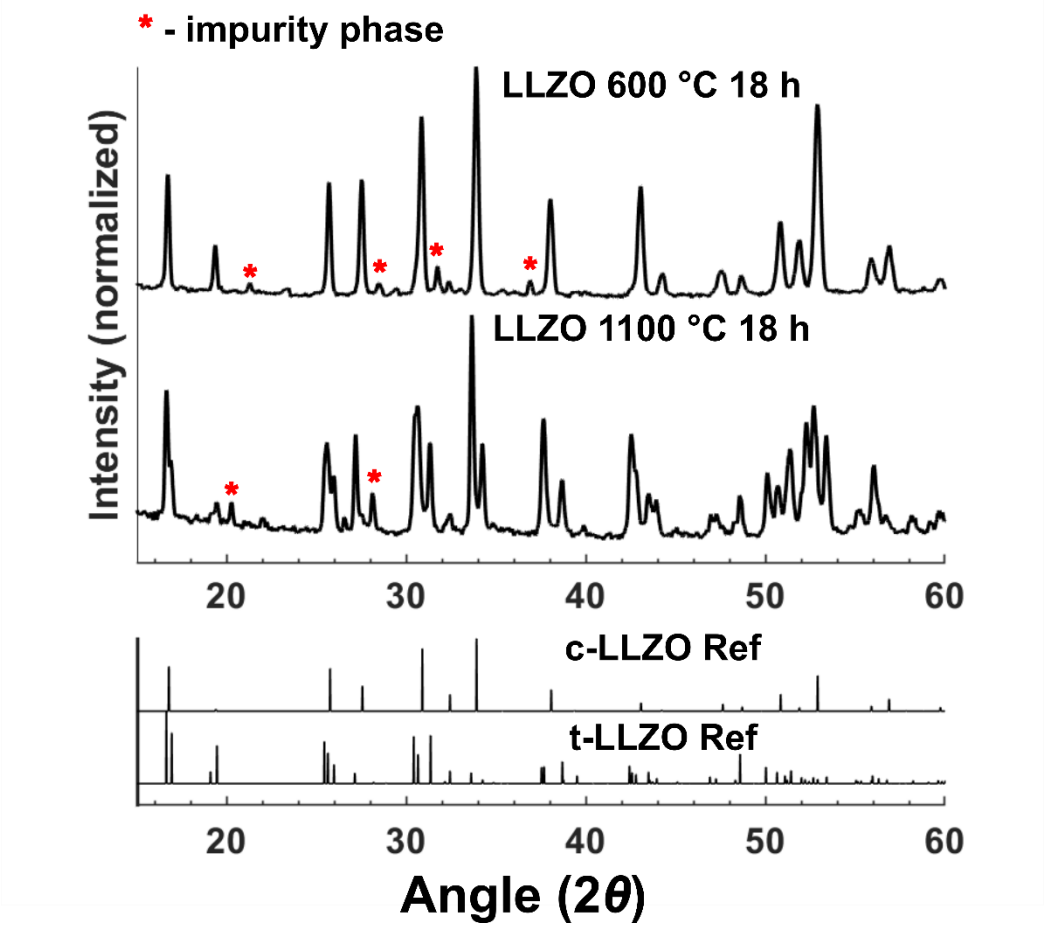

Figure A6. Comparison of XRD patterns obtained from pellets made from undoped c-LLZO nanopowders synthesized using the NAP method. The pellets were sintered at 600 °C for 18 h (where the LLZO remained cubic) or 1100 °C for 18 h (where the LLZO converted to t-LLZO). Reference patterns for c-LLZO and t-LLZO are shown below based on Logéat et al.[48] and Awaka et al.[17] respectively. Unidentified reflections from impurity phase(s) indicated with asterisks. The XRD results indicate that 600 °C is a low enough temperature to prevent significant grain coarsening that promotes the LLZO phase transformation from cubic to tetragonal, while sintering at 1100 °C results in complete conversion to t-LLZO. The presence of t-LLZO after sintering at 1100 °C demonstrates that in addition to the absence of intentional doping of the powder, no adventitious doping from the alumina crucibles occurred during combustion synthesis or sintering.

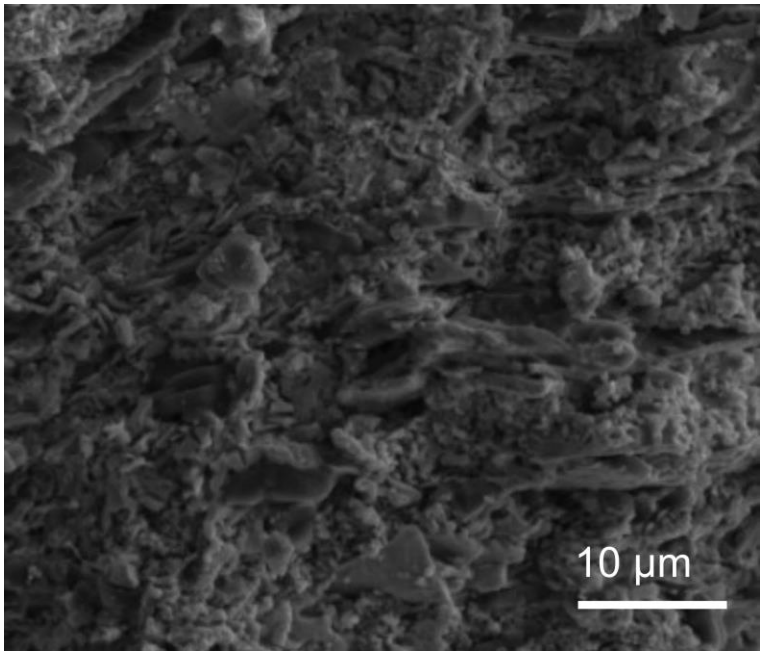

Figure A7. SEM fracture surface image of undoped c-LLZO pellet sintered at 600 °C showing high amount of porosity and only minimal sintering (relative density ~65%).

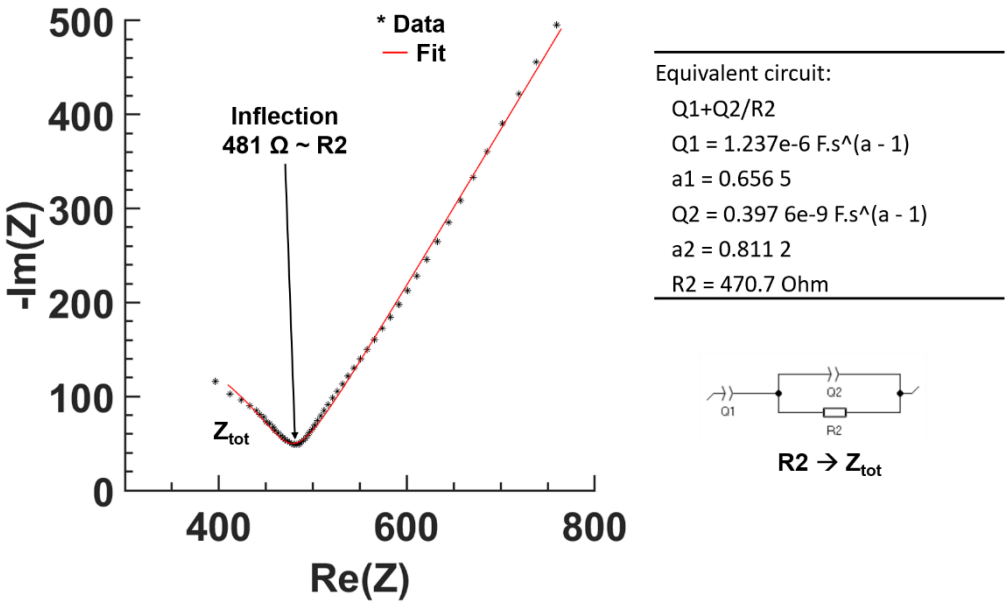

Figure A8. Typical EIS spectrum from an LLZTO sample with graphite blocking electrodes with equivalent circuit used for impedance fitting – note that the value of impedance at the inflection point corresponds well with that from impedance fitting (~ 2% error)

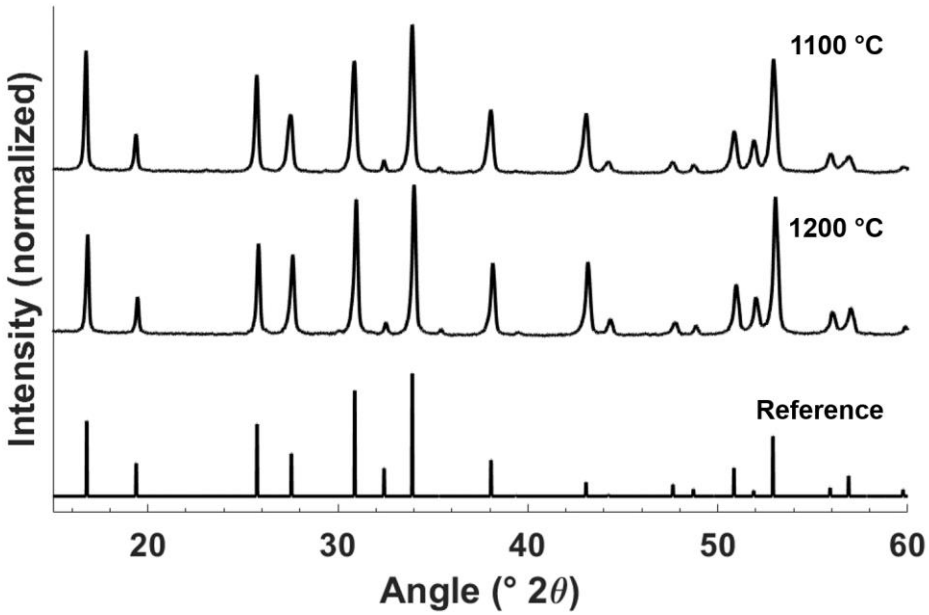

Figure A9. XRD patterns of LLZTO pellets after sintering at 1100 and 1200 °C, with reference pattern for cubic LLZTO (Logeat et al.[48]) shown below for comparison

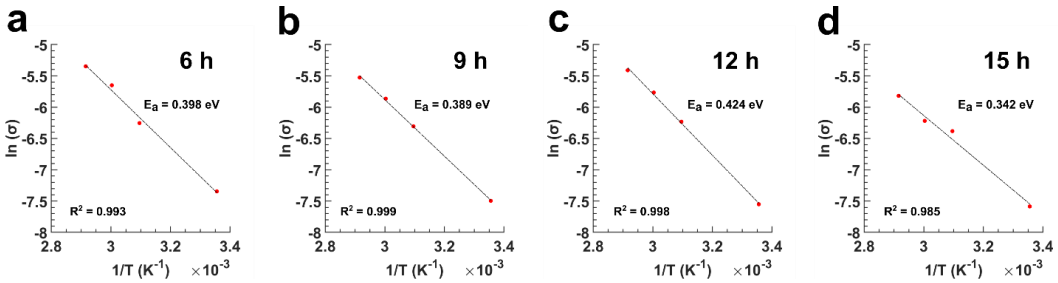

Figure A10. Arrhenius plots used for calculating activation energy for pellets sintered at 1100 °C for (**a,b,c,d** respectively) 6, 9, 12, and 15 hours, with corresponding calculated Ea values and R^2 values shown

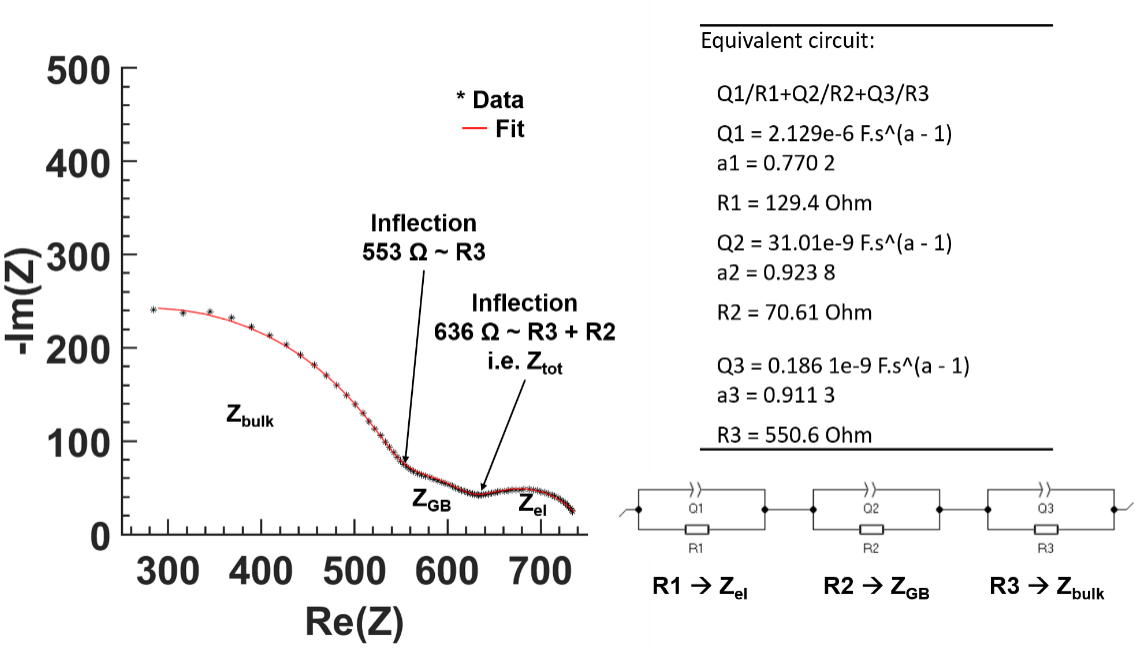

Figure A11. Comparison of typical impedance spectrum with Li electrodes with the value of impedance determined from Z-Fit routine and the inflection points of the EIS curve, showing good agreement (~ 1-2% error) between both methods of determining impedance.

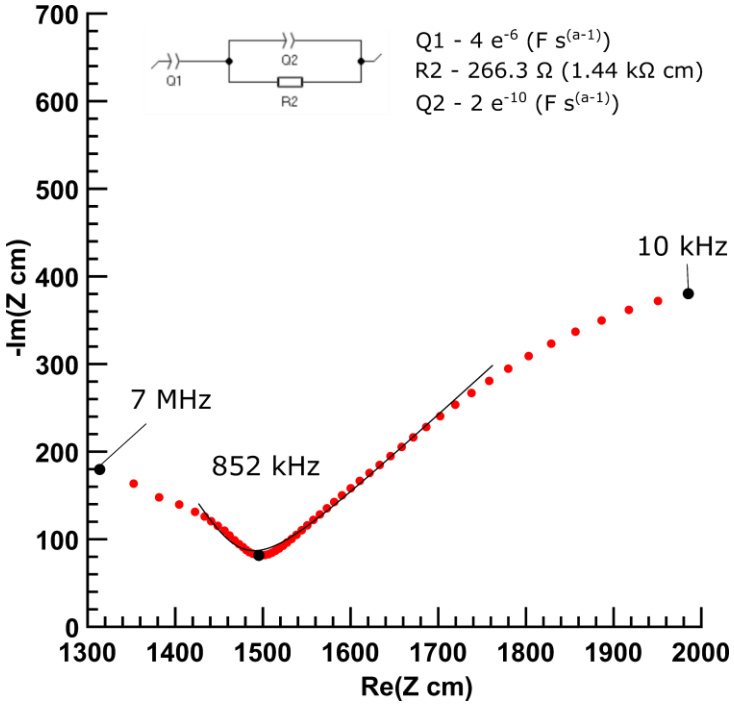

Figure A12. Nyquist plot of best NAP LLZTO pellet (1100 °C 12 h) with impedance normalized to pellet dimensions – this sample was only measured up to 10 kHz, and the first few data points were omitted from the Z-Fit due to instrument noise. Based on the resistivity at the inflection point, the conductivity is ~ 0.67 mS cm^{-1}, and based on the circuit fit the conductivity is nearly 0.7 mS cm^{-1}. The more conservative value is reported.

APPENDIX B

SUPPORTING INFORMATION FOR CHAPTER 4

B.1. Electrochemical Impedance Spectroscopy Fitting

For the samples presented in **Chapter 4**, Au electrodes were sputtered as ion-blocking electrodes for EIS. It was found that fitting the impedance data to the equivalent circuit $(R_1Q_1)(R_2Q_2)(R_3Q_3)$ gave the best fits.

In each case, the bulk ionic conductivity, σ (S/cm), was determined from the R_2 values, the pellet thickness (d), and the pellet cross-sectional area (A) using **Equation B1**:

$$\sigma = \frac{d}{R_2 A} \qquad \textbf{(B1)}$$

B.2. Supporting Tables

Table B1. Reaction temperature and duration used for exploratory MSS syntheses without added dopants. The corresponding XRD patterns for the products obtained in these experiments are shown in **Figure B2**.

Experiment #	Conditions	Results
1	500°C 1 hour	LaOCl
2	500°C 2 hours	LaOCl
3	500°C 3 hours	LaOCl
4	600°C 1 hour	LaOCl + LZO
5	600°C 2 hours	LaOCl + LZO
6	600°C 3 hours	LaOCl + LZO
7	700°C 1 hour	LaOCl + LZO
8	700°C 2 hours	LaOCl + LZO
9	700°C 3 hours	LaOCl + LZO
10	800°C 1 hour	LZO
11	800°C 2 hours	LZO
12	800°C 3 hours	LZO
13	900°C 1 hour	LZO
14	900°C 2 hours	LZO
15	900°C 3 hours	LZO + **c-LLZO**
16	900°C 6 hours	**c-LLZO**

Table B2. Z Fit parameters for EIS data of (**a**) ALLZO pellet (10% LiOH added, 18 hr sinter), (**b**) GLLZO pellet (10% LiOH added, 12 hr sinter), (**c**) GLLZO pellet (3% LiOH added, 6 hr sinter)

	a) **ALLZO (10%)**	b) **GLLZO (10%)**	c) **GLLZO (3%)**
Q_1	$44.61e^{-9}$ F	$9.611e^{-9}$ F	$0.214e^{-6}$ F
a_1	0.862	0.773	0.787
R_1	466.8 Ω	224.8 Ω	145.2 Ω
Q_2	$0.183e^{-9}$ F	$26.45e^{-9}$ F	$2.263e^{-9}$ F
a_2	0.985	0.597	0.730
R_2	**1261 Ω**	**582.1 Ω**	**472.5 Ω**
Q_3	$0.347e^{-6}$ F	$1.283e^{-6}$ F	$0.502e^{-6}$ F
a_3	0.683	0.603	0.703
R_3	307734 Ω	50,434 Ω	58837 Ω
$\chi^2/\|Z\|$	$3.12e^{-3}$	$3.30e^{-3}$	$9.27e^{-4}$
χ^2	5505	2584	302.4
X/√(N)	6.423	7.417	2.785
Thickness	0.0906 cm	0.0481 cm	0.0585 cm
Area	0.312 cm^2	0.256 cm^2	0.3338 cm^2
σ	**0.230 mS cm^{-1}**	**0.323 mS cm^{-1}**	**0.371 mS cm^{-1}**

B.3. Supporting Figures

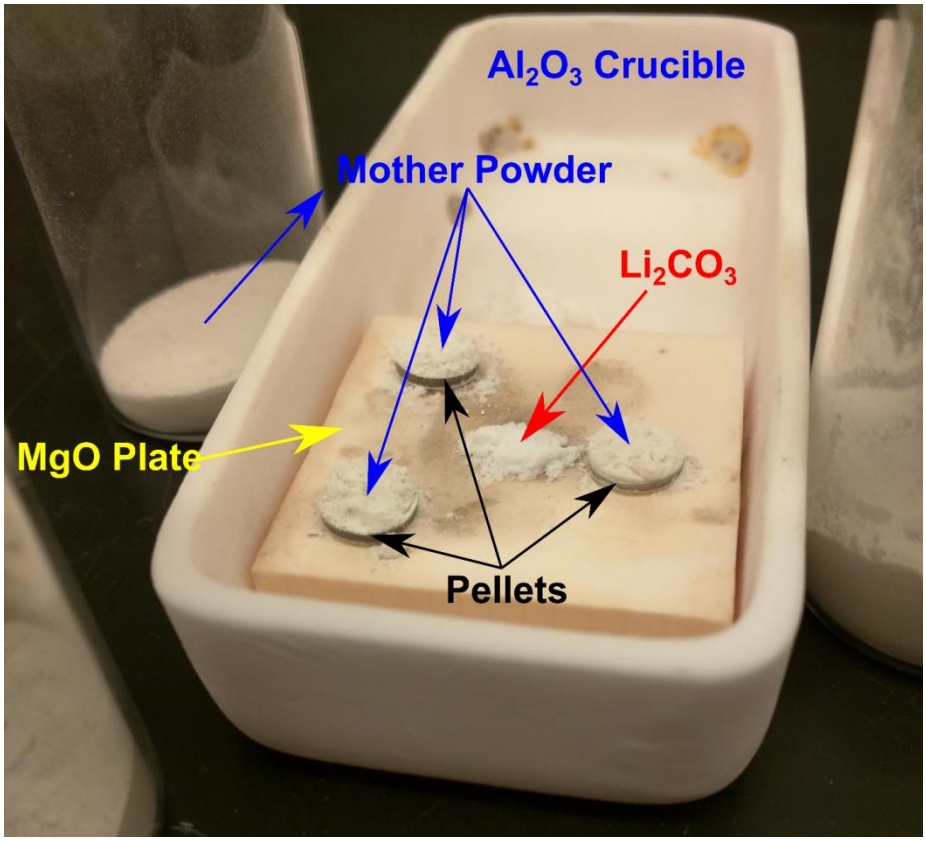

Figure B1. Photograph of typical pellet configuration for sintering. An MgO plate is set inside of a larger Al_2O_3 crucible. Then, mother powder is placed on the MgO plate. The pressed green pellets are placed on top of the mother powder and then coated with more mother powder. A small amount of Li_2CO_3 is placed on the MgO crucible in the middle of the pellets to provide Li-rich vapor during sintering. Finally, the entire assembly is covered in an Al_2O_3 lid.

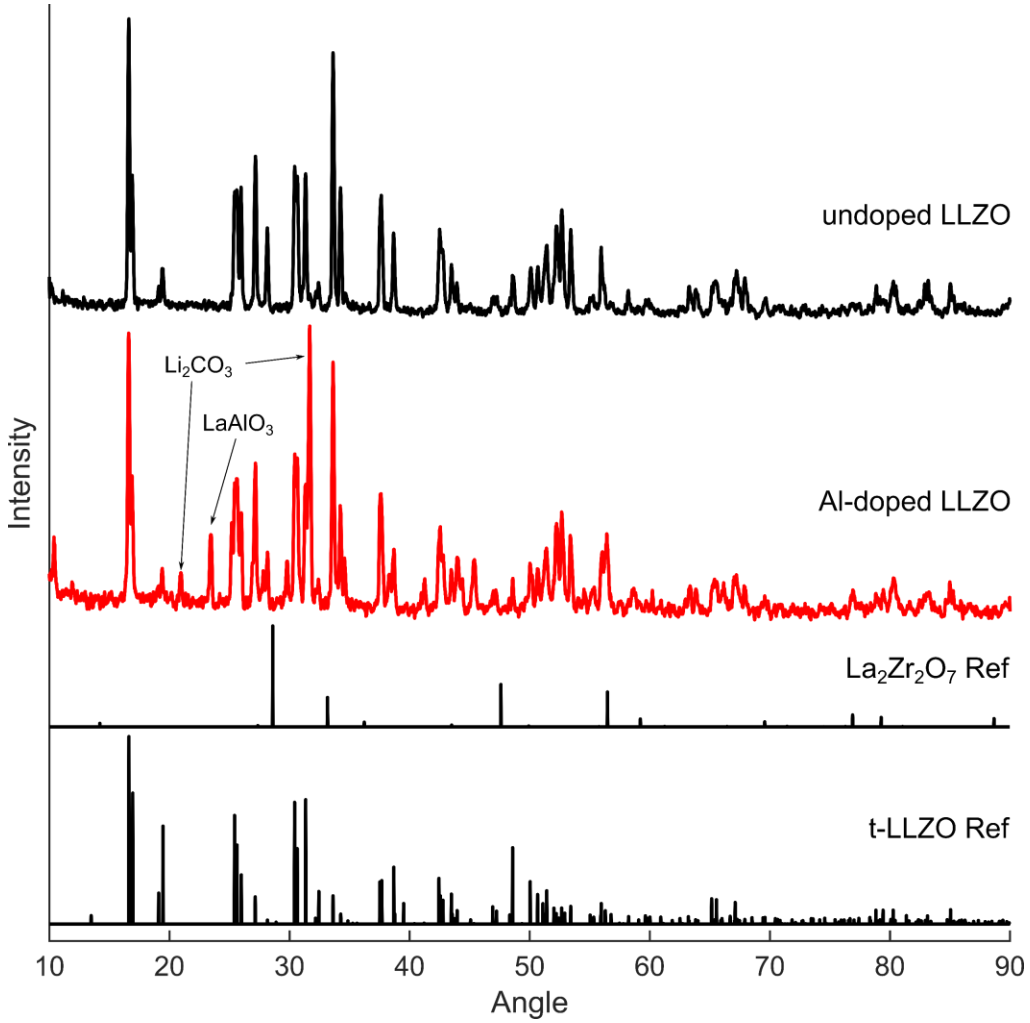

F**igure B2**. XRD patterns of undoped and Al-doped LLZO synthesis using the same $LiNO_3$-LiCl molten salt medium as was used by Reddy et al.,[122] showing inability to incorporate Al into LLZO even at 800 °C.

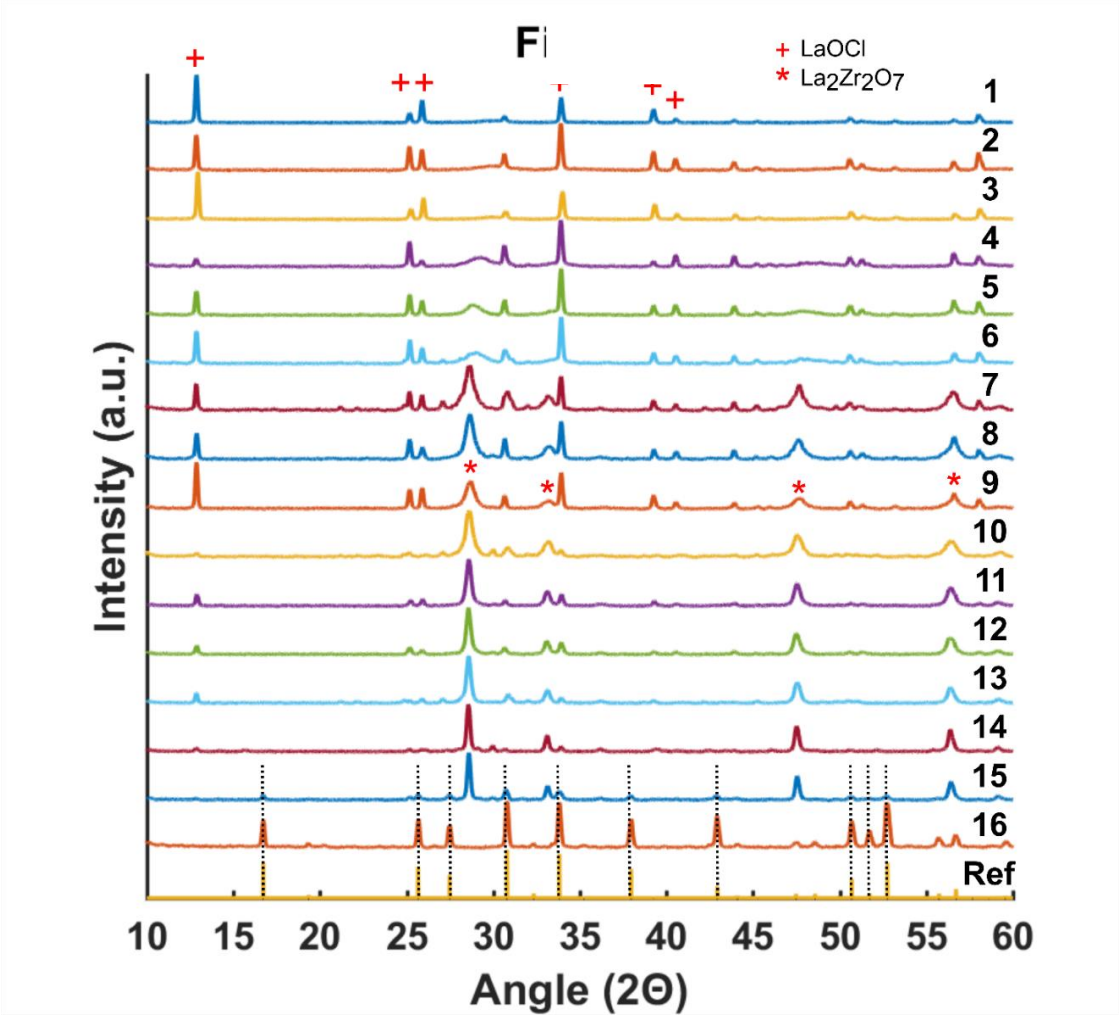

Figure B3. XRD patterns corresponding to the experimental parameters in **Table B1**, with various synthesis times and temperatures ranging from 1 to 3 hr and 500 °C to 900 °C. The LLZO reference pattern is shown at the bottom.

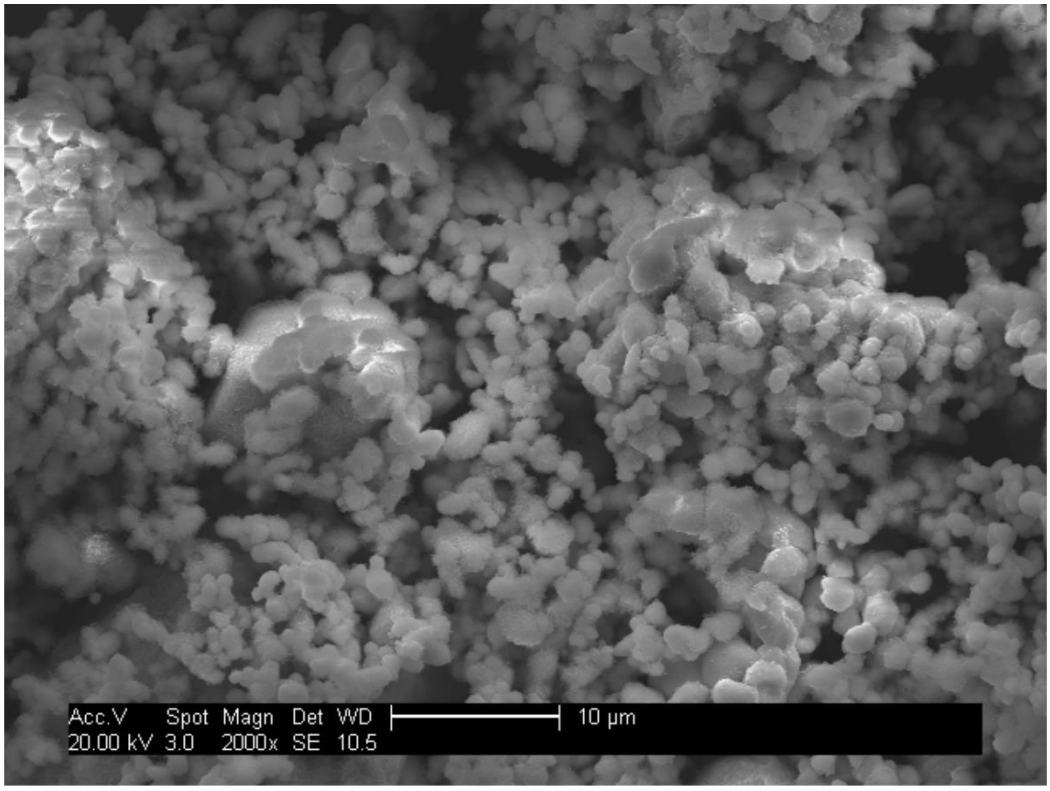

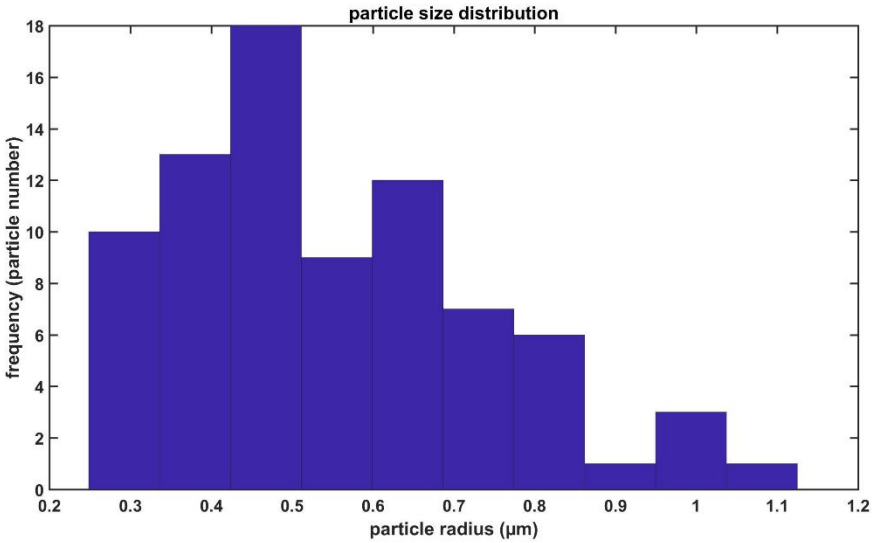

Figure B4. (**top**) SEM image of undoped c-LLZO powder synthesized at 900°C for 4 hr, (**bottom**) histogram showing particle radius distribution.

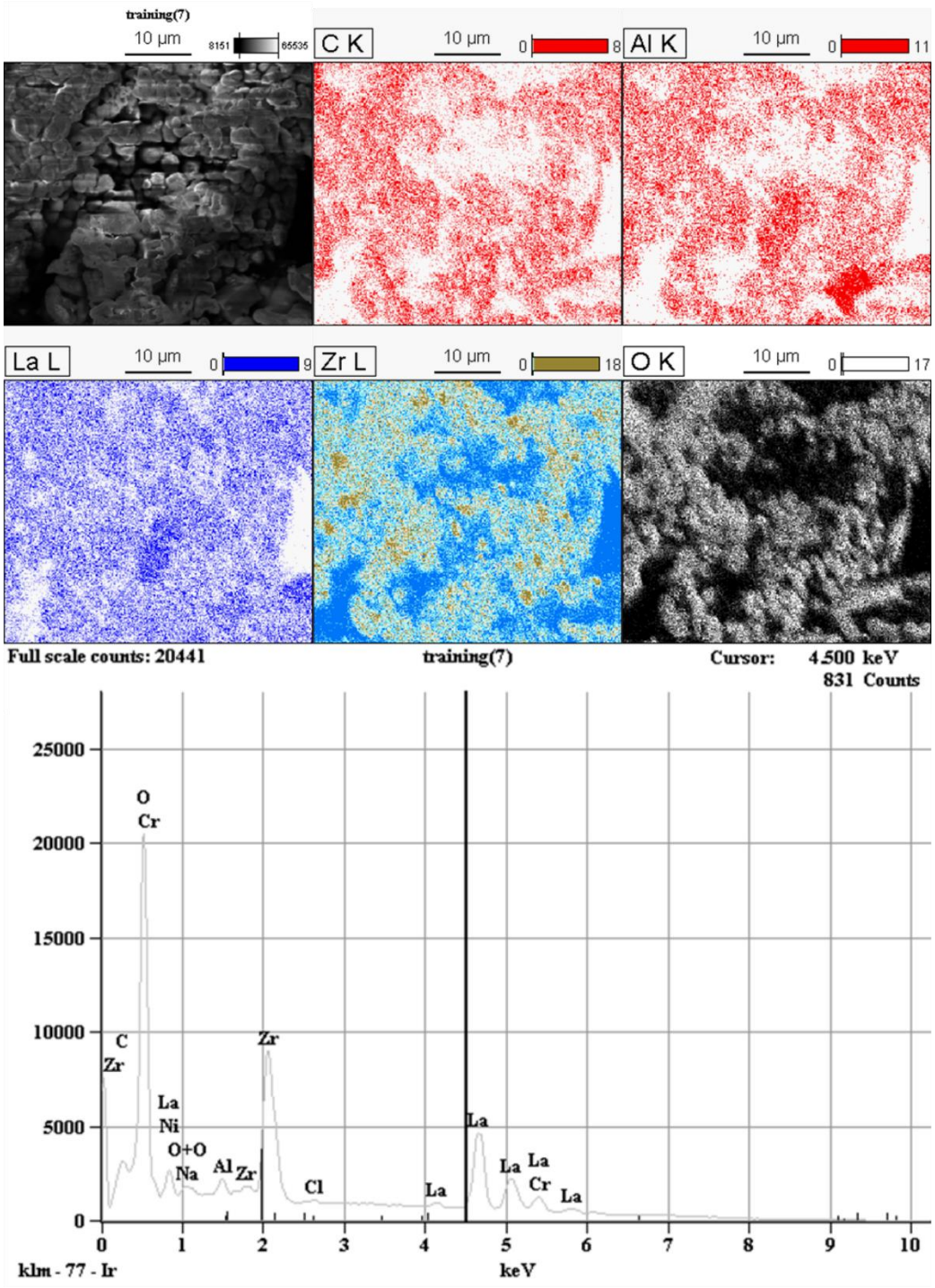

Figure B5. EDS maps and spectrum of ALLZO powders, illustrating uniform distribution of Al.

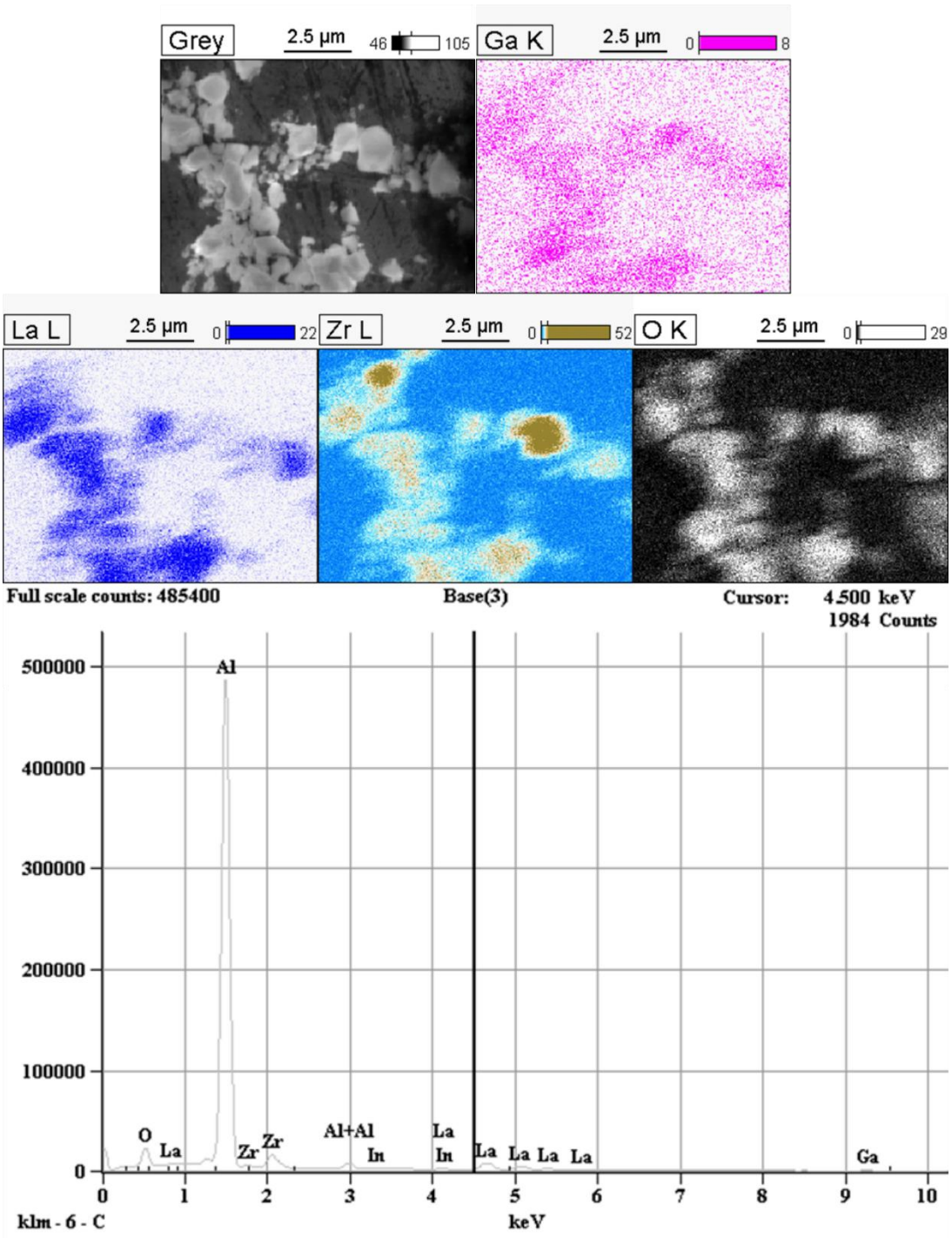

Figure B6. EDS maps and spectrum of GLLZO powders, illustrating uniform distribution of Ga (note that the Al-signal in the EDS spectrum is from the SEM substrate).

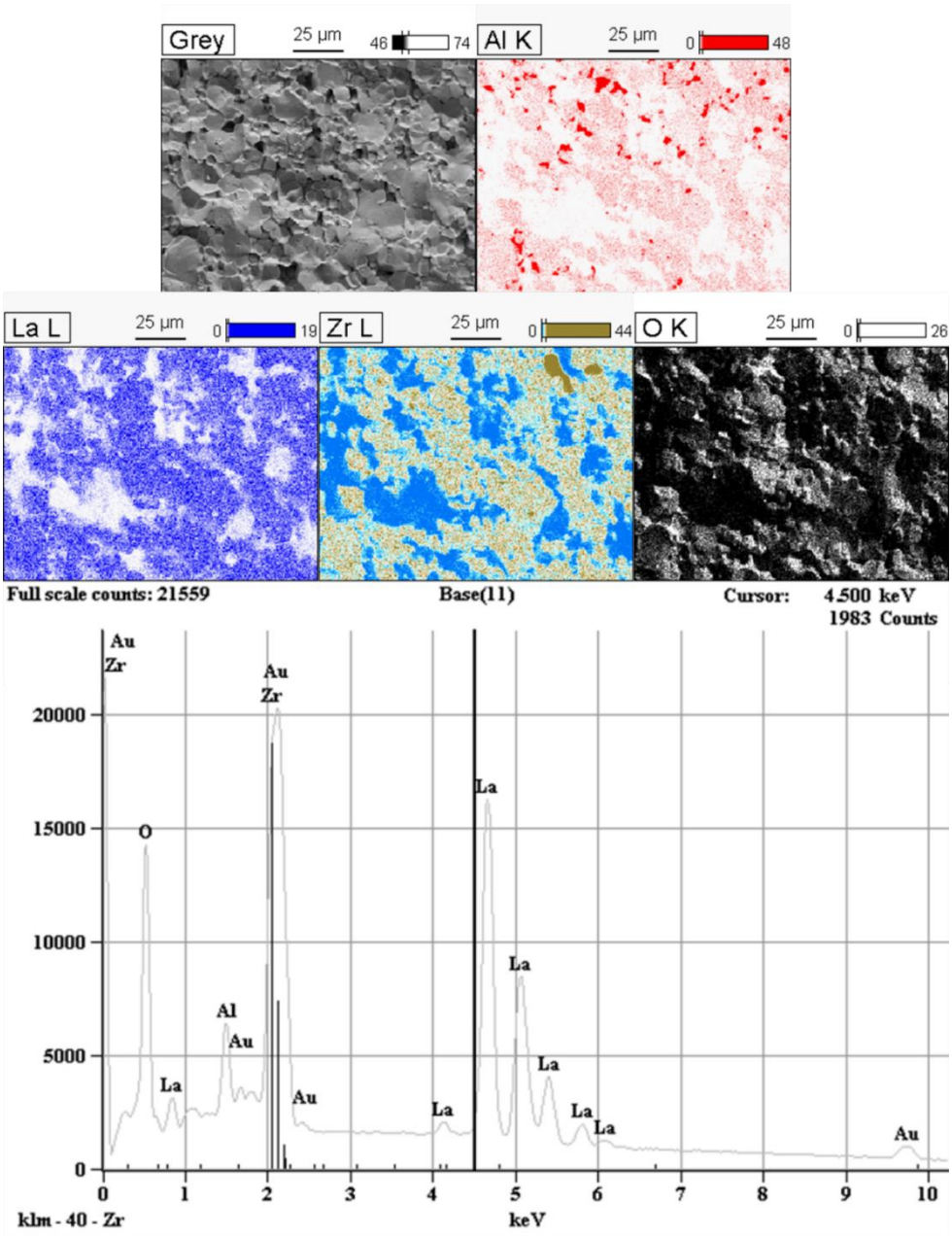

Figure B7. EDS maps and spectrum of ALLZO pellet fracture surface, illustrating uniform distribution of Al. Note that presence of Au signal is due to sputtered layer to minimize charging, and regions of higher intensity seen particularly in the Al K map may be due to X-Ray takeoff angle matching the detector acceptance angle or presence of Al-rich phases.

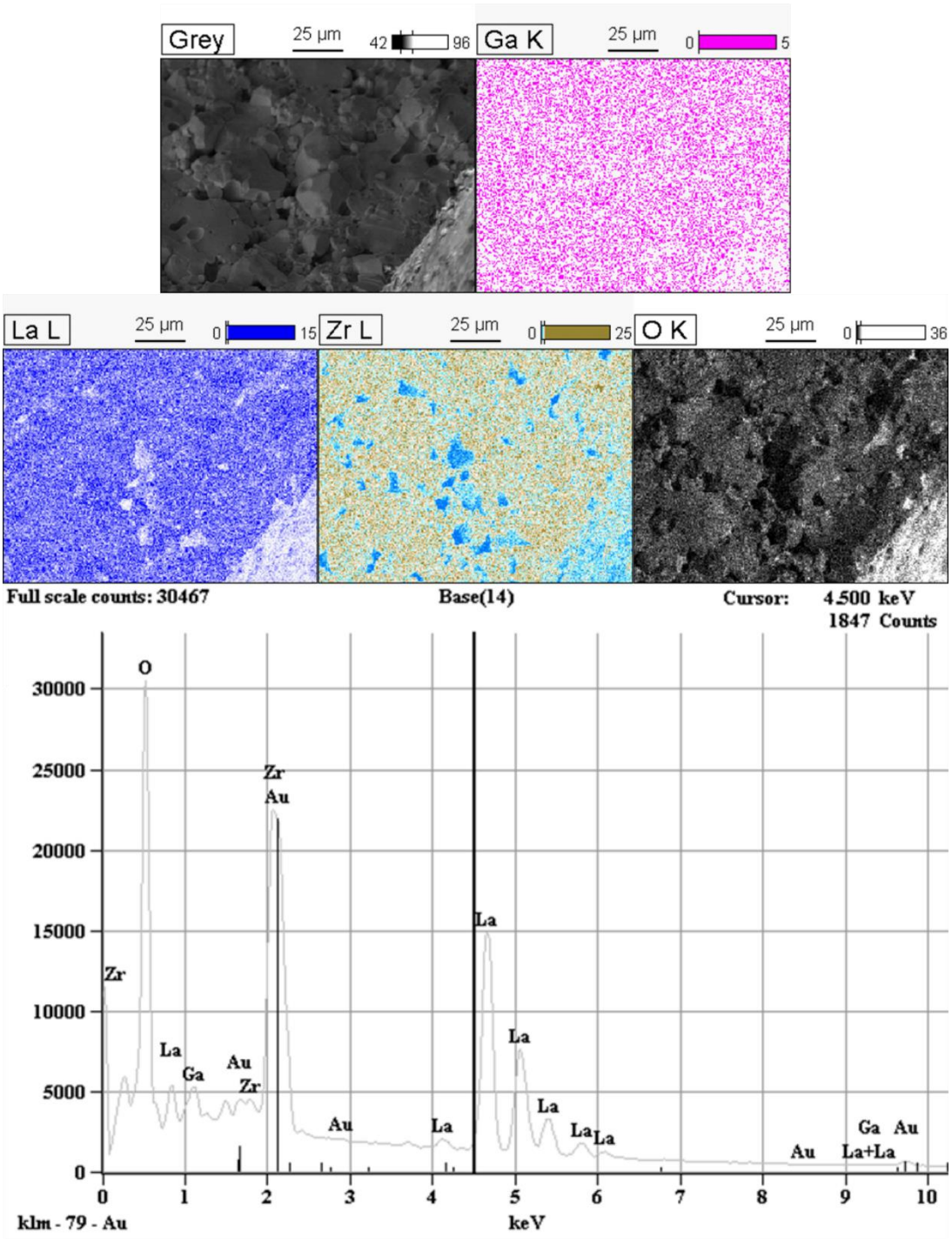

Figure B8. EDS maps and spectrum of GLLZO pellet fracture surface, illustrating uniform distribution of Ga (presence of Au signal is due to sputtered layer to minimize charging).

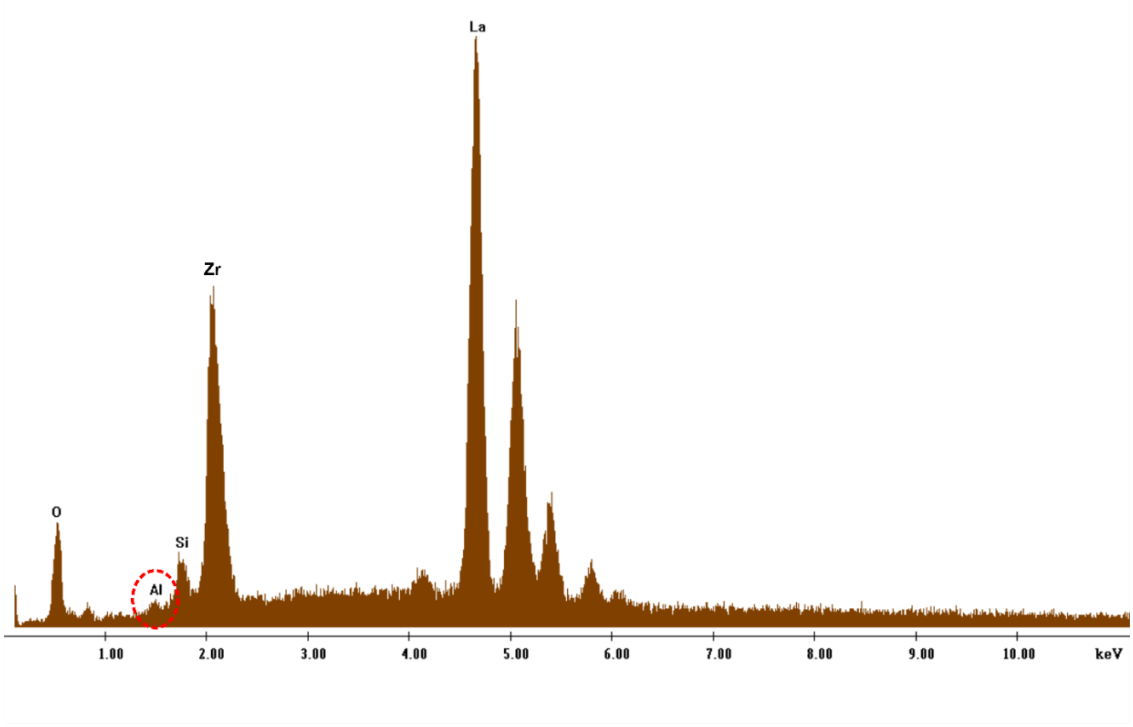

Figure B9. EDS spectrum of c-LLZO experiment # 16 (6 hr reaction time at 900 °C). A small amount of Al signal can be seen, suggesting that some adventitious Al-doping from the alumina crucible is possible. However, the relative signal level is substantially less than that of the intentionally Al-doped LLZO (see **Figure B7** EDS spectrum for example).

APPENDIX C

SUPPORTING INFORMATION FOR CHAPTER 5

C.1. Experimental Methods

C.1.1. Materials and Reagents

All reagents used were of ACS grade or higher unless otherwise noted and used as-received. Lithium nitrate ($LiNO_3$, anhydrous), lithium hydroxide (LiOH, anhydrous), zirconium oxychloride octahydrate ($ZrOCl_2 \cdot 8H_2O$), tantalum oxide (Ta_2O_5), lanthanum hydroxide ($La(OH)_3$), and lanthanum nitrate hexahydrate ($La(NO_3)_3 \cdot 6H_2O$) were obtained from Alfa Aesar. Zirconium oxynitrate hydrate ($ZrO(NO_3)_2$ x H_2O) was obtained from Sigma-Aldrich. Lithium peroxide (Li_2O_2, technical grade, 95%) was obtained from Acros Organics. Isopropanol (ACS grade) and methanol (HPLC grade) were obtained from BDH Chemical.

C.1.2. Molten Salt Synthesis of LLZTO in eutectic LiCl-KCl (chloride MSS method)

The flux forming salts (LiCl and KCl in a 0.59 : 0.41 molar ratio) were mixed with the LLZTO reagents ($LiNO_3$, $La(NO_3)_3 \cdot 6H_2O$, $ZrOCl_2 \cdot 8H_2O$ and Ta_2O_5) using a mortar and pestle in a mass ratio of 3 : 1. The Li : La : Zr : Ta molar ratio used was 9.6 : 3 : 1.4 : 0.6 (50% excess Li) for a targeted nominal composition $Li_{6.4}La_3Zr_{1.4}Ta_{0.6}O_{12}$. The mixture (typically ~ 40 g total) was placed in an alumina crucible (Coorstek high alumina, 250 mL volume) and heated at a rate of 5 °C min^{-1} to the reaction temperature in a muffle furnace (Carbolite ELF 11 type). The synthesis was performed in air. The mixture was held for 4 hours at 850 or 900 °C. It was found that Ta-doped LLZO forms at a somewhat lower temperature than undoped, Al-doped, and Ga-doped LLZO reported in our previous work.[161]

C.1.3. Molten Salt Synthesis of LLZTO in LiCl-LiOH (mixed MSS method)

The flux forming salts (LiCl and LiOH, mass ratio 1 : 1) were mixed with the same reagents at a mass ratio of 2 : 1 (total mass ~ 30 g) as described in the chloride MSS method (with the exception that for these experiments, $ZrO(NO_3)_2$ was used instead of $ZrOCl_2$), heated at a rate of 5 °C min^{-1} in alumina crucibles (Coorstek, high alumina, 100 mL) and held at 550-900 °C for various times between 1 – 8 hours in a muffle furnace (Thermo Scientific LindBerg Blu M muffle furnace or Carbolite ELF 11 type muffle furnace). The synthesis was performed in air. The ratio of flux salts to reagents was 2 : 1 by mass.

C.1.4. Molten Salt Synthesis of LLZTO in $LiNO_3$-LiOH-Li_2O_2 (HB and mHB MSS method)

In general, the flux forming salts ($LiNO_3$, LiOH, and Li_2O_2) were coarsely mixed and heated at a rate of 5 °C min^{-1} in alumina crucibles (Coorstek, high alumina, 100 mL) to the reaction temperature. Reactions were performed in a small muffle furnace (MTI Corporation KSL-1100X). For the highly basic method (HB-MSS), the molar ratio of $LiNO_3$: LiOH : Li_2O_2 was 1 : 2 : 2 while the modified highly basic method (mHB-MSS) adopted a molar ratio of 1.2 : 1 : 3.4 to afford a less viscous molten reaction medium. It should be noted that since $LiNO_3$ decomposes above 600 °C,[123] the reaction temperature used should be below 600 °C. Most reactions were performed at 550 °C. Once the desired hold temperature was reached, the furnace door was opened and mixture was briefly (~ 15 seconds) stirred by manually agitating the crucible with tongs to ensure homogeneity of the molten salts. This process must be carried out with appropriate personal protective equipment (lab coat, goggles, heat resistant gloves) to protect from heat from the furnace and against any potential accidental splashing of salts; it is also highly recommended that the furnace be placed inside a fume hood.

Reagents ($ZrO(NO_3)_2$ used for initial experiments, $ZrOCl_2$ used for majority of experiments, no noticeable difference was observed between the two Zr-sources) were pre-mixed using a mortar and pestle with some methanol followed by drying at 120 °C in air until all methanol was removed to produce a uniform reagent mixture. Subsequently, the pre-mixed, dried, stoichiometric reagents were slowly added to the molten HB or mHB flux, followed by stirring as above for roughly 15 s to ensure homogeneity of the reagents. After adding reagents, the crucible was placed back inside the furnace to maintain temperature. Then, the aforementioned stirring procedure was repeated after 5 minutes inside the furnace and the reaction was allowed to proceed for the remainder of the hold time. It should be noted that salts that contain water or may evolve gases (such as from the decomposition of nitrates) should be added to molten salts **slowly** and with **extreme care** to prevent splashing of hot molten salts. The mass ratio of flux salts to reagents was 5 : 1 for the HB-MSS method and 1.7 : 1 for the mHB-MSS method. Generally, reaction sizes of ~ 30 grams were used. The mixture was held for various times (between 0 – 4 h for HB-MSS and 4 – 24 h for mHB-MSS) at the desired temperature. The synthesis was performed in air.

C.1.5. Post-Synthesis Processing

After each of the above MSS reactions, the crucibles were cooled naturally to room temperature in the furnace. Then, ultrapure water (>18 MOhm cm) was added to the cooled crucibles and the suspension was ultrasonicated using an immersion probe (Cole-Parmer 500 W Ultrasonic Processor) to rapidly dissolve the salts and generate a slurry containing the LLZO powders. Subsequently, the slurry was vacuum filtered using poly(vinylidene fluoride) membranes (0.22 µm pore size, DuraPore, EMD) and washed thoroughly and repeatedly by water followed by a small amount of methanol to facilitate faster drying. In general, 300 mL of water was used for the reaction sizes above, followed by 50 mL of methanol. Finally, the filter membranes along with the wet powder cakes were placed in an oven at > 100 °C and dried in air. After drying, the LLZO powders were removed from the filter membranes and lightly ground with a mortar and pestle.

C.1.6. Solid-State Reaction of LLZTO for Use as Mother Powder

For use as mother powder for sintering, LLZTO of the same composition as that prepared using the MSS methods was synthesized via the solid-state reaction (SSR) method, as described in previous work[145] and in **Chapter 2.1**.

C.1.7. Preparation of Ceramic Pellets

LLZTO pellets were consolidated from powders via uniaxial cold-pressing (SpecAc Atlas 15T Manual Hydraulic Press) using a 7 mm stainless steel die. The LLZTO from the chloride, mixed, and mHB MSS were ball-milled (SPEX 8000M) before pressing and sintering to attempt to eliminate effect of particle size on sinterability. The HB-MSS powders and some mHB-MSS powders were densified without ball-milling. Pellets were uniaxially pressed using 125 MPa pressure for 5 minutes at room temperature. Additionally, 5% LiOH was added to the mixed-MSS LLZTO powder before ball-milling due to its low sinterability.

Pressed green pellets were sintered at 1200 °C for between 2 – 4 hours. One HB-MSS pellet was sintered at 1300 °C for 1 h. Sintering was performed in a Thermo Scientific Lindberg Blue M 1700 °C box furnace. For sintering, pellets were placed on a small bed of mother powder (synthesized via conventional solid-state reaction, see **Chapter 2.1**) atop a porous MgO substrate, as MgO is known[39,126] to be more inert to LLZO and Li_2O than most other crucible materials besides Pt. All pellets were sintered in MgO crucibles in air atmosphere (Tateho Ozark Technical Ceramics). For initial sintering of the HB-MSS LLZTO, a large excess of mother powder (4 : 1 mother powder mass to

pellet mass) was also placed below the porous MgO substrate and within the crucible (part # SC15020 for the crucible and part# SF150 for the lid) to maintain a high Li_2O vapor pressure, which has been shown[39] to be crucial to achieving high density. During experimentation and optimization the new mother powder composition described in **Chapter 2.1** was used wherein a mixture of mother powder and Li_2O_2 was employed. The density of the as-sintered pellets was calculated from the sample geometry (measured using a micrometer) and mass and compared to the theoretical density of $Li_{6.4}La_3Zr_{1.4}Ta_{0.6}O_{12}$ (5.5 g cm^{-3}).[41]

C.1.8. EIS Section

After sintering, dense pellets were polished initially using 240 grit silicon carbide polishing films (MTI) to result in planarized discs of LLZTO. For initial screening of samples via electrochemical impedance spectroscopy (EIS), graphite blocking electrodes were applied to these pellets by a drawing method using a soft graphite rod as in previous work.[146] Then, a subset of pellets were polished successively using 400, 1200, and 2000 grit silicon carbide polishing films (MTI) until a smooth, uniform, and reflective surface was obtained. Then Sn-Li alloy electrodes were prepared and applied as described in **Chapter 2.2.4**.

Fitting of EIS data was performed using EC-Lab v.11.10 software from Biologic. The circuit $(\mathbf{R}_{tot}/\mathbf{Q}_{tot})(\mathbf{Q}_{el})$ where 'Q' refers to a constant phase element, was used for fitting impedance spectra with blocking graphite electrodes. The circuit $(\mathbf{R}_{bulk}/\mathbf{Q}_{bulk})(\mathbf{R}_{GB}/\mathbf{Q}_{GB})(\mathbf{R}_{el}/\mathbf{Q}_{el})$ was used for fitting impedance spectra with Sn-Li electrodes, where 'bulk,' 'GB,' and 'el' are the bulk, grain boundary, and electrode components respectively. The total ionic conductivity, σ (S cm^{-1}), was determined from the R_{tot} (*i.e.*, $R_{bulk} + R_{GB}$) values, the pellet thickness (t), and the pellet cross-sectional area (A) per **Equation 2.2.4**. Additionally, the temperature dependence of ionic conductivity was investigated for representative pellets of LLZTO from the chloride, HB, and mHB-MSS methods at various temperatures in order to determine the activation energy of Li-ion conduction (E_a) based on the Arrhenius equation (**Equation 2.2.5**). Temperature dependent impedance measurements were performed as described in **Chapter 2.2.4**.

C.2. Supporting Tables

Table C1. Z-Fit parameters and pellet properties (A = area, t = thickness, ρ = relative density) from fitting the total impedance for pellets of LLZTO from mixed and mHB-MSS pellets, measured at room temperature with graphite electrodes

MSS Medium	R_{tot} (Ω)	Q_{tot} (F $s^{(a-1)}$)	A (cm^2)	t (cm)	σ_{tot} (mS cm^{-1})	ρ (%)
Mixed	615	3.2×10^{-10}	0.2771	0.0806	0.47	78.5
mHB*1	793	1.1×10^{-9}	0.3032	0.0769	0.32	88
mHB*2	850	1.3×10^{-9}	0.3001	0.0878	0.34	89

1 – ball-milled

2 – non-ball-milled

** - sintered simultaneously in the same crucible*

Table C2. Z-Fit parameters (b = bulk, gb = grain boundary, tot = total) and pellet properties (A = area, t = thickness, ρ = relative density) and from fitting the bulk and grain boundary impedances for pellets of LLZTO from chloride, HB, and mHB-MSS measured at room temperature (conductivity in mS cm^{-1}) with 1.5 mol % Sn-Li electrodes

MSS Medium	R_b (Ω)	Q_b (F $s^{(a-1)}$)	R_{gb} (Ω)	Q_{gb} (F $s^{(a-1)}$)	A (cm^2)	t (cm)	σ_b (mS cm^{-1})	σ_{tot} (mS cm^{-1})	ρ (%)
Chloride	396	1.0×10^{-10}	127	7.6×10^{-6}	0.311	0.0755	0.61	0.46	88
HB	696	1.4×10^{-10}	83	5.3×10^{-8}	0.279	0.0750	0.39	0.35	93.4
mHB	323	2.2×10^{-10}	61.3	9.1×10^{-6}	0.312	0.0737	0.73	0.61	91.1

C.3. Supporting Figures

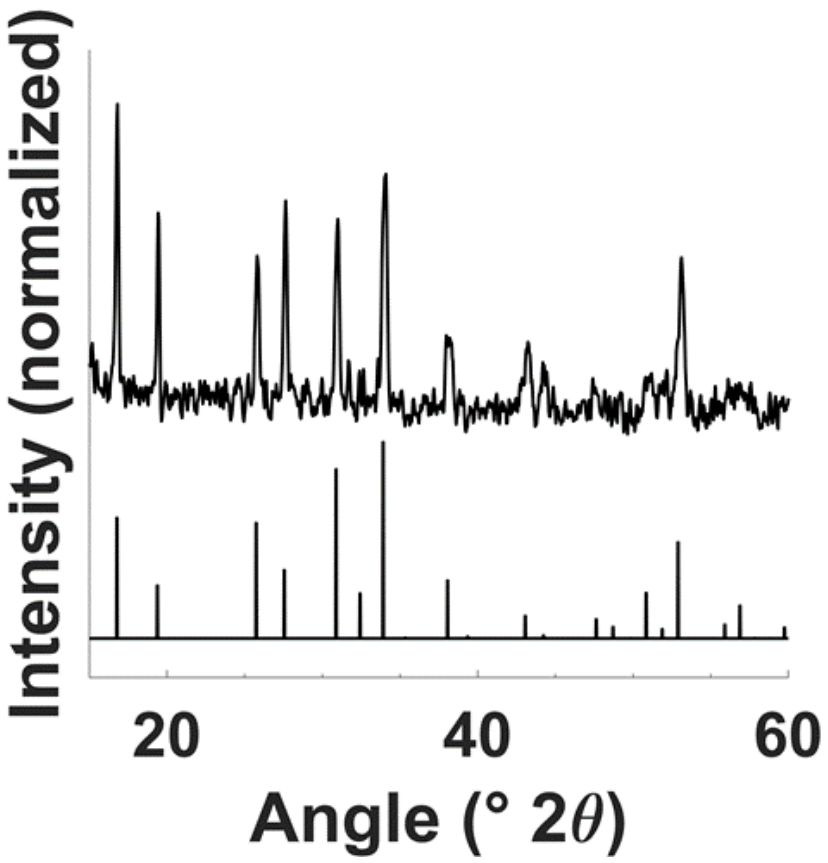

Figure C1. XRD pattern of LLZTO synthesized at 850 °C for 4 hours in the LiCl-KCl medium. Reference pattern below based on Logeat et al.[48]

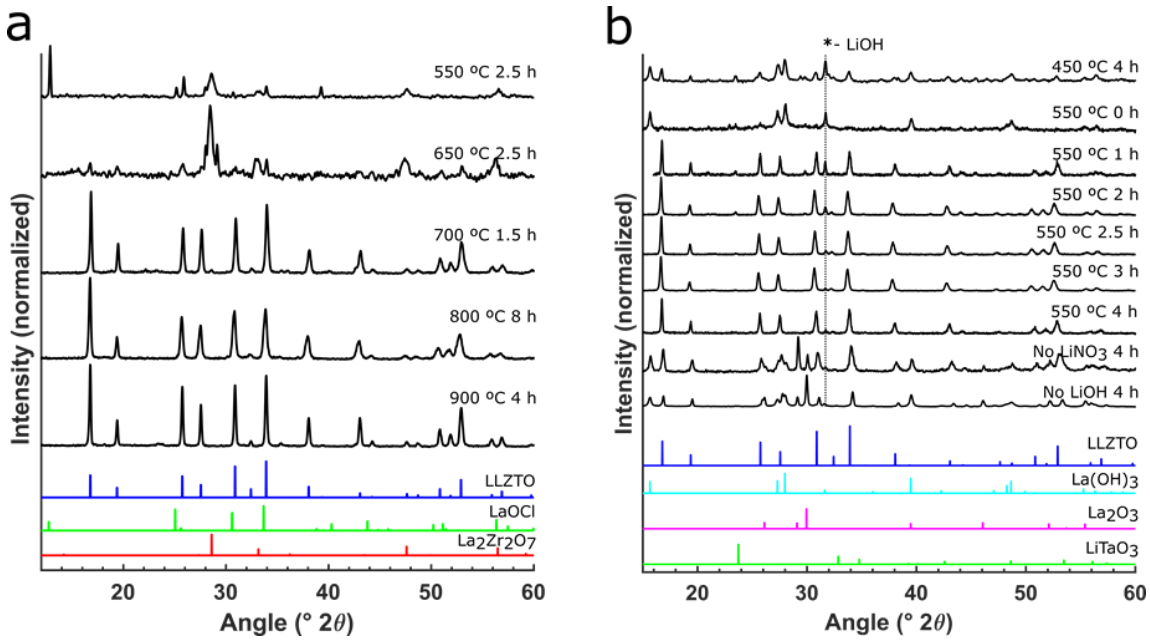

Figure C2. XRD patterns of products from LLZTO MSS reactions in **(a)** mixed and **(b)** HB melts. For the HB-MSS, the XRD patterns formed after reaction at 550 ºC for 0 – 4 h were taken (where 0 h indicates the reagents were added to the hot melt and then immediately cooled after mixing (i.e., no hold time). LiOH present in HB-MSS samples due to large amount of salts used to form the melt and some residue after washing. The reference patterns are as follows: LLZTO (Logeat et al.[48], LaOCl (PDF#00-008-0477), $La_2Zr_2O_7$ (PDF#00-017-0450), La_2O_3 (PDF#00-005-0602), and $La(OH)_3$ (PDF#00-006-0585), $LiTaO_3$ (PDF#00-029-0836).

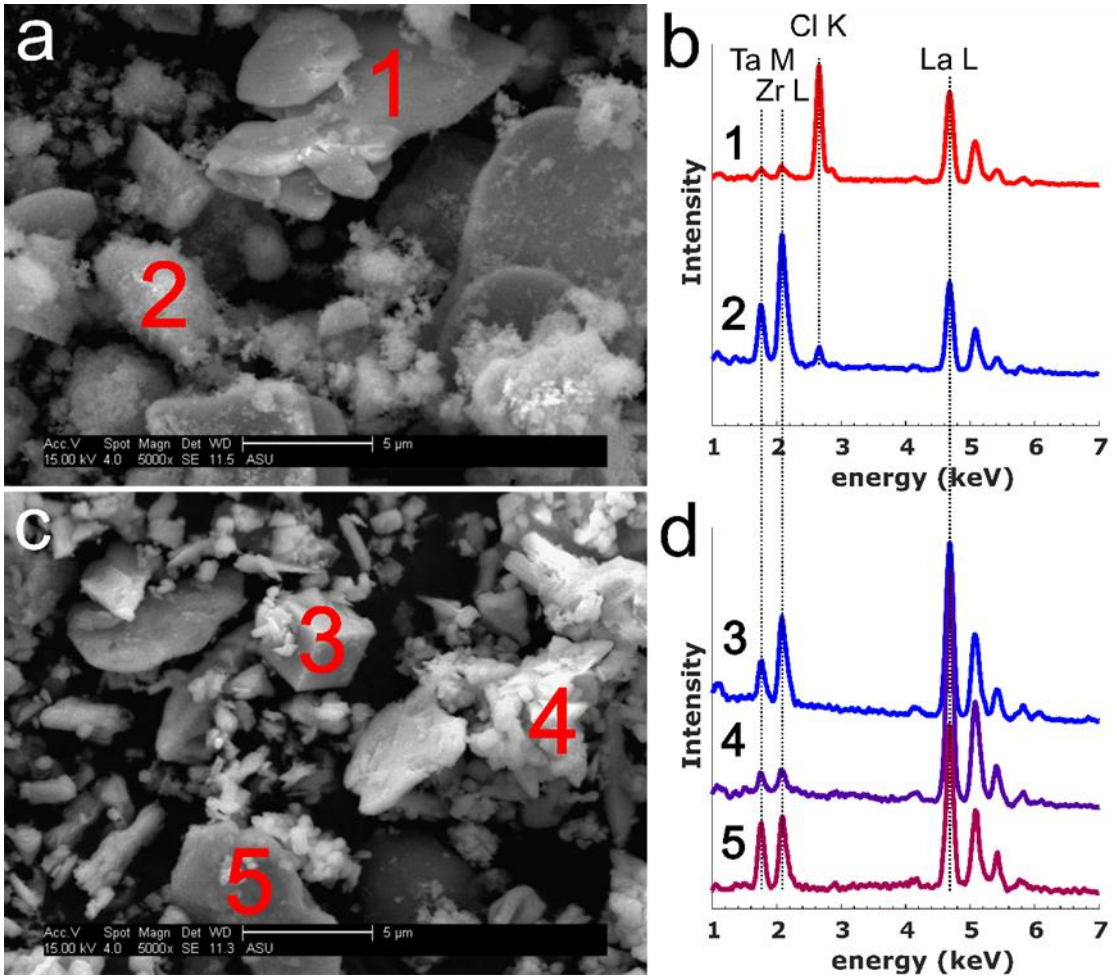

Figure C3. SEM images (**a,c**) and corresponding EDS spectra (**b,d**) of intermediate phases formed in the **(a,b)** mixed MSS medium (550 ^{o}C, 1 h) and **(c,d)** HB medium (450 ^{o}C, 4 h). In the mixed medium, plate-like LaOCl particles (**1**) exhibit La and Cl signals in the EDS and the fluffy agglomerates of LZO particles (**2**) contain La, Zr, and Ta. In the HB-MSS medium, highly faceted cube-like particles (**3**) showing mostly La with some Zr and Ta signal, fused hexagonal plate-like particles (**4**) showing almost exclusively La, and **(5)** agglomerates of small particles with a mixture of La, Zr, and Ta were formed. The plate-like particles **(4)** are likely $La(OH)_3$; assignment of particles (**3**) and **(5)** is difficult but they may be amorphous or poorly crystalline intermediates and/or and early garnet particles.

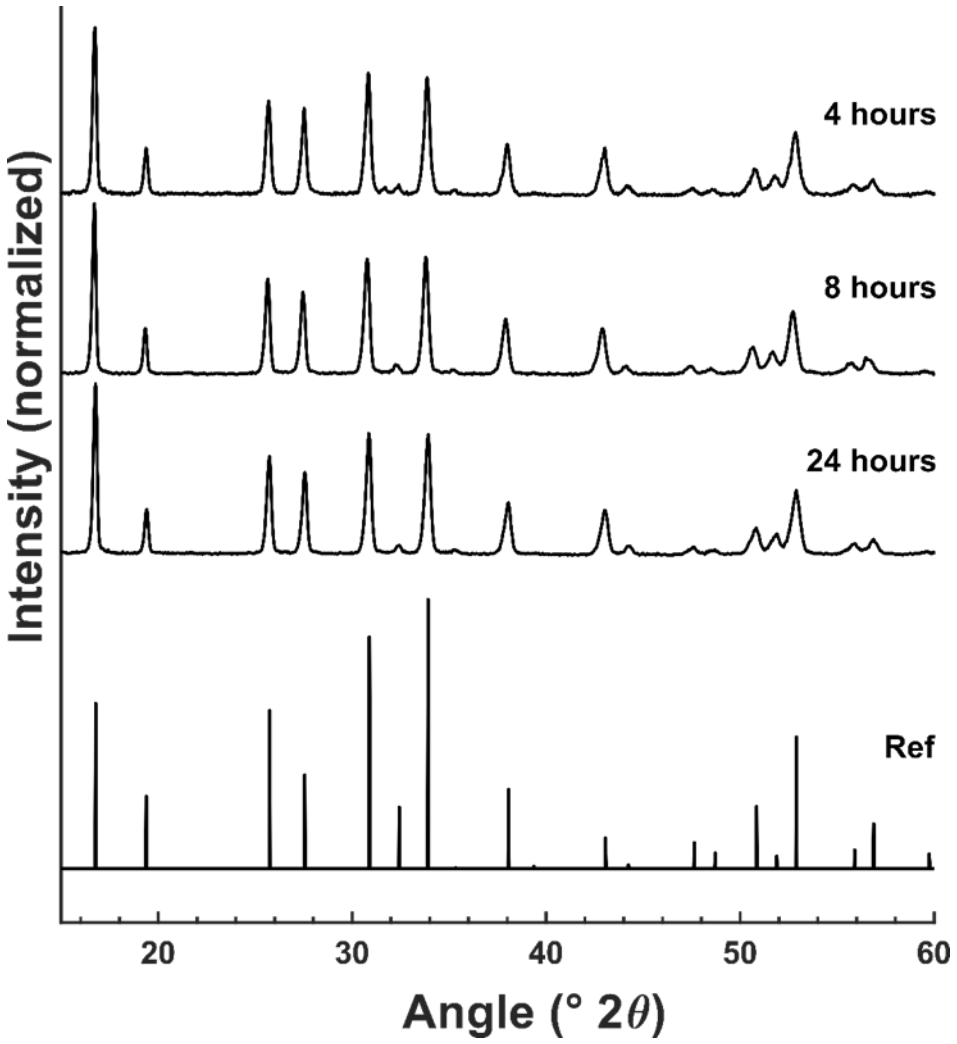

Figure C4. XRD patterns of mHB-MSS LLZTO synthesized at 550 °C for various times, showing phase purity and no appreciable difference in crystallinity, with reference pattern generated according to Logeat *et al.*[48]

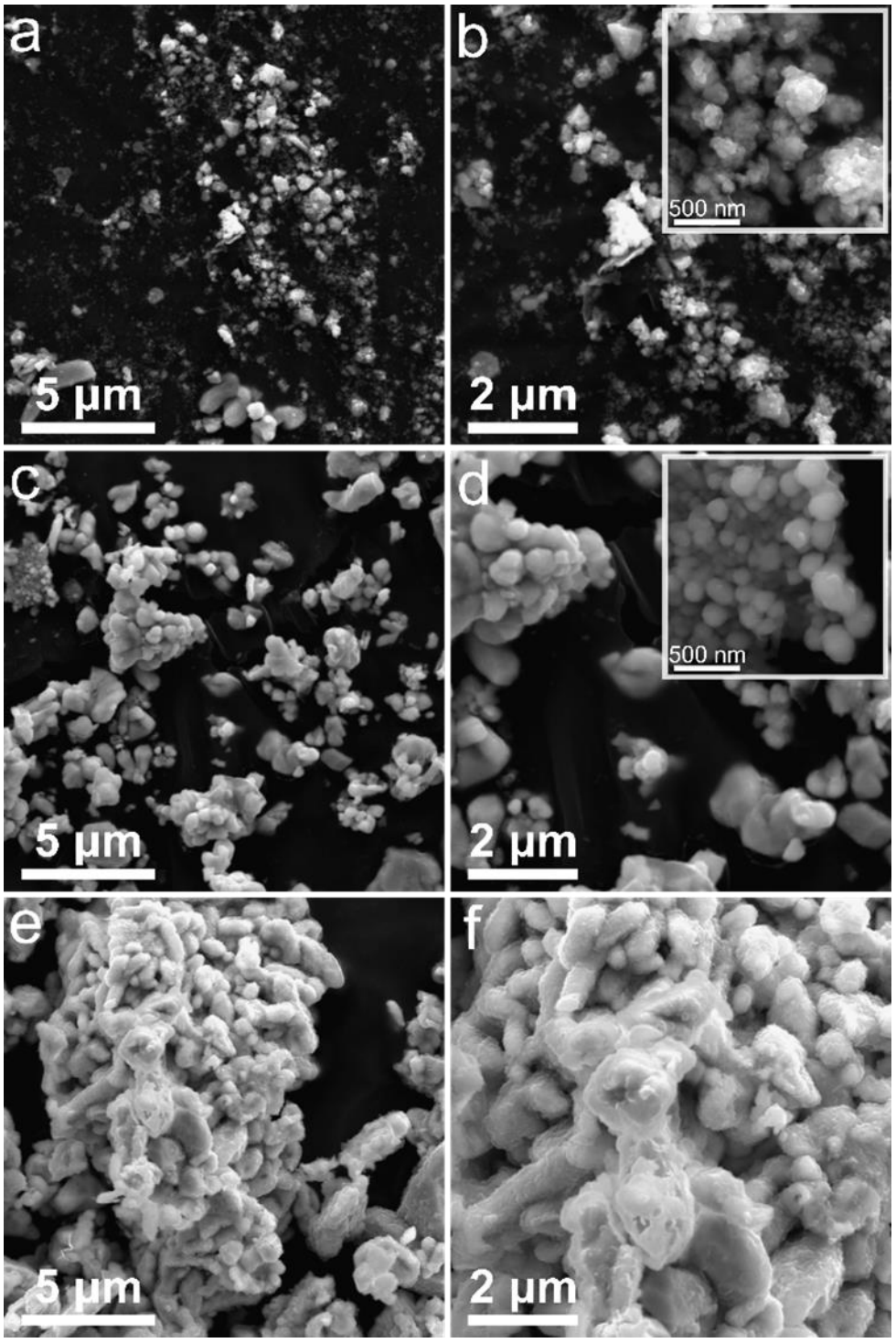

Figure C5. SEM images of mHB-MSS LLZTO synthesized at 550 °C for **(a)** 4 h, **(b)** higher magnification of (**a**) with inset showing ultrafine nuclei; **(c)** 8 h, **(d)** higher magnification of (**c**) with inset showing small nuclei; **(e)** 24 h, **(f)** higher magnification of (**e**).

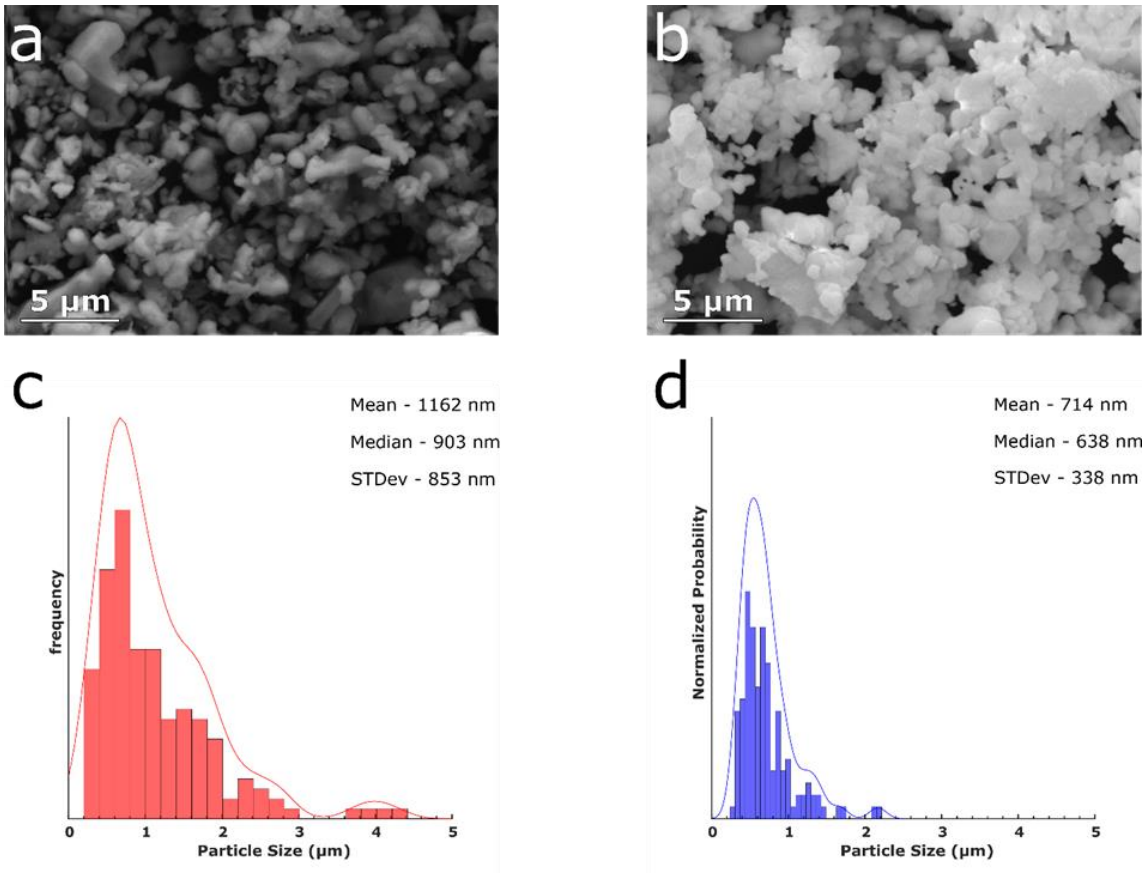

Figure C6. SEM images of **(a)** HB-MSS LLZTO synthesized at 550 °C for 3 h **(b)** mHB-MSS LLZTO synthesized at 550 °C for 8 h, **(c)** particle size distribution of HB-MSS LLZTO in (**a**), and **(d)** particle size distribution of mHB-MSS LLZTO in (**b**) – particle size distributions estimated by measuring individual particles and agglomerates using ImageJ Software.

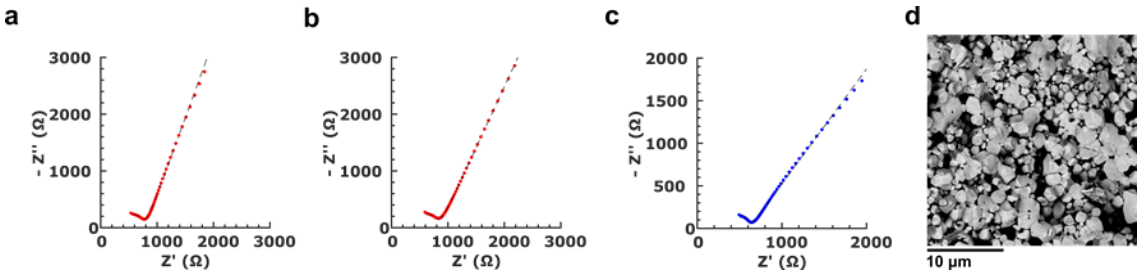

Figure C7. Nyquist plots of room temperature EIS spectra (obtained using graphite electrodes) measured from 7 MHz to 1 kHz used to determine total impedance of **(a)** mHB-MSS pellet from ball-milled LLZTO, **(b)** mHB-MSS pellet from non-ball-milled LLZTO, and **(c)** Mixed-MSS pellet (ball-milled, 5% LiOH added before milling), **(d)** backscatter SEM fracture surface image of a mixed-MSS pellet (from ball-milled powder) showing poor densification.

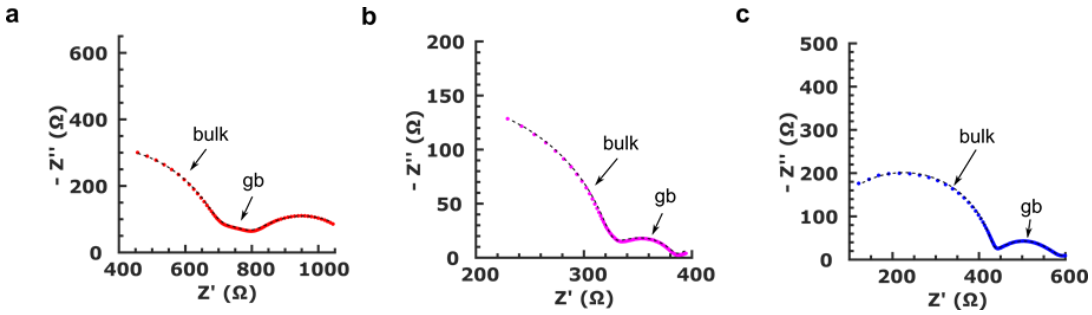

Figure C8. Nyquist plots from **Figure 5.3a** of room temperature EIS spectra (obtained using Sn-Li electrodes, measured from 7 MHz to 1 Hz) revealing bulk and grain boundary impedances for pellets of LLZTO from **(a**) HB, **(b**) mHB, and **(c**) chloride MSS. Dashed lines indicate the circuit fitted impedance spectra (values listed in **Table C3**). These EIS spectra are from the same pellets as in **Table 5.1**.

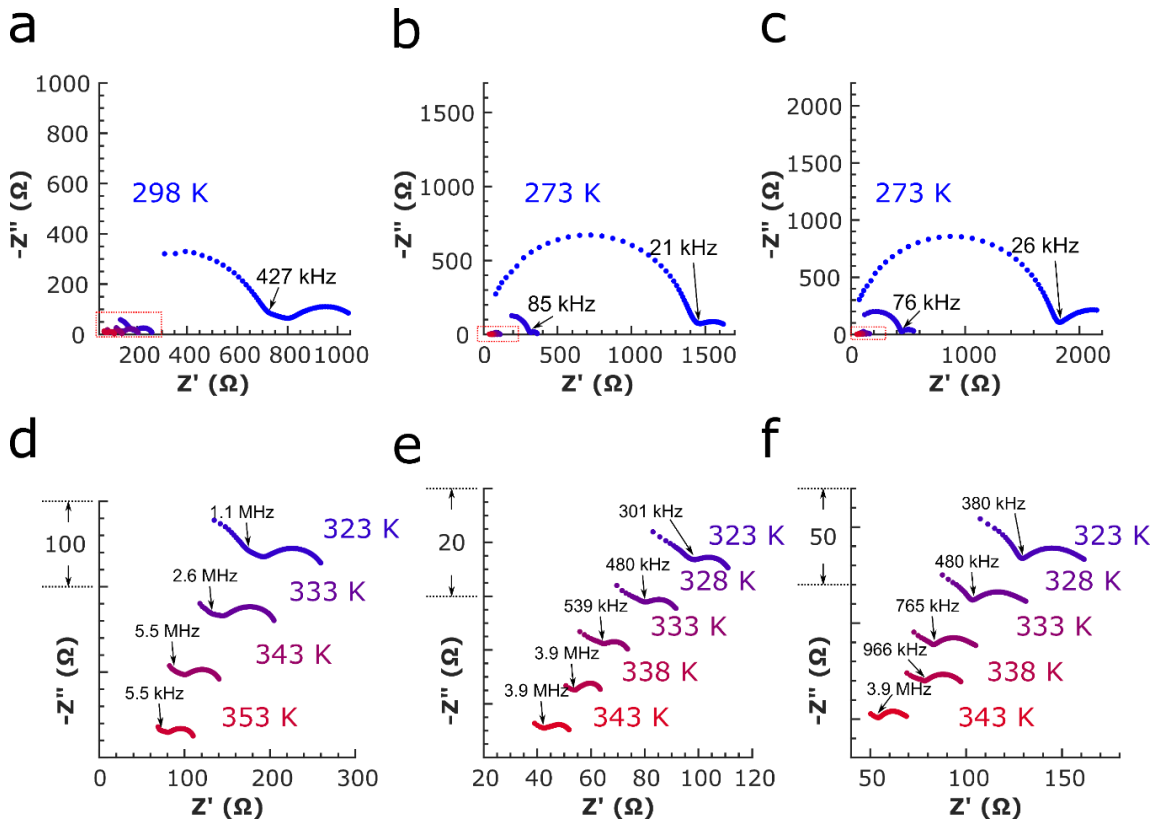

Figure C9. EIS spectra (obtained using Sn-Li electrodes) measured between 7 MHZ and 1 Hz at temperatures ranging from 273 to 353 K showing temperature dependence of impedance for pellets of LLZTO from **(a,d)** HB, **(b,e)** mHB, and **(c,f)** chloride MSS. These EIS spectra are used for the Arrhenius plot in **Figure 5.3b** and determine activation energy of Li-ion conduction.

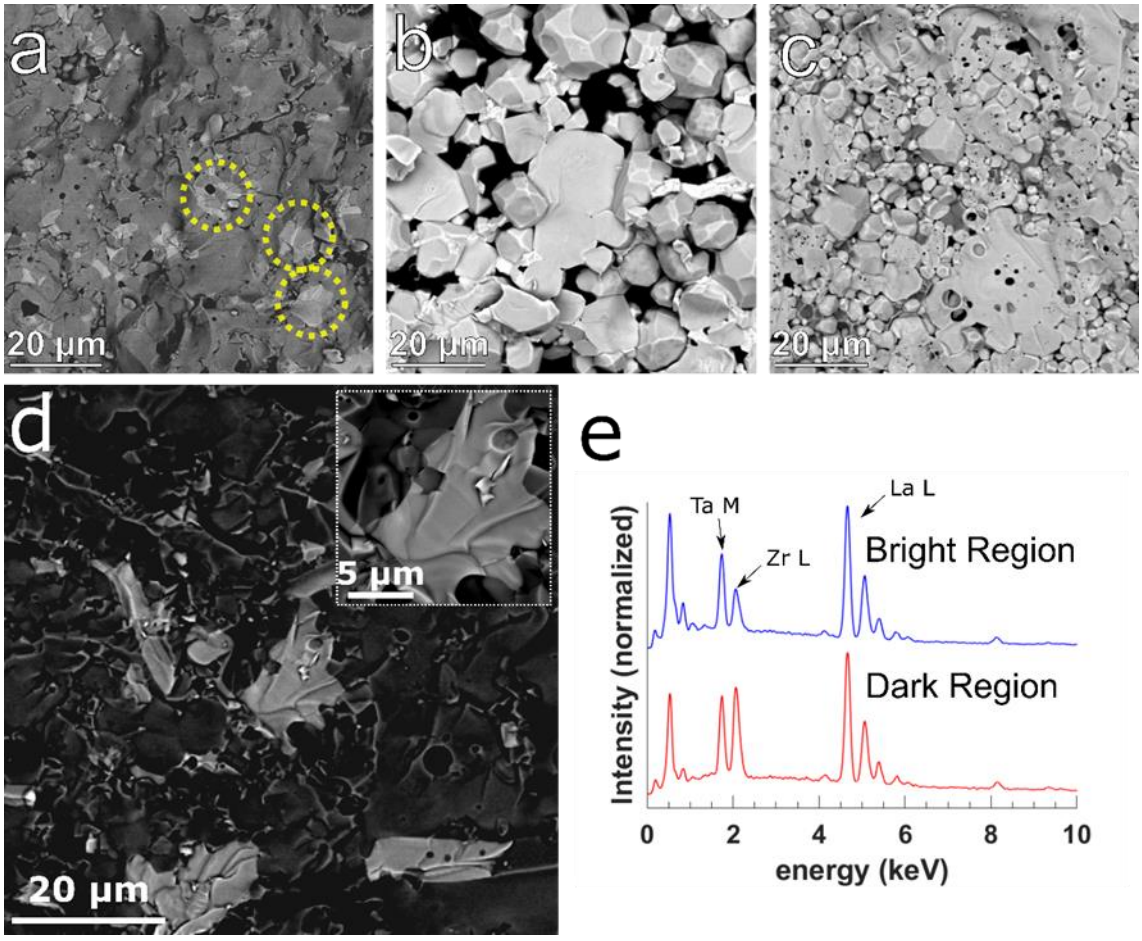

Figure C10. Backscatter SEM images of **(a)** HB-MSS LLZTO pellet sintered at 1300 °C – note the outlined regions with noticeably different contrast, **(b)** mHB-MSS LLZTO pellet sintered at 1200 °C, **(c)** Chloride-MSS LLZTO pellet sintered at 1200 °C, **(d)** BSE image of the pellet in (**a**) with contrast modified to more clearly reveal difference between various grains, **(e)** EDS spectra of a bright and dark grain showing higher Ta-content in the brighter grain

APPENDIX D

SUPPORTING INFORMATION FOR CHAPTER 6

D.1. Experimental Details

D.1.1. Materials and Reagents

All reagents used were of ACS grade or higher unless otherwise noted and used as-received. Lithium nitrate ($LiNO_3$, anhydrous), lithium hydroxide (LiOH, anhydrous), sodium hydroxide (NaOH, anhydrous), zirconium oxychloride octahydrate ($ZrOCl_2 \cdot 8H_2O$), tantalum oxide (Ta_2O_5), calcium nitrate tetrahydrate ($Ca(NO_3)_2 \cdot 4H_2O$), and lanthanum nitrate hexahydrate ($La(NO_3)_3 \cdot 6H_2O$) were obtained from Alfa Aesar. Sodium fluoride (NaF) was obtained from Sigma-Aldrich. Potassium hydroxide (KOH, anhydrous) was obtained from Spectrum Chemical. Lithium peroxide (Li_2O_2, technical grade, 95%) was obtained from Acros Organics. Methanol (HPLC grade) was obtained from BDH Chemical and de-ionized water (18 MΩ cm, EMD MilliPore NanoPure system) was used in all washing steps.

D.1.2. Molten Salt Synthesis of doped pyrochlore-type LZO in eutectic NaOH-KOH

For synthesis of pyrochlores, NaOH and KOH in a eutectic mixture (51.5 : 48.5 by mole) were first pre-heated (5 °C min^{-1}) to 400 °C in an Al_2O_3 (Coorstek High Alumina, 99.8%, 100 mL, part # 65505) or optionally a ZrO_2 (100 mL, AdValueTech, part # Zc-6100) crucible and fully mixed by gentle agitation of the crucible with tongs to form a molten eutectic mixture. The synthesis was performed in air using a KSL-1100x-type compact muffle furnace (MTI Corporation). Meanwhile, $La(NO_3)_3$, $ZrOCl_2$, and optionally dopant sources such as Ta_2O_5, $Ca(NO_3)_2$, or NaF were hand ground together using a mortar and pestle with minimal methanol (generally about 1 mL per gram of precursor) to form a fine paste-like mixture which was subsequently dried at elevated temperature (*e.g.* 120 °C) in air to evaporate the methanol and water of hydration, resulting in a foamy, brittle mixture of precursors. Once dried, the precursor mixture was hand ground again into a fine powder.

The ground precursor mixture was then added slowly in small increments (generally 250-500 mg at a time) to the molten hydroxides with intermittent agitation of the melt by grasping the crucible with tongs to ensure uniform mixing of the powders into the melt. To carry out this mixing, the crucible was first removed from the furnace interior and placed on the furnace door to minimize cooling and thermal shock. For this step, the time that the crucible was resting on the open furnace door was minimized to < 30 sec for adding reagents and mixing. If all of the precursors could not be added in < 30 sec, the crucible was returned to the furnace to reheat for at least 30 sec before repeating the precursor addition and mixing process. (In this case, the furnace contains a “drop-

down" door that swings downward and so the crucible can be rested upon it; if a furnace with a door that opens horizontally (*i.e.*, swings open/shut like a conventional door) is used, placing the crucible on a refractory fiber plate would be advisable to prevent temperature gradients.)

Once all precursors were added, the melt was agitated one more time to ensure uniformity and placed back into the furnace for the desired hold time (1 h for optimized synthesis). *It should be noted that precursor salts that contain water or may evolve gases (such as from the decomposition of nitrates) should be added to the molten salts* ***slowly*** *and with* ***extreme care*** *to prevent splashing of hot molten salts.* ***Proper protective equipment (e.g., lab goggles that entirely cover the eyes and/or face shield, nitrile gloves, lab coat, heat resistant gloves etc.) is mandatory and all operations should be performed inside of a fume hood behind the fume hood sash to contain evolved gases and also act as a physical barrier in case of any bubbling or splashing of hot molten salts****. Naturally, larger reactions require more care due to the potentially larger amount of gas released from reagent decomposition. Pre-drying of the hydrated precursors is necessary to prevent rapid off-gassing of water vapor, which in turn can cause splashing of the salts. This also motivates addition of reagents in small increments to limit reactivity of the decomposition of nitrates.*

After the synthesis was complete and the mixture cooled, de-ionized water was added to the crucible on top of the solidified hydroxides. The hydroxides were dissolved and the resultant pyrochlore products dispersed by using an immersion ultrasonic horn (Cole-Parmer 500 W Ultrasonic Processor). ***Care must be taken at this stage as the dissolution of hydroxides is highly exothermic. It is recommended to contain the crucible in a larger vessel (e.g. a 500 mL beaker for a 100 mL crucible) filled with water to disperse heat generated by this process*****.** After all of the hydroxides were dissolved and a uniform suspension obtained, the pyrochlore nanocrystals were washed by repeated centrifugation steps as follows: 1) the suspension was centrifuged at 8000 RPM until all particles were precipitated, 2) the supernatant solution was decanted and replaced with fresh de-ionized water, 3) the powders were resuspended via the same immersion ultrasonic horn until a uniform suspension was obtained. Then, steps 1-3 were repeated at least 4 more times to remove residual hydroxides and salts. Generally, this process is repeated until the pH of the supernatant solution is less than 10. Finally, the pyrochlores are dried at elevated temperature (e.g. > 120 °C) in air for subsequent use.

As a final note, the NaOH-KOH melt is somewhat corrosive, and in our experience the purity of the Al_2O_3 crucible used is crucial. Higher purity and ideally low surface roughness and high-density crucibles minimize adventitious Al-contamination of the pyrochlores originating from corrosion of the crucible. The optimized synthesis time

of 1 h as mentioned above helps to minimize Al-dissolution. Although commonly used as a dopant for LLZO, Al-contamination in this process tends to result in poor sintering of the final garnet ceramic. (I do not believe the presence of minor Al-contamination affects the garnet formation process, just the sintering process.) ZrO_2 crucibles may also be used as described above, but the susceptibility to thermal shock must be carefully considered. The pyrochlore samples which resulted in the best properties for both conventionally sintered and reactively sintered garnets (including those presented in **Figure 6.3**) were those synthesized in ZrO_2 crucibles at 400 °C for 1 h.

D.1.3. Molten Salt Synthesis of LLZTO in $LiNO_3$-LiOH-Li_2O_2 from doped pyrochlores

In general, the flux forming salts ($LiNO_3$ and LiOH ~ 1.1 : 3.2 ratio by mole, ~ 1 : 1 ratio by mass) along with a specified amount of Li_2O_2 ([0, 0.5, or 1] : 3.2 mole ratio of Li_2O_2 : LiOH for total reagent ratios of 1.1 : 3.2 : [0, 0.5, 1.] of $LiNO_3$: LiOH : [Li_2O_2]) were coarsely mixed and heated at a rate of 5 °C min^{-1} in alumina crucibles (Coorstek high alumina (99.8%) 100 mL, part # 65505) and stirred by gently agitating the melt using tongs to ensure homogeneity once the desired hold temperature had been reached. The synthesis was performed in air. Once the salt mixture was molten and at the desired reaction temperature, a thoroughly hand ground mixture of doped pyrochlore nanocrystals and extra $LiNO_3$ (1:1 by mass) was added to the mixture, stirred as before by gentle agitating of the mixture with tongs until a uniform melt was obtained, and held for various times (between 1 – 5 h) at the desired temperature and cooled naturally to room temperature in the furnace. The $LiNO_3$ mixed with the pyrochlore powder is in addition to the fixed molar ratio of $LiNO_3$: LiOH (1.1 : 3.2) in the melt, and helps facilitate rapid distribution of the pyrochlores in the melt due to the low melting point of $LiNO_3$. Generally batch sizes of ~ 12-15 g total (10:1 to 13:1 ratio of total salts to pyrochlores depending on the amount of Li_2O_2 used) were employed for exploratory synthesis and larger batches (up to 4x or ~ 60 g total) were made for testing sintering conditions. A typical small-scale synthesis consisted of 5 g $LiNO_3$, 5 g LiOH, 3 g Li_2O_2, and a mixture of 1 g pyrochlore and 1 g $LiNO_3$ (hand ground as described above) as the precursor mixture.

After synthesis, ultrapure water (>18 MΩ cm) was added to the cooled crucibles and the suspension was sonicated using an immersion ultrasonic horn (Cole-Parmer 500 W Ultrasonic Processor) to rapidly dissolve the salts and generate a slurry. Subsequently, the slurry was vacuum filtered using poly(vinylidene fluoride) membranes (0.22 µm pore size, DuraPore, EMD corporation) and washed thoroughly and repeatedly by water followed by a small amount of methanol to facilitate faster drying. For a typical reaction size, 250 mL of de-ionized water are used in total, followed by 50 mL of methanol. Naturally, under-washing or over-washing will result either in residual Li compounds

(which can be seen in the XRD patterns as LiOH or Li_2CO_3) or excessive protonation of the garnet, but the amounts used here are considered approximately optimized. Finally, the filter membranes along with the wet powder cakes were placed in an oven at > 120 °C and dried in air. After drying, the powders were removed from the filter membranes and lightly ground with a mortar and pestle to de-agglomerate the powder.

D.1.4. Solid-State Reaction of LLZTO for Use as Mother Powder

For use as mother powder for sintering, LLZTO of the same composition as that prepared using the MSS methods was synthesized via the solid-state reaction (SSR) method as in previous work.[145]

D.1.5. Preparation of Ceramic Pellets

LLZTO pellets for conventional sintering were consolidated from as-synthesized LLZTO powders via uniaxial cold-pressing (SpecAc Atlas 15T Manual Hydraulic Press) using a 7 mm stainless steel die. Pellets were uniaxially pressed using 125 MPa pressure for 5 minutes at room temperature.

For LLZTO pellets prepared by reactive sintering, doped pyrochlore ($La_{2.4}Zr_{1.12}Ta_{0.48}O_{7.04}$) powders were blended with LiOH (10 % excess by mole relative to target composition of $Li_{6.4}La_3Zr_{1.4}Ta_{0.6}O_{12}$) by ball-milling (SPEX 8000M, polymer jars with tungsten carbide inserts and tungsten carbide milling ball) in a vibratory ball-mill for 90 minutes to ensure uniformity of LiOH throughout the pyrochlore nanocrystals. Subsequently, green pellets were pressed in the same way as described above for LLZTO powder.

Pressed green pellets were sintered at 1200 °C, with 2 hours representing a roughly optimized sintering time. (Some pellets were sintered for 3 h at 1200 °C, with slightly lower ionic conductivity, and were fractured for SEM analysis of the fracture surface, as shown in **Figure 6.3a,c**.) Sintering was performed in a Thermo Scientific Lindberg Blue M 1700 °C box furnace. All pellets were sintered in MgO crucibles (Tateho Ozark Technical Ceramics) as MgO is known[39,126] to be more inert to LLZO and Li_2O than most other crucible materials besides Pt. More details of the sintering approach used are discussed in **Chapter 2.1** and in previous[197] work.

D.1.6. Materials Characterization

Synchrotron X-ray diffraction (XRD) and pair distribution function (PDF) measurements of the pyrochlore nanocrystals were performed at room temperature at beamline I15-1 of Diamond Light Source (Didcot, UK) with 2D PerkinElmer image plate detectors. Bragg data were collected at $\lambda = 0.161669$ Å and background subtracted using GSAS II.[200] The XRD patterns in **Figure 6.1a** were scaled to Cu Kα scattering angles for standardization and compared to reference patterns for $La_2Zr_2O_7$ (PDF#00-017-0450) and $La(OH)_3$ (PDF#00-006-0585).

The total scattering data were collected over a Q range of 0.5 – 25 $Å^{-1}$ with $r_{max} = 50$ and $r_{step} = 0.02$ and corrected for multiple scattering, incident beam polarization, and Compton scattering using GudrunX[201] to obtain the PDFs (*D(r)* data as defined by Keen[202]). A sample density of 6.05 g/cm^3 was used for the normalizations and $Q_{max} = 25$. PDF refinements and calculations were performed using PDFGui[151] with $Q_{damp} = 0.0267$ and $Q_{broad} = 0.0105$ (obtained from refinement of a Si standard) within the xPDFSuite[152] software package. The scale factor, lattice constant, linear atomic correlation factors *delta1* or *delta2* (coefficients for 1/r or $1/r^2$ contribution to peak sharpening at high and low temperatures, respectively), *spdiameter* (shape damping function for particle diameter in Å), and isotropic atomic displacement parameters were selected as constraints. For phase identification, the crystallographic information files for pyrochlore (ICSD coll. code 253064) and defect fluorite (ICSD coll. code 253062) were taken from the work by Paul *et al.*[192] The hexagonal form of $La(OH)_3$ was used as reference in PDF refinements (ICSD coll. code 192271, taken from ref.[216]).

Laboratory X-ray diffraction (XRD) of garnet products was performed using a Bruker D-8 powder diffractometer with CuK_α radiation for crystalline phase identification. The reference pattern for c-LLZO ($Ia\bar{3}d$) was generated according to the structure reported by Logeat *et al.*[48]

The sample morphology was examined using a FEI XL30 scanning electron microscope (SEM) equipped with an EDAX system for energy dispersive spectroscopy (EDS). To minimize charging, a carbon film was deposited on the samples before imaging using a thermal evaporator type carbon coater.

Transmission electron microscopy (TEM) was performed using an aberration corrected (CEOS image corrector) FEI Titan Environmental TEM operated at 300 kV. For high-resolution aberration corrected TEM imaging, aberrations were corrected to yield an imaging resolution better than 1 angstrom, and negative spherical aberration imaging (Cs ~ -13 µm) was employed to yield bright contrast at the positions of atom

columns. Electron diffraction (ED) patterns were obtained using a third condenser lens to allow formation of a submicrometer diameter parallel beam rather than using a selected area aperture. Scanning transmission electron microscopy (STEM) was performed using a JEOL ARM200 probe-corrected STEM (CEOS CESCOR hexapole probe aberration corrector) with a high-angle annular dark-field (HAADF) detector and JEOL energy dispersive X-ray spectrometer for elemental mapping. To prepare S/TEM samples, pyrochlore or garnet powder was ultrasonically suspended in HPLC-grade methanol. A holey carbon TEM grid (Pacific Grid Tech) was then briefly immersed into the aforementioned suspension. Finally, the grid was dried at elevated temperature (*e.g.,* 120 °C) in air to fully remove methanol. Analysis of elemental maps was performed in part using the Cornell Spectrum Imager plugin in ImageJ.[215]

D.2. Determination of ionic conductivity from EIS data

After sintering, the pellets were polished successively using 240, 400, 1200, and 2000 grit silicon carbide polishing films (MTI) until a smooth, uniform, and reflective surface was obtained. Subsequently, they were coated with Sn-Li alloy electrodes as described in **Chapter 2.2.4**.

For these samples, no appreciable grain boundary impedance (generally the maximum grain boundary semicircle is observed at frequencies in the 10's of kHz)[158] was observed, so the circuit ($\mathbf{R}_{tot}/\mathbf{Q}_{tot}$)($\mathbf{R}_{el}/\mathbf{Q}_{el}$)($\mathbf{Q}_{lf}$) was used instead for fitting impedance spectra with Sn-Li electrodes, where 'tot,' 'el,' and 'lf' are the 'total,' 'electrode,' and 'low-frequency' components to impedance respectively. The total ionic conductivity, σ (S cm^{-1}), was determined from the R_{tot} values, the pellet thickness (*t*), and the pellet cross-sectional area (*A*) per **Equation 2.2.4**.

Additionally, the temperature dependence of ionic conductivity was investigated for these pellets at various temperatures between 273-343 K as described in **Chapter 2.2.4** in order to determine the activation energy of Li-ion conduction (E_a) based on the Arrhenius equation (**Equation 2.2.5).**

D.3. Supporting Tables

Table D1. Experimental conditions for synthesis of $Li_{6.4}La_3Zr_{1.4}Ta_{0.6}O_{12}$ garnet from $La_{2.4}Zr_{1.12}Ta_{0.48}O_{7.04}$ pyrochlore quasi-single-source precursors with corresponding reaction products as determined from the XRD patterns in **Figure D2**. The temperature, reaction time, and Li_2O_2 : LiOH molar ratio was varied (the molar ratio of $LiNO_3$ to LiOH was fixed at 1.1 to 3.2). As the Li_2O_2 to LiOH ratio increases, the Lux-Flood basicity of the melt increases. Some products showing residual LiOH and/or Li_2CO_3 in the XRD patterns are considered phase-pure garnet as minor residual LiOH originates from incomplete washing after the synthesis rather than incomplete conversion to garnet, and Li_2CO_3 likewise can form from residual this LiOH.

Reaction Temperature (°C)	Li_2O_2 : LiOH (x : 3.2) Molar Ratio	Reaction Time (h)	Reaction Products
400	0	5	Pyrochlore, no garnet
	0.5	3	Garnet with $LiTaO_3$ and La_2O_3
	0.5	5	Garnet with $LiTaO_3$
	1	1	Garnet with $LiLaO_2$, $LiTaO_3$ and La_2O_3
	1	3	Garnet with $LiTaO_3$
	1	5	**Pure garnet**
450	0.5	3	Garnet with $LiTaO_3$
	0.5	5	Garnet with $LiLaO_2$, $LiTaO_3$ and La_2O_3
	1	1	Garnet with $LiLaO_2$, $LiTaO_3$ and La_2O_3
	1	3	**Pure garnet**
500	0	5	Pyrochlore, trace garnet
	0.5	1	Pyrochlore, no garnet
	0.5	3	**Pure garnet**
	0.5[a]	3	Pyrochlore, no garnet
	0.5[b]	3	**Garnet** with trace $LiAlO_2$
	1	1	**Pure garnet**
550	0	5	Pyrochlore, $LiTaO_3$, some garnet
	0.5	1	Pyrochlore, some garnet
	0.5	3	**Pure garnet**
	1	1	**Pure garnet**
	1[c]	5	**Garnet** with trace $LaAlO_3$
	1[d]	5	**Partially tetragonal garnet**
	1[e]	4	**Pure garnet**

[a] *Na_2O_2 used instead of Li_2O_2; i.e., 1.1 : 3.2 : 0.5 mole ratio of $LiNO_3$: LiOH : Na_2O_2*
[b] *$Li_{6.025}La_{2.75}Ca_{0.25}Zr_{1.4}Ta_{0.6}O_{11.375}F_{0.625}$ (LLCZTOF) (see **Figure D8**)*
[c] *$Li_{6.375}La_3Zr_2O_{11.375}F_{0.625}$ (LLZOF) (see **Figure D6**)*
[d] *$Li_{6.5}La_3Zr_2O_{11.5}F_{0.5}$ (LLZOF) (see **Figure D7**)*
[e] *Garnet synthesis using $La(NO_3)_3$, $ZrOCl_2$, and Ta_2O_5 as reagents instead of pyrochlores (see **Figure D3**)*

Table D2. Z-Fit parameters (tot = total, el = electrode, lf = low-frequency) and pellet properties (A = area, t = thickness, ρ = relative density) and from fitting the total and electrode impedances for pellets of LLZTO from pyrochlore to garnet conventional and reactive sintering measured at room temperature (21 °C) between 7 MHz and 1 Hz with 1.5 mol % Sn-Li electrodes (conductivity in mS cm^{-1}).

MSS Medium	**R_{tot} (Ω)**	**Q_{tot} (F $s^{(a-1)}$)**	**R_{el} (Ω)**	**Q_{el} (F $s^{(a-1)}$)**	**Q_{lf} (F $s^{(a-1)}$)**	**A (cm^2)**	**t (cm)**	**σ_{tot} (mS cm^{-1})**	**ρ (%)**
Conventional	532	2.5 x 10^{-10}	396	1.77 x 10^{-6}	6.03 x 10^{-3}	0.299	0.0668	0.42	88
Reactive	660	1.61 x 10^{-10}	1024	1.04 x 10^{-6}	2.33 x 10^{-3}	0.227	0.0793	0.53	94.1

Table D3. Comparison of properties of the LLZTO ($Li_{6.4}La_3Zr_{1.4}Ta_{0.6}O_{12}$ unless otherwise noted) prepared using the pyrochlore to garnet (PG) process with other pertinent literature. The synthesis conditions, sintering conditions, relative density, total ionic conductivity (σ_{tot}, at room temperature unless otherwise indicated) and activation energy (E_a) are shown for comparison.

Synthesis Method	Synthesis Conditions		Sintering Conditions		Pellet Properties			Ref.
	Temp. (°C)	Time (h)	Temp.(°C)	Time (h)	Density (%)	σ_{tot}	Ea	
Highly-Basic-MSS ($LiNO_3$: LiOH : Li_2O_2 0.5 : 1 : 1)	550	2.5	1200	3	93.4	**0.35**	0.39	Ref.[145]
Modified Highly-Basic-MSS ($LiNO_3$: LiOH : Li_2O_2 1.1 : 3.2 : 1)	550	8	1200	4	91.1	**0.61**	0.4	Ref.[145]
PG-Conventional Sintering	550	1	1200	2	88.0	**0.42**	0.42	This Work
PG-Reactive Sintering	N/A	N/A	1200	2	94.1	**0.53**	0.38	This Work
Mixed-MSS (LiCl-LiOH)	900	4	1200	2	78.5	**0.45**	NR	Ref.[145]
Chloride-MSS (LiCl-KCl)	900	4	1200	4	87.9	**0.46**	0.4	Ref[145]
Solid-state reaction*	900	2x10	1130	36	94.1	0.28[b]	NR	Ref.[34]
Solid-state reaction[≠,*]	950	2x6	1250	6	93.9	0.42	0.43	Ref.[40]
Solid-state reaction[≠,*]	950	2x6	1280/1180	0.33/5	97	0.74	0.42-0.45	Ref.[41]
Solid-state reaction[≠,*]	950	2x6	1280	5	97	0.78	0.42-0.45	Ref.[41]
Solid-state reaction[≠,*]	950	2x6	1250	0.33	97	0.64	~0.45	Ref.[39]
Solid-state reaction[≠]	900	12	1180	12	91	0.33	0.53	Ref.[33]
Solid state reaction	900	6	1200	24	84	0.15[‡]	0.40	Ref.[43]
Solid state reaction[≠]	900	6	1100	15	89	0.61	0.40	Ref.[217]
Solid state reaction[≠]	900	6	1150	15	92.8	0.79[b,†]	0.42	Ref.[44]
Solid state reaction	750	1x 6, 1 x 12	1200[Al]	18	83	0.3[c,†]	0.38	Ref.[218]
Solid state reaction	900	6	1150[Al]	12	NR	0.41	0.3	Ref.[25]
Solid state reaction*	1x at 850 / 2x at 1000	3x20	1150[Al]	5	92.7	0.71[c]	0.42	Ref.[28]
Solid state reaction**	900	NR	1140[Al]	16	NR	1.0	0.35	Ref.[38]
Co-precipitation	900	3-4	1050[hp]	1	97.1	0.39[a]	0.45	Ref.[37]
Co-precipitation	900	3-4	1050[hp]	1	97.8	0.82[b]	0.43	Ref.[37]
Solution-combustion synthesis	750	8	1125	6	NR	0.2	NR	Ref.[31]
Polymer combustion	700	4	1100	12	93.6	0.67	0.42	Ref.[146]

‡ - σ_{tot} measured at 33 °C
† - σ_{tot} measured at 27 °C
a – x = 0.75
b - x = 0.5
c - x = 0.4
hp – consolidated via hot-pressing
Al – Al_2O_3 crucibles used or Al_2O_3 added as sintering aid
≠ - high energy ball milling (e.g. planetary milling, attrition milling, etc.) of LLZTO to reduce particle size
** - repeated grinding and heating steps (e.g. 2x10 = 2 calcination steps each for 10 hours)*
*** - exact details of synthesis not reported (e.g. degree method of grinding, calcination time, etc.)*
NR – not reported

D.4. Supporting Figures

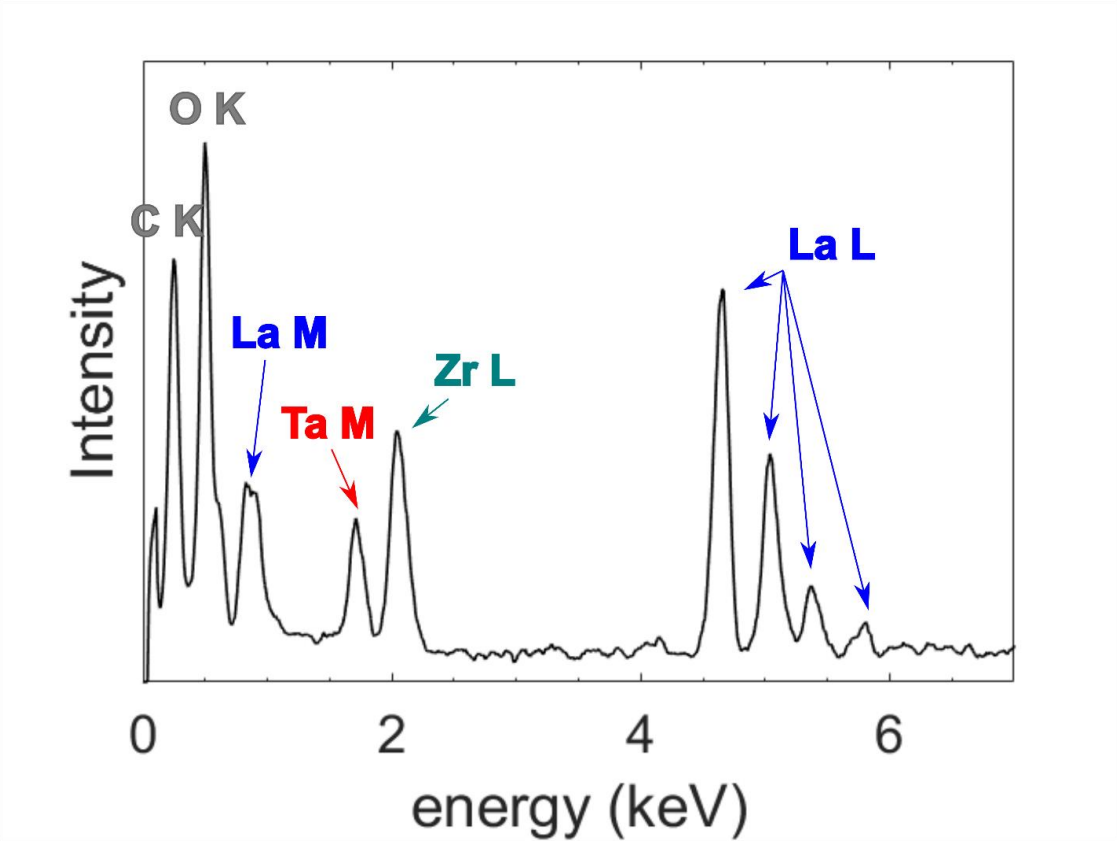

Figure D1. Average STEM-EDS spectrum obtained from EDS spectral map in **Figure 6.1e** for doped pyrochlore precursors with nominal composition of $La_{2.4}Zr_{1.12}Ta_{0.48}O_{7.04}$

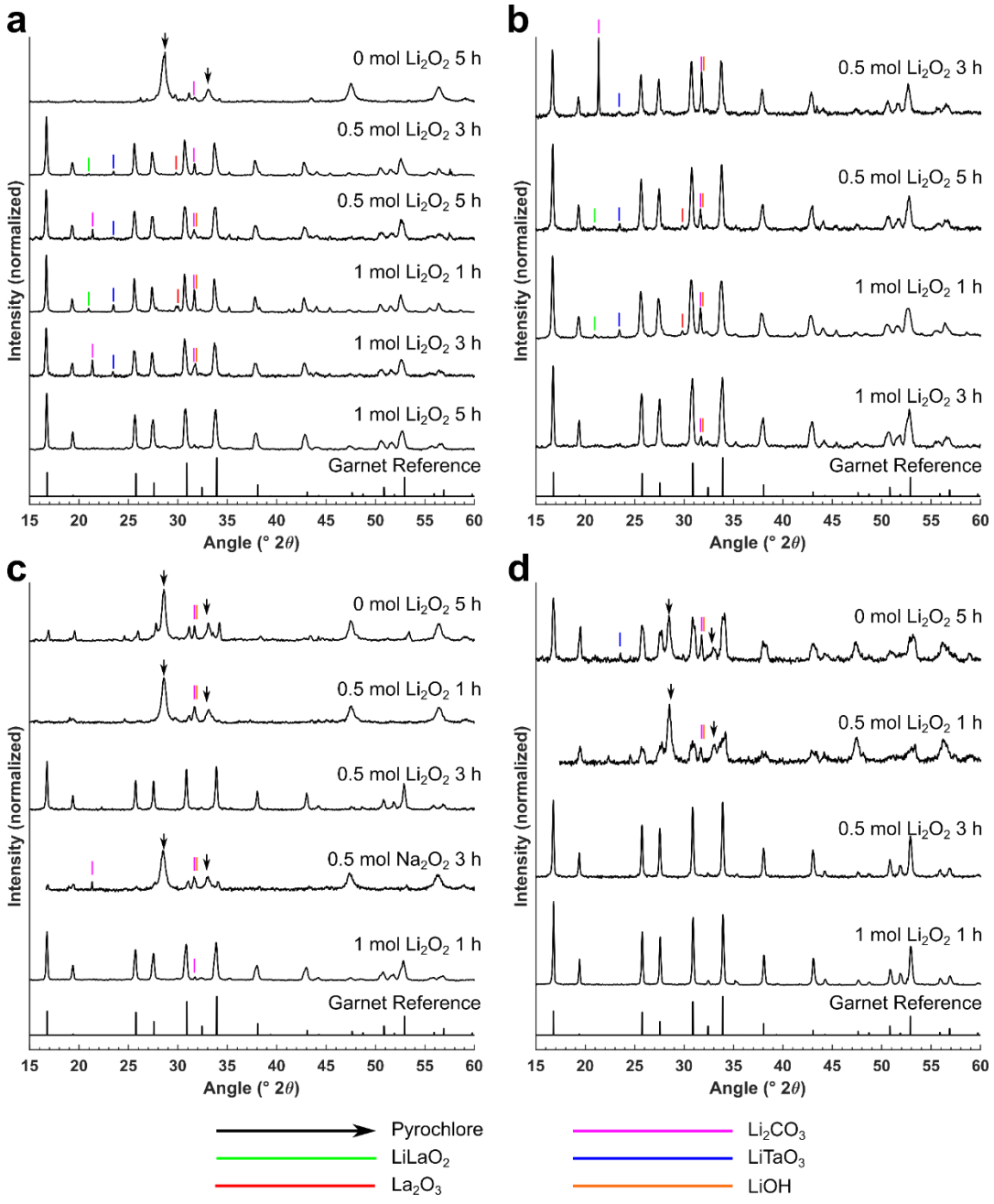

Figure D2. XRD patterns of garnets synthesized from pyrochlore precursors at **(a)** 400 °C, **(b)** 450 °C, **(c)** 500 °C, and **(d)** 550 °C. The molar ratio of Li_2O_2 to LiOH ($LiNO_3$ to LiOH molar ratio was fixed at 1.1 to 3.2) and reaction time for synthesis are next to each XRD pattern. The reference pattern (Logéat et al.[48]) for garnet is shown below. Main impurity phases besides unreacted pyrochlores (PDF#00-017-0450) are assigned to $LiLaO_2$ (mp-756544[219]), Li_2CO_3 (ICSD Coll. Code 69133), $LiTaO_3$ (PDF#00-029-0836), La_2O_3 (PDF#00-005-0602), and LiOH (ICSD Coll. Code 27543) as indicated by the vertical lines above major reflections from each phase.

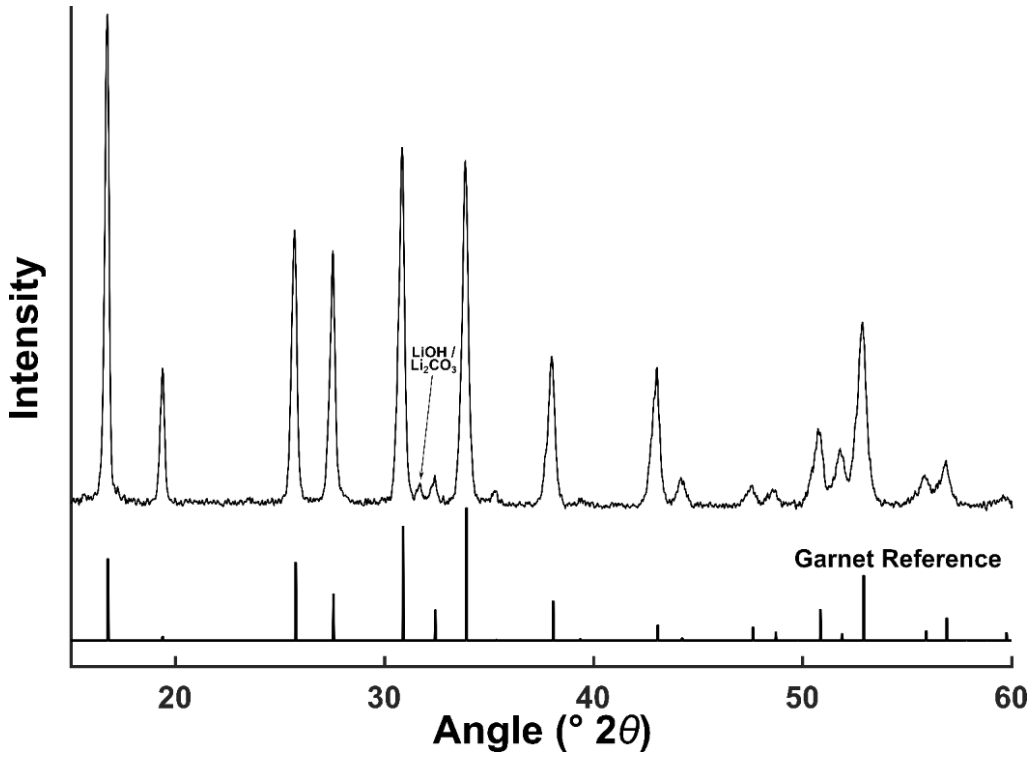

Figure D3. XRD pattern of $Li_{6.4}La_3Zr_{1.4}Ta_{0.6}O_{12}$ (LLZTO) garnet powder synthesized using $La(NO_3)_3$, $ZrOCl_2$, and Ta_2O_5 as precursors instead of doped pyrochlore nanocrystals at 550 °C in 4 h (reference pattern generated according to Logéat et al.[48]). The salt melt was $LiNO_3$-LiOH-Li_2O_2 at a molar ratio of 1.1 : 3.2 : 1. Lower synthesis temperatures resulted in only partial garnet formation. For this sample, the same synthetic approach as outlined in the experimental details**, Appendix D.1** was used, except instead of the doped pyrochlores, a ground mixture of the aforementioned reagents was used as described in our previous[145] work (see also mHB-MSS synthesis in **Appendix C**).

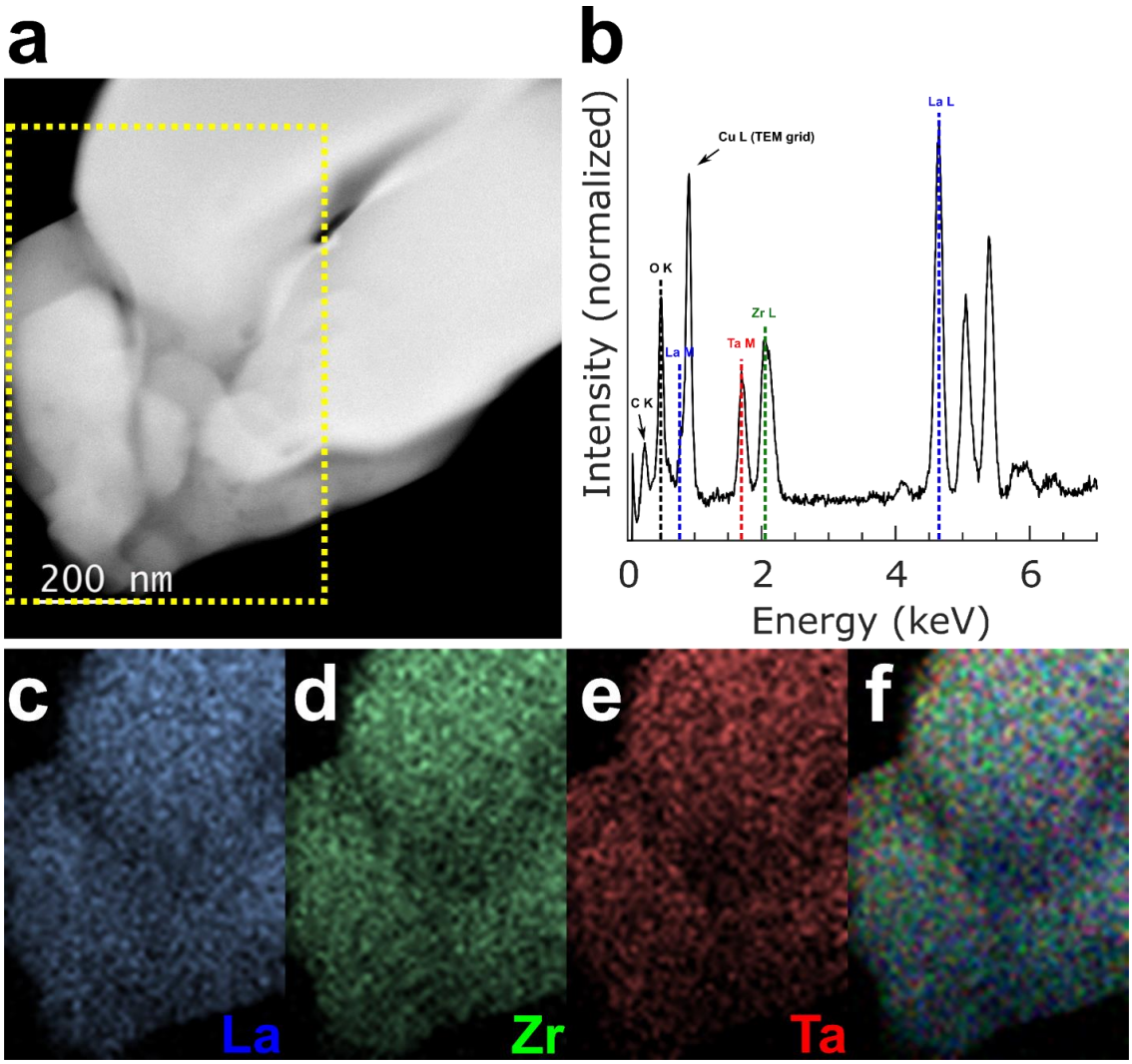

Figure D4. TEM analysis of a cluster of garnet particles with nominal composition of $Li_{6.4}La_3Zr_{1.4}Ta_{0.6}O_{12}$ (LLZTO) synthesized from $La_{2.4}Zr_{1.12}Ta_{0.48}O_{7.04}$ pyrochlore precursors. **(a)** HAADF-STEM image with region of interest shown as dotted box, **(b)** average STEM-EDS spectrum and EDS maps of **(c)** La L, **(d)** Zr L, **(e)** Ta M, **(f)** RGB composite image of particle cluster in **(a).**

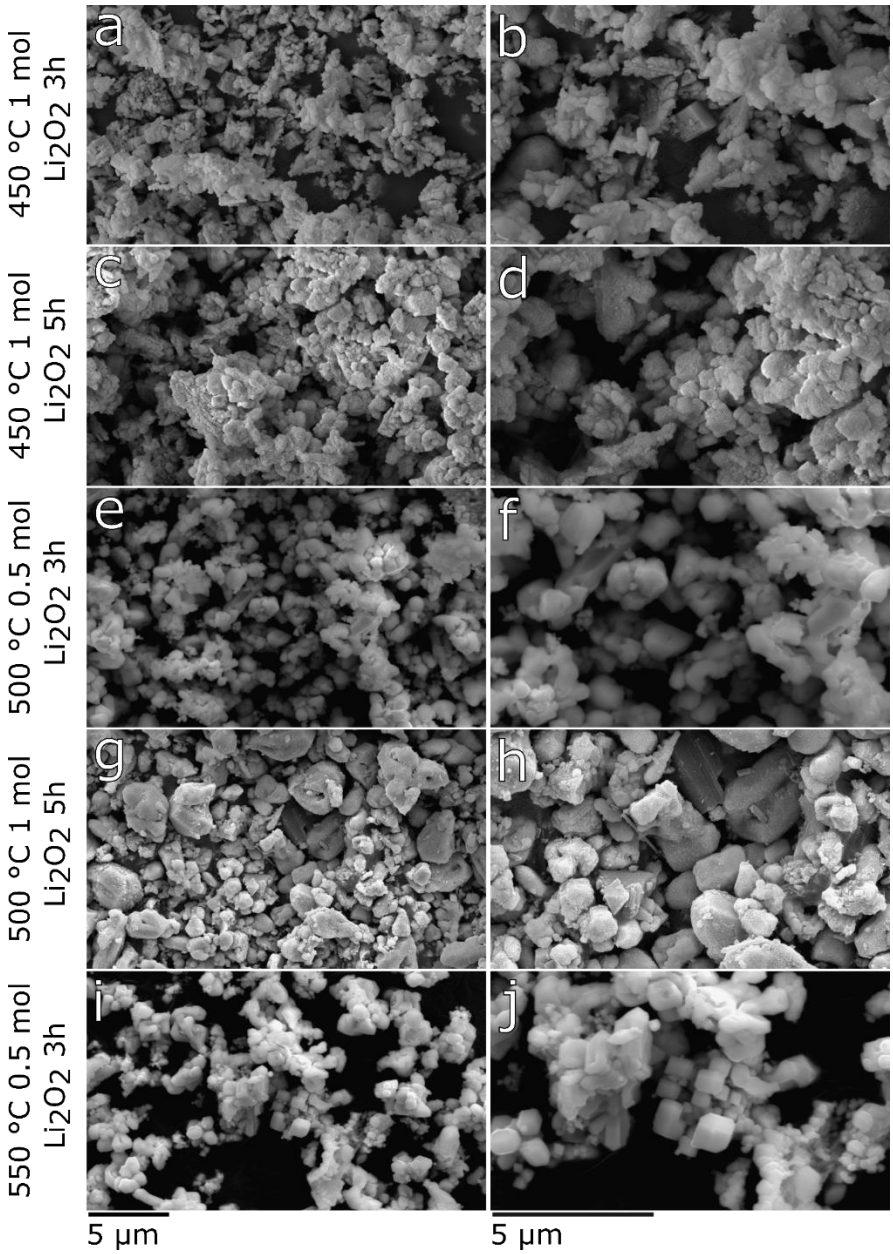

Figure D5. SEM images of LLZTO synthesized from doped pyrochlores in ternary basic molten salts ($LiNO_3$:LiOH:Li_2O_2 ratio of 1.1:3.2:[0.5 , 1]) at **a,b)** 450 °C, 3 h, 1 moles Li_2O_2, **c,d)** 450 °C, 5 h, 1 moles Li_2O_2, **e,f)** 500 °C, 3 h, 0.5 moles Li_2O_2, **g,h)** 500 °C, 5 h, 1 moles Li_2O_2, **i,j)** 550 °C, 3 h, 0.5 moles Li_2O_2. Note that some samples were sputtered with Au to minimize charging, which is the source of the texture on the surface of many particles. In general, submicrometer particles result under minimum reaction time conditions (**a-f,i-j**), which have similar size (< 1 µm) and morphology to the powder in **Figure 6.2b**. However, when the reaction time is extended (**g,h**), the particle size coarsens considerably (> 1 µm).

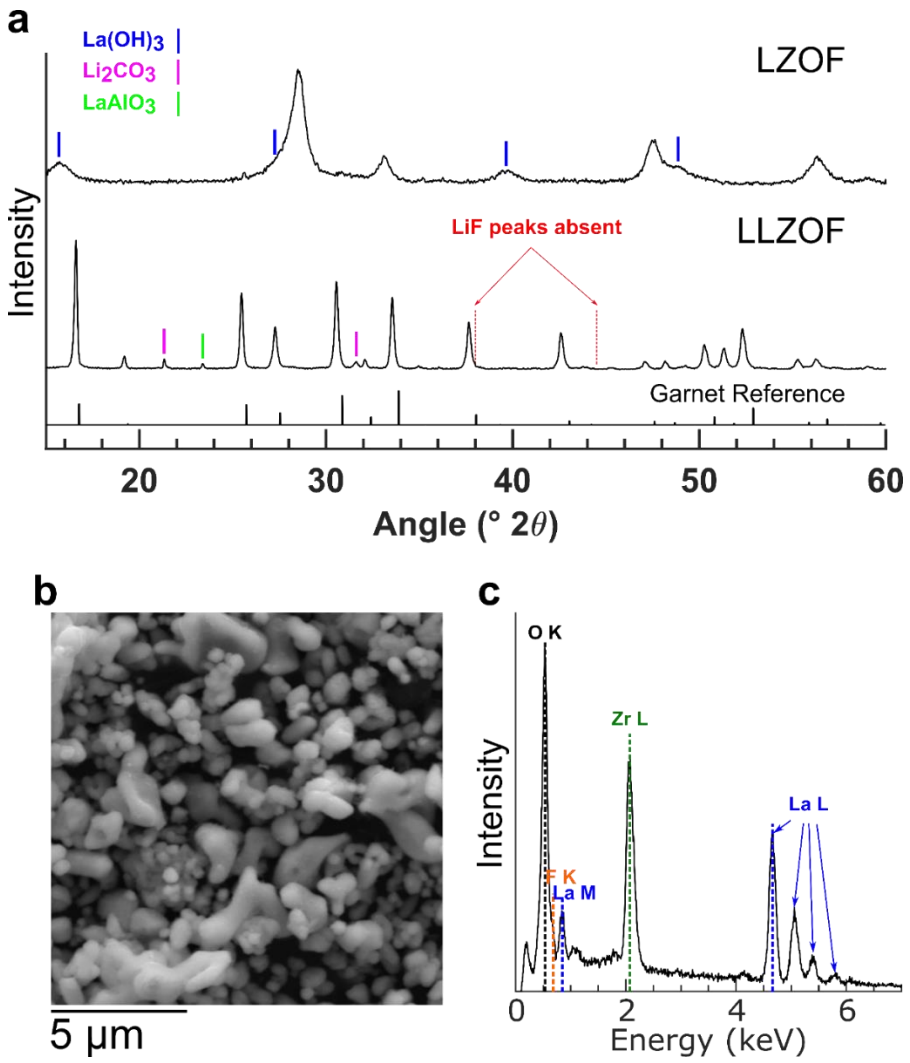

Figure D6. **(a)** XRD patterns of $La_{2.4}Zr_{1.6}O_{6.55}F_{0.5}$ pyrochlore (LZOF) synthesized at 400 °C for 4 hours (using $La(NO_3)_3$, $ZrOCl_2$, and NaF as reagents) and $Li_{6.375}La_3Zr_2O_{11.375}F_{0.625}$ (LLZOF) garnet synthesized using the pyrochlore as reagent (reaction with 1 : 3.2 moles Li_2O_2 : LiOH at 550 °C for 5 hours) with cubic garnet reference (from Logéat *et al.*[48]) and trace $LaAlO_3$ (ICSD coll. code 92521) noted, which is believed to be a contaminant phase from a worn Al_2O_3 crucible, (which can be a challenge as noted in the experimental details **Appendix D.1** above), note the absence of LiF peaks (ICSD coll. code 41409) indicating incorporation of F^- into the garnet lattice. Although some Al-containing phases are seen in the XRD pattern, the lack of Al-signal in the EDS spectrum (~1.5 keV for Al K) indicates that the cubic phase is stabilized solely by F; **(b)** SEM image and **(c)** SEM-EDS spectrum of LLZOF garnet powders synthesized from LZOF pyrochlores with locations of La, Zr, O, and F signals indicated

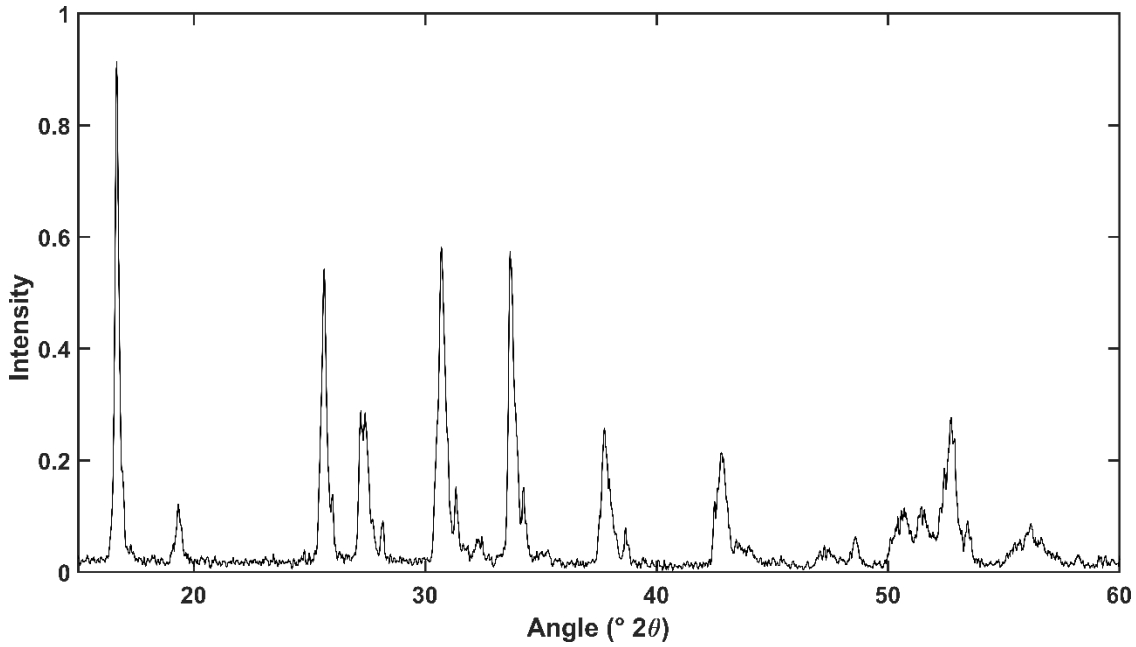

Figure D7. XRD pattern of LLZOF with nominal composition $Li_{6.5}La_3Zr_2O_{11.5}F_{0.5}$ synthesized from pyrochlores using slightly less NaF and the same synthesis time and temperature as in **Figure D6**. Note the presence of peak splitting, indicating partial tetragonal distortion.

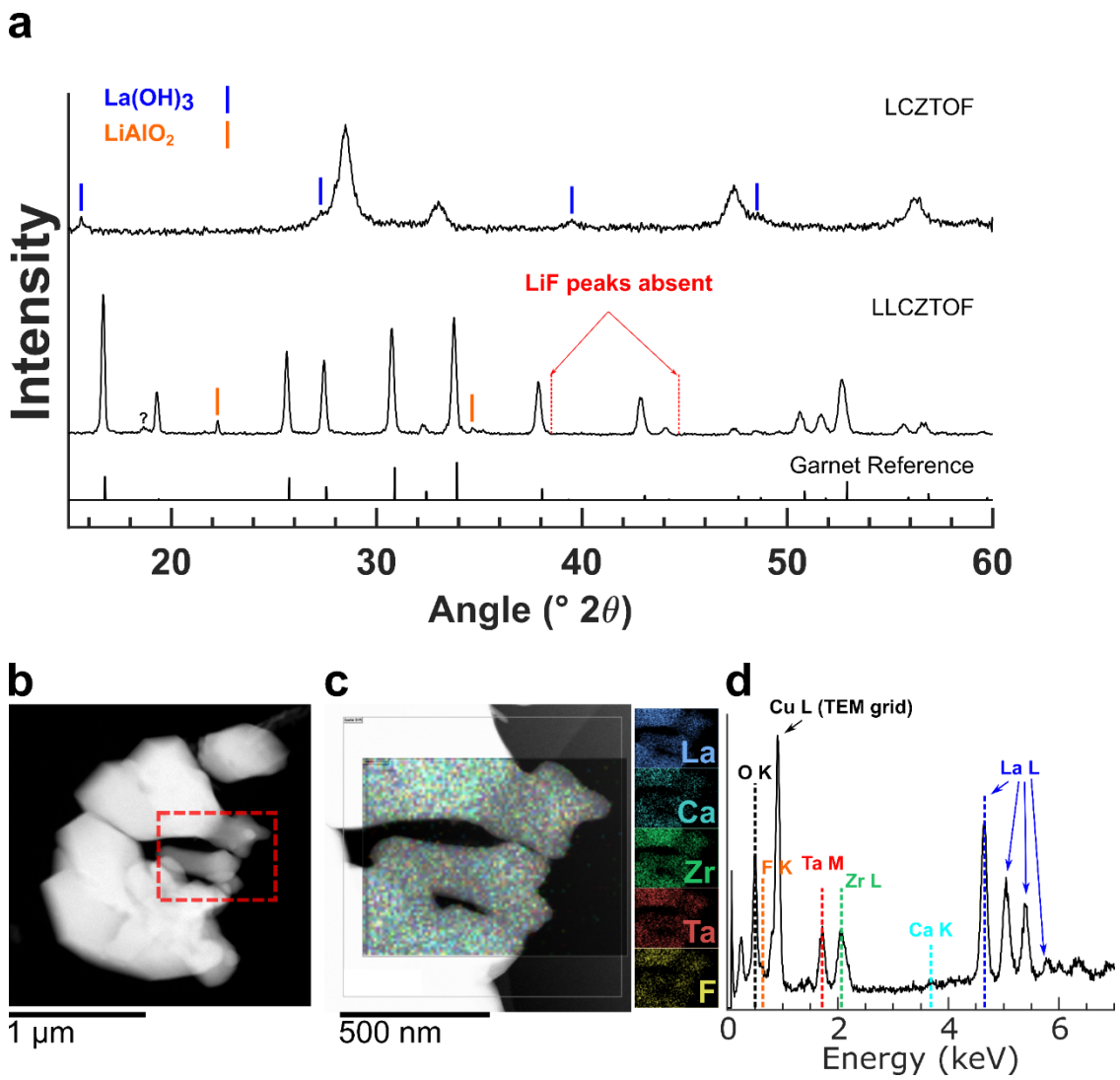

Figure D8. **(a)** XRD patterns of pyrochlore synthesized at 400 °C for 4 hours (using $La(NO_3)_3$, $ZrOCl_2$, NaF, and $Ca(NO_3)_2$ as reagents) with nominal composition of $La_{2.2}Ca_{0.2}Zr_{1.12}Ta_{0.48}O_{6.69}F_{0.5}$ (LCZTOF) and garnet with nominal composition of $Li_{6.025}La_{2.75}Ca_{0.25}Zr_{1.4}Ta_{0.6}O_{11.375}F_{0.625}$ (LLCZTOF) synthesized at 500 °C for 3 h (0.5 : 3.2 mol ratio Li_2O_2 : LiOH) from the LCZTOF multiply-doped pyrochlore with cubic garnet reference (Logéat et al.[48]) and trace impurity, in this case $LiAlO_2$ (ICSD Coll. Code 23815) noted, which is believed to be a contaminant phase from a worn Al_2O_3 crucible, (which can be a challenge as noted in the experimental details **Appendix D.1** above), note the absence of LiF peaks (ICSD Coll. Code 41409) indicating incorporation of F^- into the garnet lattice, **(b)** HAADF-STEM image of LLCZTOF garnet (region of interest for spectral mapping outlined in red), **(c)** HAAD-STEM image of (**b**) with EDS spectral mapping noted, and individual element maps shown, **(d)** average STEM-EDS spectrum from (**c**) with locations of La, Ca, Zr, Ta, O, and F signals noted.

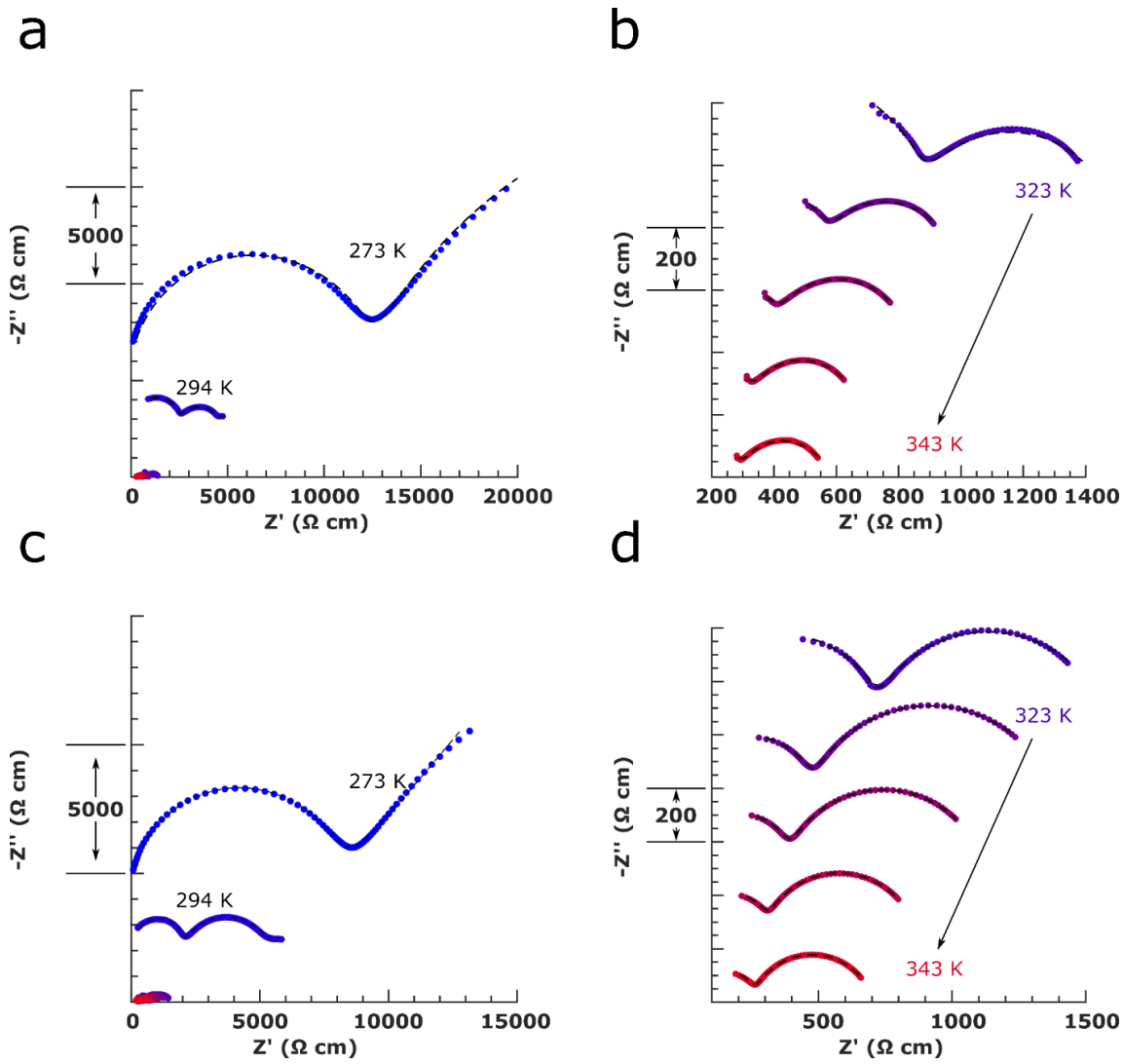

Figure D9. Nyquist plots measured between 7 MHz and 1 kHz of temperature dependence of impedance used to generate Arrhenius plot in **Figure 6.3** for conventional sintering, **a)** overview and **b)** zoomed region of (**a**) showing higher temperature EIS spectra, and reactive sintering, **c)** overview and **d)** zoomed region of (**c**) showing higher temperature EIS spectra. Black dashed lines show circuit fitted impedance spectra. For clarity, impedance spectra are vertically offset, major axis marks on -Z" axis are shown.

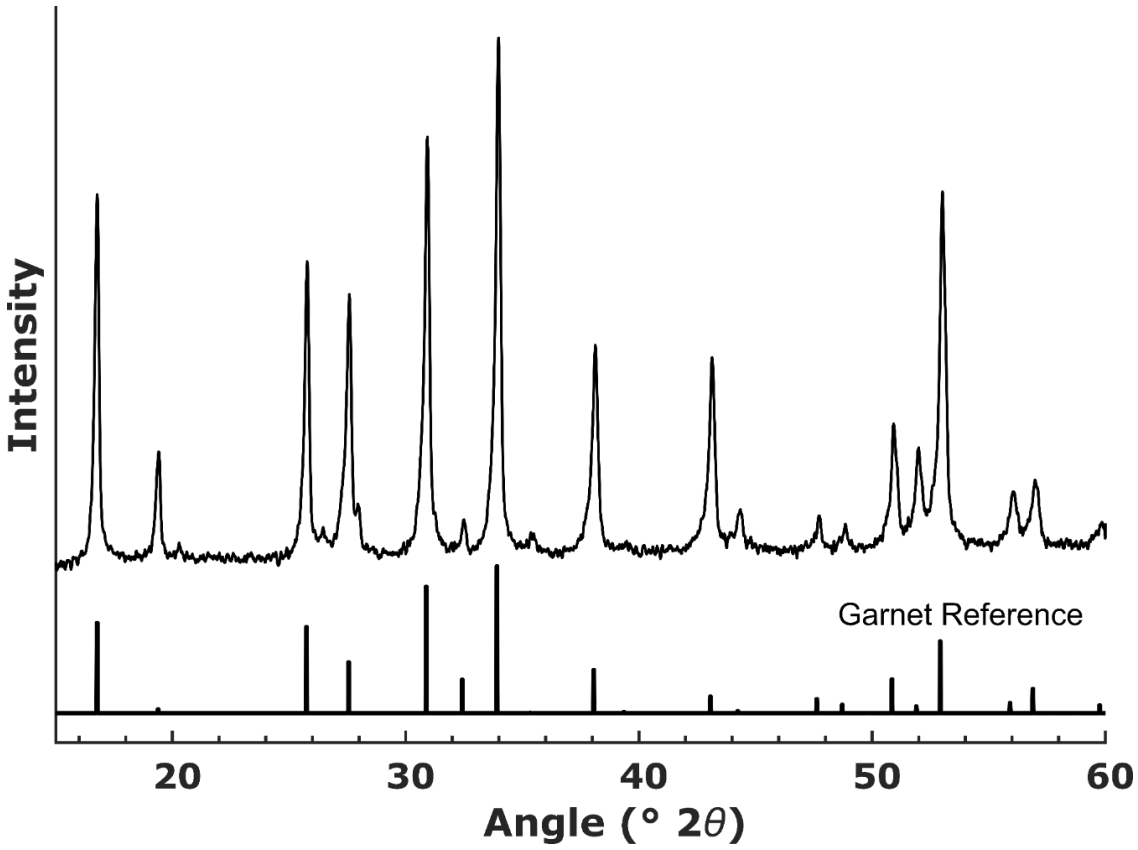

Figure D10. XRD pattern of garnet pellet obtained from *in situ* reactive sintering of pyrochlores + LiOH at 1200 °C for 3 h with cubic garnet reference pattern (from Logéat *et al.*[48]) also shown.

APPENDIX E

SUPPORTING INFORMATION FOR CHAPTER 7

E.1. Experimental Details

E.1.1. Materials and Reagents

All reagents used are of ACS grade or higher unless otherwise noted and used as-received. Lithium carbonate ($Li_2(CO_3)$) and bulk zirconium oxide (ZrO_2) powders (~ 5 µm particle size) were obtained from Sigma-Aldrich. Tantalum oxide (Ta_2O_5) and lanthanum hydroxide ($La(OH)_3$) were obtained from Alfa Aesar. Lithium peroxide (Li_2O_2, technical grade, 95%) was obtained from Acros Organics. Nanosized ZrO_2 powders (~30 nm) were procured from MSE Supplies (Tucson, AZ). Isopropanol (ACS grade) and methanol (HPLC grade) were obtained from BDH Chemical.

E.1.2. Synthesis of LLZTO by Solid-State Reaction for Comparison

For comparison with MSS LLZTO, LLZTO of the same composition was synthesized via the solid-state reaction (SSR) method via a one-step or two-step solid-state reaction. Stoichiometric $La(OH)_3$, ZrO_2, and Ta_2O_5 with 20% excess Li_2CO_3 (based on the composition $Li_{6.4}La_3Zr_{1.4}Ta_{0.6}O_{12}$) were used as reagents.

For the single step SSR method ("1x-SSR_{1000}" sample), the synthesis is as described in our previous[145] work. For the two-step SSR ("1x-SSR_{950}" and "2x-SSR_{950}" samples) approach, two sets of samples were prepared. In the first, pre-ball-milled (SPEX 8000M, 90 minutes, polymer jars and tungsten carbide inserts and milling ball) Ta_2O_5 powder (to produce submicron to nanosized powder) and ZrO_2 nanoparticles (MSE Supplies, ~ 30 nm diameter) were used as the Ta- and Zr-source. These were blended with Li_2CO_3 (10% excess based on the nominal composition) and $La(OH)_3$ by ball-milling (SPEX 8000M, 55 mL volume tungsten carbide jar with tungsten carbide milling balls) with an equivalent mass of isopropanol for 90 minutes. Then the milled slurry was collected, dried, and calcined in a MgO crucible with a MgO lid (Tateho Ozark Technical Ceramics, part # SR3005 and SF300 for the crucible and lid respectively) at 950 °C for 8 h. Half of the as-synthesized LLZTO powder was then ball-milled a second time using the same parameters, and calcined a second time also with the same parameters. These samples are thus named "N-1x-SSR_{950}" and "N-2x-SSR_{950}" respectively. The second set of samples was prepared using the same procedure, except with bulk Ta_2O_5 and ZrO_2 powders instead. These samples are thus named "B-1x-SSR_{950}" and "B-2x-SSR_{950}" respectively. Finally, before sintering experiments all the SSR samples were ball-milled in polymer jars with tungsten carbide inserts and milling ball using a SPEX 8000M mill for 60 (in the case of initial experiments with the 1x-SSR_{1000} sample) to 90 (for later experiments with the 1x-SSR_{1000} sample and the 2x-SSR samples) minutes to reduce

particle sizes and increase sinterability. Note: after the experiments performed it was observed that the furnace temperature was somewhat lower than the readout value. We believe that the actual synthesis temperature for the 1x-SSR_{950} and 2x-SSR_{950} samples synthesized herein are therefore somewhat below 950 °C but between 900-950 °C.

Some of these SSR LLZTO samples (N-2x-SSR_{950} and 1x-SSR_{1000}) were sintered at 1100-1200 °C using the same approach as in our previous works[145,146,197], which used the strategy of Huang et al.[16] to minimize Li_2O loss. Briefly, pellets were sintered in MgO crucibles with MgO lids to form a reasonably sealed sintering environment. Some mother powder was placed atop a MgO spacer, upon which the pellet was placed for sintering followed by covering with some mother powder. Additionally, a small amount of mother powder was mixed with Li_2O_2 and placed below the MgO spacer to provide sacrificial powder to maintain sufficient Li_2O vapor pressure, as described previously.[145,146,197] See also the discussion of sintering methods in **Chapter 2.1**.

E.2. Characterization Methods

X-ray diffraction (XRD) was performed using a Bruker D-8 powder diffractometer with CuK_α radiation for crystalline phase identification. The reference pattern for Ta-doped LLZO ($Ia\bar{3}d$) was generated according to the structure reported by Logéat et al.[48] X-ray total scattering measurements were performed at room temperature at beamline I15-1 of Diamond Light Source (Didcot, UK) at $\lambda = 0.161669$ Å (76 keV). The total scattering data were collected and pair distribution functions (PDFs) generated and refined using PDFgetx3[154] within xPDFsuite[152] and PDFgui[151] software packages.

To generate the PDFs, the following parameters were used: $Q_{min} = 0.1$ Å^{-1}, $Q_{max} = 25$ Å,$^{-1}$ $r_{step} = 0.01$ Å, and $r_{poly} = 0.9$. PDF refinements were carried out using PDFgui[151]. PDF refinements were performed using $Q_{damp} = 0.0247$ and $Q_{broad} = 0.0151$ (obtained from refinement of a NIST Si standard). To refine a PDF pattern, a structure file of $Li_{6.4}La_3Zr_{1.4}Ta_{0.6}O_{12}$ (generated based on the results of Logéat et al.[48]) was first selected and then the scale factor and lattice parameter were refined. After this, the atomic displacement parameters (ADP) for each element (initially set based on the CIF structure file to 0.0148 Å^2 for La, 0.0119 Å^2 for Ta and Zr, 0.02 Å^2 for Li, and 0.009 Å^2 for O) and the linear atomic scale factor (*delta1*) were refined.

The morphology of powders and sintered pellets was examined using a FEI XL-30 scanning electron microscope (SEM) equipped with an EDAX system. To minimize charging, a carbon film was deposited before imaging using a thermal evaporator type

carbon coater. Carbon was used rather than e.g. Au or Pd due to peak overlap in the EDS spectra. Transmission electron microscopy (TEM) was performed using an aberration corrected (CEOS image corrector) FEI Titan Environmental TEM operated at 300 kV or a Philips CM-200 TEM operated at 200 kV. Energy dispersive x-ray spectra (EDS) using either the Titan or CM-200 were collected using an EDAX system. Electron diffraction (ED) patterns were obtained with the FEI Titan using a third condenser lens to allow formation of a submicrometer diameter parallel beam rather than using a selected area aperture. Scanning transmission electron microscopy (STEM) was performed using a probe corrected (CEOS CESCOR hexapole aberration corrector) JEOL ARM200F STEM with a JEOL windowless energy dispersive x-ray spectrometer. To prepare TEM samples, the LLZO powder was ultrasonically suspended in HPLC-grade methanol. A holey carbon TEM grid (Pacific Grid Tech) was then briefly immersed into the aforementioned suspension. Finally, the grid was dried at elevated temperature (e.g. > 100 °C) in air to fully remove methanol.

E.3. Method for processing EDS data for Ta-content determination

In order to approximate the Ta-content of individual LLZTO particles (or grains in the case of sintered LLZTO), SEM, TEM, or STEM-EDS was employed followed by a data processing method to estimate the composition as follows. All data processing was performed using Matlab. Experimental EDS spectra were first smoothed (Savitky-Golay filter) and processed using a background subtraction algorithm (polynomial fit), followed by normalizing each individual spectrum to the most intense La L x-ray peak at ~ 4.6 keV. This normalization approach is justified by the fact that in LLZO of composition $Li_{7-x}La_3Zr_{2-x}Ta_xO_{12}$, **x** can vary such that the Zr and Ta content are within the whole solid-solution[48] of $Li_7La_3Zr_2O_{12}$ – $Li_5La_3Ta_2O_{12}$, while La must maintain a stoichiometry of 3 moles per formula unit (PFU) and can thus be considered a suitable internal standard for signal normalization. Further, neither Zr nor Ta can be expected to dope the La sites or vice-versa in LLZO due to the large difference in ionic radius.[220] After this processing approach, the relative peak intensities of the Ta M and Zr L x-ray peaks at ~ 1.7 and 2 keV respectively are compared, and the Ta M to Zr L peak ratio calculated.

For a more accurate assessment of Ta-content of each individual particle, EDS spectra for $Li_{7-x}La_3Zr_{2-x}Ta_xO_{12}$ ($0.2 < x < 1.0$) were simulated using the NIST DTSA II software (information about which may be found at: *https://www.nist.gov/services-resources/software/nist-dtsa-ii*). Simulated EDS spectra were generated for SEM at 10kV and 15 kV to correspond to the experimental SEM-EDS data acquired at these voltages, for TEM or STEM at 200 kV to correspond to the experimental TEM-EDS or STEM-EDS data acquired at 200 kV, and also for TEM at 300 kV to correspond to the

experimental TEM-EDS data acquired at 300 kV. We note that the differences between simulated EDS spectra from very different accelerating voltages are relatively minor, and the Ta M / Zr L peak ratios for a given composition at these various accelerating voltages are quite close, indicating that the Ta M / Zr L peak ratio is generally insensitive to instrumental parameters. Nevertheless, an individual simulated EDS dataset was used for each accelerating voltage and applied to the corresponding experimental data to ensure maximum reliability of the analysis. Using these simulated EDS spectra, a regression based on the intensity ratio of the Ta M and Zr L peaks and the composition used for simulation was generated. An example of the simulated EDS spectra is shown in **Figure E5**.

Finally, the actual Ta-content of each individual particle or grain measured by SEM, TEM, or STEM-EDS was approximated by applying the regression generated from simulated EDS spectra (same accelerating voltage as the experimental EDS spectra) to the processed experimental EDS data. These are the data that are presented in **Figure 7.2 and 7.5** for powder samples and **Figures 7.7 and 7.8** for pellet samples. We would like to note that for the HB-MSS samples, EDS spectra from several different but related samples were compared (same reaction medium, 550 °C synthesis temperature, 2.5, 3, and 4 h reaction times – in the case of the specific 4 h sample used, a slight difference from our previously reported method[145] was employed wherein the $ZrOCl_2$ was pre-mixed with the salts and the $La(NO_3)_3$ and Ta_2O_5 were added after the salts were molten). This is due to the initial exploratory nature of understanding the origins of compositional variability on a particle-by-particle basis, and the TEM-EDS measurements were performed for several similar but distinct samples to determine whether this variability in Ta / Zr content was a general trend. However, due to the similarity of the samples, we believe that combining the datasets gives a reasonable assessment of the elemental inhomogeneity that arises in LLZTO from the HB-MSS method. All other EDS datasets are from a single powder or pellet sample.

In this work, the distributions of Ta-content of the various powder and pellet samples are presented as kernel density plots. Briefly, the kernel density estimator explored initially by Rosenblatt[221] and then Parzen[222], is a non-parametric method of representing or estimating the probability density function of a random variable.[223] It employs a smoothing function (often a Gaussian) and a bandwidth (with an optimal value generally calculated automatically based on the dataset assuming a normal distribution[224] such as is implemented in the Matlab function ‘ksdensity,’ which is used in this work to generate kernel density plots, see notes on this at https://www.mathworks.com/help/stats/kernel-distribution.html) to estimate the actual probability density of a sample set. It is similar to a histogram but represents the probability density by a continuous curve rather than a discrete set of bins.

E.4. Supporting Tables

Table E1. Comparison of properties of the LLZO prepared using molten salt synthesis (MSS), non-aqueous polymer (NAP) combustion, pyrochlore-to-garnet molten salt synthesis (PG-MSS) and conventional solid-state reaction (sintered using the approach of our previous works[145,146,197]). The total ionic conductivity (measured at room temperature unless otherwise noted, σ_{tot}) has units of mS cm^{-1}. Density (%) is relative to the theoretical density of LLZTO of this composition (~5.5 g cm^{-3}). The entries in this table are sintered in Al_2O_3 crucibles unless otherwise indicated.

Synthesis Method	Synthesis Conditions		Sintering Conditions		Pellet Properties			Ta-content	Ref.
	Temp. (°C)	Time (h)	Temp.(°C)	Time (h)	Density	σ_{tot}	E_a		
Solid-state reaction[f]	1000	8	1200 [MgO]	3.5	93.0	**0.71**	0.41	0.6	This Work
Solid-state reaction[f]	1000	8	1100 [MgO]	12	93.7	**0.52**	NM	0.6	This Work
Solid-state reaction[f,*]	950	2x8	1200 [MgO]	2	93.2	**0.45**	0.41	0.6	This Work
Solid-state reaction[f,*]	950	2x8	1200 [MgO]	2	90.4	**0.34**	NM	0.6	This Work
HB-MSS	550	2.5	1200 [MgO]	3	93.4	**0.35**	0.39	0.6	Ref.[145]
mHB-MSS	550	8	1200 [MgO]	4	91.1	**0.61**	0.40	0.6	Ref.[145]
Mixed-MSS	900	4	1200 [MgO]	2	78.5	**0.47**	NM	0.6	Ref.[145]
Chloride-MSS	900	4	1200 [MgO]	4	87.9	**0.46**	0.40	0.6	Ref.[145]
PG-MSS	550	1	1200 [MgO]	2	88.0	**0.42**	0.42	0.6	Ref.[197]
NAP combustion	700	4	1100 [MgO]	6	90.5	**0.57**	0.40	0.6	Ref.[146]
Solid-state reaction[*]	900	2x10	1130	36	91.7	0.73	NR	0.2	Ref.[34]
Solid-state reaction[*]	900	2x10	1130	36	92.7	0.63	NR	0.25	Ref.[34]
Solid-state reaction[*]	900	2x10	1100	36	92.5	0.69	0.36	0.3	Ref.[34]
Solid-state reaction[*]	900	2x10	1130	36	92.8	0.46	NR	0.35	Ref.[34]
Solid-state reaction[*]	900	2x10	1130	36	92.8	0.47	NR	0.4	Ref.[34]
Solid-state reaction[*]	900	2x10	1130	36	93.6	0.40	NR	0.45	Ref.[34]
Solid-state reaction[*]	900	2x10	1130	36	94.1	0.28	NR	0.5	Ref.[34]
Solid-state reaction[f,*]	950	2x6	1250 [MgO]	6	93.9	0.42	0.43	0.6	Ref.[87]
Solid-state reaction[f,*]	950	2x6	1280/1180 [MgO]	0.33/5	97	0.74	0.42-0.45	0.6	Ref.[41]
Solid-state reaction[f,*]	950	2x6	1280 [MgO]	5	97	0.78	0.42-0.45	0.6	Ref.[41]
Solid-state reaction[f,*]	950	2x6	1250 [MgO]	0.33	97	0.64	~0.45	0.6	Ref.[39]
Solid-state reaction[f]	900	12	1180 [ZrO2]	12	88	0.13	0.46	0.2	Ref.[33]
Solid-state reaction[f]	900	12	1180 [ZrO2]	12	92	1.03	0.37	0.3	Ref.[33]
Solid-state reaction[f]	900	12	1180 [ZrO2]	12	96	0.67	0.46	0.4	Ref.[33]
Solid-state reaction[f]	900	12	1180 [ZrO2]	12	93	0.62	0.45	0.5	Ref.[33]
Solid-state reaction[f]	900	12	1180 [ZrO2]	12	91	0.33	0.53	0.6	Ref.[33]
Solid-state reaction[f]	750 / 900	6 / 6	1150	12	NR	0.72	0.24	0.6	Ref.[42]
Solid state reaction	900	6	1200	24	84	0.15[‡]	0.40	0.6	Ref.[43]
Solid state reaction[*]	1x at 850 / 2x at 1000	3x20	1150 [Al]	5	92.7	0.71	0.42	0.4	Ref.[28]
Solid state reaction[**]	900	NR	1140	16	NR	0.28	0.35	0.2	Ref.[38]
Solid state reaction[**]	900	NR	1140	16	NR	0.73	0.35	0.4	Ref.[38]
Solid state reaction[**]	900	NR	1140	16	NR	0.92	0.35	0.5	Ref.[38]
Solid state reaction[**]	900	NR	1140	16	NR	1.0	0.35	0.6	Ref.[38]
Solid state reaction[**]	900	NR	1140	16	NR	0.32	0.35	0.8	Ref.[38]
Solid state reaction[**]	900	NR	1140	16	NR	0.16	0.35	1	Ref.[38]
Solid state reaction	854	3	1100 [YSZ]	4	NR	~0.27	~0.44	0.2	Ref.[29]
Solid state reaction	854	3	1100 [YSZ]	4	NR	~0.5	~0.43	0.3	Ref.[29]
Solid state reaction	854	3	1100 [YSZ]	4	NR	~0.75	~0.42	0.4	Ref.[29]
Solid state reaction	854	3	1100 [YSZ]	4	NR	0.84	~0.43	0.5	Ref.[29]
Solid state reaction	854	3	1100 [YSZ]	4	NR	~0.63	~0.44	0.6	Ref.[29]

Solid state reaction	900	12	1000 *sps*	0.166	95.5	0.69	0.42	0.5	Ref.[30]
Solid state reaction	950	6	1140 *Pt*	16	96	0.50	0.38	0.5	Ref.[124]
Solid state reaction	950	6	1140	16	94	0.36	0.39	0.5	Ref.[124]
Solid state reaction	950	6	1140 *Al*	16	90	0.12	0.41	0.5	Ref.[124]
Chloride-MSS	900	5	1200 *Pt*	16	97	0.61	0.37	0.5	Ref.[124]
Chloride-MSS	900	5	1200	16	93	0.34	0.40	0.5	Ref.[124]
Chloride-MSS	900	5	1200 *Al*	16	90	0.1	0.52	0.5	Ref.[124]
Co-precipitation	900	3-4	1050 *hp*	1	97.1	0.39	0.45	0.75	Ref.[37]
Co-precipitation	900	3-4	1050 *hp*	1	97.8	0.82	0.43	0.5	Ref.[37]
Co-precipitation	650 / 900	15 / 3-4	1050 *hp*	1	96	0.87	0.22	0.25	Ref.[27]
Solution-combustion synthesis	750	8	1125	6	NR	0.2	NR	0.6	Ref.[31]
Solution-combustion synthesis *Ca*	750	8	1125	6	NR	0.28	NR	0.6	Ref.[31]
Sol-Gel	900	2	1000 *hp*	1	88	0.05	0.43	0.6	Ref.[35]
Sol-Gel *Ca*	900	2	1000 *hp*	1	89	0.2	0.36	0.6	Ref.[35]
Sol-Gel	900	4	1100 *hp*	1	92	0.48	NR	0.5	Ref.[26]
Sol-Gel	900	12	1180	36	96.7	0.52	NR	0.25	Ref.[32]
Sol-Gel	900	12	1180	36	96.2	~0.37	NR	0.5	Ref.[32]
Sol-Gel	900	12	1180	36	96.0	~0.27	NR	0.7	Ref.[32]
FZ Single Crystal Growth	850	60	FZ	FZ	100	1.1	0.39-0.47	0.4	Ref.[51]
FZ Single Crystal Growth	850	60	FZ	FZ	100	1.3	0.44	0.5	Ref.[50]

‡ - σ_{tot} measured at 33 °C

hp – consolidated via hot-pressing

sps – spark-plasma sintering

⸗ - high energy ball milling (e.g. planetary milling, attrition milling, etc.) of LLZTO to reduce particle size

** - repeated grinding and heating steps (e.g. 2x10 = 2 calcination steps each for 10 hours)*

*** - exact details of synthesis not reported (e.g. degree method of grinding, calcination time, etc.)*

Ca – Ca as co-dopant

Pt – sintered in platinum crucible

MgO – sintered in MgO crucible

ZrO_2 – sintered in ZrO_2 crucible

YSZ – sintered in yttria-stabilized ZrO_2 crucible

Al – Al_2O_3 added as sintering aid

NR – not reported

NM – not measured

~ - indicates estimated from a plot

FZ – grown by floating zone single crystal growth method, sintering not applicable

Table E2. Pellet dimensions and Z-Fit parameters / impedances for SSR LLZTO pellets measured at room temperature (conductivity in mS cm^{-1}) with or 1.5 mol % (20 wt %) Sn-Li electrodes. EIS fitting was performed as described in our previous work[11] (b = bulk, gb = grain boundary, el = electrode, tot = total).

Parameter	**Unit**	**SSR LLZTO Sample**		
		2x-SSR$_{950}$ – 1200-2h	**1x-SSR$_{1000}$ – 1200-3.5h**	**1x-SSR$_{1000}$ – 1100-12h**
Pellet area, A	cm^2	0.282	0.309	0.279
Pellet thickness, t	cm	0.0834	0.0963	0.082
Relative density, ρ	%	93.2	93.0	93.7
R_b	Ω	607	414	566
Q_b	F $s^{(a-1)}$	1.3 x 10^{-10}	1.5 x 10^{-10}	9.8 x 10^{-11}
R_{gb}	Ω	49.31	25.8	-
Q_{gb}	F $s^{(a-1)}$	2.0 x 10^{-8}	1.7 x 10^{-6}	-
R_{el}	Ω	95.5	827	864
Q_{el}	F $s^{(a-1)}$	3.4 x 10^{-6}	4.2 x 10^{-2}	1.3 x 10^{-6}
$\sigma_{lattice}$	mS cm^{-1}	0.49	0.75	0.52
σ_{tot}	mS cm^{-1}	0.45	0.71	0.52
E_a	eV $atom^{-1}$	0.41	0.41	-

Table E3. Bragg reflection full-width half-maximum (FWHM) for select major peaks for the various samples investigated in this work along with the change in FWHM (ΔFWHM) between the lowest order and highest order reflections (in this case [211] and [642]) and room temperature total ionic conductivity where measured. These data are plotted various forms in **Figure 7.5** and **Figure 7.8**.

Sample	**T_{synth}**	**[211]**	**[321]**	**[400]**	**[420]**	**[422]**	**[642]**	**ΔFWHM**	**σ_{tot}**	**Ref.**
PG-400	400	0.2	0.26	0.3	0.32	0.36	0.58	**0.38**	-	Ref[197]
PG-500	500	0.18	0.24	0.3	0.32	0.32	0.5	**0.32**	-	Ref[197]
PG-550	550	0.18	0.2	0.22	0.25	0.25	0.36	**0.18**	**0.42**	Ref[197]
HB	550	0.18	0.24	0.24	0.27	0.29	0.45	**0.27**	**0.35**	Ref[145]
mHB	550	0.23	0.28	0.27	0.32	0.33	0.49	**0.26**	**0.61**	Ref[145]
Mixed	700	0.18	0.23	0.25	0.23	0.28	0.41	**0.23**	-	Ref[145]
NAP	700	0.18	0.19	0.21	0.22	0.23	0.31	**0.13**	**0.57**	Ref[146]
Mixed	900	0.16	0.17	0.18	0.2	0.21	0.32	**0.16**	**0.47**	Ref[145]
Chloride	900	0.18	0.2	0.21	0.23	0.24	0.35	**0.17**	**0.46**	Ref[145]
N-SSR 1x 950	950	0.16	0.2	0.21	0.21	0.23	0.34	**0.18**	-	This work
N-SSR 2x 950	950	0.16	0.18	0.19	0.19	0.2	0.28	**0.12**	**0.45**	This work
B-SSR 1x 950	950	0.18	0.19	0.19	0.2	0.22	0.31	**0.13**	-	This work
B-SSR 2x 950	950	0.16	0.19	0.21	0.21	0.2	0.22	**0.16**	-	This work
SSR 1x 1000	1000	0.13	0.16	0.17	0.18	0.18	0.29	**0.16**	**0.71**	This work
Chloride-Pellet	-	0.21	0.21	0.23	0.22	0.22	0.29	**0.08**	**0.46**	This work
mHB-Pellet	-	0.17	0.18	0.22	0.21	0.2	0.25	**0.08**	**0.61**	This work
N-SSR 2x 950-Pellet	-	0.2	0.2	0.22	0.23	0.23	0.29	**0.09**	**0.45**	This work

Table E4. Tabulated PDFgui refinement parameters for Ta-doped LLZO ($Li_{6.4}La_3Zr_{1.4}Ta_{0.6}O_{12}$) from 2x-SSR (2x 8 h, 950 °C), Chloride-MSS (4 h, 900 °C), Mixed-MSS (4 h, 900 °C), mHB-MSS (8 h, 550 °C), and PG-MSS (5 h, 400 °C) LLZTO samples. For Atomic displacement parameters (ADP) the atomic species and lattice site in Wyckoff notation are indicated.

	2x-SSR 950 °C	**Chloride-MSS 900 °C**	**Mixed-MSS 900 °C**	**mHB-MSS 550 °C**
Phase	$Li_{6.4}La_3Zr_{1.4}Ta_{0.6}O_{12}$ $Ia\bar{3}d$	$Li_{6.4}La_3Zr_{1.4}Ta_{0.6}O_{12}$ $Ia\bar{3}d$	$Li_{6.4}La_3Zr_{1.4}Ta_{0.6}O_{12}$ $Ia\bar{3}d$	$Li_{6.4}La_3Zr_{1.4}Ta_{0.6}O_{12}$ $Ia\bar{3}d$
Mol Fraction	1	1	1	1
Lattice Parameter (Å)	a = 12.9236	a = 12.9441	a = 12.948	a = 13.0205
Scale Factor	0.16753	0.164406	0.163197	0.171097
Delta 1	1.89457	1.76037	1.84426	1.61292
ADP*	Li (24d): 0.0132 Li (96h): 0.0132 La (24c): 0.0112 Zr (16a): 0.0089 Ta (16a): 0.0083 O (96h): 0.0448	Li (24d): 0.0325 Li (96h): 0.0325 La (24c): 0.0148 Zr (16a): 0.0147 Ta (16a): 0.0099 O (96h): 0.0288	Li (24d): 0.0271 Li (96h): 0.0271 La (24c): 0.0121 Zr (16a): 0.0114 Ta (16a): 0.0139 O (96h): 0.0489	Li (24d): 0.1584 Li (96h): 0.1584 La (24c): 0.0159 Zr (16a): 0.0432 Ta (16a): 0.0424 O (96h): 0.0475
R_w	0.143	0.163	0.154	0.282

**Atomic displacement parameters (U_{11}= U_{22}= U_{33}, $Å^2$)*

Table E5. Summary of pertinent sample metrics for understanding relationship between synthesis temperature, deviation in Ta-content, relative density of sintered pellet, and ionic conductivity of sintered pellet. Where applicable, total and bulk ionic conductivity were both measured. For the PG-MSS sample, the pellets examined were from material synthesized at 550 °C, whereas the powders were from 500 °C. These data are plotted in **Figure 7.8**.

Sample	**T_{synth}**	**$Stdev_{powder}$**	**$Stdev_{pellet}$**	**σ_{bulk}**	**σ_{tot}**	**ρ**	**Ref**
HB-MSS	550	0.143	0.081	0.38	0.35	93.4	Ref[145]
mHB-MSS	550	0.176	0.032	0.73	0.61	91.1	Ref[145]
PG-MSS	550	0.144	0.0339	0.42	0.42	87.9	Ref[197]
NAP	700	NM	0.057	0.61	0.57	90.5	Ref[146]
Mixed-MSS	900	NM	0.052	NM	0.47	78.5	Ref[145]
Chloride-MSS	900	0.139	0.0439	0.61	0.46	88.0	Ref[145]
N-SSR	950 1x	0.189	-	-	-	-	This work
N-SSR	950 2x	0.107	0.078	0.49	0.45	93.2	This work
B-SSR	950 1x	0.186	-	-	-	-	This work
B-SSR	950 2x	0.148	-	-	-	-	This work
SSR	1000 1x	0.121*	0.059	0.75	0.71	93.0	This work
SSR	1000 1x	0.121*	0.071	0.52	0.52	93.7	This work

** - excluding one outlier, Stdev powder ~ 0.09 moles Ta per formula unit*

E.5. Supporting Figures

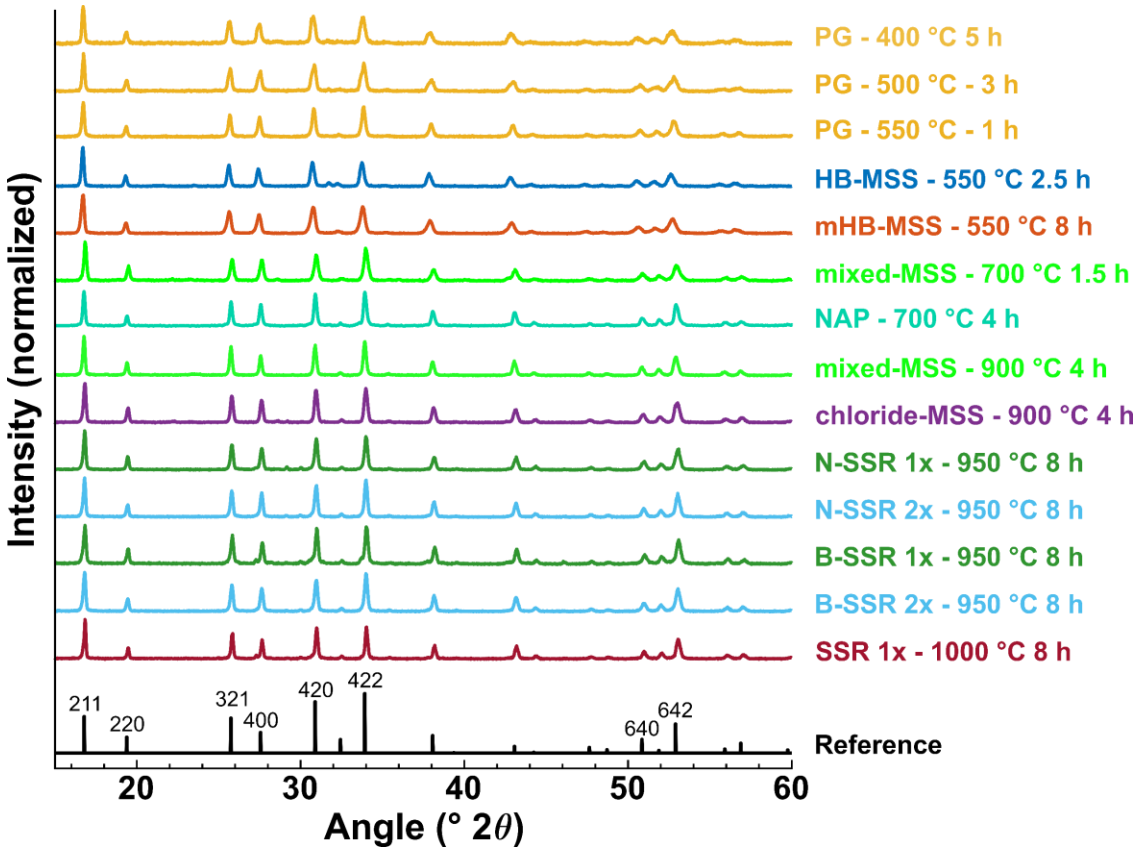

Figure E1. XRD patterns of the different LLZTO samples compared in this work labeled by synthesis method and synthesis temperature. Descriptions of each synthesis method are presented in **Table 7.1**.

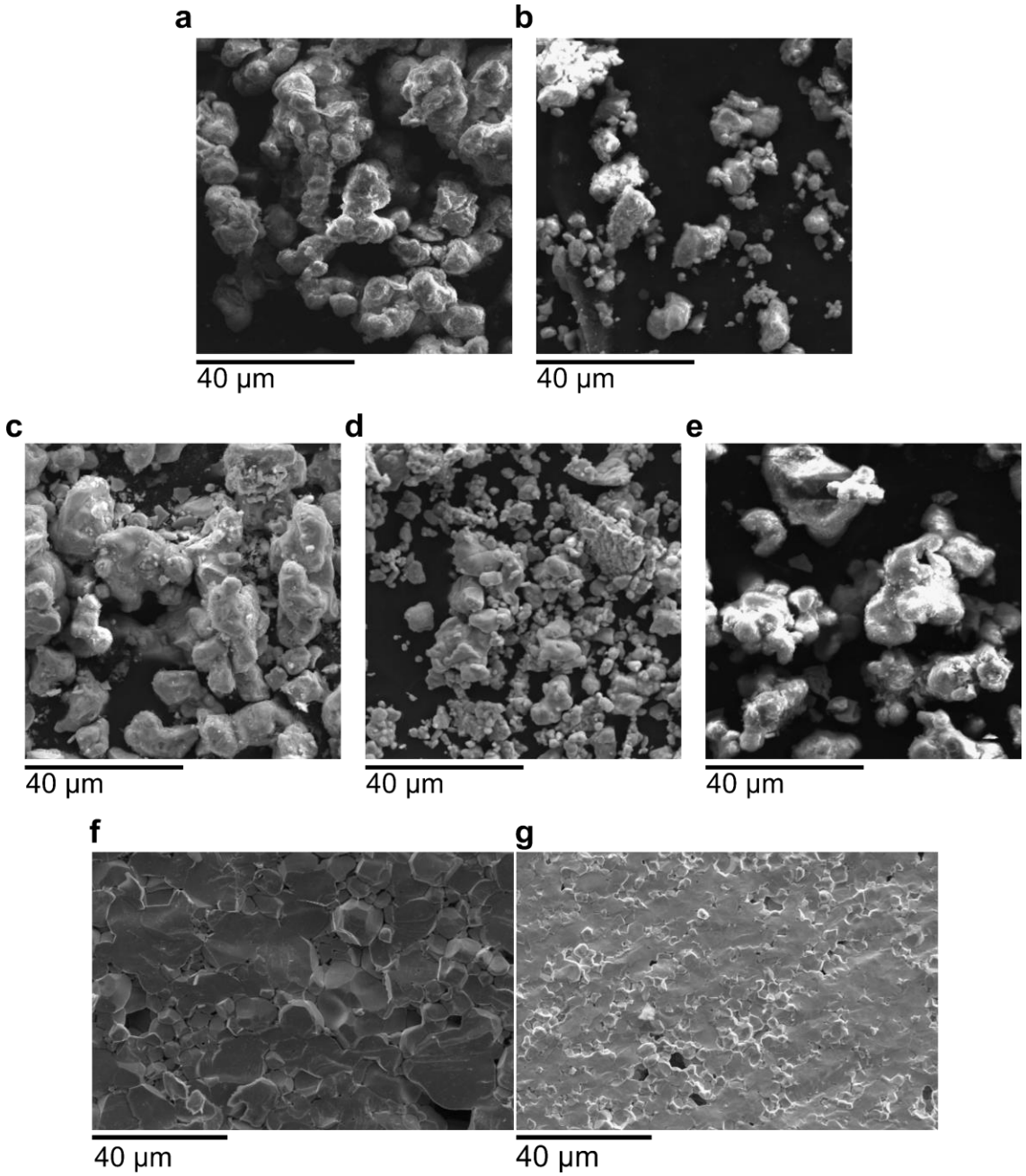

Figure E2. SEM images of (unmilled) SSR LLZTO powders: **a)** N-1x-SSR$_{950}$, **b)** N-2x-SSR$_{950}$, **c)** B-1x-SSR$_{950}$, **d)** B-2x-SSR$_{950}$, **e)** 1x-SSR$_{1000}$, SEM fracture surface image of **f**) 1x-SSR$_{1000}$ LLZTO pellet, and **g**) N-2x-SSR$_{950}$ LLZTO pellet.

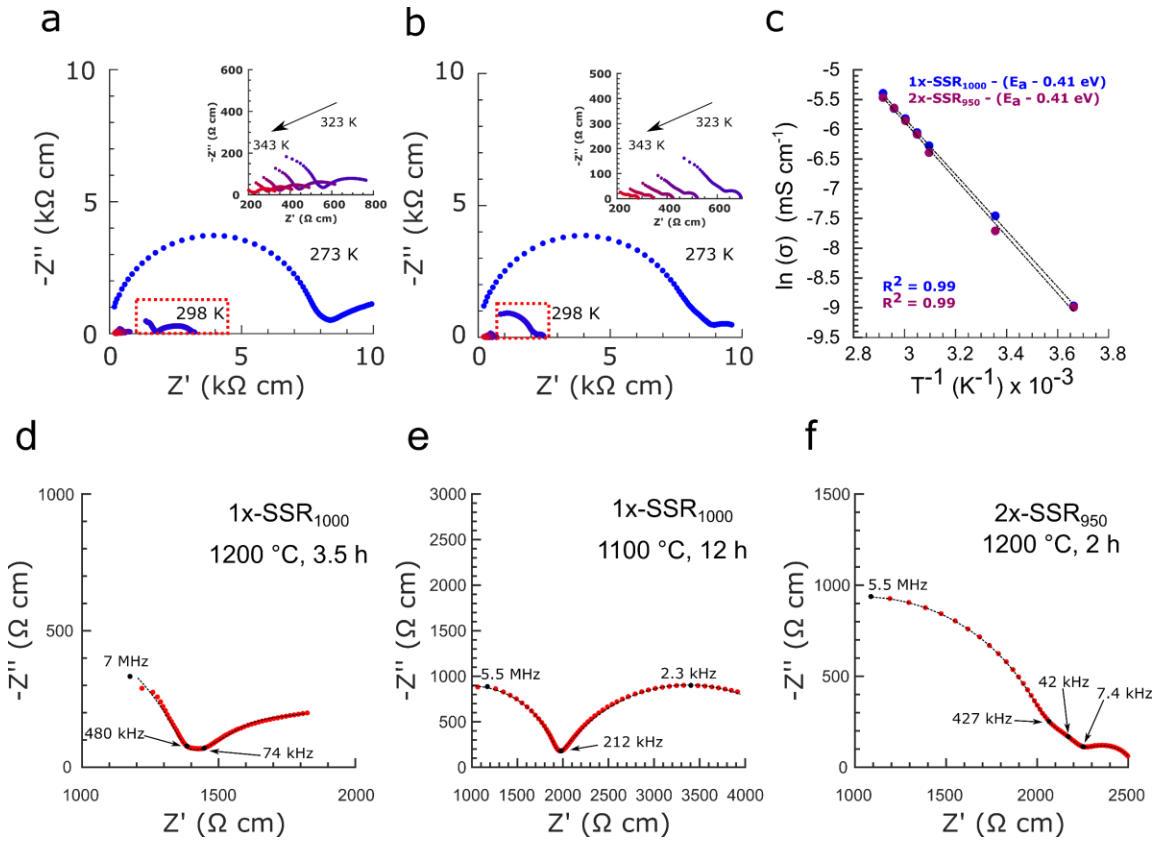

Figure E3. Nyquist plots measured between 273-343 K for **a)** 1x-SSR$_{1000}$ pellet sintered at 1200 °C for 3.5 h and **b)** N-2x-SSR$_{950}$ pellet sintered at 1200 °C for 2 h, **c)** Arrhenius plot of conductivity from samples in (**a,b**) with activation energy plotted, room temperature Nyquist plots of **d)** 1x-SSR$_{1000}$ pellet sintered at 1200 °C for 3.5 h in (**a**), **e)** 1x-SSR$_{1000}$ pellet sintered at 1100 °C for 12 h, and **f)** N-2x-SSR$_{950}$ pellet sintered at 1200 °C for 2 h in (**b**). All EIS measurements taken using 1.5 mol % (20 wt %) Sn-Li electrodes.

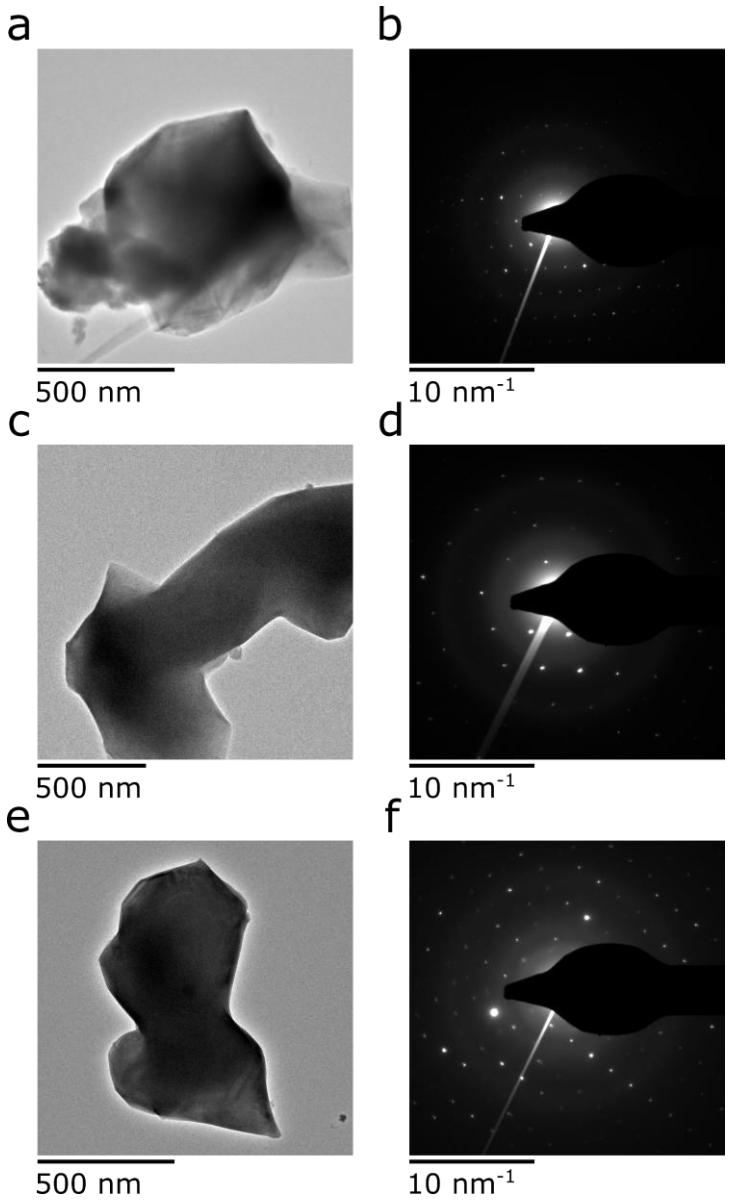

Figure E4. Collection of representative low magnification TEM images and corresponding electron diffraction patterns showing individual or fused particles from LLZTO synthesized using HB-MSS 550 °C. Note that the particle in (**a,b**) has only one set of bright diffraction spots and another very dim set, while the particles in (**c,d**) and (**e,f**) have two clear sets of diffraction spots. These results indicate that the LLZTO particles produced via HB-MSS are not highly polycrystalline and imply that individual nuclei are single crystals that may fuse together.

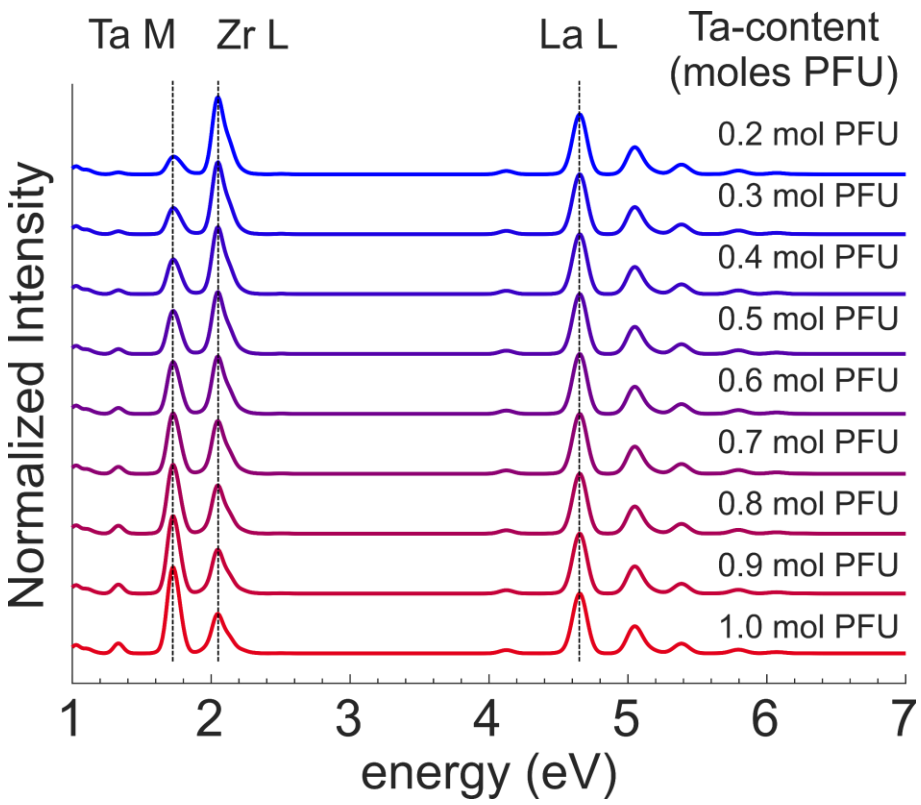

Figure E5. Simulated SEM-EDS spectra (in this case with 15 keV accelerating voltage as an example) for $Li_{7-x}La_3Zr_{2-x}Ta_xO_{12}$ with $0.2 < x < 1$ used to generate a regression to assess composition of individual LLZTO particles or grains.

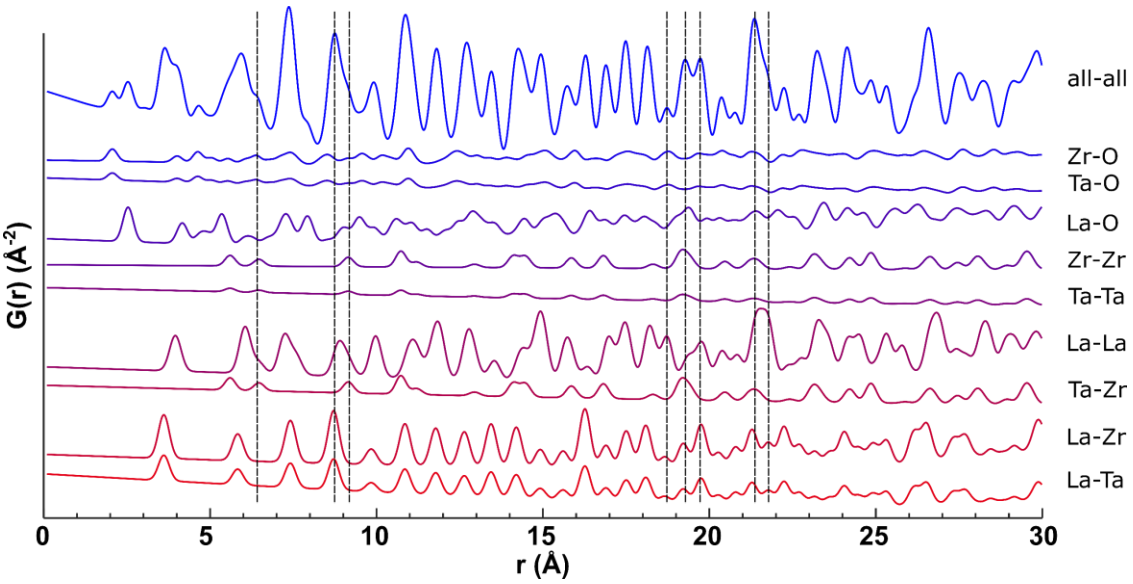

Figure E6. Calculated total and partial x-ray PDF patterns for $Li_{6.4}La_3Zr_{1.4}Ta_{0.6}O_{12}$ generated using pdfGUI with the CIF file from Logéat[48] et al. The dotted lines correspond to those indicated in **Figure 7.4** and show which atom pairs contribute to the overall signal intensity in the full calculated and experimental PDFs.

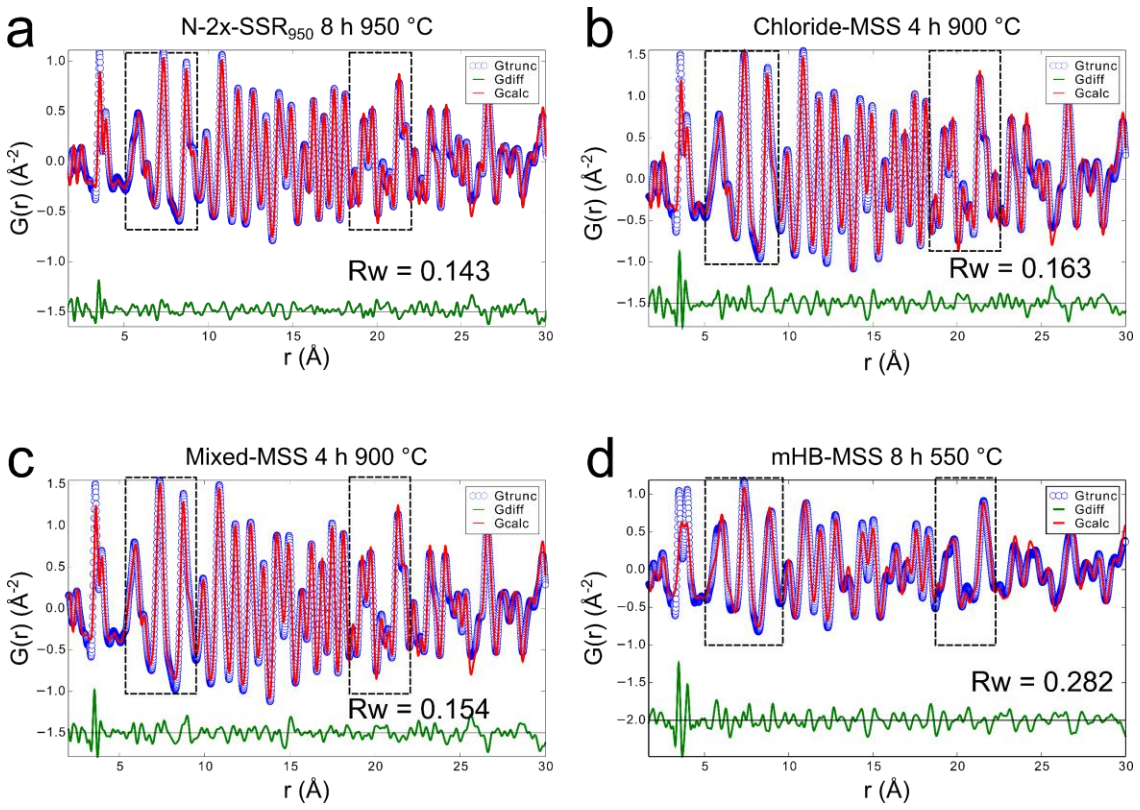

Figure E7. Refinements of PDFs for **a)** N-2x-SSR_{950} (2x 950 °C, 2x 8 h, nanosized ZrO_2 and pre-ball-milled Ta_2O_5 as reagents), **b)** Chloride-MSS (900 °C 4 h), **c)** Mixed-MSS (900 °C 4 h, **d)** mHB-MSS (8 h 550 °C). Blue circles indicate experimental data points, red lines are calculated PDFs, and green lines indicate the difference curve between experimental data and calculated PDFs respectively. The R_w values (indicating closeness of fit to the structural model) are best for the N-2x-SSR_{950} sample, which had the highest synthesis temperature and longest synthesis duration. The high temperature Chloride-MSS and Mixed-MSS samples also have reasonably good fits, while the mHB-MSS sample (550 °C) has a poor fit to the $Li_{6.4}La_3Zr_{1.4}Ta_{0.6}O_{12}$ $Ia\bar{3}d$ structural model. The standard deviation of Ta-content in the N-2x-SSR_{950}, Chloride-MSS, and mHB-MSS LLZTO powder samples are 0.107, 0.139, and 0.176 moles per formula unit respectively based on EDS analysis. While the fit quality of N-2x-SSR_{950} is the best, it is only marginally better than the Chloride-MSS sample, which has markedly higher deviation in composition, while the mHB-MSS sample has both the highest deviation in composition and worst fit quality. Black dotted boxes indicate regions of distinct features that are poorly fit in the mHB-MSS sample and correspond to the regions of 5-10 and 18-22 Å, which are highlighted in **Figure 7.4**.

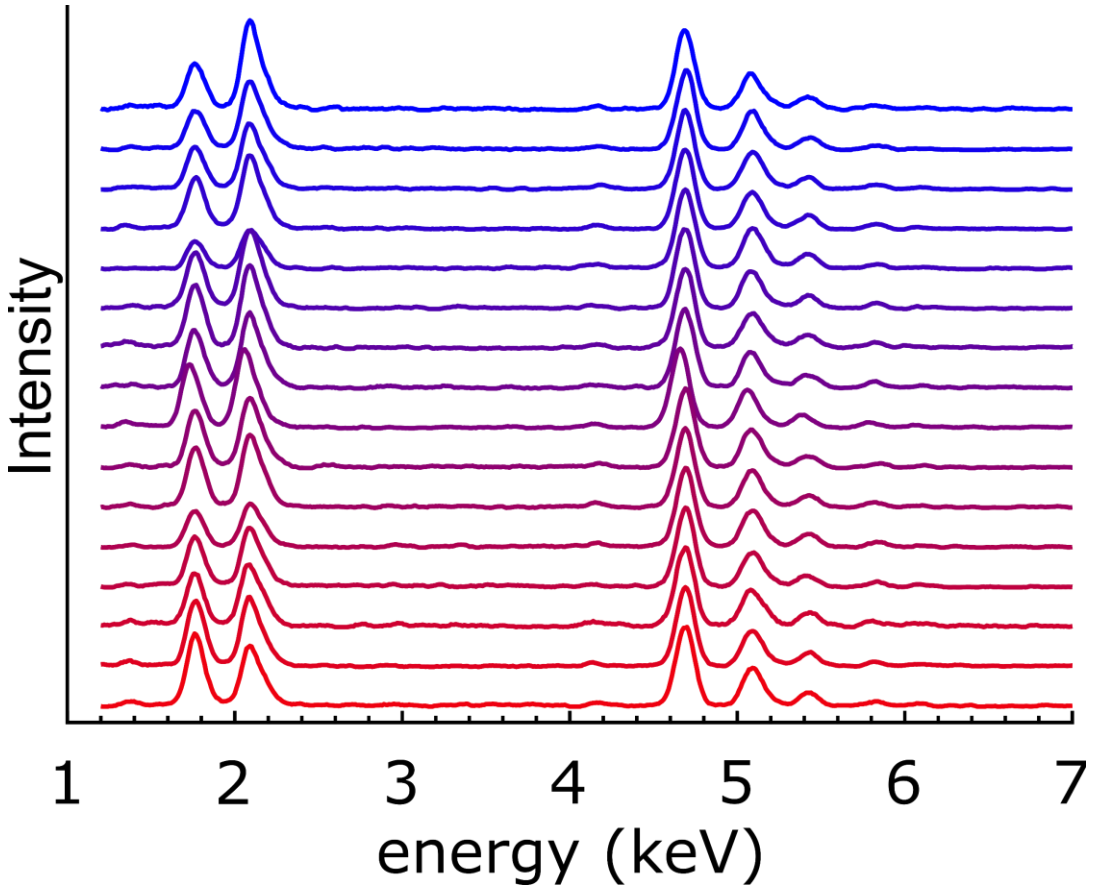

Figure E8. SEM-EDS spectra of 1x-SSR_{1000} pellet sintered at 1100 °C for 12 h (corresponding to the sample in **Figure 7.8**).

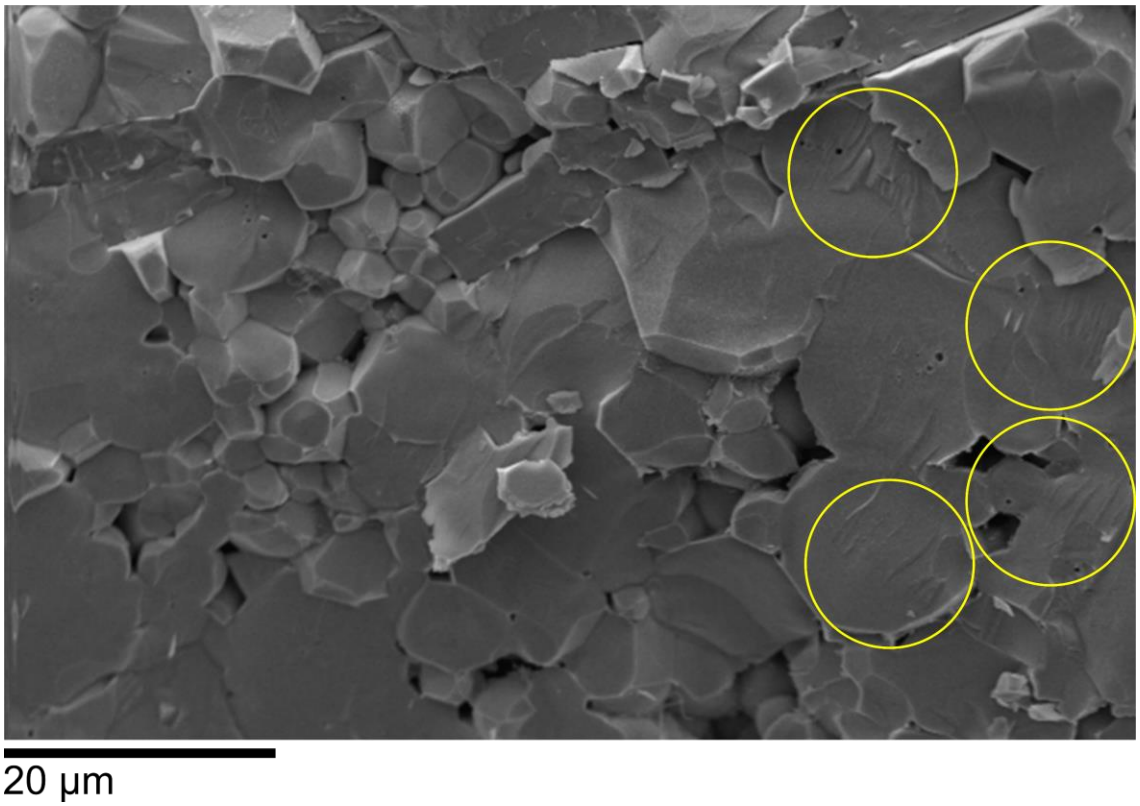

Figure E9. SEM fracture surface image of an HB-MSS LLZTO pellet with areas of striations marked indicating fracture of a tetragonal or partially tetragonal ceramic.

APPENDIX F

LIST OF PEER REVIEWED PUBLICATIONS RESULTING FROM PH.D. STUDIES

2021

1. Ahsan, M. A., Santiago, A. R. P., Sanad, M. F., **Weller, J. M.**, Fernandez-Delgado, O., Barrera, L. A., Maturano-Rojas, V., Alvarado-Tenorio, B., Chan, C. K., Noveron, J. C., Tissue paper-derived porous carbon encapsulated transition metal nanoparticles as advanced non-precious catalysts: Carbon-shell influence on the electrocatalytic behaviour. *Journal of Colloid and Interface Science*, (**2021**), 581, Part B, 905-918, https://doi.org/10.1016/j.jcis.2020.08.012 (accepted 8/3/2020)

2. Dopilka, A., **Weller, J. M.**, Ovchinnikov, A., Childs, A., Bobev, S., Peng, X., Chan C. K., Structural Origin of Reversible Li Insertion in Guest-Free, Type II Silicon Clathrates. *Advanced Energy and Sustainability Research*, (**2021**), https://doi.org/10.1002/aesr.202000114 (first published 2/5/2021)

3. **Weller, J. M.**, Dopilka, A., Chan C. K., Observation of Elemental Inhomogeneity in Li-Conducting Garnets and its Impact on Ionic Conductivity. *Advanced Energy and Sustainability Research*, (**2021**), https://doi.org/10.1002/aesr.202000109 (first published 2/23/2021)

2020

4. **Weller, J. M.**, Chan, C. K., Reduction in Formation Temperature of Ta-Doped Lithium Lanthanum Zirconate by Application of Lux–Flood Basic Molten Salt Synthesis. *ACS Applied Energy Materials*, (**2020**), 3, 7, 6466–6475

5. **Weller, J. M.**, Chan C. K., Pyrochlore Nanocrystals as Versatile Quasi-Single-Source Precursors to Lithium Conducting Garnets. *Journal of Materials Chemistry A*, (**2020)**, 8, 17405-17410, https://doi.org/10.1039/D0TA05842D

6. Badami, P., **Weller, J. M.**, Wahab, A., Redhammer, G., Ladenstein, L., Rettenwander, D., Wilkening, M., Chan C. K., Kannan, A. N. M., Highly Conductive Garnet-Type Electrolytes: Access to $Li_{6.5}La_3Zr_{1.5}Ta_{0.5}O_{12}$ Prepared by Molten Salt and Solid-State Methods. *ACS Applied Materials & Interfaces*, (**2020**), 12(43), 48580–48590. https://doi.org/10.1021/acsami.0c14056

7. Ahsan, M. A., Santiago, A. R. P., Sanad, M. F., **Weller, J. M.**, Fernandez-Delgado, O., Barrera, L. A., Maturano-Rojas, V., Alvarado-Tenorio, B., Chan, C. K., Noveron, J. C., Metal-Organic frameworks-derived multifunctional carbon encapsulated metallic nanocatalysts for catalytic peroxymonosulfate activation

and electrochemical hydrogen generation. *Molecular Catalysis*, (**2020**), 498, 111241, 10.1016/j.mcat.2020.111241

2019

1. **Weller, J.M.**; Whetten, J.A.; Chan, C.K. Nonaqueous polymer combustion synthesis of cubic $Li_7La_3Zr_2O_{12}$ nanopowders. *ACS Applied Materials & Interfaces* (**2020**), 12, 1, 953–962 (accepted 12/4/2019)

2. Rosenthal, T.; **Weller J.M.**; Chan, C.K. Needleless electrospinning for high throughput production of $Li_7La_3Zr_2O_{12}$ solid electrolyte nanofibers. *Industrial & Engineering Chemistry Research* 58 (37) 17399-17405 (**2019**). DOI: 10.1021/acs.iecr.9b03376

2018

1. Dopilka, A.; Zhao, R.; **Weller, J.M.**; Bobev, S.; Peng, X.; Chan, C.K. Experimental and computational study of the lithiation of $Ba_8Al_yGe_{46-y}$ based Type I germanium clathrates. *ACS Applied Materials & Interfaces*, 10 (44), 37981 – 37992 (**2018**). doi:10.1021/acsami.8b11509

2. Jing, H.; Cheng, Q.; **Weller, J.M.**; Chu, X.S.; Wang, Q.H.; Chan, C.K. Synthesis of TiO_2 nanosheet photocatalysts from exfoliation of TiS_2 and hydrothermal treatment. *Journal of Materials Research*, 33 (21), 3540 – 3548 (**2018**). doi.org/10.1557/jmr.2018.165

3. **Weller, J.M**.; Whetten, J.A.; Chan, C.K. Synthesis of fine cubic $Li_7La_3Zr_2O_{12}$ powders in molten LiCl-KCl eutectic and facile densification by reversal of Li^+/H^+ exchange. *ACS Applied Energy Materials*, 1 (2), 552 – 560 (**2018**). doi:10.1021/acsaem.7b00133.

2017

1. Zhao, R.; Bobev, S.; Krishna, L.; Yang, T.; **Weller, J.M.**; Jing, H.; Chan, C.K. Anodes for lithium-ion batteries based on type I silicon clathrate $Ba_8Al_{16}Si_{30}$ – role of processing on surface properties and electrochemical behavior. *ACS Applied Materials & Interfaces*, 9, 41246 – 41257 (**2017**). doi: 10.1021/acsami.7b12810

2. Chan, C.K.; Yang, T.; **Weller, J.M.** Nanostructured garnet-type $Li_7La_3Zr_2O_{12}$: Synthesis, properties, and opportunities as electrolytes for Li-ion batteries. *Electrochimica Acta*, 253, 268 – 280 (**2017**). doi: 10.1016/j.electacta.2017.08.130.

Book Chapters

1. **Weller, J.M**.; Chan, C.K. "Chapter 2. Synthesis of Nanostructured Garnets", In Solid Electrolytes for Advanced Applications. Murugan, R. and Weppner, W., (Eds). Springer Nature Switzerland AG, (**2019**). https://link.springer.com/book/10.1007/978-3-030-31581-8.

APPENDIX G

PERMISSIONS FROM ALL CO-AUTHORS

All co-authors have been contacted and have granted permission to use copyrighted materials in this Dissertation.

APPENDIX H

PERMISSIONS TO USE COPYRIGHTED MATERIAL WHOLE OR IN PART WITHIN THIS DISSERTATION FROM THE AMERICAN CHEMICAL SOCIETY, THE ROYAL SOCIETY OF CHEMISTRY, AND WILEY

Nonaqueous Polymer Combustion Synthesis of Cubic Li7La3Zr2O12 Nanopowders

Author: J. Mark Weller, Justin A. Whetten, Candace K. Chan

Publication: Applied Materials

Publisher: American Chemical Society

Date: Jan 1, 2020

Synthesis of Fine Cubic Li7La3Zr2O12 Powders in Molten LiCl–KCl Eutectic and Facile Densification by Reversal of Li /H Exchange

ACS Publications Most Trusted. Most Cited. Most Read.

Author: J. Mark Weller, Justin A. Whetten, Candace K. Chan

Publication: ACS Applied Energy Materials

Publisher: American Chemical Society

Date: Feb 1, 2018

Reduction in Formation Temperature of Ta-Doped Lithium Lanthanum Zirconate by Application of Lux–Flood Basic Molten Salt Synthesis

Author: J. Mark Weller, Candace K. Chan
Publication: ACS Applied Energy Materials
Publisher: American Chemical Society
Date: Jul 1, 2020

Content in **Chapter 3** partially reprinted (adapted) with permission from

"Weller, J. M., Whetten, J. A., & Chan, C. K. (2020). Non-Aqueous Polymer Combustion Synthesis of Cubic $Li_7La_3Zr_2O_{12}$ Nanopowders. ACS Applied Materials & Interfaces, 12(1), 953–962. https://doi.org/10.1021/acsami.9b19981"

Content in **Chapter 4** partially reprinted (adapted) with permission from

"Weller, J. M., Whetten, J. A., & Chan, C. K. (2018). Synthesis of Fine Cubic $Li_7La_3Zr_2O_{12}$ Powders in Molten LiCl-KCl Eutectic and Facile Densification by Reversal of Li^+/H^+ Exchange. ACS Applied Energy Materials, 1(2), 552–560. https://doi.org/10.1021/acsaem.7b00133"

Content in **Chapter 5** partially reprinted (adapted) with permission from

"Weller, J. M., & Chan, C. K. (2020). Reduction in Formation Temperature of Ta-Doped Lithium Lanthanum Zirconate by Application of Lux-Flood Basic Molten Salt Synthesis. ACS Applied Energy Materials, 3(7), 6466–6475. https://doi.org/10.1021/acsaem.0c00716"

"Weller, J. M., & Chan, C. K. (2020). Pyrochlore Nanocrystals as Versatile Quasi-Single-Source Precursors to Lithium Conducting Garnets. Journal of Materials Chemistry A, 8, 17405–17410. https://doi.org/10.1039/d0ta05842d" - Published by The Royal Society of Chemistry. (**Chapter 6**)

"Weller, J. M., Dopilka, A., Chan C. K., Observation of Elemental Inhomogeneity in Li-Conducting Garnets and its Impact on Ionic Conductivity. *Advanced Energy and Sustainability Research*, (**2021**), (accepted 2/19/2021) https://doi.org/10.1002/aesr.202000109" – Copyright 2021 (The Authors), Published by Wiley-VCH GmbH (**Chapter 7**)